

Università degli Studi di Napoli Federico II

Scuola Politecnica e delle Scienze di Base

Area didattica di Scienze Matematiche, Fisiche e Naturali

**Dipartimento di Scienze della Terra, dell'Ambiente e delle Risorse
(DiSTAR)**



***DOTTORATO DI RICERCA IN SCIENZE DELLA TERRA,
DELL'AMBIENTE E DELLE RISORSE – XXXIII ciclo***

***INTEGRATED MULTI-SCALE METHODS FOR MODELING
THE DEFORMATION FIELD OF VOLCANIC SOURCES***

Supervisor

Prof. Maurizio Fedi

Prof. Valeria Paoletti

Co-Supervisor

Dr. Raffaele Castaldo (IREA – CNR)

Dr. Pietro Tizzani (IREA – CNR)

Ph.D. Candidate

Andrea Barone

Anno accademico 2020/2021

ABSTRACT	5
INTRODUCTION	6
1- DEFORMATION FIELD: ELASTIC PROBLEM	12
1.1 – General solution of deformation field and its biharmonic properties.....	13
1.2 – Harmonic properties of the deformation field.....	19
1.3 – Homogeneity and local-homogeneity properties of harmonic deformation field.....	23
2- MODELING OF VOLCANIC SOURCES	25
2.1 – Analytical models satisfying the general solution.....	26
2.1.1 – <i>Induced horizontal fractures</i>	26
2.1.2 – <i>Shear and tensile faults</i>	27
2.1.3 – <i>Finite spherical magma body</i>	29
2.1.4 – <i>Dipping finite prolate spheroid</i>	29
2.1.5 – <i>Vertical volcanic conduits</i>	30
2.2 – Analytical models satisfying the Laplace’s equation.	32
2.2.1 – <i>The Mogi’s source</i>	32
2.2.2 – <i>The Prism source</i>	33
2.3 – Inherent limitations of parametric inverse algorithms.....	35
2.4 – Tomographic inverse algorithms.....	38
2.5 – Integrated multi-scale methods and procedures.....	41
2.5.1 – <i>Multiridge method</i>	41
2.5.2 – <i>ScalFun method</i>	43
2.5.3 – <i>THD technique</i>	46
2.5.4 – <i>Functional transformations for the ground deformation field</i>	47

3- APPLICATION TO HARMONIC DEFORMATION FIELDS: SYNTHETIC CASES.....	50
3.1 – Validation of the Upward Continuation transform.....	51
3.2 – Use of integrated multi-scale methods.....	54
3.2.1 – <i>Geometric parameters detection of regular sources</i>	54
3.2.2 – <i>Geometric parameters detection of irregular sources</i>	68
3.2.3 – <i>Geometric parameters detection of biharmonic field sources</i>	80
4- APPLICATION TO REAL CASES.....	87
4.1 – Multiridge and ScalFun methods: the Okmok volcano (Alaska, USA) analysed with LOS components.....	88
4.2 – Multiridge method: the Uturuncu volcano (Bolivia) analysed with cumulative vertical deformation.....	91
4.3 – THD technique: the 2012 – 2013 uplift event at Campi Flegrei caldera (Italy).....	101
4.4 – Multiridge and ScalFun methods: the Fernandina volcano (Galapagos Archipelago, Ecuador) analysed with cumulative E-W deformation.....	109
4.5 – Integrated multi-scale methods: the Yellowstone caldera (Wyoming, USA) analysed with cumulative vertical deformation.....	124
5- DISCUSSION.....	135
5.1 – Comments on the applications to the synthetic cases.....	137
5.2 – Comments on the applications to the real cases.....	141
5.2.1 – <i>The case study of Okmok volcano</i>	141
5.2.2 – <i>The multi-source case study of Uturuncu volcano</i>	142
5.2.3 – <i>The THD technique as supporting tool for Campi Flegrei caldera</i>	145
5.2.4 – <i>Source shape detection at Fernandina volcano via homogeneity properties of the ground deformation field</i>	149
5.2.5 – <i>Source analysis at Yellowstone caldera via local-homogeneity properties of the ground deformation field</i>	151

CONCLUSIONS.....153

APPENDIX A.....156

APPENDIX B.....157

APPENDIX C.....159

APPENDIX D.....163

REFERENCES.....169

ACKNOWLEDGEMENTS.....183

ABSTRACT

The modeling of volcanic deformation sources represents a crucial task for investigating and monitoring the activity of magmatic systems. In this framework, inverse methods are the most used approach to image deforming volcanic bodies by considering the assumptions of the elasticity theory. However, several issues affect the inverse modeling and the interpretation of the ground deformation phenomena, such as the inherent ambiguity, the theoretical ambiguity and the related choice of the forward problem. Despite assuming appropriate a priori information and constraints, we are led to an ambiguous estimate of the physical and geometrical parameters of volcanic bodies and, in turn, to an unreliable analysis of the hazard evaluation and risk assessment.

In this scenario, we propose a new approach for the interpretation of the large amount of deformation data retrieved by the SBAS-DInSAR technique in volcanic environments. The proposed approach is based on the assumptions of the homogeneous and harmonic elastic fields, which satisfy the Laplace's equation; specifically, we consider Multiridge, ScalFun and THD methods to provide in a fast way preliminary information on the active volcanic source, even for the analysis of complex cases, such as the depth, the horizontal position, the geometrical configuration and the horizontal extent.

In this thesis, firstly we analyse the biharmonic general solution of the elastic problem to state the deformation field surely satisfy the Laplace's equation in the case of hydrostatic pressure condition within a source embedded in a homogeneous elastic half-space. Then, we show the results of different simulations by highlighting how the proposed approach allows overcoming many ambiguities since it provides unique information about the geometrical parameters of the active source. Finally, we show the results of Multiridge, ScalFun and THD methods used for the analysis of the deformation components recorded at Okmok volcano, Uturuncu volcano, Campi Flegrei caldera, Fernandina volcano and Yellowstone caldera.

We conclude this thesis by remarking the proposed approach represents a crucial tool for fixing modeling ambiguities and to provide useful information for monitoring purposes and/or for constraining the geometry of the volcanic systems.

INTRODUCTION

Volcanic systems are nowadays investigated and monitored by using data related to different disciplines of Earth Sciences; among these, the ground deformation has been increasingly used after the development of the remote sensing technologies, allowing the measurements acquisition from both proximal and remote platforms [Sigurdsson, 1999; Dzurisin, 2007]. In particular, the Global Navigation Satellite System (GNSS) and the Differential SAR Interferometry (DInSAR) technique are now able to quickly provide a large amount of data, which is helpful to understand the ground deformation phenomenon and to retrieve information about the changes of physical and geometrical parameters of deep and shallow volcanic reservoirs [Avallone et al., 1999; Amoruso et al., 2014; D'Auria et al., 2015; Henderson et al., 2017; Pepe et al., 2019; Aloisi et al., 2020; Xue et al., 2020; Chauhan et al., 2020; Rodriguez-Molina et al., 2021].

Despite of its relatively good accuracy, GNSS measurements only provide time information about selected points, while DInSAR images areal deformation fields throughout the whole interested site and its surroundings [Fernandez et al., 2003]. Also, with the development and refinement of processing algorithm, such as the Small BAseline Subset (SBAS) [Berardino et al., 2004], the ground deformation field can be densely sampled over time. Although the modeling of volcanic deformation sources is still a tricky task, the use of this data for imaging deforming volcanic bodies represents a great approach to provide a crucial contribution in the framework of the hazard evaluation and of the risk assessment analyses [Lanari et al., 1998; Bigg et al., 2017].

From a physical point of view, we should treat the volcanic processes like to complex scenarios, such as viscoelastic or thermoelastic systems [Newman et al., 2006; Del Negro et al., 2009; Castaldo et al., 2017]; in these cases, the retrieved model makes sense if the parameters distribution of the volcanic system, as temperature, pressure, mechanical properties, physical moduli, and others, is available over space and time [Gottsmann et al., 2017]. However, this information is often unknown and its management in any modeling procedure is not very fast; therefore, this approach can be rarely considered.

The elasticity theory represents a well-established option [Dzurisin, 2007; Battaglia et al., 2013] in low computation time. In particular, two approaches are mainly considered for modeling the volcanic deformation sources: the forward modeling [Lu et al., 1998; Lu et al., 2000], based on a trial-error procedure, depends on the experience of the scientist

and on previous knowledge about the considered volcanic site; the inverse modeling [Cervelli et al., 2001; Battaglia et al., 2013], which is faster than the previous approach, is more suitable for monitoring aims and it is often preferred to the others.

The most widely used methods of inverse modeling often approximate the volcanic reservoirs to one source with geometrically regular shape. Specifically, each parameter of the causative body is described by a single value and, so, we call this approach as parametric inverse methods because their goal is the estimate of a few source parameters [Cervelli et al., 2001].

The parametric inverse approach usually considers as forward problems the volcanic deformation source Analytical Models (AM) or models by Finite Element Methods (FEM) [Masterlark et al., 2012; Walter et al., 2014; Henderson et al., 2017; Castaldo et al. 2018a]. In this framework, the AM are often preferred since they provide acceptable solutions to the inverse problem in shorter computation time.

However, the most used AM [Mogi, 1958; Sun, 1969; Okada, 1985; McTigue, 1987; Yang and Davis, 1988; Bonaccorso and Davis, 1999] are rarely able to well simulate the real physical context, leading to only model magmatic bodies embedded in homogeneous elastic half-spaces; in some cases, the AM also do not fully comply with the physical assumptions of the forward problem, as that about the pressure distribution along the source boundaries (i.e., [Yang and Davis, 1988]). In addition, 3D volcanic reservoirs have been approximated by regular sources where the physical parameters are null within regular volumes excepted at their boundaries (e.g., [Yang and Davis, 1988] and [Okada, 1985]) and, for this reason, a large overestimation of the acting source pressure could occur [Aloisi et al., 2011]. Finally, for complex and multi-source scenarios, the use of AM is often unsuitable to characterize the number and/or the type of the acting volcanic processes [Pritchard et al., 2004; Henderson et al., 2017; Chang et al., 2010; Aly and Cochran, 2011; Tizzani et al., 2015].

In this framework, FEM allows a less constrained management about the deforming system parameters; we could indeed model the volcanic region as a layered half-space [Manconi et al., 2010] or the magmatic body as an irregular volume with different deformation mechanisms. However, FEM provides acceptable solutions to the inverse problem only if many parameters are well constrained. Furthermore, the computation time increases with complex scenario, requiring a dense distribution of the mesh.

To avoid all these issues, Camacho et al. [2011; 2020] proposed a tomographic inverse procedure for the 3D elastic multi-source modeling through aggregates of elemental sources [Camacho et al., 2007]. In this case, the goal is the estimate of many source parameters. This approach provides in a fast way information about complex and multi-source scenarios with different deformation mechanisms. However, as for most of the tomographic algorithms, the acceptable solution depends on the a priori information, as the 3D partition of the volcanic system and the smoothing factor [Camacho et al., 2020].

The interpretation of deformation fields in the volcanic environment is therefore a complicated task because of several ambiguities.

The first, the inherent ambiguity [Fedi et al., 2005], regards the definition of the forward problem; consider the simplest case of the Mogi's model [Mogi, 1958],

$$\mathbf{u} = \begin{pmatrix} a^3 \Delta P \frac{1-\nu}{G} \frac{x-x_0}{|\mathbf{R}|^3} \\ a^3 \Delta P \frac{1-\nu}{G} \frac{y-y_0}{|\mathbf{R}|^3} \\ a^3 \Delta P \frac{1-\nu}{G} \frac{z-z_0}{|\mathbf{R}|^3} \end{pmatrix} \quad (1),$$

where a , ΔP and (x_0, y_0, z_0) are the radius, the pressure variation and the centre coordinates of the source, respectively, while ν and G represent the physical elastic parameters of the half-space and $|\mathbf{R}| = \sqrt{(x - x_0)^2 + (y - y_0)^2 + (z - z_0)^2}$. Equation (1) shows that different combinations of the parameters a , ΔP , ν and G may be the cause of the same deformation dataset; consequently, we can solve the inverse problem for deformation field by determining only the source depth and horizontal position.

A second ambiguity refers to the inverse modeling algorithm; the final solution indeed depends on the a priori information and the availability of constraining information. For example, tomographic inverse algorithms can provide acceptable models for different combination of the half-space partition and the smoothing factor parameters [Camacho et al., 2011]. AM parametric inverse modeling represents another example; in this framework, the determination of the source shape by analysing several forward problems for the same deformation dataset is a widely considered approach. We find that different model configurations will characterize the system with an acceptable

misfit, so that we can interpret the volcanic phenomenon in several ways [Bagnardi et al., 2013; Pepe et al., 2017].

Solving the forward problem with a wrong source geometry or with a gross mesh instead leads to a theoretical form of ambiguity. In particular, the use of an inappropriate forward problem may cause the errors on the source depth and/or its pressure variation [Fialko et a., 2001].

Other kinds of ambiguity usually characterize the interpretation of any field. For example, a sampling ambiguity arises because we always use discrete datasets to completely represent a continuous field from the source and, in the case of tomographic inverse approach, we always face an algebraic ambiguity, because the discretized source distribution leads to a system with more unknowns than data, unless reliable prior information could force the problem toward a mesh which makes the problem determined [Fedi et al., 2005].

Finally, we list the error ambiguity since experimental/instrumental errors always affect measured data and our models can no longer generate data overfitting. In this framework, we also include errors propagated by a poor distribution of the measurements, so causing a strong interpolation data error and, in turn, a related model one.

In this scenario, by considering the large amount of deformation points of the SBAS-DInSAR technique and the assumptions of the elasticity theory [Love, 1906], we propose a new approach for the interpretation of the deformation field in volcanic environments, which can provide in a fast way preliminary information on the active volcanic source, useful for monitoring purposes and/or as constraints for a more refined subsequent inverse modeling.

The proposed approach is based on studying whether the deformation field could satisfy the Laplace's equation,

$$\nabla^2 V = 0 \quad (2),$$

where $\nabla^2 = \frac{\partial^2}{\partial x^2} + \frac{\partial^2}{\partial y^2} + \frac{\partial^2}{\partial z^2}$ and V represent the Laplacian operator and the potential function (or any of its any-order derivatives), respectively. The solutions of this problem, which is the simplest example of elliptic partial differential equations, are the so-called

harmonic functions, and the related theory is often referred to as the Potential Field Theory (PFT) [Baranov, 1975; Blakely, 1996].

Besides this, we will also consider deformations satisfying the homogeneity equation [Olmsted, 1961],

$$f(tx, ty, tz) = t^n f(x, y, z) \quad (3),$$

where $t > 0$ and $n \in \mathbb{R}$ is the homogeneity degree of the homogeneous field $f(x, y, z)$. We specify that n can also take on fractional values, corresponding to fractional distributions of the source property, along the lines described by Fedi et al. [2015]. Regarding the homogeneity equation, we note that real fields are often inhomogeneous; in this case, we will consider the generalized form of equation (3) into a multi-homogeneity law [Fedi et al., 2015].

In this perspective, we will study the ground deformation field by using methodologies that have been already applied in the PFT framework (e.g., [Milano et al., 2016; Chauhan et al., 2018; Vitale and Fedi, 2020]), namely Multiridge [Fedi et al., 2009] and ScalFun [Fedi, 2007] methods, which are based on a *multi-scale* procedure; from now on, with the term *scale* we will refer to the distance between the field source and the measurement surface.

Specifically, this approach is based on the simplifying assumptions of the homogeneous and harmonic fields; in this framework, it allows overcoming many of the above-described limitations about the AM parametric and tomographic inverse methods:

- (I) it provides unique information about the geometrical parameters of source, such as its depth, its horizontal position and its morphological attributes;
- (II) it is stable vs. noise;
- (III) it is not affected by the distribution of the elastic parameters, within the elastic regime (i.e., small variations over the space and time);
- (IV) it provides geometrical information even for only one field component;
- (V) it is useful to solve complex multi-source cases, allowing the modeling of more than one source for a single deformation dataset;
- (VI) it is fast and not computationally expensive.

As we said, this methodology assumes that the ground deformation field [Love, 1906] is not only biharmonic but also harmonic (i.e., it also satisfies the Laplace's equation). This condition will surely occur in the case of hydrostatic pressure condition within a source embedded in a homogeneous elastic half-space. We remark this assumption also characterizes almost all the forward problems of the inverse modeling.

Among the properties of the harmonic functions, we also point out an edge detection technique, defined as Total Horizontal Derivative (THD), which has been already used in the PFT framework [Cella et al., 2015; Paoletti et al., 2017]. The technique allows estimating the horizontal extent of the deformation source, which is a very useful constraint for the final physical and geometrical model.

We organize this thesis as follows. Firstly, in the Chapter 1, we start from the biharmonic properties of the general solution of the elastic problem to understand the conditions under which the Laplace's equation is satisfied.

Then, in the Chapter 2, we briefly introduce the forward problems of the most used modeling approaches and describe the integrated multi-scale methods.

After, in the Chapter 3, we apply the proposed approach to simulated ground deformation patterns, generated by regular source shapes and we briefly introduce the case of geometrically irregular bodies. We analyse fields that enjoy either the harmonic or biharmonic properties to highlight the advantages and limitations of the proposed methods.

Finally, in the Chapters 4 and 5, we analyse five ground deformation patterns, that are related to the Okmok volcano (Alaska, USA), the Uturuncu volcano (Bolivia), the Campi Flegrei caldera (Italy), the Fernandina volcano (Galapagos archipelago, Ecuador) and the Yellowstone caldera (Wyoming, USA), and we highlight how this new approach represents a crucial tool for fixing modeling ambiguities and to provide constraints on the geometry of the volcanic systems.

We conclude this thesis by illustrating the future developments for the modeling of volcanic deformation source through DInSAR measurements, especially for the hazard evaluation and the risk assessment analyses of volcanoes monitoring activities.

CHAPTER 1

DEFORMATION FIELD: ELASTIC PROBLEM

In this chapter, we introduce the basic notions of the Elasticity theory [Love, 1906]. We start from the biharmonic properties of the general solution for the deformation field, and we define the conditions so that the elastic problem can be reduced to a particular solution for which the Laplace's equation is satisfied, so allowing the use of multi-scale methods for interpreting ground deformation patterns in volcanic environments. After, we discuss on the homogeneity theory and we briefly introduce the local-homogeneity approach [Fedi et al., 2015].

The solution of the elastic problem which satisfies the Laplace's equation derives from the Love's study about the Elasticity Theory [Love, 1906]; accordingly, the deformation field is the gradient of a single scalar function when the rotation component of the strain tensor vanishes, that is when the curl of the field is null.

In other works, the authors have also decomposed the deformation field with functions that satisfy the Laplace's equation (e.g., Helmholtz decomposition [Love, 1906; Sadd, 2005], Galerkin vector [Galerkin, 1930; Sadd, 2005] and Papkovitch-Neuber functions [Papkovich, 1932; Sadd, 2005]). However, the resulting fields still correspond to biharmonic functions according to the Almansi's theorem [Almansi, 1899], except for the solution of the Lamé's Strain Potential [Sadd, 2005].

1.1 General solution of deformation field and its biharmonic properties.

Generally, any system begins to deform when the acting stress field is not null and, for the elastic regime, the deformations are completely recoverable in the case of vanishing of the causative stress [Lowrie, 2007].

The tensor σ_{ij} defines the physical dimension of the stress [Sadd, 2005]:

$$\sigma_{ij} = \begin{bmatrix} \sigma_{xx} & \tau_{xy} & \tau_{xz} \\ \tau_{yx} & \sigma_{yy} & \tau_{yz} \\ \tau_{zx} & \tau_{zy} & \sigma_{zz} \end{bmatrix} \quad (1.1),$$

where σ_{xx} , σ_{yy} , σ_{zz} and τ_{xy} , τ_{xz} , τ_{yx} , τ_{yz} , τ_{zx} , τ_{zy} are called normal and shearing stresses, respectively. The stress matrix σ_{ij} characterizes each deformative mechanisms; for example, in the case of hydrostatic pressure condition P of volcanic reservoirs, σ_{ij} corresponds to [Sadd, 2005]:

$$\sigma_{ij} = \begin{bmatrix} P & 0 & 0 \\ 0 & P & 0 \\ 0 & 0 & P \end{bmatrix} \quad (1.2).$$

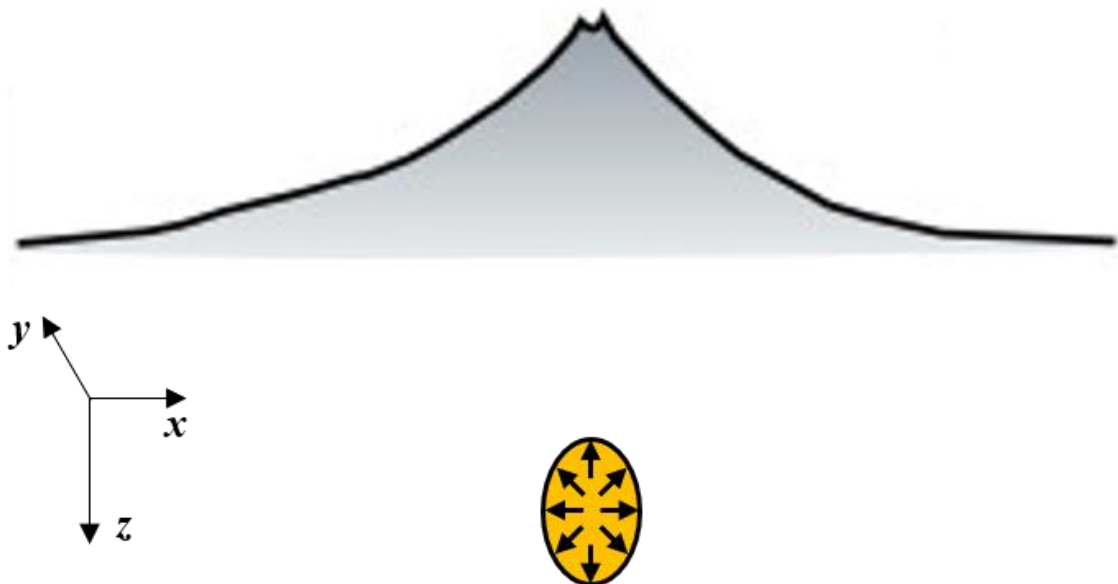


Figure 1.1. Sketch of volcanic hydrostatic pressure condition (dilatation). 2D sketch of a magma chamber (orange body), where the black arrows indicate the boundary conditions of hydrostatic pressure; the grey body and the black continuous line represents the volcanic edifice (modified from Gudmundsson [2012]).

The strain tensor e_{ij} describes the change in space of any point respect to its starting position, when a stress field is not null, as follows [Sadd, 2005],

$$e_{ij} = \begin{bmatrix} \frac{\partial u}{\partial x} & \frac{\partial u}{\partial y} & \frac{\partial u}{\partial z} \\ \frac{\partial v}{\partial x} & \frac{\partial v}{\partial y} & \frac{\partial v}{\partial z} \\ \frac{\partial w}{\partial x} & \frac{\partial w}{\partial y} & \frac{\partial w}{\partial z} \end{bmatrix} \quad (1.3),$$

where:

$$\mathbf{u} = \begin{pmatrix} u \\ v \\ w \end{pmatrix} \quad (1.4)$$

represents the deformation field; its three-components characterize each point in space and time [Sadd, 2005].

In the elastic regime, the Hooke's Law describes the relation between the applied stresses σ_{ij} and the occurred strain e_{ij} ; in particular, the generalized form of this law for linear isotropic elastic solids can be expressed as follows [Sadd, 2005]:

$$\sigma_{ij} = \lambda e_{kk} \delta_{ij} + 2\mu e_{ij} = \frac{E\nu}{2(1+\nu)} e_{kk} \delta_{ij} + \frac{E}{1+\nu} e_{ij} \quad (1.5),$$

where λ and μ , E , ν are the Lamè's constants, the Young's modulus, the Poisson's coefficient, respectively, while δ_{ij} is the Kronecker delta. Equation (1.5) can be written out in individual scalar equations as [Sadd, 2005]:

$$\sigma_{xx} = \lambda \left(\frac{\partial u}{\partial x} + \frac{\partial v}{\partial y} + \frac{\partial w}{\partial z} \right) + 2\mu \frac{\partial u}{\partial x} = \frac{E\nu}{2(1+\nu)} \left(\frac{\partial u}{\partial x} + \frac{\partial v}{\partial y} + \frac{\partial w}{\partial z} \right) + \frac{E}{1+\nu} \frac{\partial u}{\partial x} \quad (1.6.1),$$

$$\sigma_{yy} = \lambda \left(\frac{\partial u}{\partial x} + \frac{\partial v}{\partial y} + \frac{\partial w}{\partial z} \right) + 2\mu \frac{\partial v}{\partial y} = \frac{E\nu}{2(1+\nu)} \left(\frac{\partial u}{\partial x} + \frac{\partial v}{\partial y} + \frac{\partial w}{\partial z} \right) + \frac{E}{1+\nu} \frac{\partial v}{\partial y} \quad (1.6.2),$$

$$\sigma_{zz} = \lambda \left(\frac{\partial u}{\partial x} + \frac{\partial v}{\partial y} + \frac{\partial w}{\partial z} \right) + 2\mu \frac{\partial w}{\partial z} = \frac{E\nu}{2(1+\nu)} \left(\frac{\partial u}{\partial x} + \frac{\partial v}{\partial y} + \frac{\partial w}{\partial z} \right) + \frac{E}{1+\nu} \frac{\partial w}{\partial z} \quad (1.6.3),$$

$$\tau_{xy} = 2\mu \frac{\partial u}{\partial y} = \frac{E}{1+\nu} \frac{\partial u}{\partial y} \quad (1.6.4),$$

$$\tau_{yz} = 2\mu \frac{\partial v}{\partial z} = \frac{E}{1+\nu} \frac{\partial v}{\partial z} \quad (1.6.5),$$

$$\tau_{zx} = 2\mu \frac{\partial w}{\partial x} = \frac{E}{1+\nu} \frac{\partial w}{\partial x} \quad (1.6.6).$$

These stress-strain relations may be inverted to express the strain in terms of the stress; starting from equation (1.5) and setting the two free indices the same, we get [Sadd, 2005]

$$\sigma_{kk} = (3\lambda + 2\mu)e_{kk} \quad (1.7.1),$$

where:

$$\sigma_{kk} = \sigma_{xx} + \sigma_{yy} + \sigma_{zz} \quad (1.7.2),$$

$$e_{kk} = e_{xx} + e_{yy} + e_{zz} \quad (1.7.3).$$

We can solve equation (1.7.1) for e_{kk} and, substituting back into (1.5), we get:

$$e_{ij} = \frac{1}{2}\mu \left(\sigma_{ij} - \frac{\lambda}{3\lambda+2\mu} \sigma_{kk} \delta_{ij} \right) = \frac{1+\nu}{E} \sigma_{ij} - \frac{\nu}{E} \sigma_{kk} \delta_{ij} \quad (1.8),$$

in the index notation, and

$$\frac{\partial u}{\partial x} = \frac{1}{E} (\sigma_{xx} - \nu \sigma_{yy} - \nu \sigma_{zz}) \quad (1.9.1),$$

$$\frac{\partial v}{\partial y} = \frac{1}{E} (\sigma_{yy} - \nu \sigma_{zz} - \nu \sigma_{xx}) \quad (1.9.2),$$

$$\frac{\partial w}{\partial z} = \frac{1}{E} (\sigma_{zz} - \nu \sigma_{xx} - \nu \sigma_{yy}) \quad (1.9.3),$$

$$\frac{\partial u}{\partial y} = \frac{1+\nu}{E} (\tau_{xy}) \quad (1.9.4),$$

$$\frac{\partial v}{\partial z} = \frac{1+\nu}{E} (\tau_{yz}) \quad (1.9.5),$$

$$\frac{\partial w}{\partial x} = \frac{1+\nu}{E} (\tau_{zx}) \quad (1.9.6),$$

in the component form [Sadd, 2005].

The Hooke's Law, together with other conditions (not introduced here), leads to another important relation, the Navier's equation, which describes the behaviour of \mathbf{u} in the case of equilibrium condition between the surface and volume forces acting on the considered system [Sadd, 2005]:

$$\mu \nabla^2 \mathbf{u} + (\lambda + \mu) \nabla \nabla \cdot \mathbf{u} + \mathbf{F} = 0 \quad (1.10.1),$$

or

$$\begin{pmatrix} \mu \nabla^2 u + (\lambda + \mu) \frac{\partial}{\partial x} \left(\frac{\partial u}{\partial x} + \frac{\partial v}{\partial y} + \frac{\partial w}{\partial z} \right) + F_x \\ \mu \nabla^2 v + (\lambda + \mu) \frac{\partial}{\partial y} \left(\frac{\partial u}{\partial x} + \frac{\partial v}{\partial y} + \frac{\partial w}{\partial z} \right) + F_y \\ \mu \nabla^2 w + (\lambda + \mu) \frac{\partial}{\partial z} \left(\frac{\partial u}{\partial x} + \frac{\partial v}{\partial y} + \frac{\partial w}{\partial z} \right) + F_z \end{pmatrix} = 0 \quad (1.10.2),$$

in component form, where ∇ and $\nabla \cdot$ represent the gradient and the divergence operators, respectively, and $\mathbf{F}(F_x, F_y, F_z)$ are the body forces.

For equilibrium under surface tractions (i.e., $\mathbf{F}(F_x, F_y, F_z) = 0$), we get [Love, 1906]

$$\begin{pmatrix} \mu \nabla^2 u + (\lambda + \mu) \frac{\partial}{\partial x} \left(\frac{\partial u}{\partial x} + \frac{\partial v}{\partial y} + \frac{\partial w}{\partial z} \right) \\ \mu \nabla^2 v + (\lambda + \mu) \frac{\partial}{\partial y} \left(\frac{\partial u}{\partial x} + \frac{\partial v}{\partial y} + \frac{\partial w}{\partial z} \right) \\ \mu \nabla^2 w + (\lambda + \mu) \frac{\partial}{\partial z} \left(\frac{\partial u}{\partial x} + \frac{\partial v}{\partial y} + \frac{\partial w}{\partial z} \right) \end{pmatrix} = 0 \quad (1.11.1),$$

and, applying the gradient operator to first two terms of equation (1.11.1), we can write:

$$\begin{pmatrix} \mu \frac{\partial}{\partial x} \nabla^2 u + (\lambda + \mu) \frac{\partial}{\partial x} \frac{\partial}{\partial x} \left(\frac{\partial u}{\partial x} + \frac{\partial v}{\partial y} + \frac{\partial w}{\partial z} \right) \\ \mu \frac{\partial}{\partial y} \nabla^2 u + (\lambda + \mu) \frac{\partial}{\partial y} \frac{\partial}{\partial y} \left(\frac{\partial u}{\partial x} + \frac{\partial v}{\partial y} + \frac{\partial w}{\partial z} \right) \\ \mu \frac{\partial}{\partial z} \nabla^2 u + (\lambda + \mu) \frac{\partial}{\partial z} \frac{\partial}{\partial z} \left(\frac{\partial u}{\partial x} + \frac{\partial v}{\partial y} + \frac{\partial w}{\partial z} \right) \end{pmatrix} = 0 \quad (1.11.2),$$

that is equivalent to

$$\begin{pmatrix} \mu \frac{\partial}{\partial x} \nabla^2 u + (\lambda + \mu) \frac{\partial^2}{\partial x^2} (\nabla \cdot \mathbf{u}) \\ \mu \frac{\partial}{\partial y} \nabla^2 v + (\lambda + \mu) \frac{\partial^2}{\partial y^2} (\nabla \cdot \mathbf{u}) \\ \mu \frac{\partial}{\partial z} \nabla^2 w + (\lambda + \mu) \frac{\partial^2}{\partial z^2} (\nabla \cdot \mathbf{u}) \end{pmatrix} = 0 \quad (1.11.3)$$

since $\frac{\partial u}{\partial x} + \frac{\partial v}{\partial y} + \frac{\partial w}{\partial z} = \nabla \cdot \mathbf{u}$, and to

$$\begin{pmatrix} \mu \nabla^2 \frac{\partial u}{\partial x} + (\lambda + \mu) \frac{\partial^2}{\partial x^2} (\nabla \cdot \mathbf{u}) \\ \mu \nabla^2 \frac{\partial v}{\partial y} + (\lambda + \mu) \frac{\partial^2}{\partial y^2} (\nabla \cdot \mathbf{u}) \\ \mu \nabla^2 \frac{\partial w}{\partial z} + (\lambda + \mu) \frac{\partial^2}{\partial z^2} (\nabla \cdot \mathbf{u}) \end{pmatrix} = 0 \quad (1.11.4)$$

by interchanging the gradient and the Laplacian operators in the left-hand term of equation (1.11.3); then, by adding all the members of equation (1.11.4), we get:

$$\begin{aligned} & \mu \nabla^2 \frac{\partial u}{\partial x} + \mu \nabla^2 \frac{\partial v}{\partial y} + \mu \nabla^2 \frac{\partial w}{\partial z} + (\lambda + \mu) \frac{\partial^2}{\partial x^2} (\nabla \cdot \mathbf{u}) + \\ & + (\lambda + \mu) \frac{\partial^2}{\partial y^2} (\nabla \cdot \mathbf{u}) + (\lambda + \mu) \frac{\partial^2}{\partial z^2} (\nabla \cdot \mathbf{u}) = 0 \end{aligned} \quad (1.11.5),$$

that is equivalent to

$$\mu \nabla^2 \left(\frac{\partial u}{\partial x} + \frac{\partial v}{\partial y} + \frac{\partial w}{\partial z} \right) + (\lambda + \mu) \left(\frac{\partial^2}{\partial x^2} + \frac{\partial^2}{\partial y^2} + \frac{\partial^2}{\partial z^2} \right) (\nabla \cdot \mathbf{u}) = 0 \quad (1.11.6),$$

and, by remembering that $\nabla \cdot \mathbf{u} = \frac{\partial u}{\partial x} + \frac{\partial v}{\partial y} + \frac{\partial w}{\partial z}$, $\frac{\partial^2}{\partial x^2} + \frac{\partial^2}{\partial y^2} + \frac{\partial^2}{\partial z^2} = \nabla^2$ is the Laplacian operator, we obtain:

$$\mu \nabla^2 (\nabla \cdot \mathbf{u}) + (\lambda + \mu) \nabla^2 (\nabla \cdot \mathbf{u}) = 0 \quad (1.11.7),$$

and, in turn [Love, 1906],

$$(\lambda + 2\mu) \nabla^2 (\nabla \cdot \mathbf{u}) = 0 \quad (1.11.8).$$

At this stage, we decompose the deformation field \mathbf{u} with the Helmholtz theorem. Accordingly, every finite vector field, which is uniform, continuous, and vanishing at infinity, may be decomposed using an irrotational (curl-free) scalar potential φ and a solenoidal (divergence-free) vector potential Ψ , as follows [Love, 1906]:

$$\mathbf{u} = \nabla \varphi + \nabla \times \Psi \quad (1.12),$$

where $\nabla \times$ represents the curl operator.

In particular, we substitute equation (1.12) into (1.11.8),

$$(\lambda + 2\mu) \nabla^2 (\nabla \cdot (\nabla \varphi + \nabla \times \Psi)) = 0 \quad (1.13.1),$$

$$(\lambda + 2\mu) \nabla^2 (\nabla \cdot \nabla \varphi) + (\lambda + 2\mu) \nabla^2 (\nabla \cdot \nabla \times \Psi) = 0 \quad (1.13.2),$$

and, by remembering that $\nabla \cdot \nabla \times \Psi = 0$ and $\nabla^2 = \nabla \cdot \nabla$, we get:

$$(\lambda + 2\mu) \nabla^2 (\nabla \cdot \nabla \varphi) = 0 \quad (1.13.3),$$

$$(\lambda + 2\mu) \nabla^2 \nabla^2 \varphi = 0 \quad (1.13.4),$$

that is [Love, 1906]:

$$(\lambda + 2\mu)\nabla^4\varphi = 0 \quad (1.14.1).$$

Similarly, we can repeat similar procedures to show that [Love, 1906]:

$$(\lambda + 2\mu)\nabla^4\Psi = 0 \quad (1.14.2).$$

Each function satisfying equations (1.14.1) and (1.14.2) is called biharmonic. However, by equations (1.11.1) and (1.12) it follows that the general solution of the equilibrium equation satisfies the relation [Love, 1906]:

$$\nabla^4\mathbf{u} = 0 \quad (1.14.3).$$

1.2 Harmonic properties of the deformation field.

Any scalar function V is harmonic if it satisfies the Laplace's equation [Baranov, 1975]:

$$\nabla^2 V = \frac{\partial^2 V}{\partial x^2} + \frac{\partial^2 V}{\partial y^2} + \frac{\partial^2 V}{\partial z^2} = 0 \quad (1.15).$$

In particular, a vector field $\mathbf{B}(x, y, z) = (B_x, B_y, B_z)$ is a potential field if [Blakely, 1996]:

$$\mathbf{B}(x, y, z) = \nabla V = \begin{pmatrix} \frac{\partial V}{\partial x} \\ \frac{\partial V}{\partial y} \\ \frac{\partial V}{\partial z} \end{pmatrix} = \begin{pmatrix} B_x \\ B_y \\ B_z \end{pmatrix} \quad (1.16),$$

and, in turn,

$$\nabla^2 \mathbf{B}(x, y, z) = \begin{pmatrix} \frac{\partial^2 B_x}{\partial x^2} + \frac{\partial^2 B_x}{\partial y^2} + \frac{\partial^2 B_x}{\partial z^2} \\ \frac{\partial^2 B_y}{\partial x^2} + \frac{\partial^2 B_y}{\partial y^2} + \frac{\partial^2 B_y}{\partial z^2} \\ \frac{\partial^2 B_z}{\partial x^2} + \frac{\partial^2 B_z}{\partial y^2} + \frac{\partial^2 B_z}{\partial z^2} \end{pmatrix} = 0 \quad (1.17).$$

Now, we consider the Navier's relation in the form of equation (1.11.1) to discuss on the harmonic properties of the deformation field; in particular, we arrange the terms between the left- and right-hand members, as follows,

$$\mu \nabla^2 \mathbf{u} = \begin{pmatrix} -(\lambda + \mu) \frac{\partial}{\partial x} \left(\frac{\partial u}{\partial x} + \frac{\partial v}{\partial y} + \frac{\partial w}{\partial z} \right) \\ -(\lambda + \mu) \frac{\partial}{\partial y} \left(\frac{\partial u}{\partial x} + \frac{\partial v}{\partial y} + \frac{\partial w}{\partial z} \right) \\ -(\lambda + \mu) \frac{\partial}{\partial z} \left(\frac{\partial u}{\partial x} + \frac{\partial v}{\partial y} + \frac{\partial w}{\partial z} \right) \end{pmatrix} \quad (1.18.1),$$

and we divide both the members by μ to get:

$$\nabla^2 \mathbf{u} = \begin{pmatrix} -\left(1 + \frac{\lambda}{\mu}\right) \frac{\partial}{\partial x} \left(\frac{\partial u}{\partial x} + \frac{\partial v}{\partial y} + \frac{\partial w}{\partial z} \right) \\ -\left(1 + \frac{\lambda}{\mu}\right) \frac{\partial}{\partial y} \left(\frac{\partial u}{\partial x} + \frac{\partial v}{\partial y} + \frac{\partial w}{\partial z} \right) \\ -\left(1 + \frac{\lambda}{\mu}\right) \frac{\partial}{\partial z} \left(\frac{\partial u}{\partial x} + \frac{\partial v}{\partial y} + \frac{\partial w}{\partial z} \right) \end{pmatrix} \quad (1.18.2).$$

From (1.18.2) it follows that \mathbf{u} satisfies the Laplace's equation when the following relation is verified:

$$\begin{pmatrix} \left(1 + \frac{\lambda}{\mu}\right) \frac{\partial}{\partial x} \left(\frac{\partial u}{\partial x} + \frac{\partial v}{\partial y} + \frac{\partial w}{\partial z}\right) \\ \left(1 + \frac{\lambda}{\mu}\right) \frac{\partial}{\partial y} \left(\frac{\partial u}{\partial x} + \frac{\partial v}{\partial y} + \frac{\partial w}{\partial z}\right) \\ \left(1 + \frac{\lambda}{\mu}\right) \frac{\partial}{\partial z} \left(\frac{\partial u}{\partial x} + \frac{\partial v}{\partial y} + \frac{\partial w}{\partial z}\right) \end{pmatrix} = 0 \quad (1.19).$$

We consider the strain-stress relations expressed by the Hooke's Law and, by substituting equations (1.9.1), (1.9.2) and (1.9.3) into (1.18.3), as follows,

$$\begin{pmatrix} \left(1 + \frac{\lambda}{\mu}\right) \frac{\partial}{\partial x} \frac{1}{E} (\sigma_{xx} - \nu\sigma_{yy} - \nu\sigma_{zz} + \sigma_{yy} - \nu\sigma_{zz} - \nu\sigma_{xx} + \sigma_{zz} - \nu\sigma_{xx} - \nu\sigma_{yy}) \\ \left(1 + \frac{\lambda}{\mu}\right) \frac{\partial}{\partial y} \frac{1}{E} (\sigma_{xx} - \nu\sigma_{yy} - \nu\sigma_{zz} + \sigma_{yy} - \nu\sigma_{zz} - \nu\sigma_{xx} + \sigma_{zz} - \nu\sigma_{xx} - \nu\sigma_{yy}) \\ \left(1 + \frac{\lambda}{\mu}\right) \frac{\partial}{\partial z} \frac{1}{E} (\sigma_{xx} - \nu\sigma_{yy} - \nu\sigma_{zz} + \sigma_{yy} - \nu\sigma_{zz} - \nu\sigma_{xx} + \sigma_{zz} - \nu\sigma_{xx} - \nu\sigma_{yy}) \end{pmatrix} = 0 \quad (1.20.1),$$

we get:

$$\begin{pmatrix} \left(1 + \frac{\lambda}{\mu}\right) \frac{\partial}{\partial x} \left(\frac{\sigma_{xx}}{E} - \frac{\nu\sigma_{yy}}{E} - \frac{\nu\sigma_{zz}}{E} + \frac{\sigma_{yy}}{E} - \frac{\nu\sigma_{zz}}{E} - \frac{\nu\sigma_{xx}}{E} + \frac{\sigma_{zz}}{E} - \frac{\nu\sigma_{xx}}{E} - \frac{\nu\sigma_{yy}}{E}\right) \\ \left(1 + \frac{\lambda}{\mu}\right) \frac{\partial}{\partial y} \left(\frac{\sigma_{xx}}{E} - \frac{\nu\sigma_{yy}}{E} - \frac{\nu\sigma_{zz}}{E} + \frac{\sigma_{yy}}{E} - \frac{\nu\sigma_{zz}}{E} - \frac{\nu\sigma_{xx}}{E} + \frac{\sigma_{zz}}{E} - \frac{\nu\sigma_{xx}}{E} - \frac{\nu\sigma_{yy}}{E}\right) \\ \left(1 + \frac{\lambda}{\mu}\right) \frac{\partial}{\partial z} \left(\frac{\sigma_{xx}}{E} - \frac{\nu\sigma_{yy}}{E} - \frac{\nu\sigma_{zz}}{E} + \frac{\sigma_{yy}}{E} - \frac{\nu\sigma_{zz}}{E} - \frac{\nu\sigma_{xx}}{E} + \frac{\sigma_{zz}}{E} - \frac{\nu\sigma_{xx}}{E} - \frac{\nu\sigma_{yy}}{E}\right) \end{pmatrix} = 0 \quad (1.20.2),$$

that is equivalent to

$$\begin{pmatrix} \left(1 + \frac{\lambda}{\mu}\right) \frac{\partial}{\partial x} \left(\frac{\sigma_{xx}}{E} + \frac{\sigma_{yy}}{E} + \frac{\sigma_{zz}}{E}\right) - 2 \frac{\partial}{\partial x} \left(\frac{\nu\sigma_{xx}}{E} + \frac{\nu\sigma_{yy}}{E} + \frac{\nu\sigma_{zz}}{E}\right) \\ \left(1 + \frac{\lambda}{\mu}\right) \frac{\partial}{\partial y} \left(\frac{\sigma_{xx}}{E} + \frac{\sigma_{yy}}{E} + \frac{\sigma_{zz}}{E}\right) - 2 \frac{\partial}{\partial y} \left(\frac{\nu\sigma_{xx}}{E} + \frac{\nu\sigma_{yy}}{E} + \frac{\nu\sigma_{zz}}{E}\right) \\ \left(1 + \frac{\lambda}{\mu}\right) \frac{\partial}{\partial z} \left(\frac{\sigma_{xx}}{E} + \frac{\sigma_{yy}}{E} + \frac{\sigma_{zz}}{E}\right) - 2 \frac{\partial}{\partial z} \left(\frac{\nu\sigma_{xx}}{E} + \frac{\nu\sigma_{yy}}{E} + \frac{\nu\sigma_{zz}}{E}\right) \end{pmatrix} = 0 \quad (1.21.1),$$

and to

$$\left(1 + \frac{\lambda}{\mu}\right) \nabla \left(\frac{\sigma_{xx}}{E} + \frac{\sigma_{yy}}{E} + \frac{\sigma_{zz}}{E}\right) - 2\nabla \left(\frac{\nu\sigma_{xx}}{E} + \frac{\nu\sigma_{yy}}{E} + \frac{\nu\sigma_{zz}}{E}\right) = 0 \quad (1.21.2);$$

by substituting $\mu = \frac{E}{2(1+\nu)}$ and $\lambda = \frac{E\nu}{(1+\nu)(1-2\nu)}$ into equation (1.21.2), as follows,

$$\left(1 + \frac{E\nu}{(1+\nu)(1-2\nu)} \frac{2(1+\nu)}{E}\right) \nabla \left(\frac{\sigma_{xx}}{E} + \frac{\sigma_{yy}}{E} + \frac{\sigma_{zz}}{E}\right) - 2\nabla \left(\frac{\nu\sigma_{xx}}{E} + \frac{\nu\sigma_{yy}}{E} + \frac{\nu\sigma_{zz}}{E}\right) = 0 \quad (1.21.3),$$

$$\left(1 + \frac{2\nu}{(1-2\nu)}\right) \nabla \left(\frac{\sigma_{xx}}{E} + \frac{\sigma_{yy}}{E} + \frac{\sigma_{zz}}{E}\right) - 2\nabla \left(\frac{\nu\sigma_{xx}}{E} + \frac{\nu\sigma_{yy}}{E} + \frac{\nu\sigma_{zz}}{E}\right) = 0 \quad (1.21.4),$$

$$\frac{1}{1-2\nu} \nabla \left(\frac{\sigma_{xx}}{E} + \frac{\sigma_{yy}}{E} + \frac{\sigma_{zz}}{E}\right) - 2\nabla \left(\frac{\nu\sigma_{xx}}{E} + \frac{\nu\sigma_{yy}}{E} + \frac{\nu\sigma_{zz}}{E}\right) = 0 \quad (1.21.5),$$

and by remembering that $\sigma_{kk} = \sigma_{xx} + \sigma_{yy} + \sigma_{zz}$, the Laplace's equation is satisfied according to:

$$\frac{1}{1-2\nu} \nabla \left(\frac{\sigma_{kk}}{E}\right) - 2\nabla \left(\frac{\nu\sigma_{kk}}{E}\right) = 0 \quad (1.21.6).$$

A first solution to equation (1.21.6) can be obtained by considering ν as a constant value; in this case, we can write:

$$\frac{1}{1-2\nu} \nabla \left(\frac{\sigma_{kk}}{E}\right) - 2\nu \nabla \left(\frac{\sigma_{kk}}{E}\right) = 0 \quad (1.22.1),$$

$$\frac{1}{1-2\nu} \nabla \left(\frac{\sigma_{kk}}{E}\right) = 2\nu \nabla \left(\frac{\sigma_{kk}}{E}\right) \quad (1.22.2),$$

$$\frac{1}{1-2\nu} = 2\nu \quad (1.22.3),$$

that is never satisfied for $\nu \in \mathbb{R}$.

We can find another solution by again considering ν as a constant value and $\nabla \left(\frac{\sigma_{kk}}{E}\right) = 0$; in these conditions, equation (1.21.6) is always satisfied and, since σ_{kk} is a function depending on the elastic parameters E and ν according to equations (1.7.2) and (1.6.1), (1.6.2), (1.6.3), the equations (1.21.6), (1.19) and, in turn, the Laplace's equation are satisfied even only if:

$$\nabla \sigma_{kk} = 0 \quad (1.23).$$

In the framework of the modeling of volcanic deformations, equation (1.23) is always satisfied for hydrostatic pressure variation within sources embedded in a homogeneous elastic half-space.

The Mogi's model [Mogi, 1958] is the simplest example for which the Laplace's equation is satisfied, where the elastic problem is reduced to a point-spherical source distribution with hydrostatic pressure variation and embedded in a homogeneous elastic half-space. Castaldo et al. [2018b] have indeed established that the field expressions for this model are the gradient of a Newtonian potential in the form $\phi = \frac{1}{r}$, which is a harmonic function; therefore, by remembering equations (1.15) and (1.16), for the ground deformation \mathbf{u} generated by the Mogi source, we have:

$$\mathbf{u} = \nabla\phi = \begin{pmatrix} \frac{\partial\phi}{\partial x} \\ \frac{\partial\phi}{\partial y} \\ \frac{\partial\phi}{\partial z} \end{pmatrix} = \begin{pmatrix} u \\ v \\ w \end{pmatrix} \quad (1.24).$$

1.3 Homogeneity and local-homogeneity properties of harmonic deformation field.

A homogeneous function f of degree n satisfies the following scaling law, called homogeneity equation, in the region R [Stavrev and Reid, 2007; Fedi, 2016; Vitale and Fedi, 2020]:

$$f(tx, ty, tz) = t^n f(x, y, z) \quad (1.25),$$

where $t > 0$ and $n \in \mathbb{R}$ is the homogeneity degree of the homogeneous field f .

When f is continuously differentiable and homogeneous of degree n in R , Euler's theorem [Olmsted, 1961] shows that its homogeneity may be expressed by the differential equation:

$$\nabla f(\mathbf{r}) \cdot (\mathbf{r} - \mathbf{r}_0) = -nf(\mathbf{r}) \quad (1.26),$$

where \mathbf{r}_0 represent the source position.

In the PFT framework, n is an important parameter since it often reflects the falloff rate of the potential field anomaly with the scale variation [Thompson, 1982; Reid et al., 1990; Fedi, 2007] and, in the case of fields of ideal sources, also known as one-point sources [Vitale and Fedi, 2020] (i.e., a field generated by a source distribution having its support in just one point), n is constant at any considered scale and either integer or fractional [Fedi et al., 2015]. For the gravity case, $n = 1$ and $n = -2$ characterize the boundary values of the homogeneity degree, and they are referred to fields generated by 3D non-concentrated (i.e., a contact) and concentrated (i.e., a pole source) bodies, respectively, with a constant density distribution.

Similarly, Castaldo et al. [2018b] have shown that a pole source with hydrostatic variation of the pressure (i.e., constant distribution) generates a homogeneous ground deformation field with $n = -2$.

The homogeneity law is therefore useful to characterize the source type; the field parameter n is indeed related to the homogeneity degree of the source n_s which, according to equation (1.24), can be expressed as:

$$n_s = n + p - 2 \quad (1.27),$$

where p is the differentiation order of the analysed potential function respect to its Newtonian potential, and we can define the Structural Index N , as follows [Fedi, 2007]:

$$N = -n_s \quad (1.28).$$

N takes on an important meaning since it represents a source parameter characterizing its shape [Fedi, 2016]. For gravity and magnetic fields, Poisson's equation relates the homogeneity properties of the magnetic and gravity gradient to those of susceptibility and density, respectively [Fedi, 2016]. Similarly, this relation occurs between the field gradient and the pressure variation for the deformation case.

Following Fedi et al. [2015; 2016], we define N as an integer number varying from 0 to 3 going from a 3D non-concentrated to concentrated sources when the distribution of the pressure variation is constant; on the contrary, fractional values of N characterize the ideal sources.

In a more realistic case, the causative bodies are complex sources generating inhomogeneous fields, whose homogeneity degree is not a constant function at different scales. Fedi et al. [2015] show how to handle this case by generalizing the homogeneity equation into a local-homogeneity law:

$$f(tx, ty, tz) = t^{n(x,y,z)} f(x, y, z) \quad (1.29),$$

so that the differential Euler equation becomes

$$\nabla f(\mathbf{r}) \cdot (\mathbf{r} - \mathbf{r}_0) = -n(\mathbf{r})f(\mathbf{r}) \quad (1.30),$$

where $n(\mathbf{r}) \in \mathbb{R}$.

Therefore, equation (1.29) allows the use of homogeneous fields as suitable models to approximate in a local sense (i.e., at different scale) the behaviour of any real field, even inhomogeneous [Fedi et al., 2015; Chauhan et al., 2018; Vitale and Fedi, 2020].

CHAPTER 2

MODELING OF VOLCANIC SOURCES

In this chapter, we describe the forward problems of the most used AM for modeling volcanic reservoirs; these forward problems are based on analytical equations and express how the elastic problem reduces to particular solution for different source mechanisms. Despite of their usefulness for inverse modeling, we will stress that the AM reflect specific physical and geometrical conditions approximating the volcanic system.

We firstly deal with the AM whose forward problems are described by biharmonic and non-harmonic functions; then, we treat the cases in which these solutions also satisfy the Laplace's equation (harmonic criteria).

We briefly introduce the most used inverse approach for modeling volcanic deformation sources and, finally, we will describe the proposed integrated multi-scale methods, enjoying the properties of the harmonic functions.

Moreover, we will evidence that the harmonic and biharmonic properties of the deformation field are preserved also in the case of DInSAR measurements along LOS, since they represent a linear combination between the deformation components and the LOS vector for ascending and descending satellite orbits.

All the equations reported in this chapter are referred to source centres located at the points $(x_0, y_0) = (0,0)$ and assume a reference z -level = 0.

2.1 Analytical models satisfying the general solution.

In this paragraph, we briefly describe the forward problems of AM whose fields are biharmonic but non-harmonic. Such models are used to simulate the deformation field of volcanic systems, as sills, dikes, pipes, vertical conduits, and 3D finite spherical magma chambers.

Many of these models involve sources where the physical parameters are null within the volume excepted at their boundary, and all of them involve sources embedded in a homogeneous elastic half-space.

For each model, we apply the Laplacian operator to their analytical expressions to verify whether the Laplace's equation is satisfied. We do not show their biharmonic properties since every solution of the elastic problem can be expressed by biharmonic functions, according to equation (1.14.3) [Love, 1906].

2.1.1 Induced Horizontal Fractures.

R. J. Sun [1969] proposed a simple model for environmental purposes, which also simulates a sill-like source. It indeed describes the deformations generated by a horizontal circular crack by considering the tensile component of the stress, as follows:

$$\mathbf{u} = \begin{pmatrix} \frac{Brz_0}{a} \{A1_x - A2_x\} \\ \frac{Brz_0}{a} \{A1_x - A2_x\} \\ B \left(\sqrt{k} \sin \frac{A3}{2} - \frac{z_0}{a\sqrt{k}} \cos \frac{A3}{2} \right) \end{pmatrix} \quad (2.1),$$

where: B , a , z_0 and r are the maximum separation, the radius, the depth and the radial distance characterizing the hydraulically induced fracture;

$$A1 = \frac{(a + a\sqrt{k} \sin \frac{A3}{2})}{\left[(z_0 + a\sqrt{k} \cos \frac{A3}{2})^2 + \left((a + a\sqrt{k} \sin \frac{A3}{2}) \right)^2 \right]}; \quad \sqrt{k} = \left[\left(\frac{r^2}{a^2} + \frac{z_0}{a^2} - 1 \right)^2 + \left(\frac{2z_0}{a} \right)^2 \right]^{\frac{1}{4}};$$

$$A2 = \frac{(z_0\sqrt{k} \cos \frac{A3}{2} - a\sqrt{k} \sin \frac{A3}{2} + ak \cos A3)}{\left[(z_0\sqrt{k} \cos \frac{A3}{2} - a\sqrt{k} \sin \frac{A3}{2} + ak \cos A3)^2 + (a\sqrt{k} \cos \frac{A3}{2} + h\sqrt{k} \sin \frac{A3}{2} + ak \sin A3)^2 \right]};$$

$$A3 = \cot^{-1} \frac{r^2 + z_0^2 - a^2}{2az_0}.$$

As we can observe from equation (2.1), the deformation field only depends on the position, the radius, and the thickness of the crack source.

The expressions describing this model do not satisfy the Laplace's equation, indeed:

$$\nabla^2 \begin{pmatrix} \frac{Brz_0}{a} \{A1_x - A2_x\} \\ \frac{Brz_0}{a} \{A1_x - A2_x\} \\ B \left(\sqrt{k} \sin \frac{A3}{2} - \frac{z_0}{a\sqrt{k}} \cos \frac{A3}{2} \right) \end{pmatrix} \neq 0 \quad (2.2).$$

2.1.2 Shear and tensile faults.

A more useful model was proposed by Okada [1985; 1992] to simulate the deformation field due to the shear and tensile faults. Specifically, the tensile-component solution is widely used in the volcanic framework to simulate sources as sills and dikes.

Accordingly, by defining the components of the dislocation vector at the fault plane as U_1, U_2, U_3 , and the depth, the areal extension and the dip of this plane as $z_0, \Delta S$ and θ , respectively, the deformation fields generated by a point source with mechanism of strike-slip (\mathbf{u}_{ss}), dip-slip (\mathbf{u}_{sd}) and tensile (\mathbf{u}_t) faults are expressed as follows:

$$\mathbf{u}_{ss} = \begin{pmatrix} -\frac{U_1}{2\pi} \left(\frac{3x^2 q_r}{R^5} + I_1 \sin \theta \right) \Delta S \\ -\frac{U_1}{2\pi} \left(\frac{3xy q_r}{R^5} + I_2 \sin \theta \right) \Delta S \\ -\frac{U_1}{2\pi} \left(\frac{3x z_0 q_r}{R^5} + I_4 \sin \theta \right) \Delta S \end{pmatrix} \quad (2.3),$$

$$\mathbf{u}_{sd} = \begin{pmatrix} -\frac{U_2}{2\pi} \left(\frac{3xp q_r}{R^5} + I_3 \sin \theta \cos \theta \right) \Delta S \\ -\frac{U_2}{2\pi} \left(\frac{3yp q_r}{R^5} + I_1 \sin \theta \cos \theta \right) \Delta S \\ -\frac{U_2}{2\pi} \left(\frac{3z_0 p q_r}{R^5} + I_5 \sin \theta \cos \theta \right) \Delta S \end{pmatrix} \quad (2.4),$$

$$\mathbf{u}_t = \begin{pmatrix} -\frac{U_3}{2\pi} \left(\frac{3x q_r^2}{R^5} + I_3 \sin^2 \theta \right) \Delta S \\ -\frac{U_3}{2\pi} \left(\frac{3y q_r^2}{R^5} + I_1 \sin^2 \theta \right) \Delta S \\ -\frac{U_3}{2\pi} \left(\frac{3z_0 q_r^2}{R^5} + I_5 \sin^2 \theta \right) \Delta S \end{pmatrix} \quad (2.5),$$

where: $I_1 = \frac{\mu}{\lambda+\mu} y \left[\frac{1}{R(R+z_0)^2} - x^2 \frac{3R+z_0}{R^3(R+z_0)^3} \right]$; $I_2 = \frac{\mu}{\lambda+\mu} x \left[\frac{1}{R(R+z_0)^2} - y^2 \frac{3R+z_0}{R^3(R+z_0)^3} \right]$;

$$I_3 = \frac{\mu}{\lambda+\mu} x \left[\frac{x}{R^3} \right] - I_2; \quad I_4 = \frac{\mu}{\lambda+\mu} \left[-xy \frac{2R+z_0}{R^3(R+z_0)^2} \right]; \quad I_5 = \frac{\mu}{\lambda+\mu} \left[\frac{1}{R(R+z_0)} - x^2 \frac{2R+z_0}{R^3(R+z_0)^2} \right]; \quad \text{and}$$

$$p = y \cos \theta + z_0 \sin \theta, \quad q_r = y \sin \theta - z_0 \cos \theta, \quad R^2 = x^2 + y^2 + z_0^2 = x^2 + p^2 + q_r^2.$$

Through integrations of equations (2.3), (2.4) and (2.5), it is possible to derive the deformation field generated by a finite rectangular fault with length D and width W ; in particular, by introducing the spatial variables (ξ, η) , we can write the expression of the deformation field $f_u(\xi, \eta)$ according to the Chinnery's notation ||:

$$f_u(\xi, \eta)|| = f_u(x, p) - f_u(x, p - W) - f_u(x - D, p) + f_u(x - D, p - W) \quad (2.6).$$

Therefore, the deformation field produced by sill- and dike-like sources is modeled by the tensile component of a rectangular finite fault \mathbf{u} as:

$$\mathbf{u} = \left(\begin{array}{c} \frac{U_3}{2\pi} \left(\frac{q_r^2}{R(R+\eta)} - I_3 \sin^2 \theta \right) || \\ \frac{U_3}{2\pi} \left(\frac{-\tilde{z}_0 q_r}{R(R+\xi)} - \sin \theta \left\{ \frac{\xi q_r}{R(R+\eta)} - \tan^{-1} \frac{\xi \eta}{q_r R} \right\} - I_1 \sin^2 \theta \right) || \\ \frac{U_3}{2\pi} \left(\frac{-\tilde{y} q_r}{R(R+\xi)} - \cos \theta \left\{ \frac{\xi q_r}{R(R+\eta)} - \tan^{-1} \frac{\xi \eta}{q_r R} \right\} - I_5 \sin^2 \theta \right) || \end{array} \right) \quad (2.7),$$

$$\text{where: } I_1 = \frac{\mu}{\lambda+\mu} \left[\frac{-1}{\cos \theta} \frac{\xi}{R+\tilde{z}_0} \right] - \frac{\sin \theta}{\cos \theta} I_5; \quad I_3 = \frac{\mu}{\lambda+\mu} \left[\frac{1}{\cos \theta} \frac{\tilde{y}}{R+\tilde{z}_0} - \ln(R + \eta) \right] + \frac{\sin \theta}{\cos \theta} I_4;$$

$$I_4 = \frac{\mu}{\lambda+\mu} \frac{1}{\cos \theta} [\ln(R + \tilde{z}_0) - \sin \theta \ln(R + \eta)]; \quad \tilde{y} = \eta \cos \theta + q_r \sin \theta;$$

$$I_5 = \frac{\mu}{\lambda+\mu} \frac{2}{\cos \theta} \tan^{-1} \frac{\eta(X+q_r \cos \theta) + X(R+X) \sin \theta}{\xi(R+X) \cos \theta}; \quad \tilde{z}_0 = \eta \sin \theta - q_r \cos \theta;$$

$$R^2 = \xi^2 + \eta^2 + q_r^2 = \xi^2 + \tilde{y}^2 + \tilde{z}_0^2; \quad X^2 = \xi^2 + q_r^2;$$

and when $\cos \theta = 0$, the coefficients are rewritten as:

$$I_1 = -\frac{\mu}{2(\lambda+\mu)} \frac{\xi q_r}{(R+\tilde{z}_0)^2}, \quad I_3 = \frac{\mu}{2(\lambda+\mu)} \left[\frac{\eta}{R+\tilde{z}_0} + \frac{\tilde{y} q_r}{(R+\tilde{z}_0)^2} - \ln(R + \eta) \right], \quad I_5 = -\frac{\mu}{\lambda+\mu} \frac{\xi \sin \theta}{R+\tilde{z}_0}.$$

As described by equation (2.7), the Okada's model simulates a source that better approximates the volcanic system respect to what proposed by Sun. Indeed, the former is a finite body also characterized by the dip and strike parameters to both simulate sill- and dike-like sources. We again find that this model does not satisfy the Laplace's equation since the Laplacian of equations (2.3), (2.4), (2.5) and (2.7) is not equal to zero.

2.1.3 Finite spherical magma body.

This model was proposed by McTigue [1987] considering higher order corrections for the stress tensor to approximate the deformation generated by a pressurized finite spherical source with null physical parameters within the volume excepted at their boundary. We can express the deformation field \mathbf{u} generated by hydrostatic variation of pressure ΔP , source radius a and depth z_0 , as follows:

$$\mathbf{u} = \begin{pmatrix} a^3 \Delta P \frac{(1-\nu)}{G} \left(1 + \left(\frac{a}{z_0} \right)^3 \left(\frac{(1-\nu)}{2(-7+5\nu)} + \frac{15z_0^2(-2+\nu)}{4R^2(-7+5\nu)} \right) \right) \frac{x}{R^3} \\ a^3 \Delta P \frac{(1-\nu)}{G} \left(1 + \left(\frac{a}{z_0} \right)^3 \left(\frac{(1-\nu)}{2(-7+5\nu)} + \frac{15z_0^2(-2+\nu)}{4R^2(-7+5\nu)} \right) \right) \frac{y}{R^3} \\ a^3 \Delta P \frac{(1-\nu)}{G} \left(1 + \left(\frac{a}{z_0} \right)^3 \left(\frac{(1-\nu)}{2(-7+5\nu)} + \frac{15z_0^2(-2+\nu)}{4R^2(-7+5\nu)} \right) \right) \frac{z_0}{R^3} \end{pmatrix} \quad (2.8),$$

where G and ν represent the shear modulus and the Poisson's coefficient of the considered medium, respectively, and $R = \sqrt{x^2 + y^2 + z_0^2}$. In this case, the Laplace's equation is still not satisfied:

$$\nabla^2 \begin{pmatrix} a^3 \Delta P \frac{(1-\nu)}{G} \left(1 + \left(\frac{a}{z_0} \right)^3 \left(\frac{(1-\nu)}{2(-7+5\nu)} + \frac{15z_0^2(-2+\nu)}{4R^2(-7+5\nu)} \right) \right) \frac{x}{R^3} \\ a^3 \Delta P \frac{(1-\nu)}{G} \left(1 + \left(\frac{a}{z_0} \right)^3 \left(\frac{(1-\nu)}{2(-7+5\nu)} + \frac{15z_0^2(-2+\nu)}{4R^2(-7+5\nu)} \right) \right) \frac{y}{R^3} \\ a^3 \Delta P \frac{(1-\nu)}{G} \left(1 + \left(\frac{a}{z_0} \right)^3 \left(\frac{(1-\nu)}{2(-7+5\nu)} + \frac{15z_0^2(-2+\nu)}{4R^2(-7+5\nu)} \right) \right) \frac{z_0}{R^3} \end{pmatrix} \neq 0 \quad (2.9).$$

This model may be useful to separate the contributions of the source pressure change and its radius. However, it leads to a wrong estimate of the pressure change because of the assumed null distribution of the physical parameters within the source volume.

2.1.4 Dipping finite prolate spheroid.

Yang et al. [1988] proposed this model for simulating deformations in volcanic environment. The following parameters mainly characterize this spheroidal source: semi-major axis (a_z); semi-minor axis (a_{xy}); distance between centre of the spheroid and focal points (c); intensities of double forces (P_d) and centres of dilatation (P_c); dip angle (θ).

For this model, the effect of double forces and centres of dilatation between the spheroid foci, which satisfies the constant pressure boundary condition on its surface, expresses the deformation field; in particular, the general relation (u_i) on which this model is based can be summarized as follow:

$$u_i = \int_{-c}^{+c} \left\{ P_c \lambda \frac{\partial u_{ij}}{\partial \xi_j} + P_d 2\mu \left[\frac{\partial u_{iy}}{\partial \xi_y} \cos^2 \theta + \frac{\partial u_{iz}}{\partial \xi_z} \sin^2 \theta + \sin \theta \cos \theta \left(\frac{\partial u_{iy}}{\partial \xi_z} + \frac{\partial u_{iz}}{\partial \xi_y} \right) \right] \right\} d\xi \quad (2.10),$$

where u_{ij} is the i^{th} component of displacement at (x, y, z) due to forces of unit magnitude acting in the j -direction at (ξ_x, ξ_y, ξ_z) .

As described in equation (2.10), this model allows simulating different volcanic sources since the expressions take into account the aspect ratio (included in the P_c and P_d terms), the dip and also the strike angles of the source; therefore, the Yang's source model can approximate both 3D finite and pipe-like sources through high and low values of the aspect ratio parameter, respectively. However, the elastic problem is here simplified with a line integral instead of a volume one, and the condition of hydrostatic pressure of the source is not fully satisfied.

We again find that the mathematical formulas describing such model do not satisfy the Laplace's equation since the Laplacian of equations (2.10) is not equal to zero.

2.1.5 Vertical volcanic conduits.

As for the previous one, this model was proposed by Bonaccorso and Davis [1999] to simulate the magma ascent along a vertical conduit, that is a pipe-like source. In their work, the authors describe three cases in dilatation condition related to the closed pipe, the open pipe, and the pipe-shaded region.

For example, the deformation field \mathbf{u} generated by a pressure variation ΔP within a closed pipe with radius a can be expressed as:

$$\mathbf{u} = \begin{bmatrix} \frac{a^2 \Delta P}{4G} \left(\frac{c_1^3}{R_1^3} + \frac{2c_1(-3+5\nu)}{R_1} + \frac{5c_2^3(1-2\nu) - 2c_2 r^2(-3+5\nu)}{R_2^3} \right) \frac{x}{r^2} \\ \frac{a^2 \Delta P}{4G} \left(\frac{c_1^3}{R_1^3} + \frac{2c_1(-3+5\nu)}{R_1} + \frac{5c_2^3(1-2\nu) - 2c_2 r^2(-3+5\nu)}{R_2^3} \right) \frac{y}{r^2} \\ \frac{a^2 \Delta P}{4G} \left(\frac{c_1^2}{R_1^3} + \frac{2(-2+5\nu)}{R_1} + \frac{5c_2^2(3-10\nu) - 2r^2(-2+5\nu)}{R_2^3} \right) \end{bmatrix} \quad (2.11),$$

where c_1 and c_2 are the depth to the top and to the bottom of the source, respectively, while $r = \sqrt{x^2 + y^2}$, $R_1 = \sqrt{r^2 + c_1^2}$ and $R_2 = \sqrt{r^2 + c_2^2}$.

Equation (2.11) is very simple, but it just represents a simplification of the Yang's relations in the case of negligible width of the vertical spheroidal source. Once more, it does not satisfy the Laplace's equation:

$$\nabla^2 \left[\begin{array}{l} \frac{a^2 \Delta P}{4G} \left(\frac{c_1^3}{R_1^3} + \frac{2c_1(-3+5\nu)}{R_1} + \frac{5c_2^3(1-2\nu) - 2c_2 r^2(-3+5\nu)}{R_2^3} \right) \frac{x}{r^2} \\ \frac{a^2 \Delta P}{4G} \left(\frac{c_1^3}{R_1^3} + \frac{2c_1(-3+5\nu)}{R_1} + \frac{5c_2^3(1-2\nu) - 2c_2 r^2(-3+5\nu)}{R_2^3} \right) \frac{y}{r^2} \\ \frac{a^2 \Delta P}{4G} \left(\frac{c_1^2}{R_1^3} + \frac{2(-2+5\nu)}{R_1} + \frac{5c_2^2(3-10\nu) - 2r^2(-2+5\nu)}{R_2^3} \right) \end{array} \right] \neq 0 \quad (2.12).$$

2.2 Analytical models satisfying the Laplace's equation.

In this paragraph, we describe the forward problems of AM whose fields are both biharmonic and harmonic so that, in turn, satisfy the Laplace's equation. Such models are used to simulate the deformation field of simple volcanic systems, where the depth to the source is larger than its extents.

2.2.1 The Mogi's source.

The Mogi's source model [1958] represents the simplest and most used AM for modeling the volcanic deformation sources. For this reason, we deeply study its properties; in particular, the outcomes of this study have been already published in the following paper:

Castaldo, R., Barone, A., Fedi, M., Tizzani, P. (2018b). Multiridge Method for Studying Ground-Deformation Sources: Application to Volcanic Environments. Scientific Reports, 8:13420, DOI:10.1038/s41598-018-31841-4.

Here, we report an excerpt of this paper treating both the harmonic and homogeneity properties of the Mogi's source model:

“We show that the ground deformation field modeled with the Mogi source also encompasses harmonic properties.

The deformation field modeled by a hydrostatic pressure change within a spherical cavity embedded in an elastic half-space, with a radius much smaller than its depth [Mogi, 1958], is given by:

$$\mathbf{u} = \begin{pmatrix} a^3 \Delta P \frac{1-\nu}{G} \frac{x-x_0}{|\mathbf{R}|^3} \\ a^3 \Delta P \frac{1-\nu}{G} \frac{y-y_0}{|\mathbf{R}|^3} \\ a^3 \Delta P \frac{1-\nu}{G} \frac{z-z_0}{|\mathbf{R}|^3} \end{pmatrix} \quad (2.13),$$

where (x_0, y_0, z_0) represents the coordinates of the source centre, a the radius of the sphere, ΔP the variation in pressure, z_0 the depth of the source from the centre of the sphere, $|\mathbf{R}| = \sqrt{(x - x_0)^2 + (y - y_0)^2 + (z - z_0)^2}$, G the shear modulus and ν the Poisson ratio.

It is simple to argue that \mathbf{u} is the gradient of the Newtonian potential in the form $1/r$, which is a harmonic function. Therefore, all the components of the deformation field \mathbf{u} are also harmonic, and we find that:

$$\nabla \cdot \nabla \mathbf{u} = \nabla^2 \mathbf{u} = 0 \quad (2.14).$$

In the case of the LOS satellite data analysis, the projection of the modeled deformation (u_{LOS}) can be simply calculated by combining the ground deformation field components (u, v, w) with the LOS unit vector, as follows:

$$u_{los} = u c_x + v c_y + w c_z \quad (2.15),$$

where $c_x, c_y,$ and c_z are the components of the LOS vector \mathbf{c}_1 . Also, u_{los} is a harmonic function since we consider the mean values of $c_x, c_y,$ and c_z .

Consider again the ground deformation field modeled through the Mogi source, and let us evaluate its homogeneity properties. By inserting equation (1.26) into (2.13), it is obvious that each component of \mathbf{u} for Mogi's source model is homogeneous of degree $n = -2$.

The homogeneity degree of the field (n) may be used to estimate the homogeneity degree of the source (n_s) and, in turn, the Structural Index (N); in particular, by remembering equations (1.27) and (1.28) we conclude that the Mogi source is characterized by $n_s = -3$ and $N = 3$ since $p = 1$."

2.2.2 The prism source.

Geerstma and Van Opstal [1973] proposed this model for predicting subsidence above compacting reservoirs and, in the last years, different authors [Camacho and Fernandez, 2019; Camacho et al., 2020] have considered it to study different phenomena, including the volcanic one.

The model is based on the linear poroelasticity theory of strain nuclei to reproduce the deformation field of a reservoir with its lateral extent much larger than its thickness and, so, when the lateral strain is neglected.

Accordingly, the deformation field \mathbf{u} generated by a hydrostatic pore-pressurized (ΔP) prismatic body with sides Δx , Δy , and Δz_0 can be expressed as:

$$\mathbf{u} = \begin{pmatrix} \Delta P \frac{1-\nu}{G} \frac{3}{4\pi} \int_{-\frac{\Delta x}{2}}^{+\frac{\Delta x}{2}} \int_{-\frac{\Delta y}{2}}^{+\frac{\Delta y}{2}} \int_{-\frac{\Delta z_0}{2}}^{+\frac{\Delta z_0}{2}} (x - \xi) \frac{d\xi d\eta d\zeta}{((x-\xi)^2 + (y-\eta)^2 + (z-\zeta)^2)^{\frac{3}{2}}} \\ \Delta P \frac{1-\nu}{G} \frac{3}{4\pi} \int_{-\frac{\Delta x}{2}}^{+\frac{\Delta x}{2}} \int_{-\frac{\Delta y}{2}}^{+\frac{\Delta y}{2}} \int_{-\frac{\Delta z_0}{2}}^{+\frac{\Delta z_0}{2}} (y - \eta) \frac{d\xi d\eta d\zeta}{((x-\xi)^2 + (y-\eta)^2 + (z-\zeta)^2)^{\frac{3}{2}}} \\ \Delta P \frac{1-\nu}{G} \frac{3}{4\pi} \int_{-\frac{\Delta x}{2}}^{+\frac{\Delta x}{2}} \int_{-\frac{\Delta y}{2}}^{+\frac{\Delta y}{2}} \int_{-\frac{\Delta z_0}{2}}^{+\frac{\Delta z_0}{2}} (z - \zeta) \frac{d\xi d\eta d\zeta}{((x-\xi)^2 + (y-\eta)^2 + (z-\zeta)^2)^{\frac{3}{2}}} \end{pmatrix} \quad (2.16),$$

where (ξ, η, ζ) represent the coordinates of the source centre. By assuming the direct proportionality between the thickness Δz_0 and \mathbf{u} , the volume integration (2.16) can be simplified with an integration in the horizontal plane, as follows:

$$\mathbf{u} = \begin{pmatrix} \Delta P \frac{1-\nu}{G} \frac{3}{4\pi} I_x \Delta z_0 \\ \Delta P \frac{1-\nu}{G} \frac{3}{4\pi} I_y \Delta z_0 \\ \Delta P \frac{1-\nu}{G} \frac{3}{4\pi} I_z \Delta z_0 \end{pmatrix} \quad (2.17),$$

where:

$$I = I_i \left(x + \frac{\Delta x}{2}, y + \frac{\Delta y}{2}, z \right) - I_i \left(x + \frac{\Delta x}{2}, y - \frac{\Delta y}{2}, z \right) - I_i \left(x - \frac{\Delta x}{2}, y + \frac{\Delta y}{2}, z \right) + I_i \left(x - \frac{\Delta x}{2}, y - \frac{\Delta y}{2}, z \right)$$

$$\text{and } I_i(p, q_r, r) = \begin{pmatrix} \arcsin h \frac{p}{\sqrt{q_r^2 + r^2}} \\ \arcsin h \frac{q_r}{\sqrt{p^2 + r^2}} \\ \frac{1}{2} \frac{p}{|p|} \frac{q_r}{|q_r|} \left\{ \arcsin \frac{p^2 q_r^2 - r^2 (p^2 + q_r^2 + r^2)}{(p^2 + r^2)(q_r^2 + r^2)} + \frac{\pi}{2} \right\} \end{pmatrix}.$$

Equation (2.17) satisfies the Laplace's equation, indeed:

$$\nabla^2 \begin{pmatrix} \Delta P \frac{1-\nu}{G} \frac{3}{4\pi} I_x \Delta z_0 \\ \Delta P \frac{1-\nu}{G} \frac{3}{4\pi} I_y \Delta z_0 \\ \Delta P \frac{1-\nu}{G} \frac{3}{4\pi} I_z \Delta z_0 \end{pmatrix} = 0 \quad (2.18).$$

However, the prism side extent respect to the scale is crucial since a very small source produces a field tending to the Mogi's one, while a very large one produces a field affected by the uniaxial compaction assumption, on which this model is based.

2.3 Inherent limitations of parametric inverse algorithms.

Let us begin defining as \mathbf{m} and \mathbf{d} the column vectors of the Earth model parameters and of the discrete data. To derive the properties of the Earth, we must be able to calculate theoretical data for an assumed Earth model. When we are able to establish a theoretical relationship between data and model (even approximate) we have solved the so-called forward problem:

$$\mathbf{d} = \mathcal{g}(\mathbf{m}) \quad (2.19).$$

If the forward problem is solved in terms of simple relationship, characterized by a small number of parameters, the problem is called parametric. The aim of the parametric inverse algorithms is to infer the model parameters by iteratively fitting the observed data with the theoretical predictions from the assumed expressions of the relative forward problems and by finding an optimal value of a misfit function to minimize. The misfit function expresses the differences between the observations and the data calculated, under a specific forward problem, by considering the found Earth model at each step of an iteration cycle. The misfit is therefore expressed in function of the iteration step and, in case the problem is nonlinear, it will be characterized by several minima [Sen and Stoffa, 2013].

The local optimization methods usually start from a guess model and lead to nearest local misfit minimum. The global optimization methods instead search directly for the global minimum, defined by the lowest misfit in a set of local minima. Therefore, these procedures are known as Global or Local Optimization methods depending on whether they have been conceived to find global or local minima [Sen and Stoffa, 2013].

In particular, the application of the forward modeling operator \mathcal{g} (equation 2.19) to any possible solution \mathbf{m} gives back the synthetic data vector \mathbf{d}_{syn} :

$$\mathbf{d}_{syn} = \mathcal{g}(\mathbf{m}) \quad (2.20).$$

The inverse problem now reduces to determining a model that minimize the misfit between the observed data, \mathbf{d}_{obs} , and the computed data \mathbf{d}_{syn} .

The misfit function, also called objective function, must be defined in terms of a suitable norm L and, considering that the error vector \mathbf{e} is given by

$$\mathbf{e} = \mathbf{d}_{obs} - \mathbf{d}_{syn} = \mathbf{d}_{obs} - \mathcal{g}(\mathbf{m}) \quad (2.21),$$

a general norm L_l is defined as

$$\|\mathbf{e}\|_l = [\sum_{i=1}^{ND} |e_i|^l]^{\frac{1}{l}} \quad (2.22),$$

where ND is the number of data points. The usual norm is L_2 , given by $l = 2$ and, if $\|\mathbf{e}\|_2$ is divided by ND, we get the well-known and commonly used root mean square (RMS) error [Sen and Stoffa, 2013].

In this framework, many algorithms have been proposed to search for the minima of a defined objective function of multiple variables by considering a general nonlinear form of $\mathcal{g}(\mathbf{m})$ [Sen and Stoffa, 2013].

The simplest approach is when the forward problem relationship is linear. In this case, \mathcal{g} is a linear operator expressed by a matrix \mathbf{G} , and linear algebra methods are used to solve the inverse problem [Sen and Stoffa, 2013].

If the forward problem is nonlinear the standard strategy adopted in geophysical inversion involves the conversion of the nonlinear problem into an approximate linear form by expanding the functional $\mathcal{g}(\mathbf{m})$ in Taylor series about an initial guess \mathbf{m}^0 :

$$\mathbf{d} - \mathcal{g}(\mathbf{m}) = \mathbf{d} - \mathcal{g}(\mathbf{m}^0) - \sum_{j=1}^M \frac{\partial \mathcal{g}_i(\mathbf{m}^0)}{\partial m_j} dm_j \quad (2.23).$$

For notational simplicity, let us define the vector $\mathbf{y} = \mathbf{d} - \mathcal{g}(\mathbf{m}^0)$ as representing the differences between the actual data and the those calculated for our initial model, and denote the quantities $\frac{\partial \mathcal{g}_i}{\partial m_j}$ and $d\mathbf{m}$ as the matrix \mathbf{J} and the vector \mathbf{x} . We can restate equation (2.23) as

$$\mathbf{d} - \mathcal{g}(\mathbf{m}) = \mathbf{y} - \mathbf{J}\mathbf{x} \quad (2.24),$$

which has again a linear form and where \mathbf{J} is the Jacobian matrix, \mathbf{x} is the unknown perturbation model that is determined as \mathbf{m} for the linear problem. Updating the linearization process within a cycle of iterations, we will finally determine the solution of the nonlinear problem.

In order to search for a global minimum, the enumerative or grid-search methods involve sampling the model space by using different starting points in a grid and so finally determine the global minimum. However, when the model space is large, this is not a practical solution. In this last case, the most used approach is the Monte Carlo methods,

used for a random sampling of the model space, hoping that in some small and finite numbers of trials we may be able to finally determine the global minimum. The approach is a blind search and, so, it can be very computationally expensive. In some cases, the search is guided by some directivity during the random sampling, as for the simulated annealing (SA) and the genetic algorithms (GAs) [Sen and Stoffa, 2013].

We note here some features of the parametric inverse algorithm for the ground deformation field in the volcanic environment:

- the forward problem is often relative to a too simple approximation of the distribution of the model in the Earth;
- the forward problem operator \mathcal{G} may be affected by theoretical approximations, leading to theoretical errors, unless it is supported by strong a priori information;
- the best model is often a priori chosen after a misfit analysis among different forward problem definitions (i.e., different operators \mathcal{G}), each one with different inherent theoretical errors, and, therefore, it can be wrongly selected;
- \mathcal{G} is in general a non-linear operator and the derived error function will not have only one well-defined minimum; however, the local-minimum solution can be valid if the starting model is supported by strong a priori information;
- the generation of \mathbf{d}_{syn} is a highly time-consuming task, especially in the case of complex forward problems.

It follows that parametric inverse modeling provide unambiguous solutions to the inverse problem only if valid constraints about the starting model parameters and the source shape are available.

2.4 Tomographic inverse algorithms.

The tomographic inverse algorithm involves the partition of the subsoil volume into 3D blocks to infer the source property of each of them by finding an optimal value of a misfit function.

For the ground deformation field in the volcanic environment, Camacho et al. [2011] proposed this approach for simultaneous inversion of surface deformation and gravity data. Then, Camacho et al. [2020] has proposed some advances of this procedure by only considering geodetic data, which we will describe below.

In this algorithm, the considered forward problems are four elementary source models: the strike-slip (equation 2.3), dip-slip (equation 2.4) and tensile components of buried dislocations points (equation 2.5) [Okada, 1985], and the pressure elemental prismatic body (equation 2.17) [Geerstma and Van Opstal, 1973]. So, more deformation mechanisms are considered to interpret the observed data.

The required a priori information is: the 3D partition of the subsoil (number of blocks m and their centres position x_i, y_i, z_i , volume $\Delta V_i = \Delta x_i \Delta y_i \Delta z_i$ of the blocks for the pressure elemental prismatic body or small dislocation surfaces ΔS_i for the buried dislocations points), which affects the distribution of the source property; the physical elastic parameters of the half-space, as the shear modulus G and the Poisson's Coefficient ν , or the Lamé's Constants λ and μ . Furthermore, it is assumed that hydrostatic conditions characterize the system and, in turn, ΔP , U_1 , U_2 and U_3 are constant.

The causative 3D source is in practice the aggregation of elemental sources according to an iterative growth process [Camacho et al., 2007; 2011] that fits the dataset within some regularity conditions.

The procedure is able to solve for the following unknown parameters for each block: the deformation mechanisms (strike-slip, dip-slip, tensile dislocations or pressure variation of a prismatic body); the position (x_0, y_0, z_0) along the x, y, z directions; the constant pressure variation ΔP for the elemental prismatic body; the constant dislocation $(U_1, U_2$ and $U_3)$, the dip (θ) and strike (α) angles for the buried dislocations points.

In particular, the misfit is:

$$\boldsymbol{\varepsilon} = \mathbf{dr} - \mathbf{dr}^c \quad (2.25),$$

where \mathbf{dr} , \mathbf{dr}^c and $\boldsymbol{\varepsilon}$ are the vectors of the observed data, the forward-calculated ones, and the residual values; \mathbf{dr}^c corresponds to the accumulation of the effects of the filled blocks (i.e., the blocks which are selected as idoneous to be added to the source property distribution) for $i \in \Phi_P$, the set of pressured blocks, $i \in \Phi_S$, the set of strike dislocations blocks, $i \in \Phi_D$, the set dip-slip and thrust dislocation blocks, and $i \in \Phi_T$, the set for tensile dislocation blocks).

The forward problem is:

$$\mathbf{dr}^c = \sum_{\Phi_P} \begin{pmatrix} u \\ v \\ w \end{pmatrix} + \sum_{\Phi_S, \Phi_D, \Phi_T} \begin{pmatrix} u \\ v \\ w \end{pmatrix} \quad (2.26),$$

where (u, v, w) are defined by equations (2.3), (2.4), (2.5) and (2.17).

Equation (2.26) expresses a linear relationship for the set Φ_P and a non-linear one vs. θ , α for the sets Φ_S , Φ_D and Φ_T of the filled blocks.

To solve the inverse problem the Tikhonov objective function is minimized:

$$\Phi(\mathbf{M}) = \boldsymbol{\varepsilon}^T \mathbf{Q}_D^{-1} \boldsymbol{\varepsilon} + \gamma \mathbf{M}^T \mathbf{Q}_M^{-1} \mathbf{M} = \min \quad (2.27),$$

where: \mathbf{Q}_D is the covariance matrix for observed data, by assuming that the measurements are normally distributed; \mathbf{M} is the unknown vector; \mathbf{Q}_M is a suitable covariance matrix corresponding to the physical configuration of blocks and data points. Finally, γ is the regularization parameter, which is optimally chosen as the value generating a null autocorrelation distribution of the residuals respect to the observed and modeled data.

As we said, the problem is solved by adopting an *exploration approach*, where, at each step, successive explorations allow the selection of only one new block whose properties, in turn, are aggregated to the final source.

The model space to be explored is composed by: m neighbouring blocks to be added to the body, four deformation mechanisms, positive or negative value for each pressure/dislocation and 190 possible orientations for dislocation elements (from 0° to 180° and from 0° to 90° for α and θ , respectively, with step 10°). The unknowns ΔP , U_1 , U_2 and U_3 are linearly related to the data and the problem is solved by a normalized linear fit.

In particular, for any $(k + 1)^{th}$ step of the growth process a new block is filled, according to:

$$\mathbf{dr} = l_{k+1} \mathbf{dr}^c + \boldsymbol{\varepsilon} \quad (2.28),$$

$$\Gamma_{k+1}(\mathbf{M}) = \boldsymbol{\varepsilon}^T \mathbf{Q}_D^{-1} \boldsymbol{\varepsilon} + \gamma l_{k+1}^2 \mathbf{M}^T \mathbf{Q}_M^{-1} \mathbf{M} = \min \quad (2.29),$$

where $0 < l_{k+1} < l_k$ is a normalizing factor for fitting the provisional modeled data with respect to the observed one. The process continues until l reaches a prescribed small value or when the selection of a new block leads l and Γ to increase.

The choice of a priori information is therefore crucial for the final solution since different regularization parameters and 3D partitions of the subsoil may lead to different acceptable models. Moreover, the wrong definition of the system elastic parameters may cause an equally wrong definition of the source parameters. Finally, the assumption of constant pressure of the deformation sources may affect the final solution of a multi-source case.

We conclude that the tomographic inverse methods also provide ambiguous solutions if valid constraints are unavailable.

2.5 Integrated multi-scale methods and procedures.

In this paragraph, we describe the proposed methods for analysing the ground deformation field in the volcanic environment and the related procedures. These methods can be used if the elastic field conditions expressed by equation (1.23) are satisfied, that is in the case of hydrostatic pressure variation of sources embedded in a homogeneous elastic half-space.

2.5.1 Multiridge method.

The Multiridge method [Fedi et al., 2009] is a multi-scale procedure based on the analysis of so-called ridges, which are defined as lines passing through the extrema of the considered field, and of its derivatives, at different scales. The method provides geometrical parameters of the source, as its position (i.e., depth and horizontal location). Here, we describe the method for the ground deformation field by reporting an excerpt from Castaldo et al. [2018b]:

“We consider a coordinate system where the x - and y -directions are represented by the North-South and East-West directions, respectively, and the z -axis is definite and positive downward. If $P_f(x, y, z)$ is a generic field generated by a simple point source $P_s(x_0, y_0, z_0)$ and by considering the cross section $y = y_0$, it is possible to obtain three equations for the ridges [Fedi et al., 2009]:

$$\begin{aligned}x &= x_0 \\x - x_0 &= \vartheta(z - z_0) \\x - x_0 &= -\vartheta(z - z_0)\end{aligned}\tag{2.30},$$

where ϑ is the angular coefficient of the straight line $\vartheta = \tan \beta$ and β represents the angle of the ridge line from the vertical z -axis. Since the three ridges intersect at the source centre (x_0, z_0) , its position can be simply individuated with this geometric method.

Specifically, the Multiridge method mainly consists of three phases:

- (1) the creation of a multi-scale dataset by performing upward continuation;*
- (2) individuation of the multiridge subset at different scales;*
- (3) representation and continuation of the ridges down to the source-region, to individuate the correct depth of the source at the intersection of more ridges.*

We clarify that more than one subset can be defined: a multiridge subset, R_1 , that is individuated by the zeros of the horizontal derivatives; a multiridge subset, R_2 , that is individuated by the zeros of the first-order vertical derivative; and a multiridge subset, R_3 , that is individuated by the maxima of the field [Fedi et al., 2009].

Moreover, since the method involves the field at different scales (i.e., multi-scale), high-wavenumber noise can be easily recognized in the multiridge subsets and excluded from the analysis.

We specify that each ridge is determined by a best-fit linear regression within a 95% confidence interval; in particular, we calculate the determination coefficient R^2 , where R is the correlation coefficient, which represents a statistical measure of how the data (multiridge subset) are close to the fitted regression line (ridges).

Moreover, we evaluate the solution uncertainties (intersection at the ridges) by considering the error on the best-fit linear regression coefficients (intercept and slope constants).”

The Multiridge method therefore provides constraints about the position of the causative body according to the multipolar expansion of potential fields and their asymptotic expressions.

In the case of fields of ideal sources, the ridges converge to the singularities of the sources and their slope is constant with the scale. For example, the ridges of a point source field just intersect each other in the source centre, that is where the source distribution has its support; while, in the case of a fields of an infinite vertical line or a thin sheet, the ridges converge to the top or the edges of the source, respectively.

For regular sources, defined here as bodies that can be approximated by ideal ones, the ridges tend to converge to the singular points of the sources but their slope changes with the scale. Indeed, the ridges of a vertical prolate ellipsoidal source tend to intersect to its top at low scale and to its centre at larger one, which is consistent with the asymptotic expression of the multipolar expansion of potential fields.

The same behavior occurs for any source distribution. For instance, for a horizontal prism, the ridges tend to converge to the edges of the source at low scales and to the center at larger ones.

2.5.2 ScalFun method.

The ScalFun [Fedi, 2007] method is based on the properties of the so-called scaling function, which, given the availability of a multi-scaled dataset, provides information about the morphological features of the field source through the Structural Index parameter (N).

Here, we describe the method for the ground deformation field by reporting an excerpt from Castaldo et al. [2018b]:

“The ScalFun method is based on the properties of the scaling function, which was introduced into the framework of the DEXP theory [Fedi, 2007] to estimate the homogeneity degree of the observed field (n); this is, in turn, related to the homogeneous property of the source (n_s). For any p_{th} -order vertical derivative of Newtonian potential of a pole source $f_p(z)$ at $x = x_0$ and $y = y_0$, we define the scaling function τ_p of order p_{th} as:

$$\tau_p = \frac{\partial \log(f_p(z))}{\partial \log(z)} = -\frac{(p_{th}+1)z}{z-z_0} \quad (2.31),$$

where $n = -(p + 1)$ represents the degree of homogeneity of f_p .

Equation (2.31) can be rewritten putting $z = \frac{1}{q}$; therefore, τ_p becomes a function of q :

$$\tau_p(q) = \frac{n}{1-z_0q} \quad (2.32),$$

which means that when $q \rightarrow 0$, $\tau_p(q)$ tends to n .

Hence, in a plot diagram of τ_p as function of q , the intercept gives an estimate of the homogeneity degree n .

Starting from the z_0 source depth retrieved by using the Multiridge method, we can use equation (2.32) to estimate n , n_s and N ; these values give us information about the geometry of the source.”

Therefore, the use of ScalFun method depends on both the harmonic and homogeneity properties of the deformation field since we need to analyse a multi-scale dataset retrieved by upward continuation transform.

According to equation (2.32), ScalFun method provides information about the type of a source if its depth is known.

Another approach does not require this information and it is based on finding the depth value such that the slope of τ_p in function of q is null. However, we use the first approach through the depth information given by Multiridge.

The simplest analysis can be performed under the approximation of the ideal sources with constant source distribution [Thompson, 1984; Reid et al., 1990].

For example, $N \sim 3$ characterizes fields where the multipolar terms of potential field expressions vanish and, therefore, we are analysing the field generated by a source that can be associated to one concentrated point, that is its centre, or to any equivalent source volume having the same centre and the same product among the pressure variation ΔP , the radius a and the medium elastic parameters ν and G , as specified by the Mogi's model [Mogi, 1958].

Instead, in the case of $N \sim 2$, a linear source (i.e., a concentrated source along only two directions) is the cause of the analysed field and the Multiridge depth value may refer to the top or the centre of a vertically or horizontally elongated one, respectively [Thompson, 1984; Reid et al., 1990]; this may be the case of a pipe-like or prolate ellipsoidal sources, with high value of aspect ratio.

On the contrary, in the case of planar bodies (i.e., a concentrated source along only one direction, such as sills or dykes), with the Multiridge analysis we are able to identify the source edges of the sill or the top of the dyke and $N \sim 1$ will characterize the retrieved depth solution.

Finally, when $N \sim 0$ we are analysing the field from a contact-like source, while for $N \sim 0.4$ the field from a fault with a finite throw.

This last case, $N \sim 0.4$, strictly refers to an inhomogeneous field source, whose homogeneity degree changes with the scales [Fedi et al., 2015]. In these cases, we have to resort to a more complex theory based on the local-homogeneity.

However, approximate estimates may be made even no resorting to this theory: for example, at larger scales, we should expect N between 3 and 2, which characterizes the

depth solution as representative of the centre source, while at low scales we should find N between 2 and 1, which characterizes the depth solution as representative of the top.

We remark that the Structural Index parameter (N) is a property of the source and it does not change with the differentiation order p of the analysed function respect to its Newtonian potential.

For example, consider the field of a point source; according to equation (2.31) and (2.32), in a plot diagram of τ_p as function of q , when $q \rightarrow 0$, $\tau_p(q)$ tends to n , which is ~ -2 ; for equation (1.27) and (1.28), it corresponds to $n_s = -3$ and $N = 3$ since $p = 1$. Similarly, the analysis of the second-order vertical derivative of the same field will get $n \sim -4$ but $n_s \sim -3$ and $N \sim 3$, since $p = 3$.

In **Table 2.1**, we summarize the values of n and N for different orders p (expressed respect to the Newtonian potential) and related to the ideal sources case.

Table 2.1. Summary of n and N values. Values of n and N parameters by considering different order p (expressed respect to the Newtonian potential) related to ideal sources.

<i>SOURCE TYPE</i>	<i>p</i>	<i>n</i>	<i>N = -n_s = n + p - 2</i>
<i>Point Source *</i>	1	-2	3
	2	-3	
	3	-4	
	4	-5	
<i>Linear Source **</i>	1	-1	2
	2	-2	
	3	-3	
	4	-4	
<i>Planar Source ***</i>	1	0	1
	2	-1	
	3	-2	
	4	-3	

*the values are referred to the source centre.

**the values are referred to the top or centre of a vertical or horizontal source.

***the values are referred to the edges or the top of a horizontal or vertical source.

2.5.3 THD technique.

The Total Horizontal Derivative (THD) is another widely employed technique [Cella et al., 2015; Paoletti et al., 2017] in the PFT framework, based on the source edges detection, and known as Horizontal Gradient (HG) or Horizontal Derivative (HD) [Blakely, 1996]. This technique provides information about the horizontal sizes and positions of multipolar field sources; therefore, we can not apply it to the Mogi's source model for which it yields not the radius information but only the centre position one.

In particular, the technique has been defined in the following paper:

Pepe, S., De Siena, L., Barone, A., Castaldo, R., D'Auria, L., Manzo, M., Casu, F., Fedi, M., Lanari, R., Bianco, F., Tizzani, P. (2019). Volcanic structures investigation through SAR and seismic interferometric methods: The 2011-2013 Campi Flegrei unrest episode. Rem. Sensing of Environment, 234, 111440, <https://doi.org/10.1016/j.rse.2019.111440>.

Here, we report an excerpt of this paper describing the technique:

“We use the Total Horizontal Derivative (THD) technique to perform a basic detection of the deformation source boundaries; we remark that the THD technique is an edge detection filter commonly employed for analysing potential field data [Blakely, 1996; Florio et al., 1999] and it is based on analysing the maxima of the horizontal gradient magnitude, as computed from the first order x - and y -derivatives of the field; their distribution depends on the source geometry since the maxima occur where the physical property has the greatest variation, that is at the boundaries of the sources. This is also true for higher-order field derivatives of related quantities such as the enhanced horizontal derivative method [Fedi and Florio, 2001; Luiso et al., 2018]. In particular, the maxima horizontal gradient magnitude matches with the physical edges of the source; despite some limitations in its applicability and accuracy, it is a powerful boundary analysis technique and it provides reliable results in the case of abrupt lateral contrasts of the investigated property [Blakely et al., 1996], typical of volcanic areas.

The THD_w for the vertical deformation is defined here as:

$$THD_w = \sqrt{\left(\frac{\partial w(x,y,z)}{\partial x}\right)^2 + \left(\frac{\partial w(x,y,z)}{\partial y}\right)^2} \quad (2.33),$$

where $w(x, y, z)$ represents the vertical component of the ground deformation at spatial coordinates (x, y, z) . The horizontal derivatives are calculated using simple finite-difference formulas.”

The THD technique provides reliable information on the horizontal extent (boundaries) of magmatic reservoirs and/or volcanic structures modulating the observed deformation patterns, with an overestimation which however increases with the scale.

2.5.4 Functional transformations for the ground deformation field.

The most important functional transformation used in this work is certainly the upward continuation [Baranov, 1975; Blakely, 1996] since it allows the creation of the multi-scale dataset. While it is a rather popular and well-known transformation for gravity and magnetic fields, its role for the deformation field is less obvious from a physical point of view, but nevertheless valid and relevant.

Here, we describe its application to the ground deformation field by reporting an excerpt from Castaldo et al. [2018b]:

“Regarding the application of the upward continuation operator to the deformation field, we specify that we are clearly not considering that the deformation field could propagate into the air. The upward-continued deformation field instead corresponds to that which would have been produced by the same source in a region that was upper extended by the same amount of upward continuation.

For example, if the analysed field is observed by a source with a depth of $z_0 = 2$ km, the upward-continued field towards a 1-km altitude is generated by the same source but with a centre depth at $z_0 = 3$ km.”

A particular type of upward continuation filter, known as draped-to-flat [Blakely, 1996], is also used before the application of Multiridge, ScalFun methods and THD technique to refer each point of the field to the same scale. This procedure is referred as constant-level reduction procedure in the framework of Castaldo et al. [2018b], as follows:

“We remark that in the case of irregular (not flat) data measurement levels, we have to perform another procedure before applying the Multiridge method. Since the method

is based on a level-to-level algorithm, and the ground deformation field is measured at the topographic surface (which is generally detailed), the dataset must be processed to numerically generate a ground deformation field that could have been measured in the case of constant distance between the source volume and the measurement surface. This transformation relocates the analysed field onto the constant reduction level, which is performed in this study by using a CWT-domain algorithm [Ridsdill-Smith, 1999].”

However, we specify that the reliability of this procedure depends on the topographical gradient; indeed, the greatest errors are expected at points where the field gradient is large.

The last crucial and considered functional transformation is the Vertical Derivative filter [Rao et al., 1981; Gupta et al., 1982; Butler et al., 1984] of order p which, however, enhances the high-wavenumber part of the field and which is in turn related to the shallowest portion of the subsoil.

The results of Multiridge and ScalFun methods depend on the scale. For example, let consider a vertically elongated deep ellipsoid with small aspect ratio; although the latter can be well approximated by an ideal linear source, at large scales the information retrievable from the field about its morphological features is attenuated and we could not be able to retrieve this information with Multiridge and ScalFun analysis. However, at low scales, thanks to the enhancement of the high-wavenumber part of the field signal we will likely achieve more detailed information on the morphological features of the source.

This filter is also crucial for solving other cases, as when the local-homogeneity properties are relatively stable within a particular scale-interval. When instead a ground deformation pattern is the result of the interference among field signals related to different sources it could be interesting to use a vertical derivative filter.

In the coordinate system where the x - and y -directions are represented by the North-South and East-West directions, respectively, and the z -axis is definite positive downward, the vertical derivative operator (here defined VD_s) corresponds to the difference between fields, $f(x, y, z_0)$ and $f(x, y, z_0 + \Delta z)$ where Δz is small:

$$\frac{\partial}{\partial z} f(x, y, z) \sim \frac{f(x, y, z_0) - f(x, y, z_0 + \Delta z)}{\Delta z} \quad (2.34).$$

Here, we use the properties of the proposed solution to the elastic problem to calculate the vertical derivative operator in the wavenumber-domain.

Indeed, in the wavenumber domain, for harmonic functions the p_{th} -order vertical derivative is given by [Blakely, 1996; Cooper et al., 2004]:

$$\mathbf{A}'(\mathbf{k}) = \mathbf{A}(\mathbf{k})|\mathbf{k}|^p \quad (2.35),$$

where $\mathbf{A}(\mathbf{k})$ indicates the signal amplitude, \mathbf{k} and p are the wavenumbers and the differentiation order, respectively.

Therefore, the p_{th} -order vertical derivative is finally retrieved by substituting $\mathbf{A}(\mathbf{k})$ with $\mathbf{A}'(\mathbf{k})$ and anti-transforming the so obtained Fourier transform of the deformation field back to the space-domain (here defined VD_F).

In this way, we can perform this procedure also in the real case of measured deformation field.

CHAPTER 3

APPLICATION TO HARMONIC DEFORMATION FIELDS: SYNTHETIC CASES

In this Chapter, we apply the integrated multi-scale approach to synthetic fields which satisfy the relation (1.23) and, in turn, the Laplace's equation. The fields are in the case of hydrostatic pressure variation of sources embedded in a homogeneous elastic half-space.

Where not specified, the simulated ground deformation field is calculated by using the FEM approach (COMSOL Multiphysics software package) to accurately reproduce the required physical scenario.

We remark this work is developed for analysing DInSAR measurements; therefore, we do not consider the North-South component of the ground deformation field in these simulations; although this component should be important for further constraining the volcanic scenario, the combination between LOS ascending and descending data does not provide information about the North-South deformation with acceptable accuracy.

From now on and according to the paragraph 2.5.2 and equations (2.31) and (2.32), the homogeneity degree of the field n is calculated through τ ; in particular, the value assuming $\tau(q)$ when q tends to 0 is observed since, in this condition, $\tau(q)$ tends to n . Moreover, n_s and N parameters are calculated by considering the differentiation order p of the analysed function respect to its Newtonian potential.

3.1 Validation of the Upward Continuation transform.

Although the FEM allows reproducing the essential physical conditions for this validation, numerical upward continuation is affected by edge errors related to the lack of enough extension of the measurements surface. From a practical point of view, the higher the continuation scale, the larger the measurement surface should be. However, we can attenuate this error by resorting to some extrapolation algorithms (e.g., zero padding, smooth extension of order 0 or 1 [Fedi et al., 2012]).

In the FEM framework, the domain discretization is strictly related to the mesh size and to the dimension of the modeled half-space, which should be theoretically infinitely vertically and horizontally extended; it is indeed difficult to reproduce the half-space condition.

To evaluate the error of FEM geometrical limitations for the upward continuation transform, we perform a first simulation by considering the deformation field at ground or zero level due to an over-pressurized (2 GPa) point-spherical source (radius equal to 0.05 m) embedded in a homogeneous elastic half-space; we therefore reproduce the conditions of the Mogi model, for which we have already verified that its analytical expressions satisfy the Laplace's equation and so admits upward continuation [Castaldo et al., 2018b]. For this case, we estimate the error on the upward continuation transform and we use it as reference value to assert the validity of the other solutions by using source with different geometry.

For all the simulations reported in this paragraph, we fixed the half-space physical and geometrical parameters as follows: Young's modulus $E = 1$ GPa; Poisson's coefficient $\nu = 0.25$ (adimensional); extent along the x - and y - direction equal to 100 km; extent along the z - direction equal to 50 km; tetrahedral mesh of the entire domain and source with ranging dimension from 0.2 to 8 km and from 0.005 to 0.01 km, respectively; mapped mesh for the free-surface with 0.4 km sampling step; fixed constraint and roller as boundary conditions of the half-space bottom and sides, respectively.

Starting from the field of a source located at the depth $z_0 = 1$ km and with horizontal coordinate $(x_0, y_0) = (50, 50)$ km along both the x - and y -directions, we evaluate the percentage error of the upward continued field to +4 km with respect to the zero level (i.e., the modeled ground deformation field on the flat free surface). We consider both the

vertical and E-W deformation components (**Figure 3.1**) and, as expected, in the case of the point-spherical source, we retrieve a very low error, calculated by normalizing the difference between the +4 km continued field and the simulated one at that scale. Its maximum value is equal to 0.36 % (**Figure 3.1a**) at the source centre, and 0.65 % (**Figure 3.1b**) at the half-space lateral sides for both the vertical and the E-W components of the deformations, respectively. We consider these error values as reference ones.

As first representative test, we analyse a prism with the z-extent less than the others; in particular, we build a 0.1 km thick body with an extent along the x - and y -directions equal to 0.5 km. In this case, we retrieve a discrepancy between the continued and the expected field with maximum error of 0.44% (**Figure 3.1c**) at the source centre and 0.65 % (**Figure 3.1d**) at the half-space lateral sides for the vertical and the E-W ground deformation components, respectively.

As second representative test, we consider a vertical cylinder with radial dimension equal to 0.2 m and 0.8 m vertical extent. Also in this case, the upward continuation procedure leads to a very low error, with maximum value of 0.47% (**Figure 3.1e**) for the vertical deformation and 0.65% (**Figure 3.1f**) for the E-W one, at the source centre and half-space lateral sides, respectively.

Finally, we also tested other source configurations, whose results are reported in the **Table A.1** and **Figure A.1** of the **Appendix A**.

All these results show the correct application of the upward continuation filter and, in turn, they validate equation (1.23), according to which the elastic problem reduces to a harmonic solution in the case of sources with hydrostatic variation of pressure and embedded in a homogeneous elastic half-space, whatever the geometrical source configurations is. We specify that this operator works finely for both the vertical and E-W components of the deformation field and, so, it is also valid in the case of DInSAR measurements with LOS components since equations (2.15) is satisfied.

We remark that it is also possible to resort to the draped-to-level upward continuation and to the VD_F , for which please refer to the **Appendix B** and **C**, respectively.

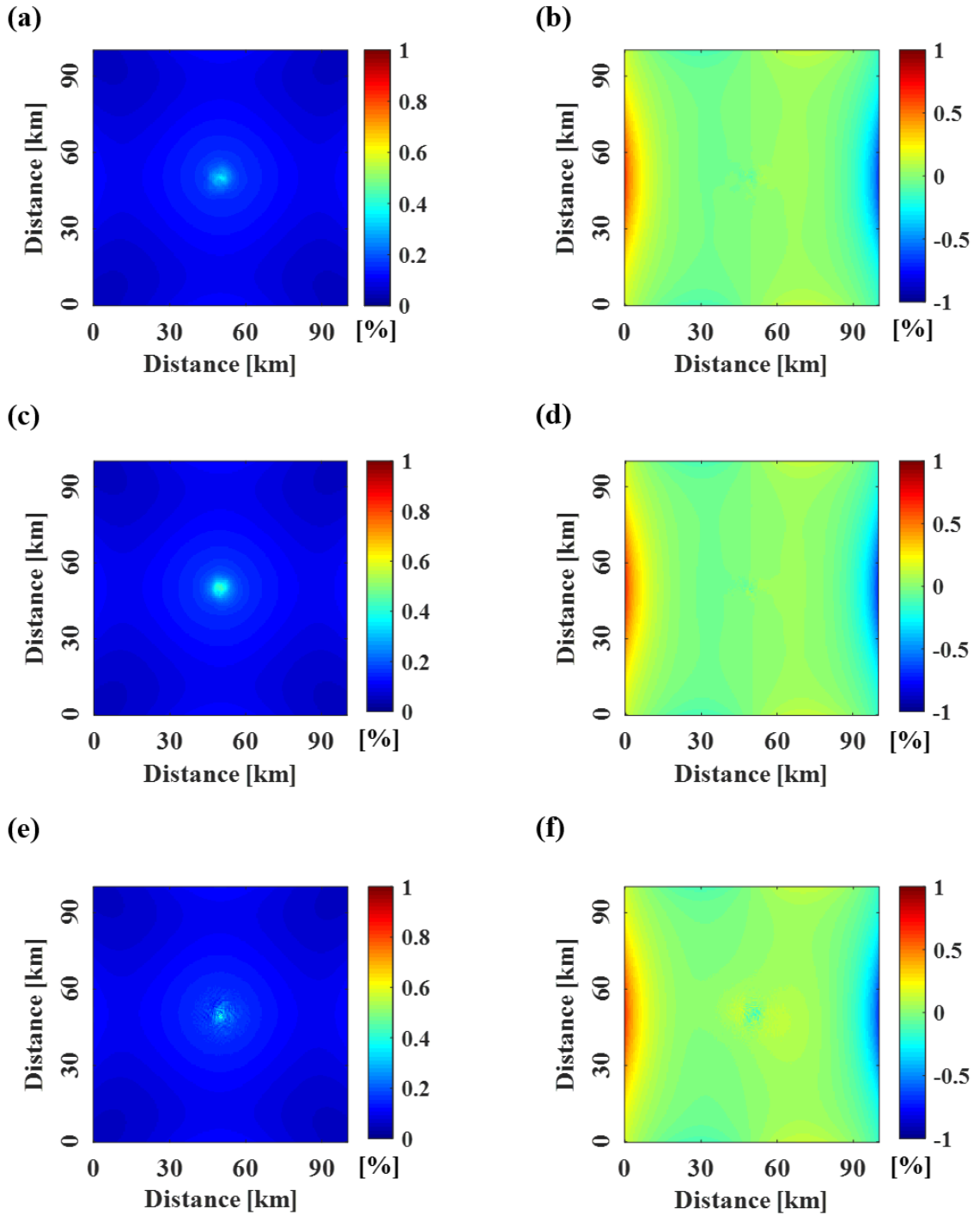


Figure 3.1. Validation of the Upward Continuation transform. Error maps [%] for the upward continuation applied to the (a) vertical (b) and E-W components of the deformation field at ground level generated by a point-spherical source, (c-d) horizontal prism and (e-f) vertical cylinder.

3.2 Use of integrated multi-scale methods.

We show several cases by simulating harmonic and biharmonic fields, and biharmonic but non-harmonic ones. Moreover, we consider deformation sources with geometrically regular and irregular shapes; this allows exploiting the homogeneity and local-homogeneity properties of the proposed solution of the elastic problem.

Among the regular sources, we analyse the cases of a vertically elongated body for simulating the volcanic scenarios of ascent pipe and reproducing shape like the Yang's AM [Yang and Davis, 1988], and of a horizontal planar one for sills emplacement and the Okada's AM [Okada, 1985]. We consider the analysis of both the vertical and E-W components of the deformation field. Note that these bodies approximate the ideal sources and, therefore, they can be treated according to the homogeneity theory.

We remark that the homogeneity properties are primarily important for this work; so, for briefly introducing the approach about geometrically irregular sources and the local-homogeneity, we consider only two cases, which are the vertical deformations of a 3D complex body and a multi-source scenario.

In **Appendix D**, we also report the results of tests about Multiridge and ScalFun methods starting from the field of a Mogi source and by considering the noise in the dataset, the LOS components and the constant-level reduction procedure.

3.2.1 Geometric parameters detection of regular sources.

We start with the application of Multiridge and ScalFun methods for analysing vertically elongated bodies, which are representative of ascent pipe mechanisms and whose shapes are equivalent to the Yang's AM.

In particular, we model three scenarios: (I) the Sphere Case, where the semi-axes of the source $r_x = r_y = r_z = 0.5$ km and for which a point source describes its behaviour; (II) the Ellipsoid 1 Case, where $r_x = r_y = 0.5$ km while $r_z = 1.5$ km (aspect ratio of the ellipsoid equal to 0.33); (III) the Ellipsoid 2 Case, where $r_x = r_y = 0.5$ km while $r_z = 2.5$ km (aspect ratio of the ellipsoid equal to 0.2) and for which at low scales a linear ideal source describes its behaviour.

In these cases, the depth to the source and its over-pressure are fixed to 3 km and 5 MPa, respectively; the other parameters of the model setting are equal to the already described test in the Paragraph 3.1, except for the source mesh size, which is here ranging from 0.01 to 0.1 km.

We consider the vertical deformation modeled at zero level, for which **Figure 3.2a-b-c** shows the anomalies of the different source geometries. We extract the AB profile (black dashed line in **Figure 3.2a-b-c**) passing through the maximum value of the three anomalies (**Figure 3.2d**), in order to define the multiridge subset (green dots, red stars and black triangles in **Figure 3.2e**), to represent the ridges (green dashed lines, red and black continuous lines in **Figure 3.2e**) and to compare their trends at different scales.

First, we analyse the Sphere Case. We apply the Multiridge method by calculating a multi-scale dataset from the zero level to the 10 km upward continued field, with 0.4 km of continuation sampling. We represent the ridges (solid green dashed lines **Figure 3.2e**) through linear regression, whose slopes are constant at any scale. Their intersection indicates a source located at 50 km along the x -direction at exactly 3 km of depth. We apply the ScalFun method to the central ridge; the results (green stars in **Figure 3.2f**) indicate that $n \sim -2$ (exact value: 2.01) and, so, since $p = 1$, $N \sim 3$ (**Table 2.1**) characterizes the retrieved source at 3 km of depth, which is the point where the source distribution has its centre.

For the second scenario, the Ellipsoid 1 Case, we apply the Multiridge method in the same way of the previous test. The ridges above the 4.8 km scale line up along the same straight line of the previous one, while below this scale they slightly change their slope. However, we use only the ridges above the 4.8 km scale (black continuous lines in **Figure 3.2e**) which intersect at exactly 3 km of depth and horizontally at 50 km along the x -direction. As in the previous case, we apply the ScalFun method (black stars in **Figure 3.2f**) characterizing this source with $n \sim -2$ (exact value: -2.06) and $N \sim 3$ (**Table 2.1**).

Similar considerations arise from the last case of Ellipsoid 2, whose source behaves at low scale like a linear source. We apply the Multiridge method by considering the upward continued field until 12 km. In this case, the ridges stabilize along a straight line as the Sphere Case from 8.8 km scale (red continuous lines in **Figure 3.2e**) by intersecting at the point $x_0 = 50$ km and $z_0 = 2.8$ km. Also in this case, the result of the ScalFun method (red stars in **Figure 3.2f**) suggests that the retrieved information is related to the

centre of the deformation source, since the $n \sim -2$ (exact value: -2.07) and, therefore, $N \sim 3$ (**Table 2.1**). Instead, at lower scales the ridges change their slope tending to converge to the singular point of the source, that is its top (red dashed lines in **Figure 3.2e**).

These results are consistent with the asymptotic expression of the multipolar expansion of potential fields. Indeed, at large scales the multipolar terms vanish allowing the identification of the source centre, while at low ones they do not vanish affecting the slope ridges. However, we will show in the next tests how the VD_F enhances the high-wavenumber part of the field allowing a better characterization of the source shape.

We underline these results are expected since we are analysing bodies which approximate the ideal sources and change their homogeneity properties with the scale.

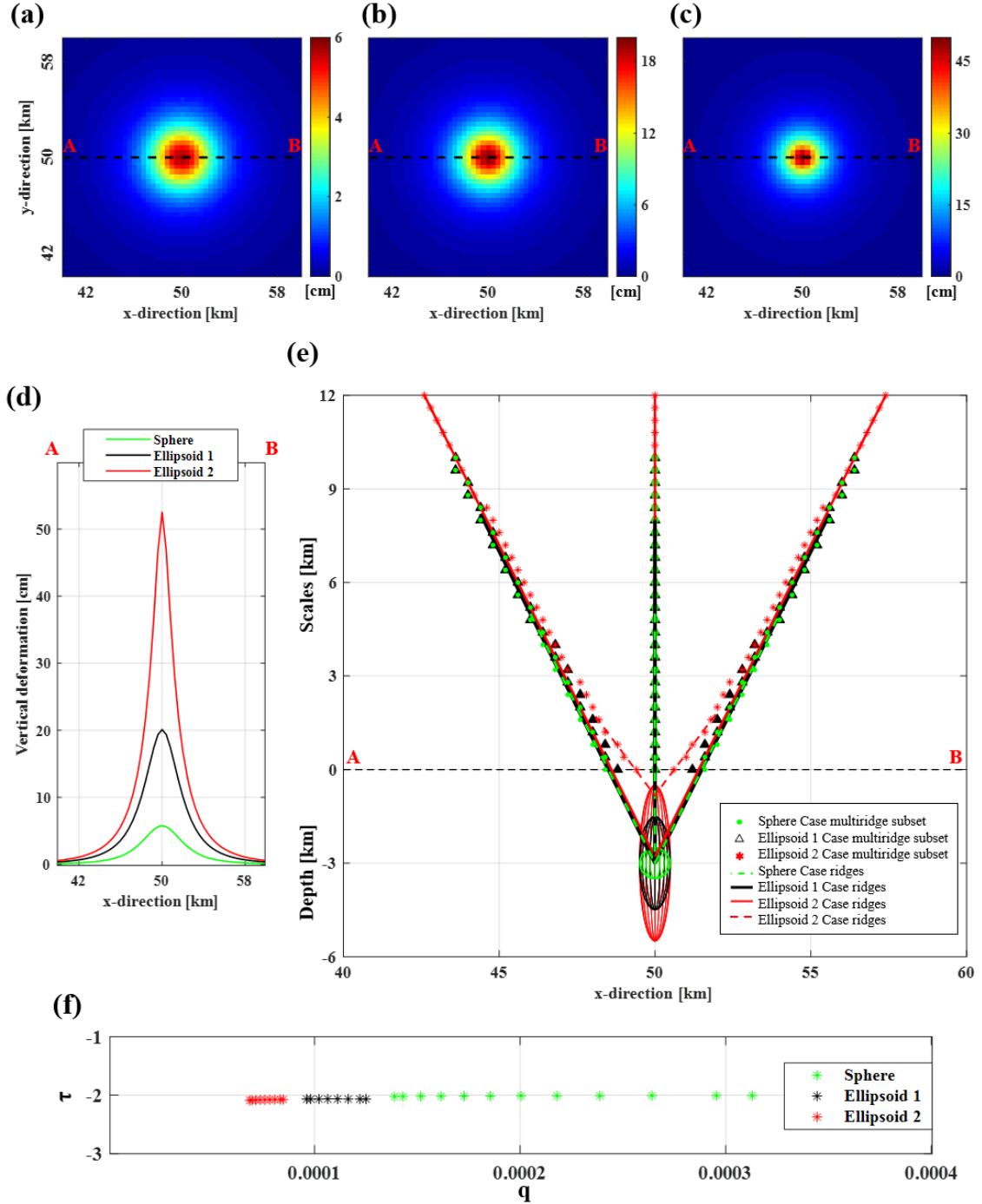


Figure 3.2. Vertically elongated sources test: vertical component. Modeled vertical component related to the (a) Sphere, (b) Ellipsoid 1 and (c) Ellipsoid 2 cases, to which Multiridge and ScalFun methods are applied. (d) Vertical deformation profiles extracted along the AB trace (black dashed lines) for the three considered fields. (e) Results of Multiridge method for the three considered cases; the horizontal black dashed line indicates the modeled data reference level. (f) Results of ScalFun method applied on the central ridge for each case; $q = \frac{1}{z}$ while $\tau = \frac{\partial \log(w(z))}{\partial \log z}$, where w and z represent the vertical deformation and the vertical scale, respectively.

Subsequently, we use Multiridge and ScalFun methods to analyse the horizontal planar bodies, which are representative of sill emplacement mechanisms and whose shapes are like the Okada's AM.

Also, we model three scenarios: (I) the Cube Case, where the source sides $L_x = L_y = L_z = 1$ km; (II) the Prism 1 Case, where $L_z = 1$ km, while $L_x = L_y = 2.5$ km; (III) the Prism 2 Case, where $L_z = 1$ km, $L_x = L_y = 5$ km and for which at low scale a planar ideal source describes its behaviour.

The other model setting parameters are the same of the above-described set of tests.

We start from the vertical deformation modeled at zero level, for which **Figure 3.3a-b-c** shows the anomalies of the different cases, and we extract the CD profile (black dashed line in **Figure 3.3a-b-c**) passing through the maximum value of the three anomalies (**Figure 3.3d**). After, we define the multiridge subset (green dots, red stars and black triangles in **Figure 3.3e**) to represent the ridges (green dashed lines, red and black continuous lines in **Figure 3.3e**) and to compare their trends at different scales.

We first consider the simple Cube Case where we create a multi-scale dataset from the zero level to the upward continued field to 10 km, with 0.4 km of continuation sampling. In this case, constant slopes characterize the represented ridges at different scales (green dashed lines in **Figure 3.3e**), which are like those of the Sphere Case (green dashed lines in **Figure 3.2e**) since they line up along the same single straight line. This behaviour is consistent with the asymptotic expression of the multipolar expansion of potential fields since the scale is not so low to enhance the multipolar terms of the field. The retrieved intersection indicates a body located at 50 km along the x -direction at exactly 3 km of depth and the ScalFun method (green stars in **Figure 3.3f**) characterizes it with $n \sim -2$ (exact value: -2.01) and $N \sim 3$ (**Table 2.1**) since $p = 1$.

Subsequently, we analyse the Prism 1 Case by considering the upward continued field until 15 km. We note the ridges up to 7.2 km scale have different slopes respect to those at larger ones, where they intersect in the point at 50 km along the x -direction and at exactly 3 km of depth (black continuous lines in **Figure 3.3e**); while, at low scales the singularities of the body, or its edges, affect the ridges, which do not tend to converge in a point within the source. However, at larger scales the multipolar terms vanish, and the ridges intersect at the source centre. Indeed, the results of ScalFun method (black stars in

Figure 3.3f) characterizes the retrieved source at larger scales with $n \sim -2$ (exact value: -2.03) and $N \sim 3$ (**Table 2.1**).

Finally, we observe a similar behaviour for the Prism 2 Case, for which we consider the upward continued field up to 17 km. In this case, the singularities of the body are so well defined to affect the multiridge subset that, at low scales, tend to the edges of the body. When the multipolar terms vanish, that is above the 11.2 km scale for this case, the ridges converge to the point with horizontal position and depth of 50 km along the x -direction and 3 km, respectively (red continuous lines in **Figure 3.3e**). Values as $n \sim -2$ (exact value: -2.05) and $N \sim 3$ (**Table 2.1**) characterize this source through ScalFun method (red stars in **Figure 3.3f**), which confirms that this solution represents the centre of the source.

We again underline that these results are expected since we are analysing bodies which approximate the ideal sources and change their homogeneity properties with the scale. Moreover, we specify for studying the singularities of such planar body we must resort to VD_F , as it will be shown in the next tests.

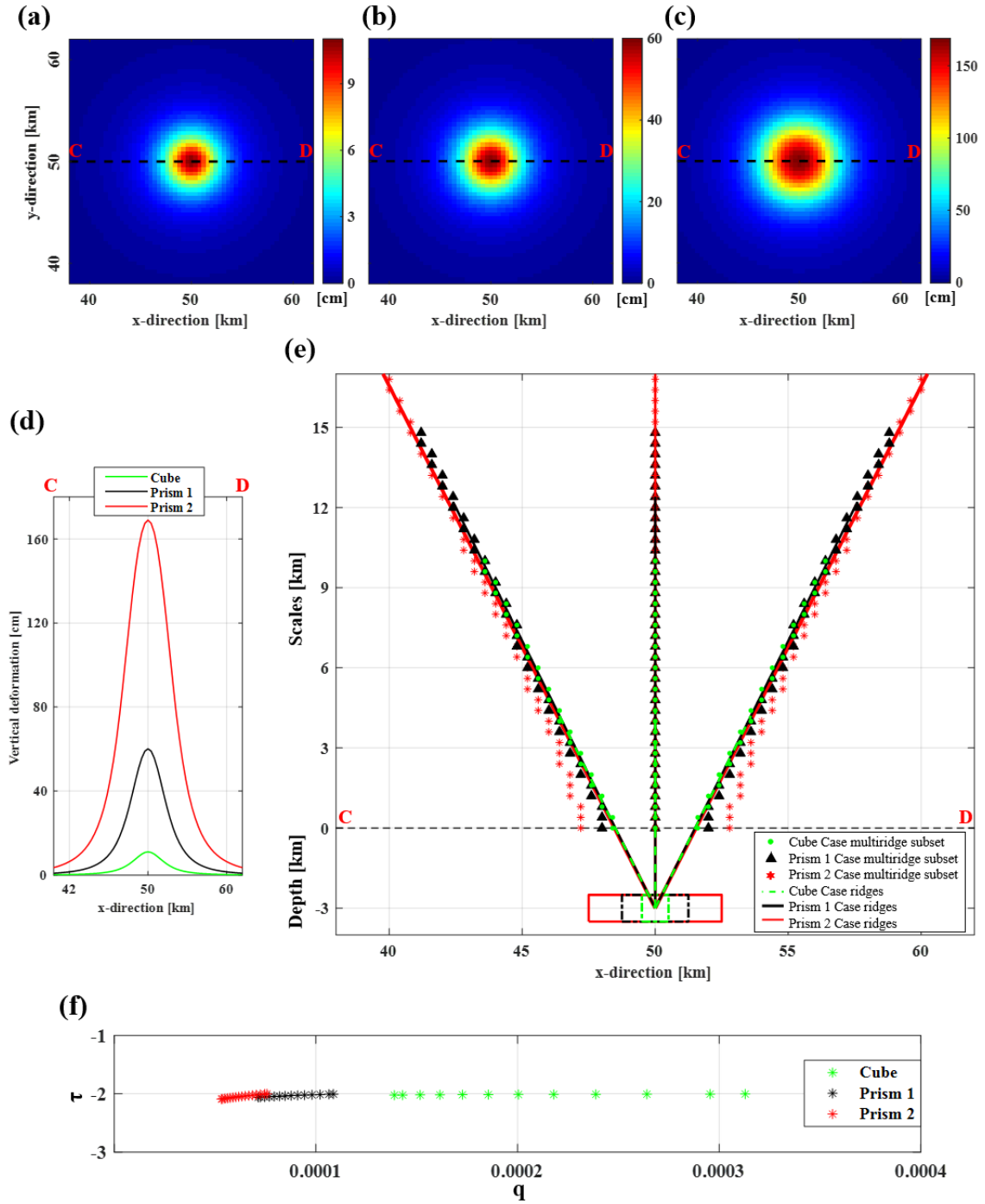


Figure 3.3. Horizontal planar sources test: vertical component. Modeled vertical component related to the (a) Cube, (b) Prism 1 and (c) Prism 2 cases, to which Multiridge and ScalFun methods are applied. (d) Vertical deformation profiles extracted along the CD trace (black dashed lines) for the three considered fields. (e) Results of Multiridge method for the three considered cases; the horizontal black dashed line indicates the modeled data reference level. (f) Results of ScalFun method applied on the central ridge for each case; $q = \frac{1}{z}$ while $\tau = \frac{\partial \log(w(z))}{\partial \log z}$, where w and z represent the vertical deformation and the vertical scale, respectively.

To complete the analysis with the components of the field, we consider the E-W deformation for both the Ellipsoid 2 (**Figure 3.4a**) and Prism 2 (**Figure 3.4b**) cases.

We extract the same EF profile (black dashed line in **Figure 3.4a-b**) passing through the maximum value of the field for both models (**Figure 3.4c**).

For the first and second cases, we create the multi-scale datasets up to the 12 km and 15 km scales, respectively, with 0.4 km of continuation sampling.

We firstly discuss about the ridges behaviour at low scales. Similar for the vertical component, in the first case, they intersect nearby the singular point of the source, that is its top for the vertically elongated one (blue dashed lines in **Figure 3.4d**); in the second case, the edges of the body affect the distribution of the multiridge subset (**Figure 3.4d**).

Then, we analyse the larger scales case. In particular, we represent the ridges as linear regression up to 6 km and to 7 km for the Ellipsoid 2 (blue continuous lines in **Figure 3.4d**) and Prism 2 (red dashed lines in **Figure 3.4d**). The retrieved intersections show that the sources are located at 50 km along the x -direction at depths of 3.02 and 3.04 km for the first and second cases, respectively (**Figure 3.4d**). We validate these source solutions by applying the ScalFun method on the ridges representative of the maximum value of the considered field and for both the cases values as $n \sim -2$ (exact value: -2.07 and 2.01 for the Ellipsoid 2 and Prism 2 cases) and $N \sim 3$ (**Table 2.1**) characterize these sources (blue stars and red dots in **Figure 3.4e** for the first and second cases). The results confirm that these source solutions are representative of the centres of the bodies.

We remark these analyses are consistent with the asymptotic expression of the multipolar expansion of potential fields.

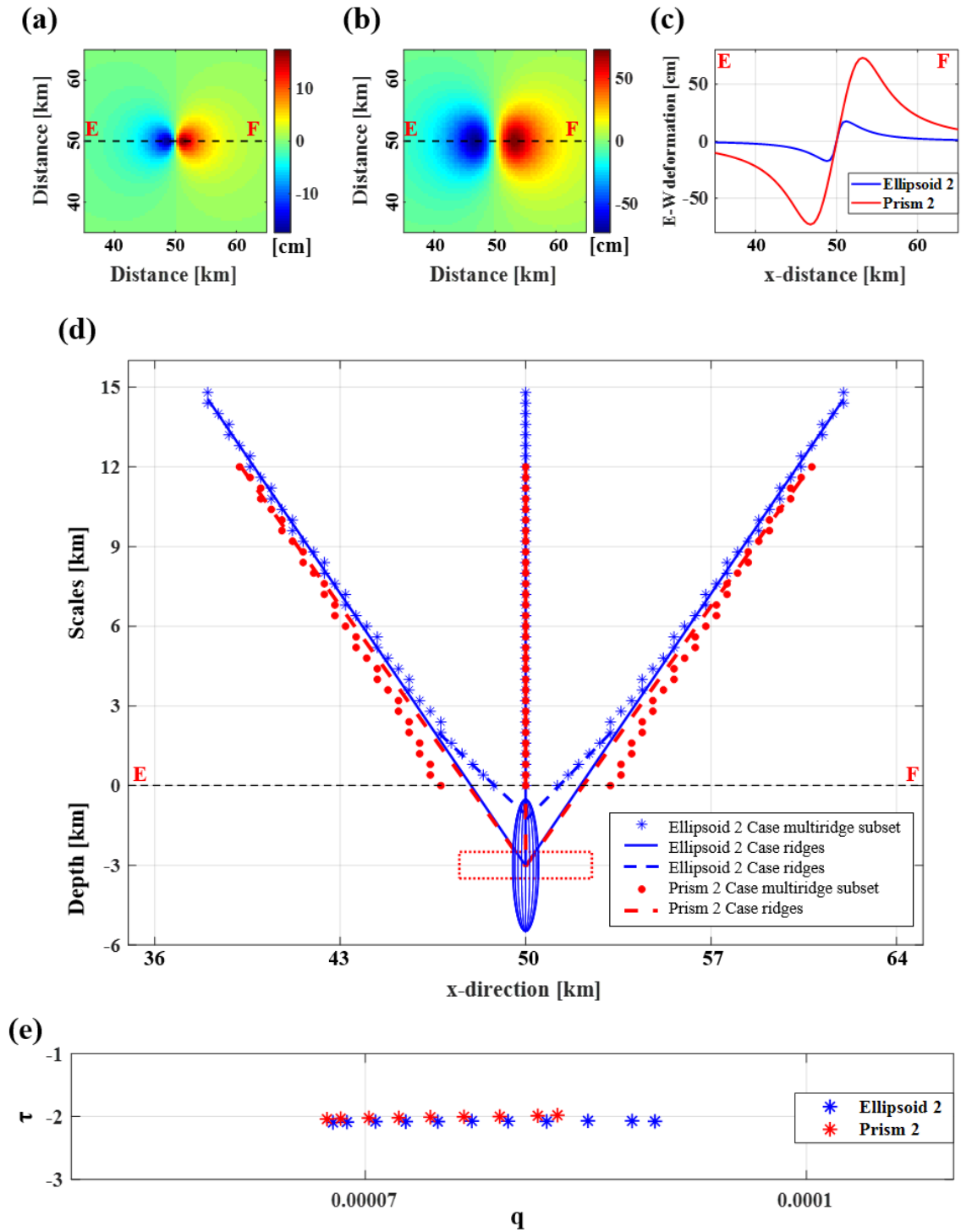


Figure 3.4. Vertically elongated and Horizontal planar sources test: E-W component.

Modeled E-W component related to the (a) Ellipsoid 2 and (b) Prism 2 cases, to which Multiridge and ScalFun methods are applied. (c) E-W deformation profiles extracted along the EF trace (black dashed lines) for both the considered cases. (d) Results of Multiridge method for both the cases; the horizontal black dashed line indicates the modeled data reference level. (e) Results of ScalFun method applied on the right-hand ridge for each case; $q = \frac{1}{z}$ while $\tau = \frac{\partial \log(u(z))}{\partial \log z}$, where u and z represent the E-W deformation and the vertical scale, respectively.

At this stage, we consider the VD_F , by equation (2.35), to better investigate about the deformation sources and their morphological attributes, for which the field analysis has already provided preliminary information. This filter indeed enhances the high-wavenumber part of the field and its multipolar terms, allowing a better characterization of the shallowest singularities of the source.

We still consider the homogeneity properties of the ideal sources and the most interesting cases of the Ellipsoid 2 and Prism 2.

We start from the vertical deformations and we calculate the first ($p = 2$) and the second order ($p = 3$) VD_F for the Ellipsoid 2 (**Figure 3.5a**) and Prism 2 (**Figure 3.5b**) cases; we extract the same GH profile (black dashed line in **Figure 3.5a-b**) passing through the maximum value of the field for both models (**Figure 3.5c-d**) and we consider a multi-scale datasets up to the 6 km with 0.4 km of continuation sampling. Note that we consider lower scales, compared to the previous cases, since our aim is focusing the analysis on the shallowest portion of the source.

For the Ellipsoid 2 Cases, we individuate two sets of ridges: the first one (blue dashed lines in **Figure 3.5e**), characterized by large horizontal distance to the source, tends to converge to the centre of the body; the second and most interesting one (blue continuous lines in **Figure 3.5e**) instead allows the individuation of a 0.51 km depth source at the point with $x = 50$ km. Specifically, the ScalFun method characterizes this solution with values as $n \sim -2$ (exact value: -2.01) and $N \sim 2$ (**Table 2.1**) since $p = 2$ (blue stars in **Figure 3.5f**). Therefore, we can model this as a vertical or horizontal linear source, whose top or centre is located at 0.51 km. However, we exclude the second possibility since the field anomaly suggests the sources is not horizontally elongated.

For the Prism 2 Case, the ridges converge to two points with coordinates $(x, z) = (47.6, 2.4)$ km and $(x, z) = (52.4, 2.4)$ km (red solid lines in **Figure 3.5e**), nearby the edges of the bodies. The ScalFun method characterizes these solutions with values as $n \sim -2$ (exact value: -2.02) and $N \sim 1$ (**Table 2.1**) since $p = 3$ (red stars in **Figure 3.5f**). Therefore, we can interpret these solutions as the edges of a horizontal planar source or the tops of two vertical planar bodies. However, the field anomaly (**Figure 3.2c**) suggests the source is only one and we exclude the second possibility.

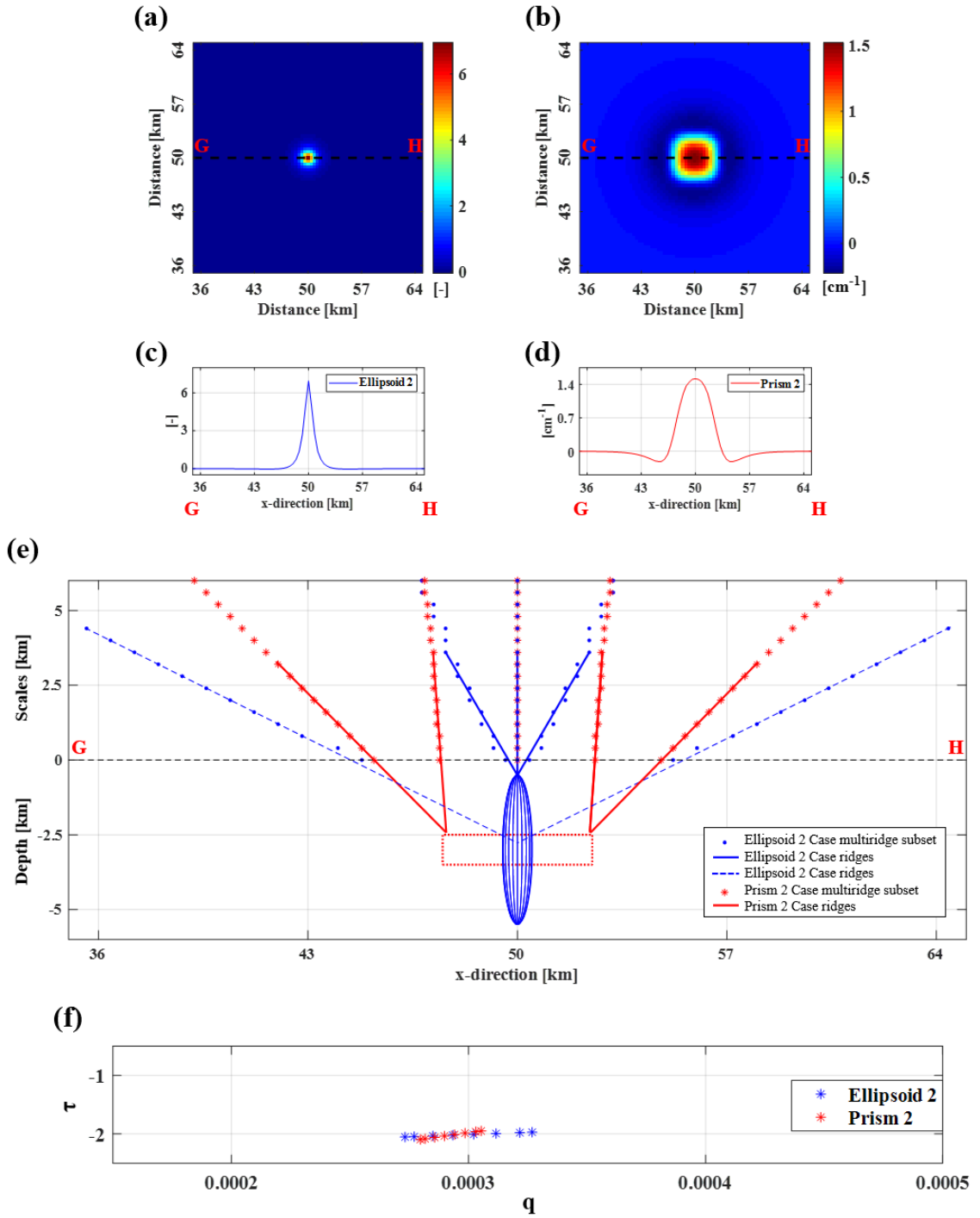


Figure 3.5. Vertically elongated and Horizontal planar sources test: VD_F of vertical deformation. Modeled first and second order VD_F of the vertical component related to the (a) Ellipsoid 2 and (b) Prism 2 cases, respectively, to which Multiridge and ScalFun methods are applied. (c-d) Deformation profiles extracted along the GH trace (black dashed lines) and (e) results of Multiridge method for both the considered cases; the horizontal black dashed line indicates the modeled data reference level. (f) Results of ScalFun method applied on the central ridge for each case; $q = \frac{1}{z}$ while $\tau = \frac{\partial \log(VD_F(z))}{\partial \log z}$, where z represents the vertical scale.

Furthermore, we also consider the analysis of the E-W component by calculating its second-order ($p = 3$) VD_F for both Ellipsoid 2 (**Figure 3.6a**) and Prism 2 (**Figure 3.6b**) cases; we extract the same IL profile (black dashed line in **Figure 3.6a-b**) passing through the maximum value of the field for both models (**Figure 3.6c**) and we consider a multi-scale datasets up to the 6 km with 0.4 km of continuation sampling.

The results are like the previous test.

For the Ellipsoid 2 Cases, the ridges tend to converge at 50 km along the x -direction and 0.6 km of depth (blue continuous lines in **Figure 3.6d**); the ScalFun method characterizes this solution with values as $n \sim -3$ (exact value: -3.02) and $N \sim 2$ (**Table 2.1**) since $p = 3$ (blue stars in **Figure 3.6e**).

For the Prism 2 Case, the ridges converge to two points with coordinates $(x, z) = (47.6, 2.4)$ km and $(x, z) = (52.4, 2.4)$ km (red continuous lines in **Figure 3.6d**), nearby the edges of the bodies. The ScalFun method characterizes these solutions with values as $n \sim -2$ (exact value: -2.05) and $N \sim 1$ (**Table 2.1**) since $p = 3$ (red stars in **Figure 3.6e**).

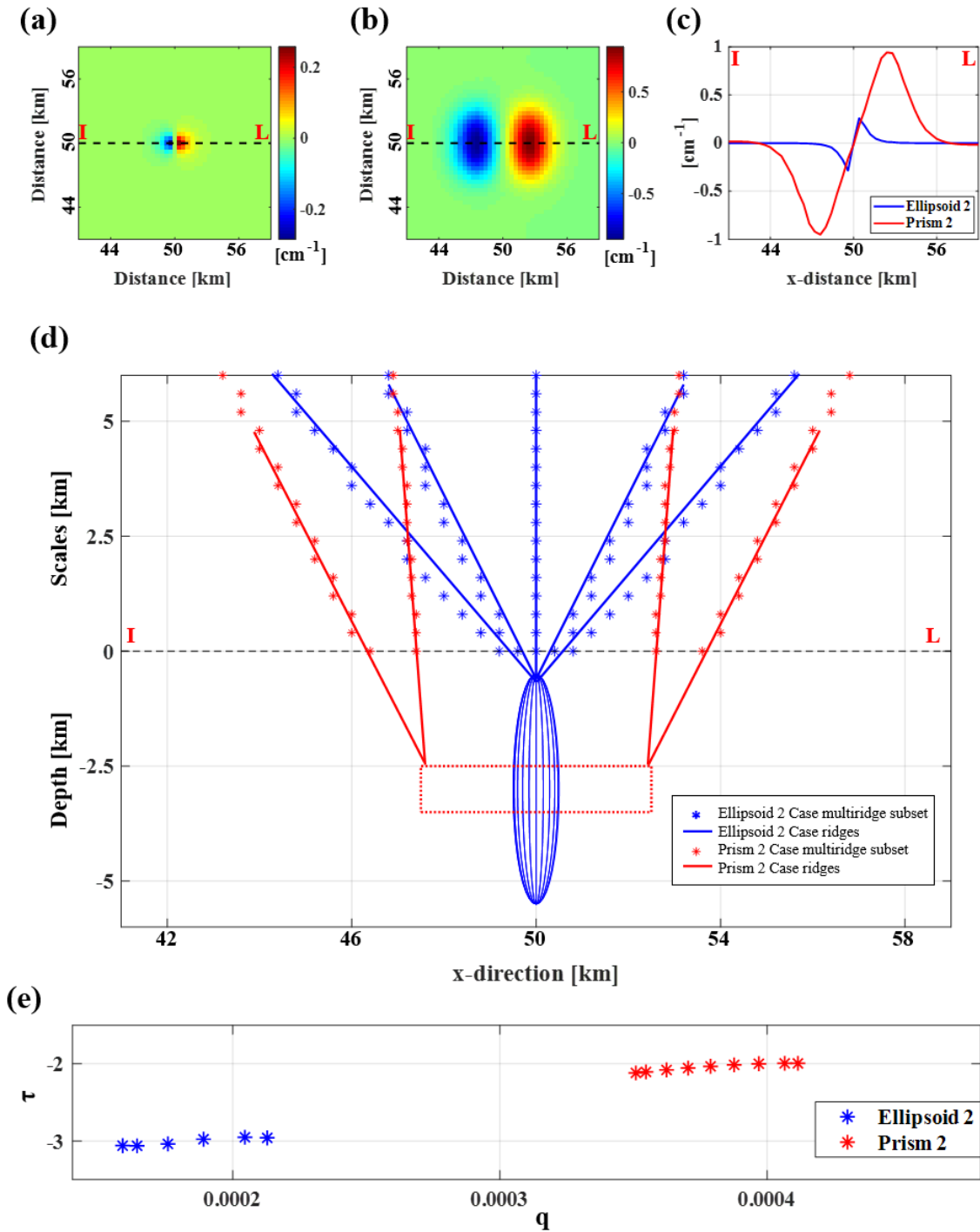


Figure 3.6. Vertically elongated and Horizontal planar sources test: VD_F of E-W deformation. Modeled second-order VD_F of the E-W component related to the (a) Ellipsoid 2 and (b) Prism 2 cases, respectively, to which Multiridge and ScalFun methods are applied. (c) Deformation profiles extracted along the IL trace (black dashed lines) and (d) results of Multiridge method, for both the considered cases; the horizontal black dashed line indicates the modeled data reference level. (e) Results of ScalFun method; $q = \frac{1}{z}$ while $\tau = \frac{\partial \log(VD_F(z))}{\partial \log z}$, where z represents the vertical scale.

Finally, we conclude this paragraph by applying the THD technique for the detection of the sources horizontal extent. We remark that the use of this technique depends on the depth to the source respect to its extent and on its geometrical configuration. Therefore, we consider the low (i.e., Prism 2) and large (i.e., Prism 1) scale cases.

We calculate the THD_w on the vertical deformation (**Figure 3.3b-c**) for both the cases (**Figure 3.7**). As expected, in the first case we retrieve acceptable results on the exact horizontal sizes of source since the maxima of THD_w tend to match with the boundaries of the deformation body (**Figure 3.7a**); while, in the second one we retrieve an overestimation of its horizontal extent (2.5 km) ~ 0.8 km; indeed, the maxima of THD_w indicate a ~ 3.3 km horizontally extended source (**Figure 3.7b**).

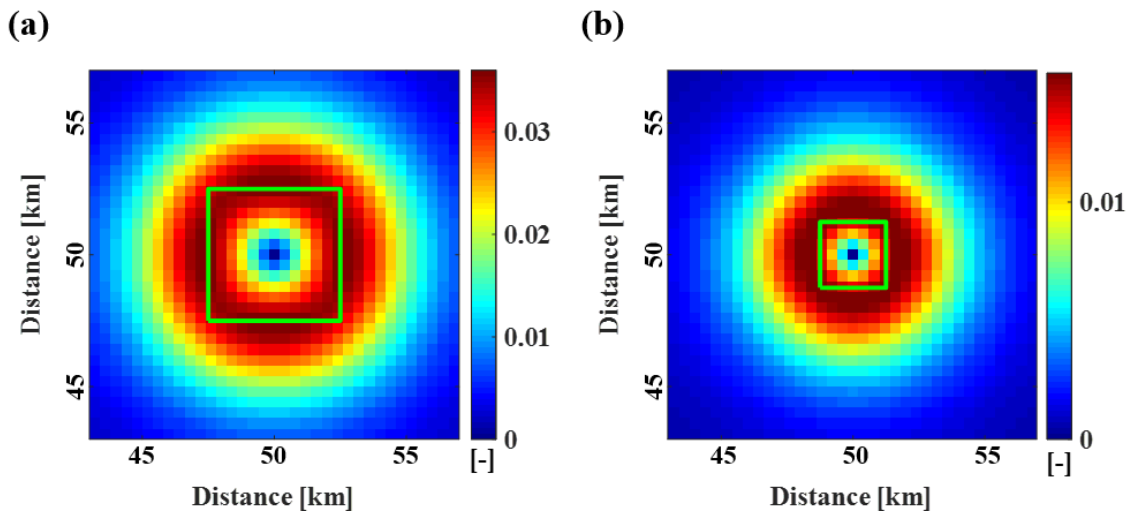


Figure 3.7. THD_w for the detection of source horizontal extent. Results of THD_w (adimensional) for the vertical deformations of the (a) low and (b) large scale cases. The green continuous lines represent the projection of the sources boundaries on the horizontal plane.

3.2.2 Geometric parameters detection of irregular sources.

We apply the integrated multi-scale approach to analyse deformation field of sources with irregular geometry. We remark that the aim of these tests is just to introduce how approaching to the inhomogeneous fields by considering the local-homogeneity properties.

In particular, we consider only two cases: Case 1, in which the deformation source is unique and complex one (**Figure 3.8a**) and it produces the vertical deformation mapped in **Figure 3.8b**; Case 2, in which the analysed vertical component (**Figure 3.8d**) is produced by two separated sources, as shown in **Figure 3.8c**.

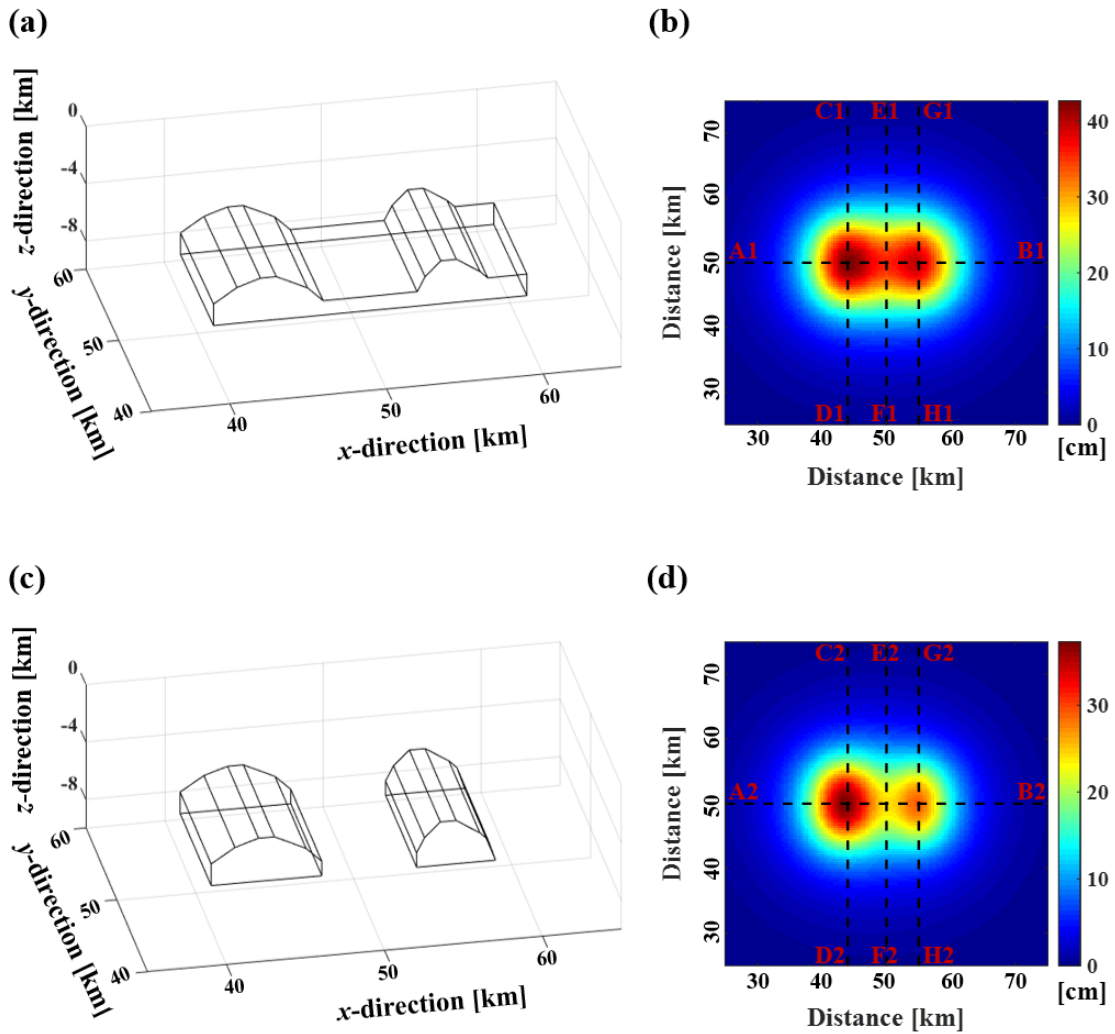


Figure 3.8. Geometrical configurations for irregular sources. Geometrical configuration of the considered sources and the associated vertical deformation [cm] for (a-b) the Case 1 and (c-d) the Case 2, respectively. The black dashed lines represent the traces we use to show the results.

In the Case 1 (**Figure 3.8a**) the source extends 20 and 10 km along the x - and y -directions, respectively, with a variable depth from 4 to 7 km. In the Case 2 (**Figure 3.8b**), instead, we have a reproduction of the previous one without both the morphologically flat portions. The settled physical scenario satisfies the equation (1.23) according to which the deformation field satisfy the Laplace's equation in the case of hydrostatic pressure variation of the source embedded in a homogeneous elastic half-space; the other model parameters are similar to those set in the previous simulations, except for the over-pressure of the source, which here is equal to 0.5 MPa, and the mesh size, which is ranging from 0.3 to 6 km for both the source and the entire domain. For each case, we consider the results of Multiridge and ScalFun methods by selecting four profile (black dashed lines in **Figure 3.8b** and **3.8d**).

We start from the Case 1 by considering the E-W oriented profile A1-B1, passing through both the highest morphological zones of the source (black dashed lines in **Figure 3.8b**). We analyse the second-order VD_F ($p = 3$) because of the complexity of source geometry.

The Multiridge and ScalFun analysis provide information from four ridge intersections (**Figure 3.9a**): the first one (blue continuous lines in **Figure 3.9a**) is almost centred with respect to the first highest morphological part of the source at a depth of about 6 km; stable not integer values of $n \sim -3.5$ and $N \sim 2.5$ (blue stars in **Figure 3.9b**) characterizes this source; the second one (green continuous lines in **Figure 3.9a**) is located almost at the centre between the second highest morphological zone and the second flat morphologically portion of the source; the retrieved depth is almost equal to 6.5 km and the associated stable not integer value of $n \sim -3.5$ (green stars in **Figure 3.9b**) corresponds to $N \sim 2.5$; the third (red continuous lines in **Figure 3.9a**) and the fourth (magenta continuous lines in **Figure 3.9a**) intersections correspond to two points lying on the top of the body with depth values equal to 4 and 4.5 km, respectively; these retrieved sources are characterized by locally stable not integer values of $n \sim -2.25$ (red stars in **Figure 3.9b**) and $n \sim -2.35$ (magenta stars in **Figure 3.9b**), which correspond to $N \sim 1.25$ and $N \sim 1.35$ for the third and fourth ones, respectively.

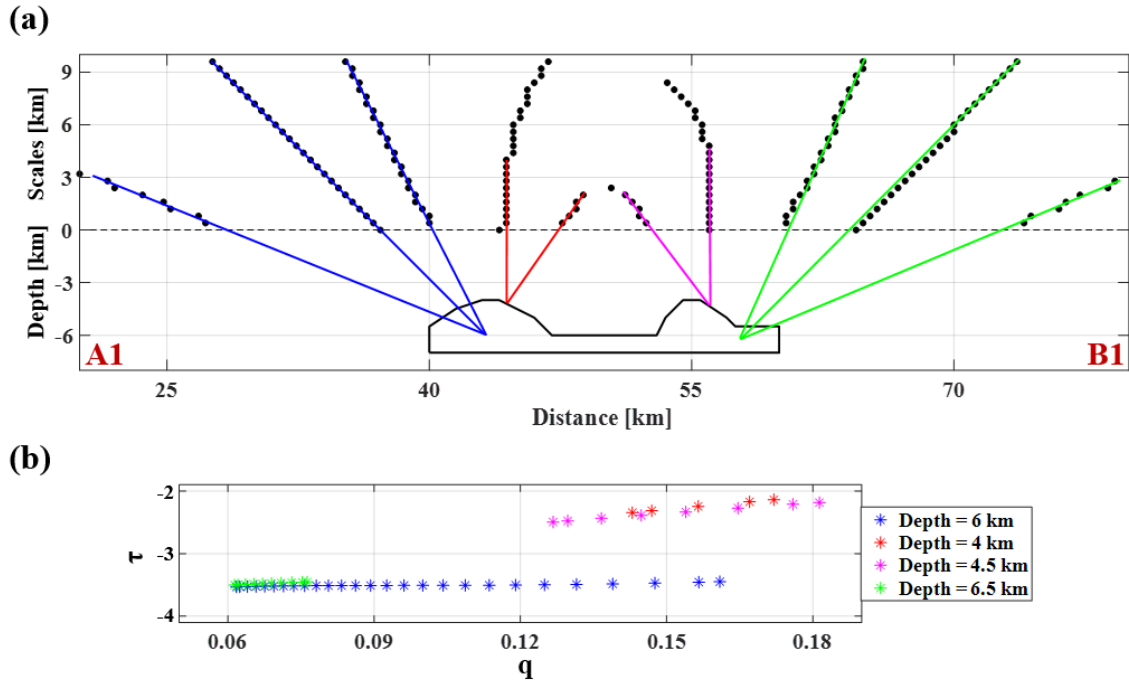


Figure 3.9. Case 1 detection: profile A1-B1. (a) Multiridge results related to the A1-B1 extracted profile of the second-order VD_F of the vertical component. (b) ScalFun results related to the four retrieved solutions by Multiridge method. The horizontal black dashed line indicates the modeled data reference level; $q = \frac{1}{z}$ while $\tau = \frac{\partial \log(VD_F(z))}{\partial \log z}$, where z represents the vertical scale.

The second trace is a N-S oriented one, named as C1-D1 (**Figure 3.8b**), passing through the first morphologically highest zone of the source. We consider the second-order VD_F ($p = 3$) of the vertical deformation and we retrieve information about three intersections: (**Figure 3.10a**): the first one (red continuous lines in **Figure 3.10a**) is almost locally centred respect to the source at a depth of about 6 km and it is characterized by a stable not integer values of $n \sim -3.6$ (red stars in **Figure 3.10b**) and $N \sim 2.6$; the second (blue continuous lines in **Figure 3.10a**) and the third ones (green continuous lines in **Figure 3.10a**) almost correspond to the boundaries of the source at a depth almost equal to 4 km, and the related values of $n \sim -2.4$ and $n \sim -2.3$ are locally stable not integer ones (blue and green stars in **Figure 3.10b**) which correspond to $N \sim 1.4$ and $N \sim 1.3$ for the second and third intersections, respectively.

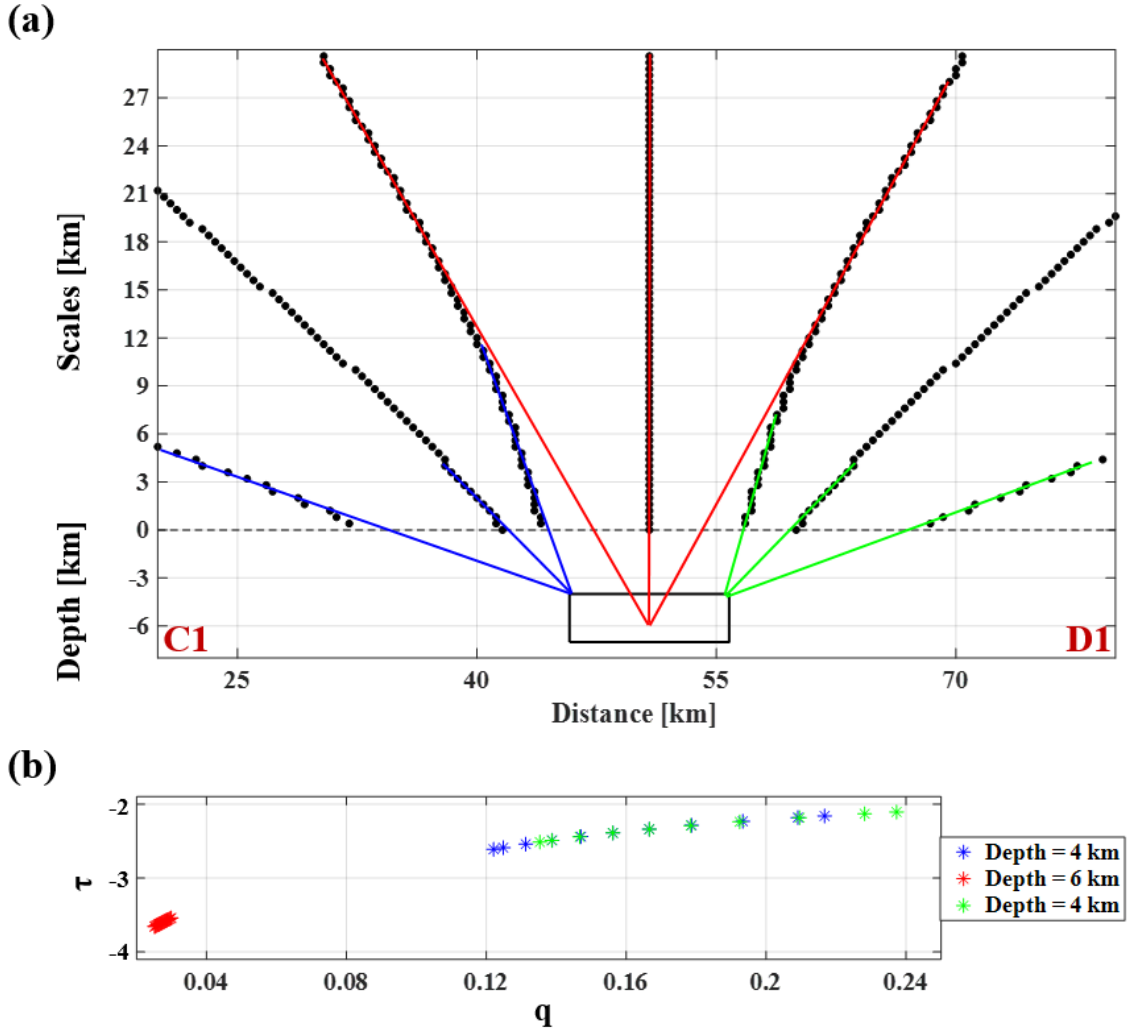


Figure 3.10. Case 1 detection: profile C1-D1. (a) Multiridge results related to the C1-D1 extracted profile of the second-order VD_F of the vertical component. (b) ScalFun results related to the three retrieved solutions by Multiridge method. The horizontal black dashed line indicates the modeled data reference level; $q = \frac{1}{z}$ while $\tau = \frac{\partial \log(VD_F(z))}{\partial \log z}$, where z represents the vertical scale.

The third N-S profile, E1-F1 (**Figure 3.8b**), passes through the morphologically flat portion of the source. We show the results related to the first-order VD_F ($p = 2$) of the vertical deformation, for which we retrieve only one intersection (**Figure 3.11a**). This last (green continuous lines in **Figure 3.11a**) is almost locally centred respect to the source at a depth of about 6.5 km and stable not integer values of $n \sim -2.8$ and $N \sim 2.8$ (green stars in **Figure 3.11b**) characterize this last.

We note that at low scales the central ridges tend to converge in a region not occupied by sources, for which the ScalFun method provides not acceptable values of n . We will better analyse this case in the next test.

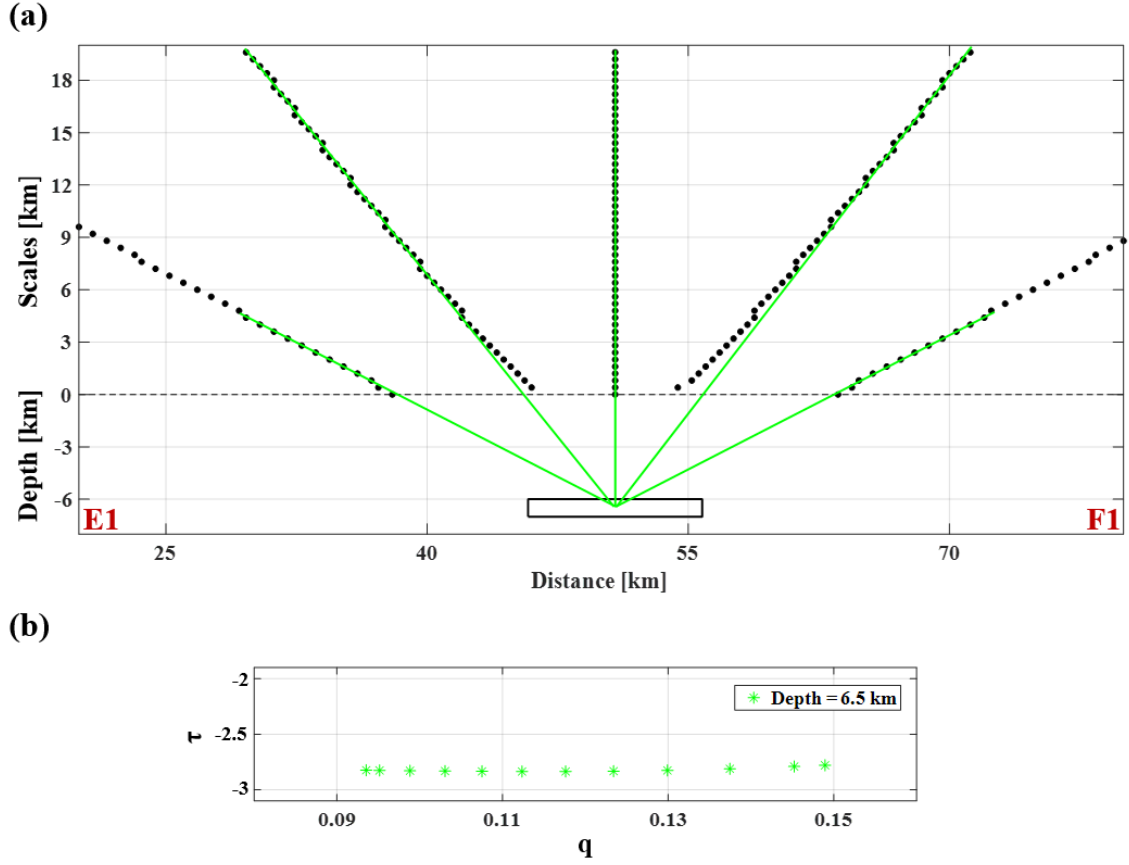


Figure 3.11. Case 1 detection: profile E1-F1. (a) Multiridge results related to the E1-F1 extracted profile of the first-order VD_F of the vertical component. (b) ScalFun results related to one retrieved solution by Multiridge method. The horizontal black dashed line indicates the modeled data reference level; $q = \frac{1}{z}$ while $\tau = \frac{\partial \log(VD_F(z))}{\partial \log z}$, where z represents the vertical scale.

The last considered N-S profile, named as G1-H1 (**Figure 3.8b**), passes through the second morphologically highest region of the source. We consider the second-order VD_F ($p = 3$) of the vertical deformation and we retrieve information about three intersection (**Figure 3.12a**): the first one (green continuous lines in **Figure 3.12a**) is representative of the local centre of the source, with depth almost equal to 6 km, and it is characterized by a stable not integer values of $n \sim -3.7$ (green stars in **Figure 3.12b**) and $N \sim 2.7$; instead,

the second (blue continuous lines in **Figure 3.12a**) and the third (red continuous lines in **Figure 3.12a**) ones identify the source boundaries at a depth of about 4 km, and the related values $n \sim -2.3$ (blue stars in **Figure 3.12b**) and $n \sim -2.2$ (red stars in **Figure 3.12b**), which correspond to $N \sim 1.3$ and $N \sim 1.2$ for the second and third intersections, respectively.

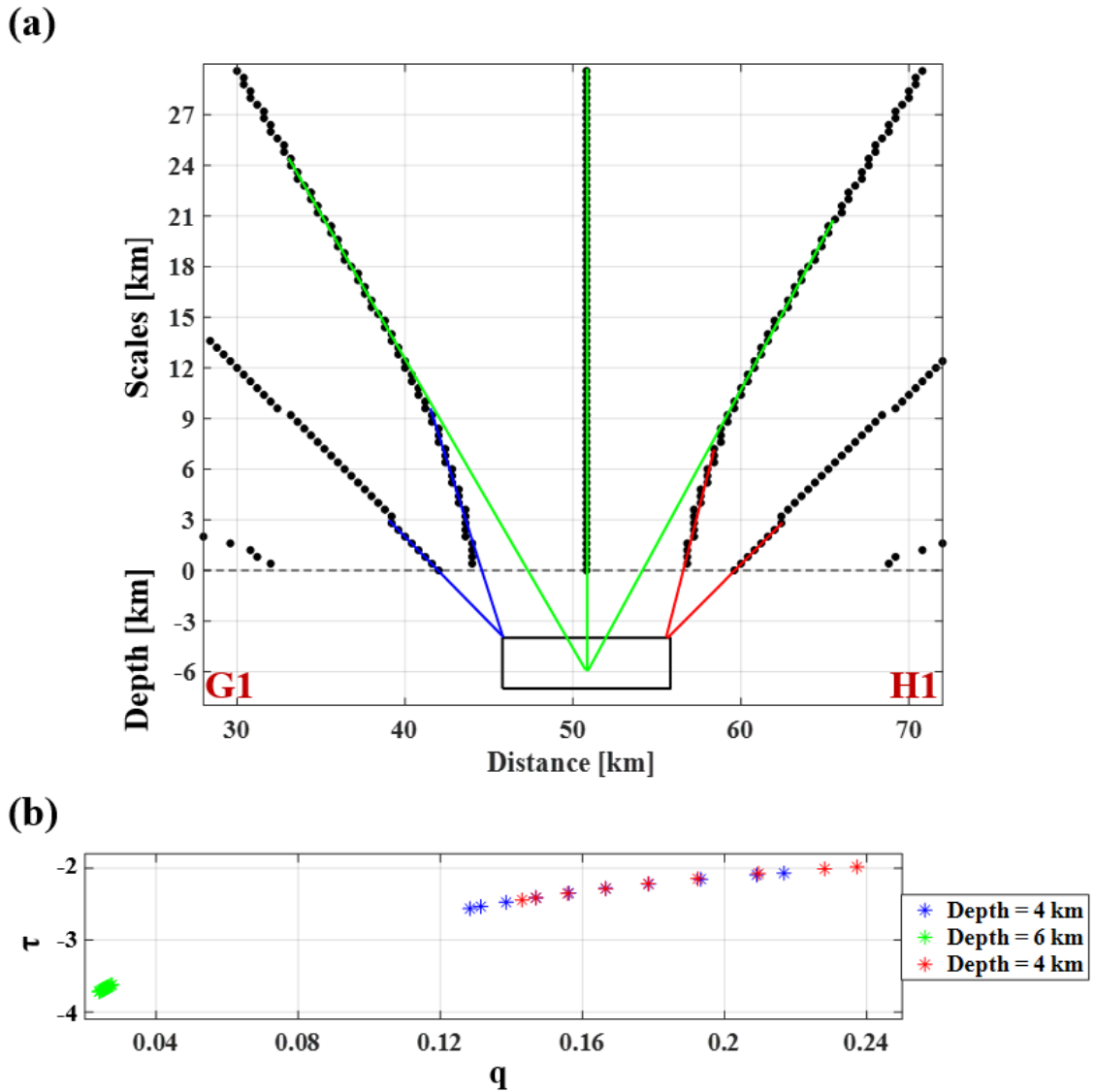


Figure 3.12. Case 1 detection: profile G1-H1. (a) Multiridge results related to the G1-H1 extracted profile of the second-order VD_F of the vertical component. (b) ScalFun results related to the three retrieved solutions by Multiridge method. The horizontal black dashed line indicates the modeled data reference level; $q = \frac{1}{z}$ while $\tau = \frac{\partial \log(VD_F(z))}{\partial \log z}$, where z represents the vertical scale.

We go on with the Case 2 analysis by considering the same E-W oriented profile A2-B2, passing at the same time through both the highest morphological zones of both the sources (black dashed lines in **Figure 3.8d**). We firstly consider the first-order VD_F ($p = 2$) of the vertical component, from which the Multiridge and ScalFun analysis provide information about two intersections (**Figure 3.13a**), both located near the source centres: the first one (blue continuous lines in **Figure 3.13a**) with about 6 km depth and characterized by a stable not integer value of $n \sim -2.55$ (blue stars in **Figure 3.13b**), which corresponds to $N \sim 2.55$; the second one (red continuous lines in **Figure 3.13a**) at a depth of almost 6.3 km with the associated value $n \sim -2.53$ that is still a stable not integer one (red stars in **Figure 3.13b**) and corresponding to $N \sim 2.53$.

Then, we consider the second-order VD_F ($p = 3$) of the vertical deformation and, again, we retrieve two intersections (**Figure 3.13c**), corresponding this time to the source top: the first (blue continuous lines in **Figure 3.13c**) and the second (red continuous lines in **Figure 3.13c**) ones occur at depth values almost equal to 4 and 4.5 km, respectively, and we can characterize them by locally stable not integer values of $n \sim -2.2$ (blue stars in **Figure 3.13d**) and $n \sim -2.5$ (red stars in **Figure 3.13d**), which correspond to $N \sim 1.2$ and $N \sim 1.5$ for the first and second intersections, respectively.

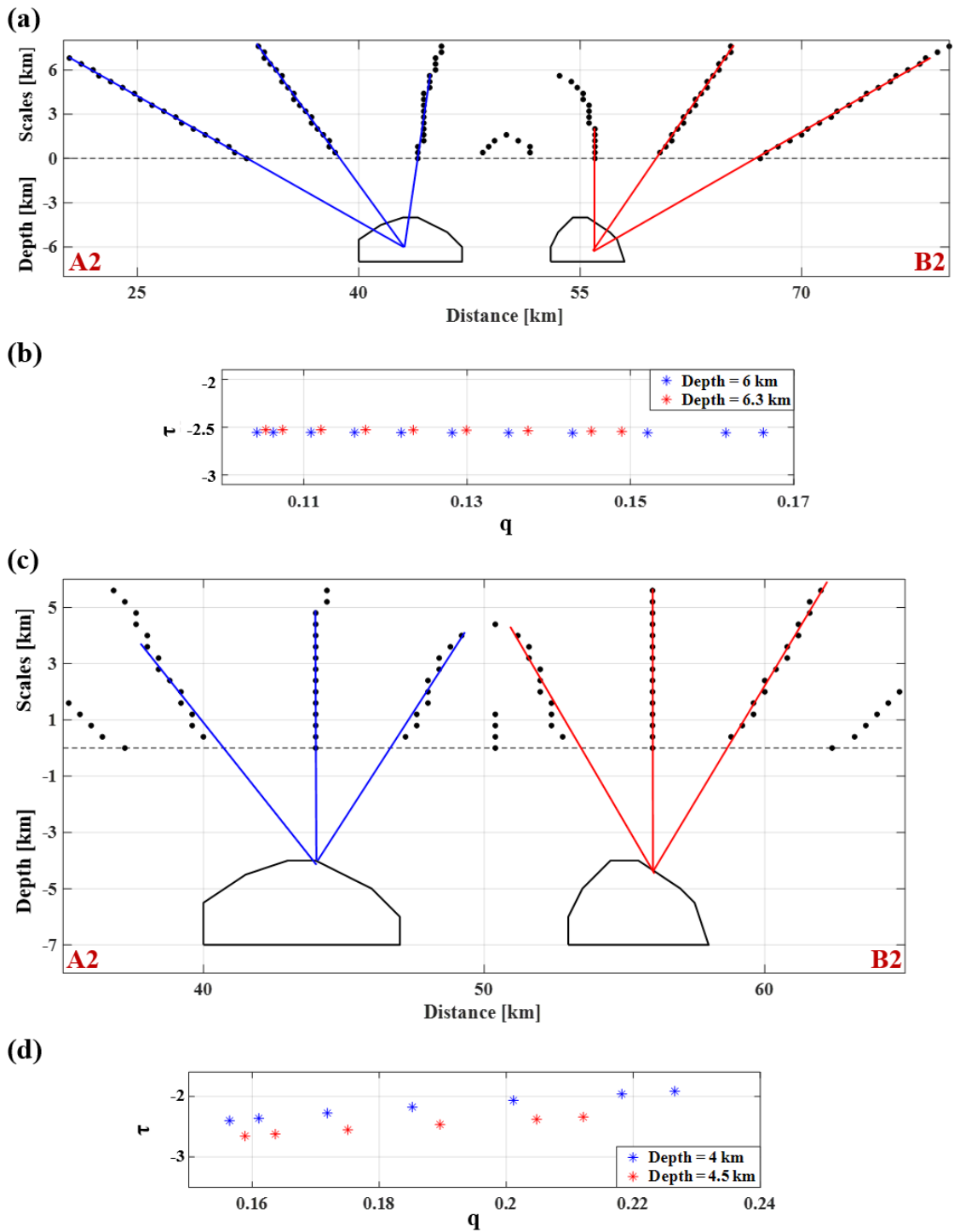


Figure 3.13. Case 2 detection: profile A2-B2. Multiridge and ScalFun methods results related to the A2-B2 extracted profile of the (a-b) first- and (c-d) second-order VD_F of the vertical component. The horizontal black dashed line indicates the modeled data reference level; $q = \frac{1}{z}$ while $\tau = \frac{\partial \log(VD_F(z))}{\partial \log z}$, where z represents the vertical scale.

The second considered profile is a N-S oriented one, named as C2-D2 (**Figure 3.8d**), passing through the morphologically highest zone of the first source. We consider the second-order VD_F ($p = 3$) of the vertical deformation and we retrieve information about three intersections (**Figure 3.14a**): the first one (green continuous lines in **Figure 3.14a**) is almost locally centred respect to the source at a depth of about 6 km and it is characterized by a stable not integer value of $n \sim -3.7$ (green stars in **Figure 3.14a**), which corresponds to $N \sim 2.7$; the second (blue continuous lines in **Figure 3.14a**) and the third ones (red continuous lines in **Figure 3.14a**) almost correspond to the boundaries of the source at a depth almost equal to 4 km, and the related $n \sim -2.4$ values are locally stable not integer ones (blue and red stars in **Figure 3.14b**), which correspond to $N \sim 1.4$ for both the intersections.

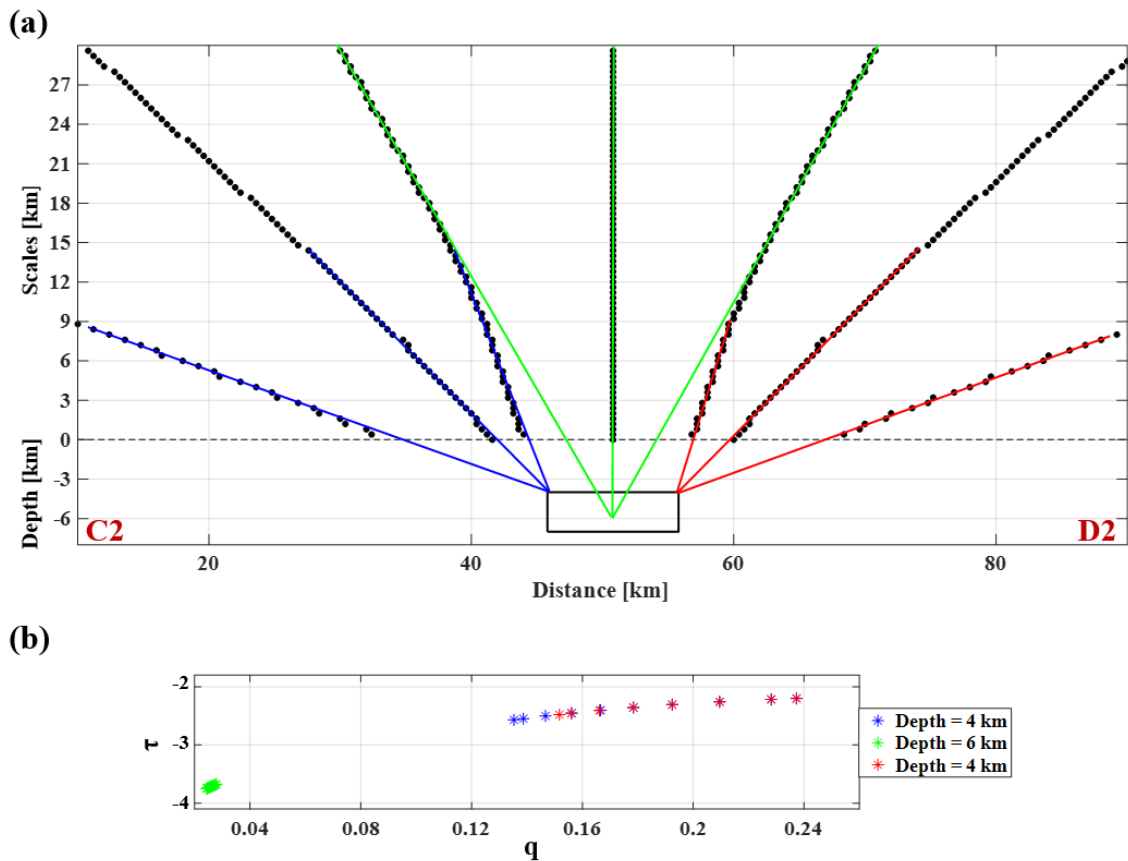


Figure 3.14. Case 2 detection: profile C2-D2. (a) Multiridge results related to the C2-D2 extracted profile of the second-order VD_F of the vertical component. (b) ScalFun results related to the three retrieved solutions by Multiridge method. The horizontal black dashed line indicates the modeled data reference level; $q = \frac{1}{z}$ while $\tau = \frac{\partial \log(VD_F(z))}{\partial \log z}$, where z represents the vertical scale.

The third considered profile is a N-S oriented one, E2-F2 (**Figure 3.8d**), passing through the area with no sources between them. We show the retrieved results using the first-order VD_F ($p = 2$) of the vertical component (**Figure 3.15**).

Here, we retrieve only one intersection (red dashed lines in **Figure 3.15a**): the related n values are very unstable and, for some low-intermediate scales they are not acceptable (red stars in **Figure 3.15b**).

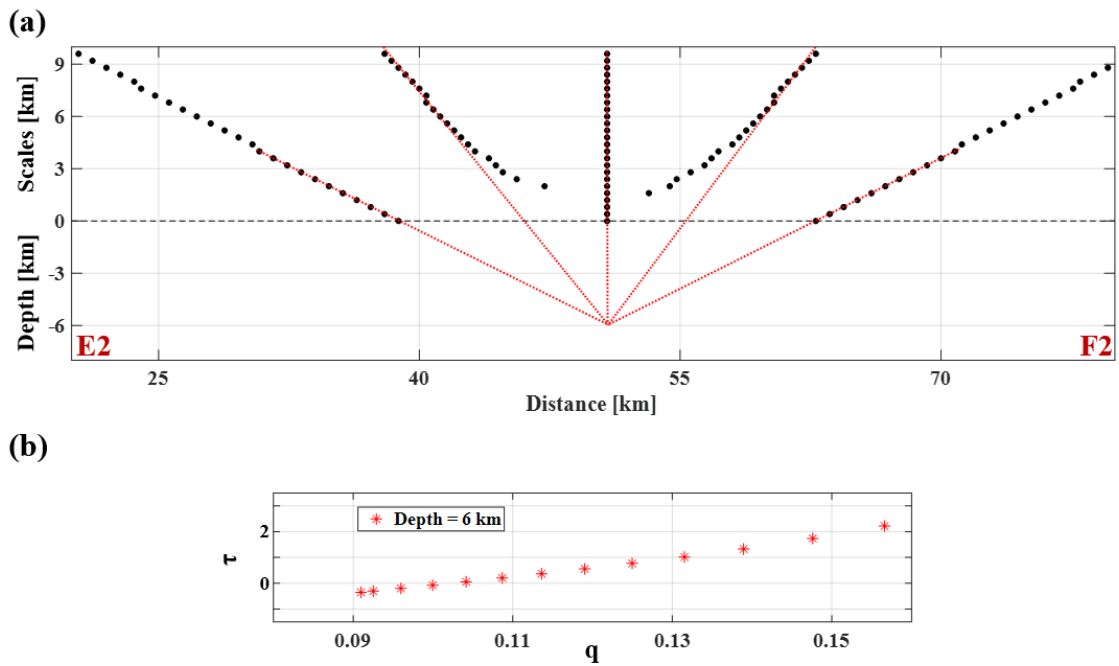


Figure 3.15. Case 2 detection: profile E2-F2. (a) Multiridge results related to the E2-F2 extracted profile of the first-order VD_F of the vertical component. (b) ScalFun results related to the only one retrieved solution by Multiridge method. The horizontal black dashed line indicates the modeled data reference level; $q = \frac{1}{z}$ while $\tau = \frac{\partial \log(VD_F(z))}{\partial \log z}$, where z represents the vertical scale.

As last profile, we analyse the N-S oriented one, named as G2-H2 (**Figure 3.8d**), which is passing through the morphologically highest zone of the second source.

We use the second-order VD_F ($p = 3$) of the vertical deformation for retrieving information about three intersections (**Figure 3.16a**): the first one (green continuous lines in **Figure 3.16a**) is representative of the source centre with a depth value almost equal to

6 km and it is characterized by a stable not integer values of $n \sim -3.6$ (green stars in **Figure 3.16a**) and $N \sim 2.6$; the second (blue continuous lines in **Figure 3.16a**) and the third (red continuous lines in **Figure 3.16a**) ones almost correspond to the boundaries of the source with depth values of about 4 km, while the related $n \sim -2.4$ values are locally stable not integer ones (blue and red stars in **Figure 3.16b**), which correspond to $N \sim 1.4$ for both the intersections.

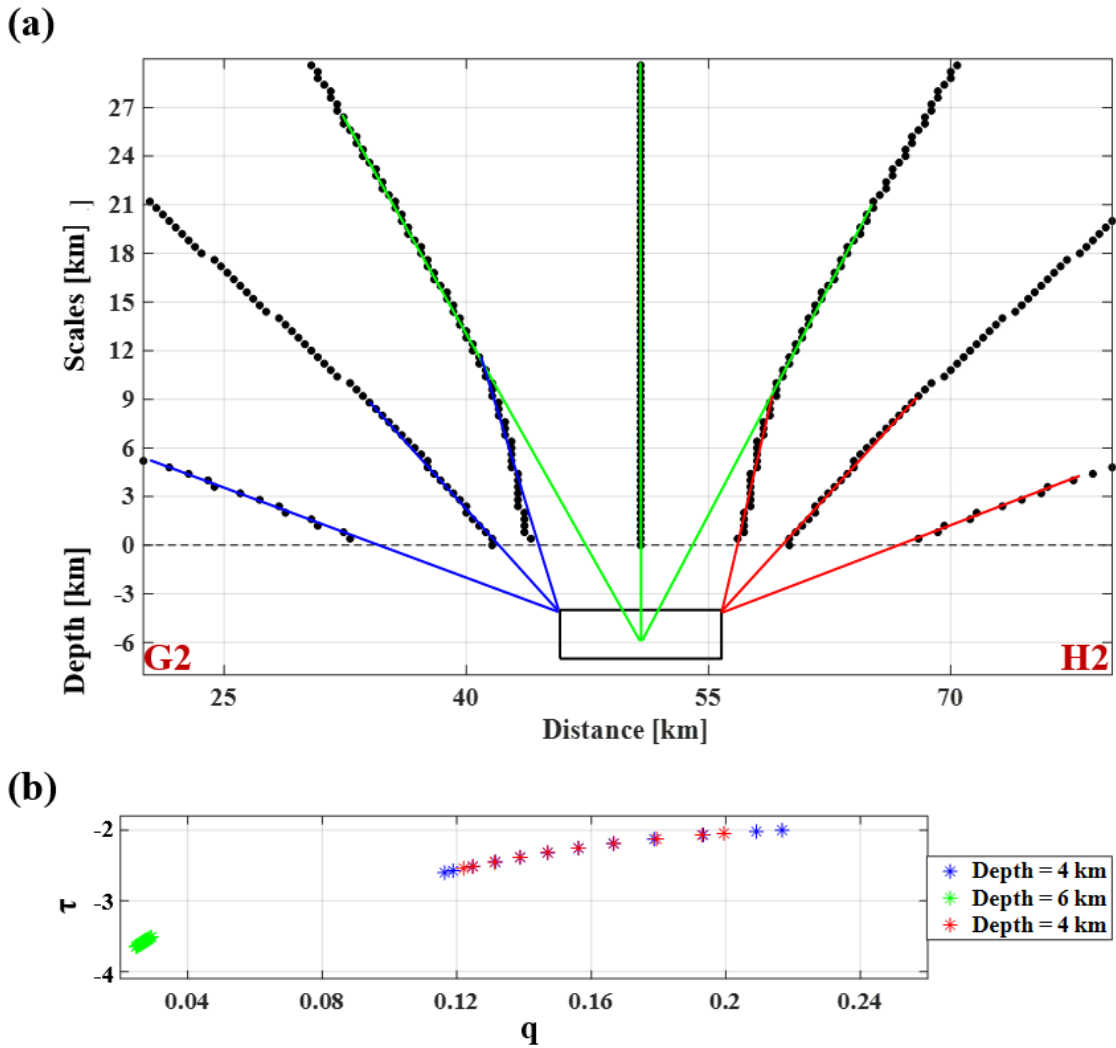


Figure 3.16. Case 2 detection: profile G2-H2. (a) Multiridge results related to the G2-H2 extracted profile of the second-order VD_F of the vertical component. (b) ScalFun results related to the three retrieved solutions by Multiridge method. The horizontal black dashed line indicates the modeled data reference level; $q = \frac{1}{z}$ while $\tau = \frac{\partial \log(VD_F(z))}{\partial \log z}$, where z represents the vertical scale.

Finally, we apply the THD technique to accomplish the study of the geometrically irregular sources. We calculate the THD_w , whose results are reported in **Figure 3.17**, for both the vertical deformations of Case 1 and Case 2 (**Figure 3.8b** and **3.8d**).

In the Case 1, the maxima of THD_w highlight the presence of a single source and its intensity distribution is greater at the western part respect to the eastern one. This result suggests the presence of a source at different local depth, or at the same one but with irregular distribution in the space (**Figure 3.17a**).

On the other hand, for the Case 2, the maxima of THD_w almost well line up in correspondence of two different bodies and, similarly to the previous case, the western expected source is characterized by a larger intensity of the THD_w anomaly (**Figure 3.17b**).

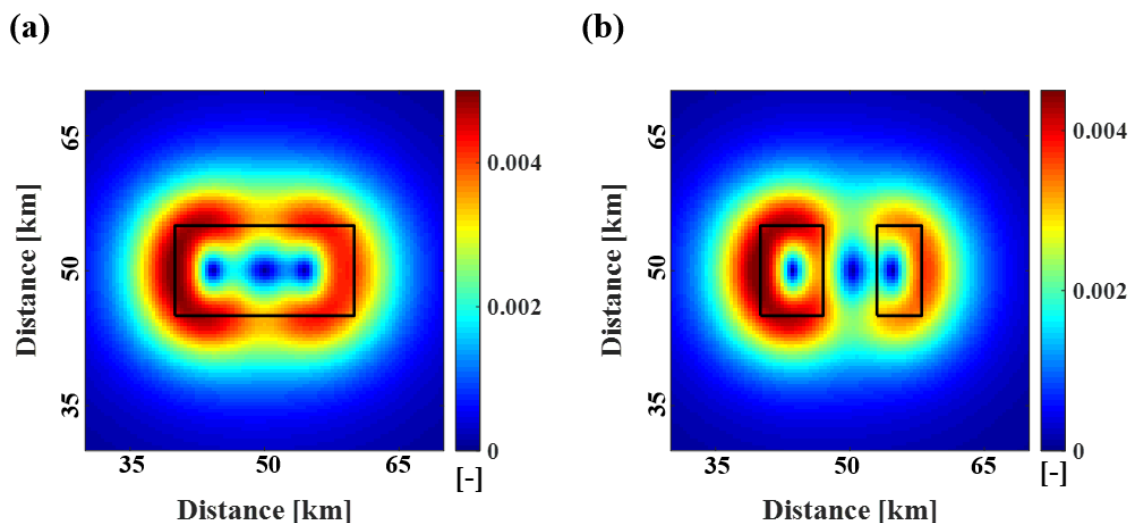


Figure 3.17. THD_w for the detection of geometrically irregular sources. Results of THD_w (adimensional) for the vertical deformations of the (a) Case 1 and (b) Case 2. The black continuous lines represent the projection of the sources boundaries on the horizontal plane.

3.2.3 Geometric parameters detection of biharmonic field sources.

We apply the integrated multi-scale approach to biharmonic but non-harmonic deformation fields, which satisfy only the equation (1.14.3).

The first test simulates the case occurring when the distribution of physical parameters of the half-space is not homogeneous and the Laplace's equation is therefore not satisfied, according to equations (1.23).

We consider a spherical source embedded in a multi-layer elastic space, characterized by the increasing of the Young's modulus E with the depth (**Figure 3.18a**); we set the model parameters as follows: depth to the source centre $z_0 = 2$ km, E-W position of the source $x_0 = 60$ km, N-S position of the source $y_0 = 60$ km, radius of the source $a = 0.3$ km, overpressure of the source $\Delta P = 10$ Mpa, Poisson's coefficient of the medium $\nu = 0.25$ (-), $E_1 = 4$ GPa from 0 to 1 km, $E_2 = 5$ GPa from 1 to 2 km; $E_3 = 7$ GPa from 2 to 3 km and $E_4 = 9$ GPa from 3 km to 20 km.

The other model specifications are set like the upward continuation test described in Paragraph 3.1.

The modeled vertical component is reported in **Figure 3.18b**.

By analysing the X-X' profile (**Figure 3.18c**), we retrieve a source at 2.1 km depth and 60 km along the x -direction (**Figure 3.18d**). The application of the ScalFun method provides $n \sim -2$ (exact value: 2.04) and $N \sim 3$ (**Figure 3.18e**), since $p = 1$.

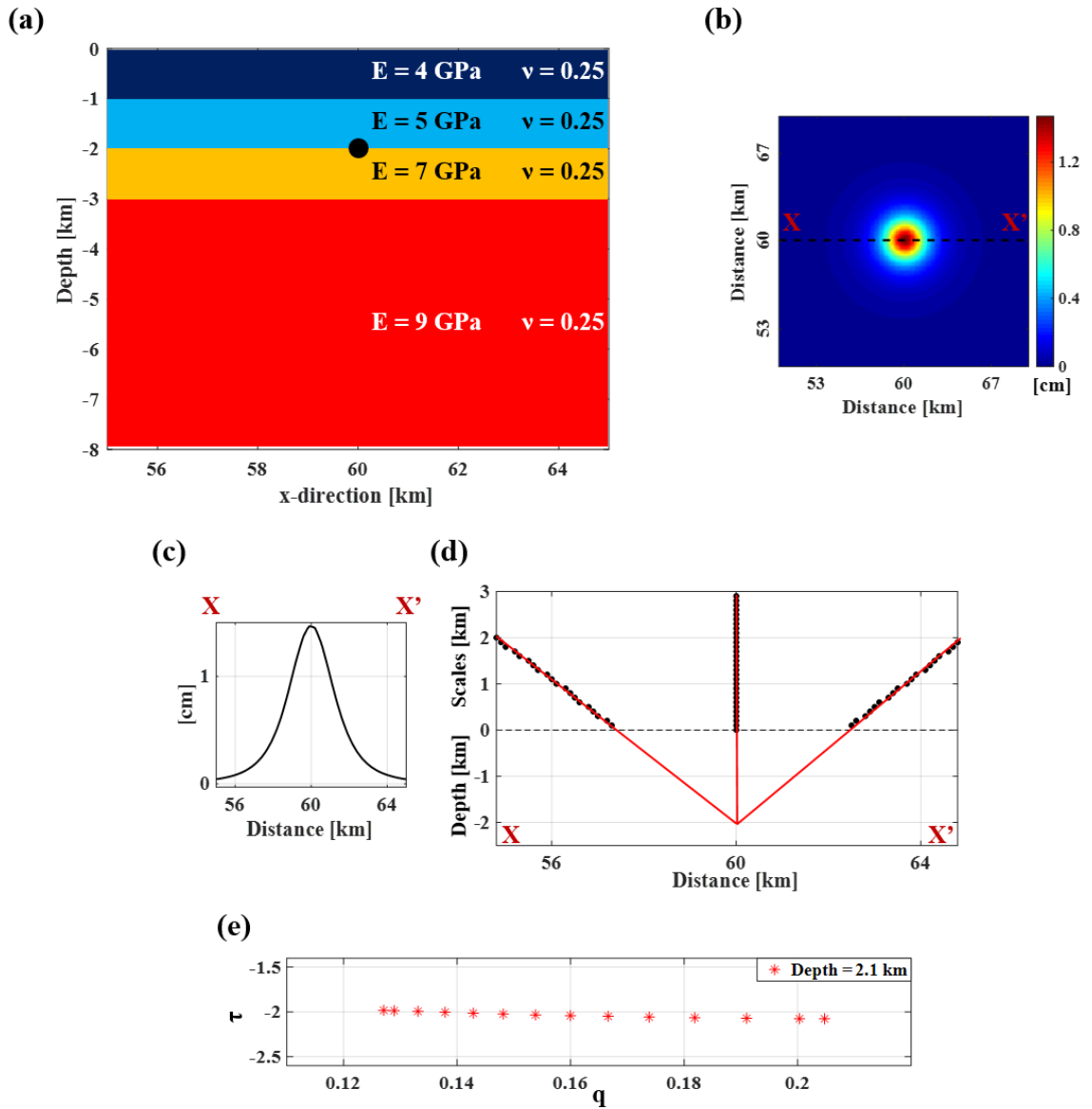


Figure 3.18. Detection of a spherical source embedded in a heterogeneous medium. (a) 2D section of the heterogeneous 3D model used for the performed test; the black body represents the source projection on the considered plane. (b) Vertical component of the deformation field produced by this model configuration; the black dashed line represents the XX' trace which deformation trend is reported in (c). Results of the (d) Multiridge method applied along the XX' trace and (e) ScalFun method applied on the central ridge. The horizontal black dashed line indicates the modeled data reference level; $q = \frac{1}{z}$ while $\tau = \frac{\partial \log(w(z))}{\partial \log z}$, where w and z represent the vertical deformation and the vertical scale, respectively.

In the second test, we instead consider a vertical cylinder embedded in a multi-layer elastic space characterized by a larger variation of the Young's modulus E of the medium (**Figure 3.19a**); we set the model parameters as follows: depth to the source centre $z_0 = 1$ km, E-W position of the source $x_0 = 50$ km, N-S position of the source $y_0 = 50$ km, radius of the cylinder $r_h = 0.2$ km, vertical extent of the cylinder $L_z = 0.8$ km, overpressure of the source $\Delta P = 10$ Mpa, Poisson's coefficient of the medium $\nu = 0.25$ (-), $E_1 = 0.5$ GPa from 0 to 0.5 km, $E_2 = 1$ GPa from 0.5 to 1.5 km; $E_3 = 8$ GPa from 1.5 to 100 km.

The other model specifications are set as for the already described test in Paragraph 3.1.

The modeled vertical component is reported in **Figure 3.19b**.

By analysing the X1-X1' profile (**Figure 3.19c**), we retrieve a source depth of approximately 0.8 km at $x = 50$ km (**Figure 3.19d**). The ScalFun method provides $n \sim -2.09$ (**Figure 3.19e**) and $N \sim 3$, since $p = 1$.

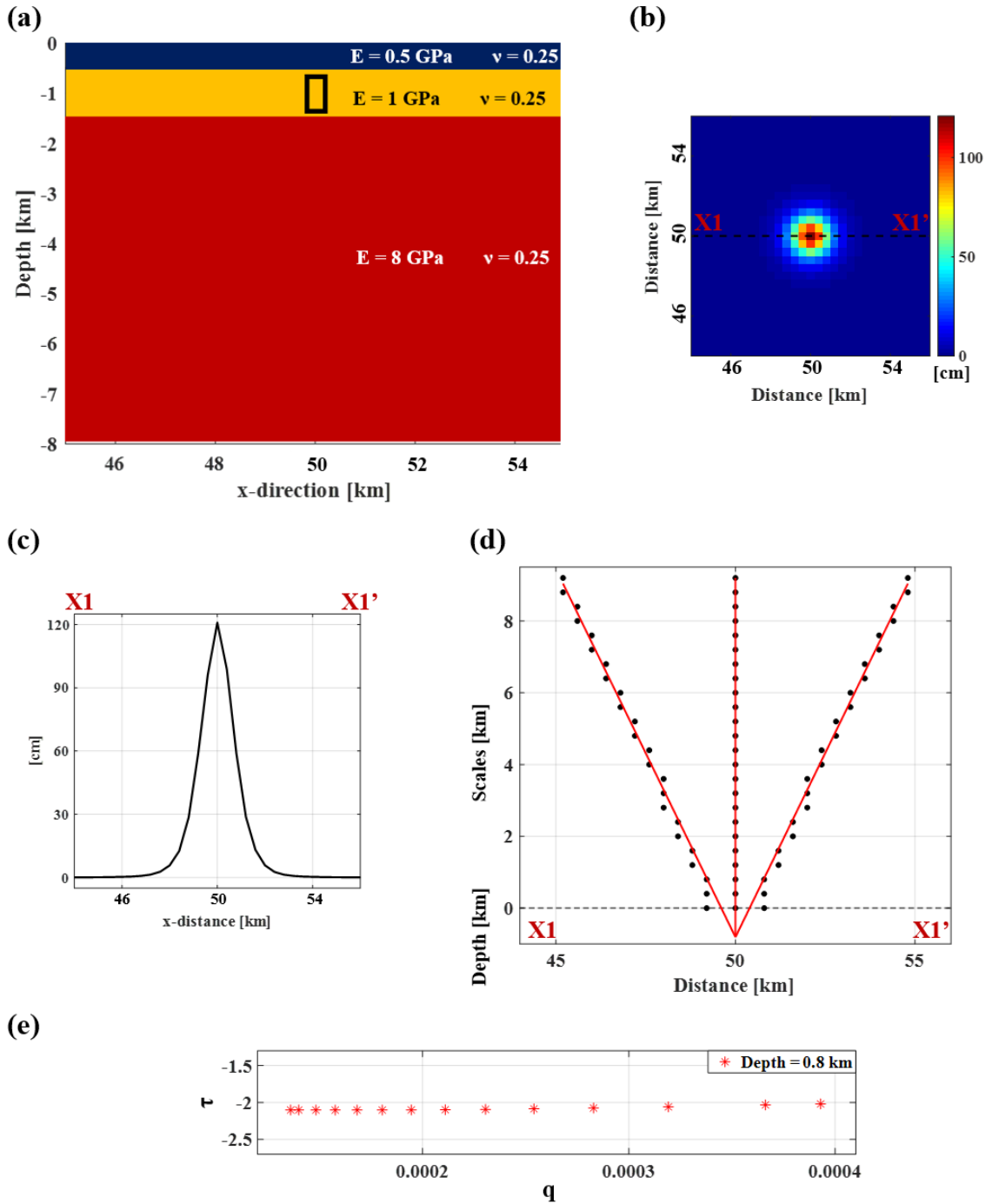


Figure 3.19. Detection of a vertical cylinder embedded in a heterogeneous medium. (a) 2D section of the heterogeneous 3D model used for the performed test; the black continuous lines represent the source projection on the considered plane. (b) Vertical component of the ground deformation field produced by this model configuration; the black dashed line represents the X1-X1' trace which deformation trend is reported in (c). Results of the (d) Multiridge method applied along the X1-X1' trace and (e) ScalFun method applied on the central ridge. The horizontal black dashed line indicates the modeled data reference level; $q = \frac{1}{z}$ while $\tau = \frac{\partial \log(w(z))}{\partial \log z}$, where w and z represent the vertical deformation and the vertical scale, respectively.

On the contrary, the third considered test simulates the case of non-hydrostatic variation of the source pressure, where, according to equations (1.23), the Laplace's equation is still not satisfied. Therefore, we consider the same vertical cylinder of the previous test embedded in a homogeneous elastic half-space characterized by a Poisson's coefficient of the medium $\nu = 0.25$ (-) and a Young's modulus $E = 1$ GPa. Here, the overpressure $\Delta P = 10$ Mpa is applied only to the upper and lower bases of the cylinder. The modeled vertical component is reported in **Figure 3.20a**.

By analysing the X2-X2' profile (**Figure 3.20b**), we retrieve a source depth of approximately 0.65 km, and a location of 50 km along the x -direction (**Figure 3.20c**). However, the ScalFun method provides acceptable n values only in correspondence of low scale interval of the upward continued field, where $n \sim -2.08$ (**Figure 3.20d**) and $N \sim 3$, since $p = 1$.

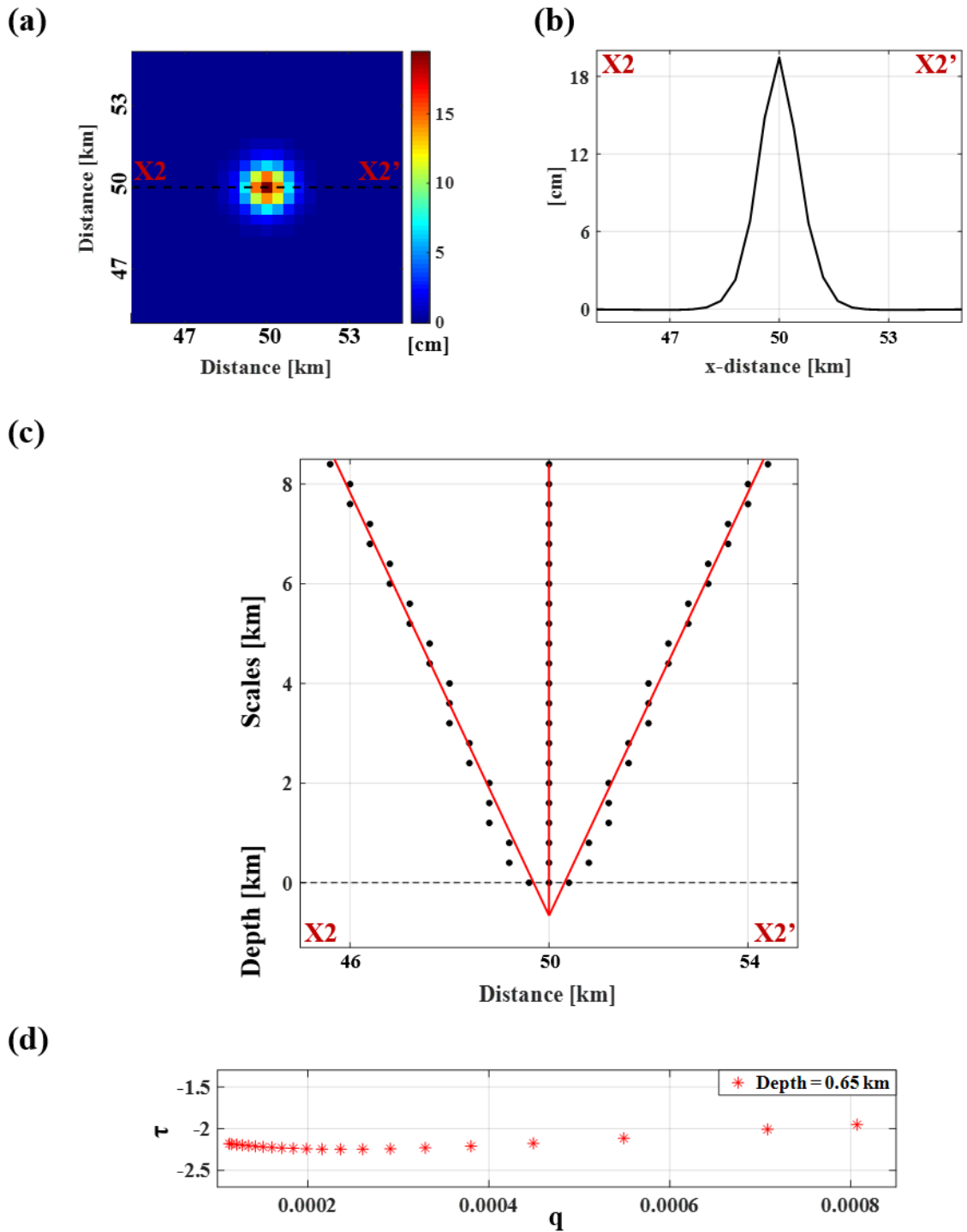


Figure 3.20. Detection of a no hydrostatically over-pressurized source. (a) Vertical component of the deformation field; the black dashed line represents the X2-X2' trace, which deformation trend is reported in (b). Results of the (c) Multiridge method applied along the X2-X2' trace and (d) ScalFun method applied to the central ridge. The horizontal black dashed line indicates the modeled data reference level; $q = \frac{1}{z}$ while $\tau = \frac{\partial \log(w(z))}{\partial \log z}$, where w and z represent the vertical deformation and the vertical scale, respectively.

We conclude this Chapter with the THD test. We simulate a sill-like source by considering the tensile rectangular fault model AM (i.e., Okada [1985]), for which the Laplace's equation is not satisfied. The model parameters are set as follows: depth to the source centre $z_0 = 1$ km, E-W position of the source $x_0 = 6$ km, N-S position of the source $y_0 = 6$ km; length of the source $D = 3$ km; width of the source $W = 3$ km; opening of the source $U_3 = 0.001$ km; dip θ and strike of the source $\alpha = 0^\circ$. We apply the THD technique on the modeled vertical component, which is reported in **Figure 3.21a**. Specifically, the THD_w maxima distribution delineates the presence of an about 3×3 km squared deformation source (**Figure 3.21b**). We also show the results by considering the profile X3-X3' passing through the maximum value of the vertical deformation (**Figure 3.21c**).

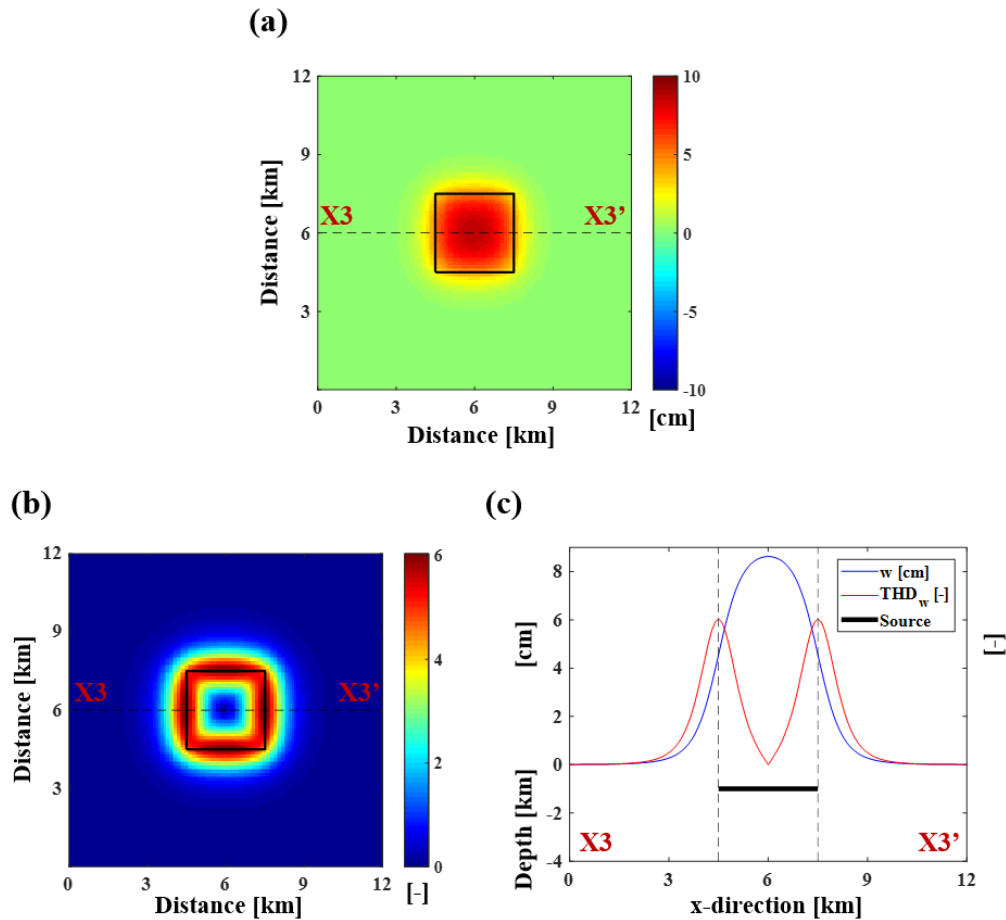


Figure 3.21. THD technique for the analysis of non-harmonic fields. (a) Vertical component of the deformation field produced by a rectangular tensile fault source model. (b) Results of THD_w computed on (a); the black dashed line represents the X3-X3' trace along which the deformation trend and the THD_w results are reported in (c); the black vertical dashed lines correspond to the maxima of the THD_w . The black continuous lines represent the projection of the source on the considered plane in (b) or profile in (c).

CHAPTER 4

APPLICATION TO REAL CASES

In this Chapter, we show the application of the proposed integrated multi-scale methods to real ground deformation patterns. Therefore, we consider Multiridge, ScalFun methods and THD technique to perform the geometrical modeling of the volcanic deformation sources. Specifically, we analyse five volcanic sites characterized by different scenarios.

The first application is to the Okmok Volcano (Alaska, USA), for which we consider a single interferogram related to the 2003-2004 time interval. We apply the Multiridge and ScalFun methods on the LOS component of the measured ground deformation field. This analysis represents a validation case study since it is the first application of the proposed approach to model the deformation sources [Castaldo et al., 2018b].

The second volcanic site is the Uturuncu Volcano (Bolivia), where we consider the cumulative 2005-2008 vertical deformation to perform a multi-source analysis through Multiridge method. In this case study, we show how to investigate more than one source by analysing the same deformation dataset [Barone et al., 2019].

The third analysis concerns the vertical unrest episode occurred at Campi Flegrei caldera (Italy); here, we apply the THD technique as supporting tool to understand the physical phenomenon occurring during the 2012-2013 time interval. This analysis still represents a validation case study since we apply for the first time this technique to study volcanic reservoirs [Pepe et al., 2019].

The 2013 unrest event at Fernandina Volcano (Galapagos Archipelago, Ecuador) represents the fourth case study, for which we use Multiridge and ScalFun methods to define the depth and the source type by considering the homogeneity properties of the cumulative E-W component of the measured ground deformation field.

Finally, we study the uplift phenomena occurred at Yellowstone caldera (Wyoming, USA) by considering the Mallard Lake and Sour Creek resurgent domes; in this framework, we apply the integrated multi-scale methods to analyse the 2005-2007 cumulative vertical deformation by using a local-homogeneity approach.

4.1 Multiridge and ScalFun methods: the Okmok Volcano (Alaska, USA) analysed with LOS components.

“The Okmok volcano is an active caldera field located on the oceanic crust of the central Aleutian arc (Alaska – USA) [Finney et al., 2008] that represents the surface expression for the subduction of the Pacific Plate as it moves northwards beneath the North American Plate.

In particular, it is a dominantly a basaltic shield volcano covering most of the northeastern end of Umnak Island in Alaska [Lu et al., 2005]. The Okmok physiography is dominated by a central caldera, with a diameter of 10 km; the rim and caldera floor have elevations of approximately 900 and 400 m a.s.l., respectively [Masterlark et al., 2012]. This physiography is the result of two different and large ($\approx 15 \text{ km}^3$) caldera-forming events [Finney et al., 2008] caused by catastrophic pyroclastic eruptions that occurred approximately 12.0 and 2.05 kyr ago, respectively [Byers, 1959; Finney et al., 2008]. These eruptions began with a small Plinian rhyodacite event, followed by the emplacement of a dominantly andesitic ash-flow unit, whereas effusive inter- and post-caldera lavas have been more basaltic [Finney et al., 2008]. Subsequent eruptions produced a field of small cones [Miller, 1998].

For the past 200 years, the Okmok volcano has had an effusive and basaltic eruption every 10-20 years, generally from the intracaldera cones [Miller, 1998]. The most recent eruption, in 2008, originated from several new vents and occurred near the eastern rim of the caldera [Masterlark et al., 2012], while the three previous eruptions (1945, 1958 and 1997) originated near the southwest rim of the caldera [Larsen et al., 2009]. In particular, the 1997 eruption began with steam and ash plumes and progressed into moderate Strombolian activity, producing explosive ash plumes and lava that flowed toward the centre of the caldera. Geochemical analyses of the erupted products are consistent with the primitive magma from the depth and brief storage of the shallow reservoirs [Finney et al., 2008].

We analyse the Okmok volcano ground deformation pattern retrieved by processing the ENVISAT SAR images. The interferogram is related to the period 15 July 2003 – 29 June 2004, with images acquired by the ENVISAT satellite (ESA) along the descending orbit (Track 115). The ENVISAT dataset was processed by using the online P-SBAS web tool available within ESA’s Grid Processing On Demand (G-POD) environment, which

is within the framework of ESA's Geohazards Exploitation Platform (GEP) [De Luca et al., 2015; De Luca et al., 2017]. The P-SBAS results from the ENVISAT data were spatially averaged (i.e., multilooked) to obtain a pixel size of approximately 80 m by 80 m on the ground. The ENVISAT satellite look angle is 23° , and the mean values of the LOS unit vector are $[0.346, -0.081, 0.935]$ relative to the satellite descending orbit.

After the processing steps, the descending interferogram is unwrapped to retrieve the LOS deformation measurements (**Figure 4.1a**). In the considered period, the DInSAR measurements shown an uplift phenomenon, with a maximum deformation value of approximately 12 cm. Since the measurement surface is detailed (i.e., the Okmok volcano topography), the LOS deformation dataset is processed to obtain the ground deformation field evaluated at the constant reduction scale, specifically at 1.5 km a.s.l. (**Figure 4.1b**).

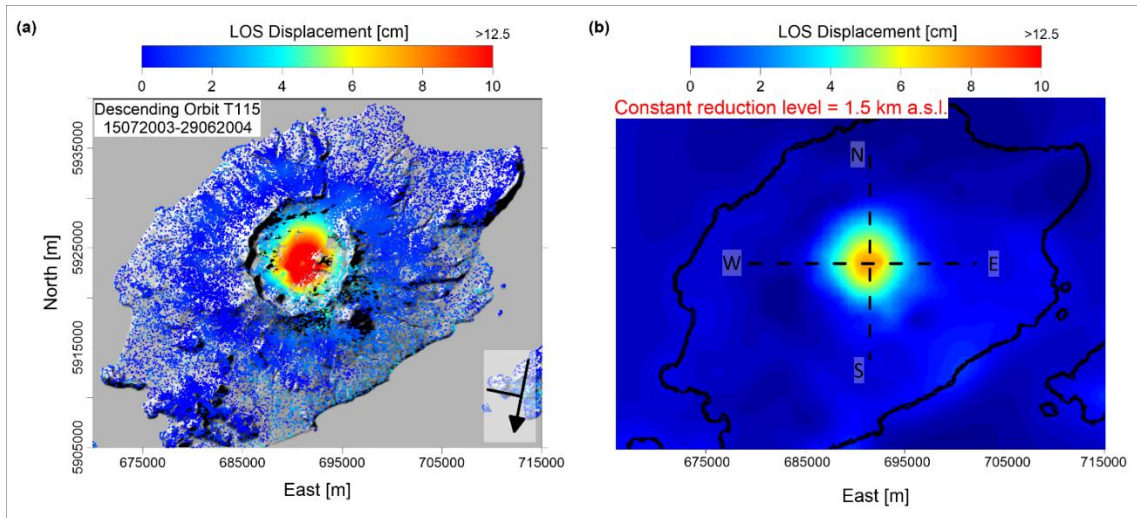


Figure 4.1. Okmok DInSAR measurements. (a) Descending LOS deformation map between 15 July 2003 and 29 June 2004, which is superimposed onto the Okmok volcano topography. (b) Descending LOS deformation map reduced to a flat surface, which is located 1.5 km a.s.l. The black dashed lines indicate the positions of the E-W and N-S profiles, while the black continuous line represents the island coastline.

At this stage, we applied our methodology to the DInSAR measurements to evaluate the geometric parameters of the active source; we applied both the Multiridge and ScalFun methods along the E-W (**Figure 4.2a**) and N-S (**Figure 4.2b**) profiles to retrieve the following results:

- **Multiridge method:** a source was located at a -4.9 ± 0.06 km depth (**Figures 4.2c** and **4.2d**) from the constant reduction scale (1.5 km a.s.l.) along the z-axis, which corresponded to a depth of -3.4 ± 0.06 km b.s.l. with horizontal UTM coordinates

equal to 690.9 ± 0.08 km East (**Figure 4.2c**) and 5924 ± 0.07 km North (**Figure 4.2d**);

- *ScalFun method*: a homogeneity degree of $n \sim -2$ (**Figures 4.2e** and **4.2f**) was computed on the central cyan ridge for both the E-W and N-S profiles; this value corresponds to a Structural Index of $N \sim 3$, suggesting that the source geometry related to the measured ground deformation field can be well-approximated by a point-spherical reservoir.

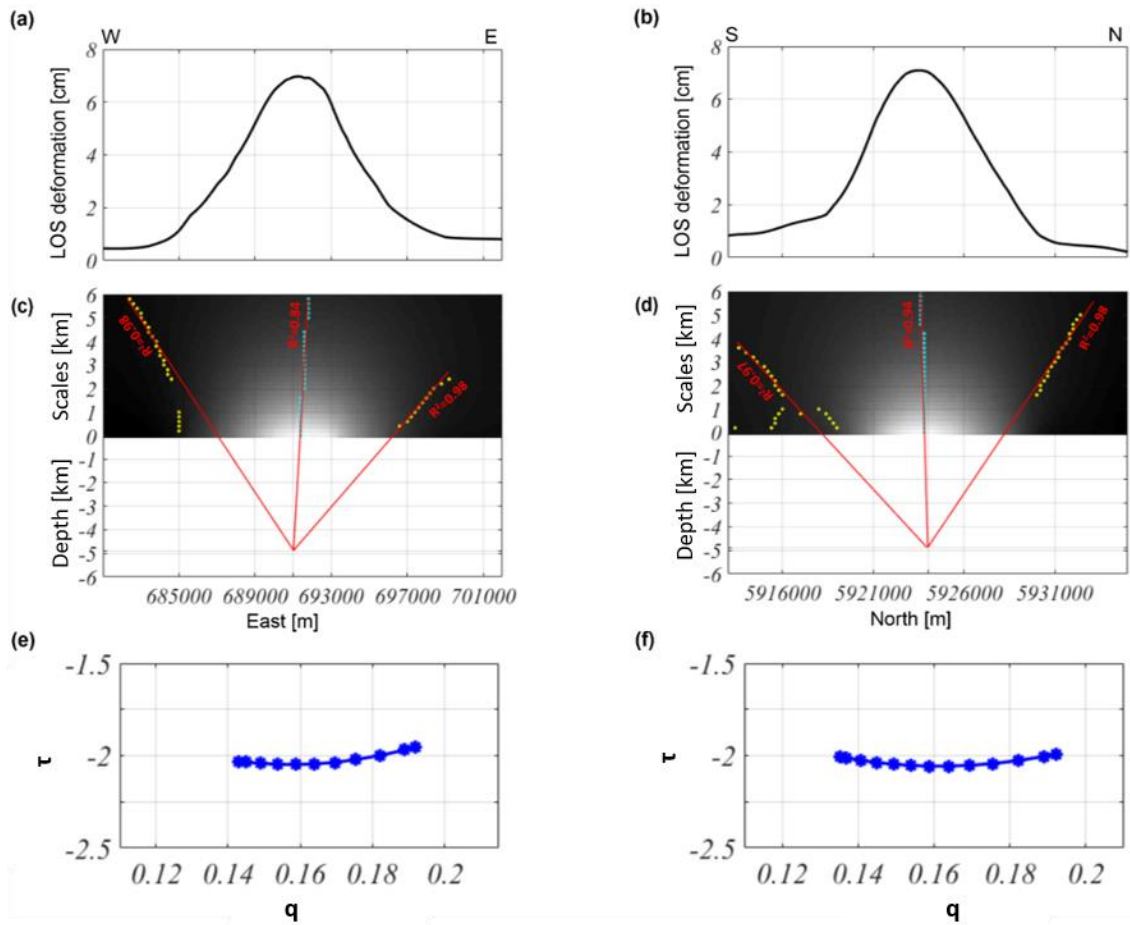


Figure 4.2. Multiridge and ScalFun methods: the Okmok volcano case. (a-b) LOS deformation in the E-W and N-S profiles evaluated from Figure 4.1b. (c-d) The results of the Multiridge method applied to the E-W and N-S profiles; the red solid lines, which represent the regression lines, estimate the source position at their intersection. For each regression line we indicate the coefficient of determination (R^2); (e-f) the results of the ScalFun method applied to the central cyan multiridge subsets reported in (c-d); $q = \frac{1}{z}$ while $\tau = \frac{\partial \log(\chi(z))}{\partial \log z}$, where χ and z represent the LOS deformation and the vertical scale, respectively.”

From Castaldo et al. [2018b].

4.2 Multiridge method: the Uturuncu Volcano (Bolivia) analysed with cumulative vertical deformation.

“The Andean Central Volcanic Zone represents one of the largest updoming volcanic zones on the Earth [Pritchard et al., 2018; Gottsmann et al., 2017], in which almost at its centre the Uturuncu volcano (southwestern Bolivia) lies (Figure 4.3). The magmatism in this area is the result of eastwards subduction of the Nazca oceanic plate beneath the South American continent [De Silva and Gosnold, 2007]. In this setting, tectonic and magmatic processes have shaped the broad elevated (≈ 4 km) Altiplano Puna Volcanic Complex (APVC), which has been related at depth to a large continental crustal magma body, known as Altiplano Puna Magma Body (APMB) [Allmendinger et al., 1997; Schmitz et al., 1997; Schilling et al., 1997; Chmielowski et al., 1999; Sparks et al., 2008; Perkins et al., 2016].

Uturuncu volcano is a long-dormant effusive stratovolcano [Muir et al., 2014]; the volcanic edifice is a dominant morphological peak that rises for ≈ 6 km and covers a ≈ 400 km² area. Its activity has been related to minor degassing and low-temperature fumaroles, while its products are dominated by Pleistocene dacitic lava domes and flows [Sparks et al., 2008; Michelfelder et al., 2014]; even the youngest summit lavas are excessively abraded by glaciers [de Silva, 1989]. Geochronological analysis outcomes reveal the activity range around Uturuncu is about 10-15 Ma, with its deposits covered by 0.9-0.5 Ma lava flows; the youngest dating, and so the evidence of the last eruptive activity, is related to the 0.27 Ma summit lava dome [Sparks et al., 2008].

This region was studied within the PLUTONS project [PLUTONS project, 2009], focused on large-scale surface uplift areas through an interdisciplinary analysis [Pritchard et al., 2018]. Several geophysical and geochemical studies show some evidences of a deep magma body, connected to the APMB, and of a possible shallower source: teleseismic and local receiver function analysis results highlight low-velocity zones at about 19 km [Chmielowski et al., 1999] and 20 km [Zandt et al., 2003] depth b.g.l., respectively. Seismic tomography turns out to be characterized by a deep Vp/Vs anomaly from 1-2 to 75-76 km depth [Kukarina et al., 2017], while about 4 to 25 km depth low-velocity zone is retrieved by seismicity and receiver function analysis [Ward et al., 2014; Ward et al., 2017; McFarlin et al., 2017]; vertically elongated low-density 3D structures rooted at the top of the APMB (15 km of depth) are highlighted from the gravity

measurements modeling [Del Potro et al., 2013]. At the same time, petrological studies, besides a dacitic magma intrusion at depth major than 17 km, support the hypothesis of a shallow magma storage with a depth major than 1.5 km [Sparks et al., 2008]; seismicity and ambient noise tomography show a shallow low-velocity zone [Jay et al., 2012]; several earthquakes occur at 4-6 km depth for the 2010-2012 time interval [Alvizuri and Tape, 2016]; the existence of a shallow magma storage is supported by geochemical analysis [Muir et al., 2014]. Furthermore, evidence of low-resistivity zones is also emphasized by magnetotelluric data modeling. In particular, Comeau et al., [2015] show a 2D regional model estimating a depth of the APMB at about 18-19 km, whereas [2016], by performing a 3D model, highlight the existence of two low-resistivity anomalies located at 3-5 km and 13-14 km depth, respectively. All these studies are summarized in [Pritchard et al., 2018], in which the authors describe the main aspect of each magmatic system interpretation. Accordingly, we remark that a comparison between the above reviewed results should be careful since the used methodologies have a different resolution and are related to a specific physical parameter distribution.

Since 1992 the APVC area knowledge has significantly increased thanks to the exploitation of satellite Synthetic Aperture Radar (SAR) sensors [Pritchard and Simons, 2002; Pritchard and Simons, 2004; Fialko and Pearse, 2012; Henderson and Pritchard, 2013; Hickey et al., 2013; Walter and Motagh, 2014; Gottsmann et al., 2017; Henderson and Pritchard, 2017; Lau et al., 2018]. The interpretation of these measurements is focused on the characterization of the APMB deep source (about 15-30 km b.s.l.): Pritchard et al. [2004] study ERS satellite data between 1992-2000 to simultaneously model the deformation source as a sphere (17.3 km depth), a horizontal and vertical ellipsoid (18.8 and 18.2 km depth, respectively), a point and finite crack (25 and 12 km depth, respectively); Fialko et al. [2012] proposed an ascending diapiric source, with depth > 15 km, by considering the 1992-2010 time interval; Henderson et al. [2013] identified a 19-20 km depth point-spherical source by analysing the 1992-2011 time interval; Hickey et al. [2013] studied the 1996-2010 time interval by modeling the deformation source as a sphere (30.4 km depth b.g.l.), a prolate and oblate spheroid (20.6 and 32.8 km depth b.g.l., respectively); Walter et al. [2014] modeled the ENVISAT satellite measurements related to the 2003-2009 time interval by considering an inflating flat-topped source at $17-18 \pm 9$ km depth; for the 1992-2011 time interval, Gottsmann et al. [2017] suggested the use of the magmatic column source model for the APMB, with

the top and bottom at 13 and 25 km depth, respectively, while Henderson et al. [2017] proposed a dipole source model whose top is located at 15.4-30.4 km depth. Otherwise, Gottsmann et al. [2017] and Lau et al. [2018] have shown the evidences of shallow sources, although their results are not directly related to volcanic deformations.

Starting from the information collected by the geodetic studies, the classical procedures of the geodetic modeling seem to be suitable to investigate only the existence of the deep source, related to APMB. To investigate a further shallower source beneath the Uturuncu volcano, we propose an alternative approach, based on the analysis of the 2003-2010 ENVISAT Differential SAR Interferometry (DInSAR) measurements. We apply two multi-scale methods to investigate possible active multi-source localized at different depths. In particular, focusing on the vertical component relevant to the 2005-2008 time interval, we use the Cross-correlation analysis [Stanton et al., 2001; Tizzani et al., 2007] and the Multiridge method [Fedi et al., 2009; Castaldo et al., 2018b] to emphasize the spatial and temporal multi-scale properties of the field during the considered period.

We consider a catalogue of SAR images acquired by ENVISAT satellite (European Spatial Agency - ESA) sensor during the 2003-2010 time interval. We process 26 and 31 images acquired along ascending (track 89 – look angle ϑ equal to 36.35°) and descending (track 282 – look angle ϑ equal to 20.45°) orbits, respectively. The ENVISAT dataset was processed by using the online Parallel Small Baseline Subset (P-SBAS) web tool available within ESA's Grid Processing On Demand (G-POD) environment, which is within the framework of ESA's Geohazards Exploitation Platform (GEP) [De Luca et al., 2015; De Luca et al., 2017]. In detail, we perform 76 and 89 interferograms for the ascending and descending orbits, respectively. The P-SBAS results from ENVISAT data were spatially averaged (i.e., multilooked) to obtain a pixel size of approximately 80 m by 80 m on the ground. The use of the Small Baseline Subset (SBAS) approach [Berardino et al., 2002; Casu et al., 2014] allows retrieving the spatial-temporal evolution of the Earth's surface deformation, since its results provide the mean deformation velocity maps and the corresponding time-series for each coherent pixel.

The Line Of Sight (LOS) mean velocity maps, both along ascending and descending orbits (**Figure 4.3a**), show the deformation phenomenon of a wide area (about 900 km^2) in the APVC zone, with maximum velocity values $\approx 0.6\text{-}0.8 \text{ cm/a}$. The 2003-2010 LOS time-series of two selected pixels (black solid triangles in the **Figure 4.3a**) are reported

in **Figure 4.3b**; the P1 pixel, almost localized at centre of APVC area (Easting 680650 [m]; Northing 7535580 [m] – UTM WGS84 coordinate system), shows a general quasi-linear deformation trend; the P2 pixel, localized at Uturuncu volcano (Easting 687460 [m]; Northing 7537700 [m] – UTM WGS84 coordinate system), shows a long-term deformation trend with a period of unrest between August 2006 and February 2007.

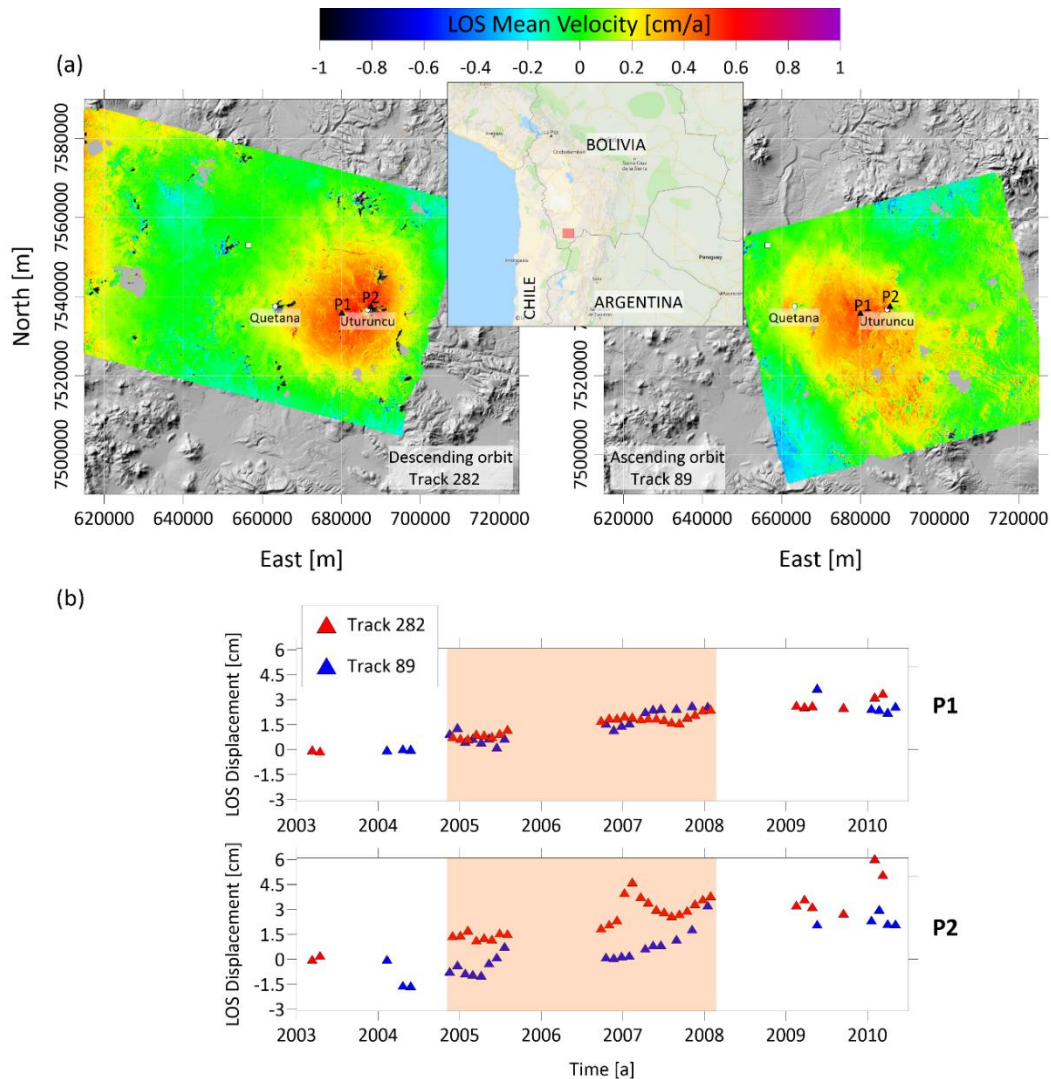


Figure 4.3. DInSAR measurements of APVC and Uturuncu volcano. (a) LOS mean velocity maps (cm/a) retrieved by ENVISAT satellite data acquired along ascending (right – track 89) and descending (left – track 282) orbits, superimposed on Shuttle Radar Topography Mission (SRTM) Digital Elevation Model (DEM); the reference map in upper centre shows the study area (red box); the white solid square shows the reference point, the white solid circles indicate the Uturuncu and Quetana volcanoes location, while the solid black triangles show the location of the selected P1 and P2 pixels; (b) LOS displacement time-series (cm) related to the 2003-2010 interval at the P1 (up) and P2 (down) pixels; the blue and red triangles represent the time-series related to the tracks 89 and 282, respectively, while the light red rectangle indicates the considered 2005-2008 time interval for the following analysis.

The displacement time-series of the selected coherent pixels are representative of deformation behavior of their surrounding zone.

*Subsequently, in order to estimate the vertical and horizontal East-West components of the ground deformation field, we combine the LOS DInSAR measurements along ascending and descending orbits [Manzo et al., 2006]; only the coherent pixels in both ascending and descending mean velocity maps have been combined and, since both images are acquired at different times, the time-series are resampled via linear interpolation to common constant sampling interval before applying the combination procedure. This operation is possible since nonlinear deformation events, such as eruption or earthquake, occur within the temporal sampling. We specify that by comparing the temporal sampling between the measurements acquired along ascending and descending orbits, we restrict our analysis to the 2005-2008 time interval (light red rectangle in **Figure 4.3b**), since a similar sampling both for ascending and descending LOS displacements is observed.*

*The retrieved vertical mean velocity map relevant to 2005-2008 time interval (left in the **Figure 4.4a**) shows a wide uplift zone at APVC, with maximum velocity values $\approx 0.6-0.8$ cm/a, while the East-West component (right in the **Figure 4.4a**) does not display a relevant pattern. The AA' profile (blue continuous line in the **Figure 4.4a**) of vertical velocity, is reported in **Figure 4.4b** and highlights a high deformation rate of the Uturuncu volcanic edifice. This result is also confirmed by the analysis of the vertical deformation time-series at P1 and P2 pixels (**Figure 4.4c**), revealing the existence of two different deformation trends: the first one is characterized by a quasi-linear uplift trend for the 2005-2008 time interval, while the second one shows a higher velocity episode during the August 2006 - February 2007 time interval (marked by the blue dashed lines in the **Figure 4.4c**), showing an abrupt change of the long-term uplift deformation.*

*We carry out this analysis by evaluating the correlation coefficients with respect to P1 and P2 deformation time-series, setting as lower threshold a value of 0.97. These results, reported in **Figure 4.5**, show that a large number of pixels, covering the central part of APVC, are characterized by the same deformation trend observed at P1 (red solid circles at the left of **Figure 4.5**), while the Uturuncu volcano area is entirely interested by the same deformation trend recorded at P2 (blue solid circles at the right of **Figure 4.5**). The performed Cross-correlation analysis highlights the existence of two distinctive*

areas with different temporal deformation behavior that gives us a further evidence supporting the multi-source scenario.

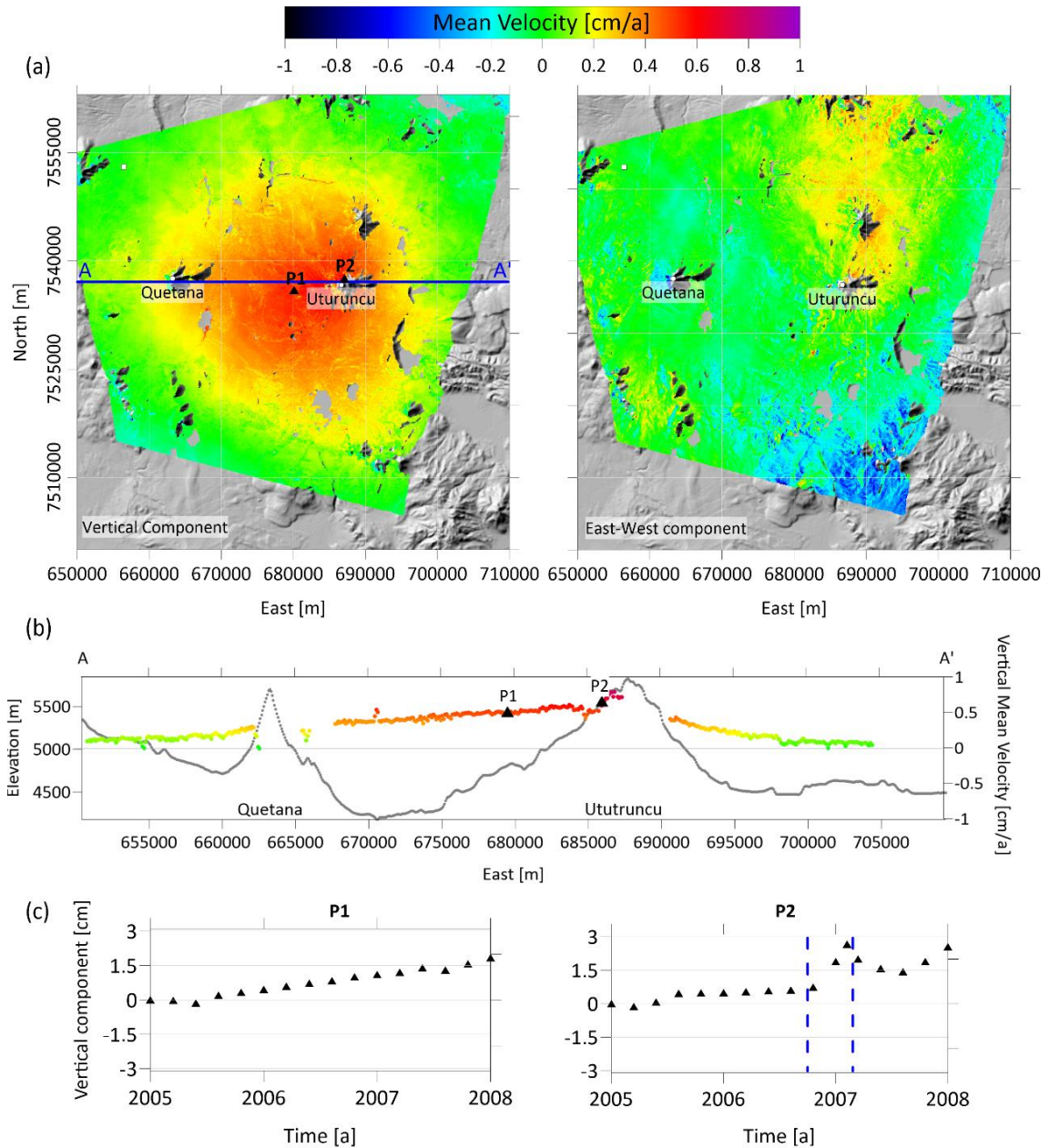


Figure 4.4. Vertical and East-West deformations at APVC and Uturuncu volcano. (a) Mean deformation velocity maps (cm/a) of vertical (left) and East-West (right) components, superimposed on the SRTM DEM; the white solid square shows the reference point, the white solid circles indicate the Uturuncu and Quetana volcanoes location, the solid black triangles show the location of the P1 and P2 pixels, while the blue continuous line represents the AA' trace; (b) AA' profile of the vertical mean velocity (colored solid circles) and of the topography (grey solid circles); the black solid triangles represent P1 and P2 pixels on the AA' profile; (c) Vertical deformation time-series at the pixels P1 (left) and P2 (right) related to the analysed 2005-2008 interval; the blue dashed lines indicate the time interval in which an higher uplift deformation rate is observed.

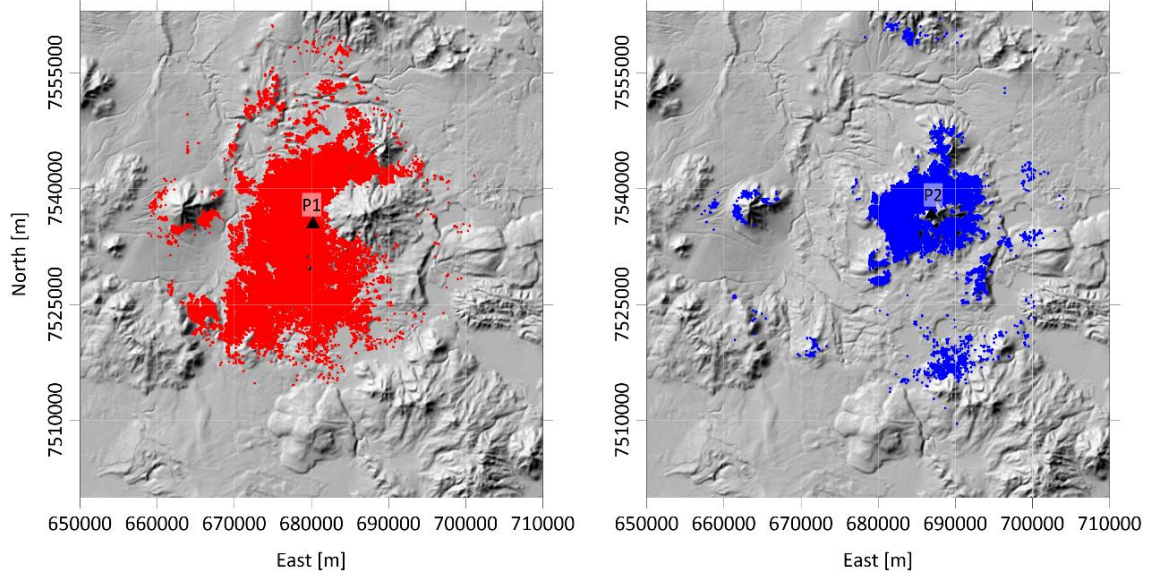


Figure 4.5. Spatial-temporal Cross-correlation analysis. Cross-correlation map: the red and blue points indicate coherent cluster pixels with respect to the deformation time series at P1 and P2 pixel (black solid triangles), respectively, during the 2005-2008 time interval; these points are characterized by a correlation coefficient greater than 0.97.

The 2005-2008 cumulative vertical deformation, reported in **Figure 4.6a**, appears as a very long-wavelength signal, covering a wide ground area. We apply the Multiridge method to the VD_F of the cumulative deformation by considering mostly the multiridge subsets related to large scales. In this context, we exploit the VD_F because it increases the signal resolution due to different interfering components and so it can represent an important tool to solve multi-source case. Furthermore, we take into account large-scales interval since they are related to the contribution of the deep source (i.e., long wavelength), while we do not treat the multiridge subsets regarding to the low scales, even avoiding the ridges portion affected by other signal interference effects, probably due to a contribution of high-wavenumber noise and/or a shallower source.

We show the inferred results by considering the E-W and N-S profiles (black dashed lines in **Figure 4.6a**), passing through about the maximum of the deformation field. In particular, from both cases, the depth and the horizontal position of the active source are detected at two-ridges intersection (**Figure 4.6b**): from the BB' profile analysis (along the E-W direction), we deduce a depth value equal to -18.7 ± 0.3 km at the point with East UTM coordinate equal to 682800 ± 200 m (left in the **Figure 4.6b**), while, by analysing the CC' profile (along the N-S direction), we infer a -18.7 ± 0.8 km depth at the point with North UTM coordinate equal to 7532300 ± 200 m (right in the **Figure 4.6b**).

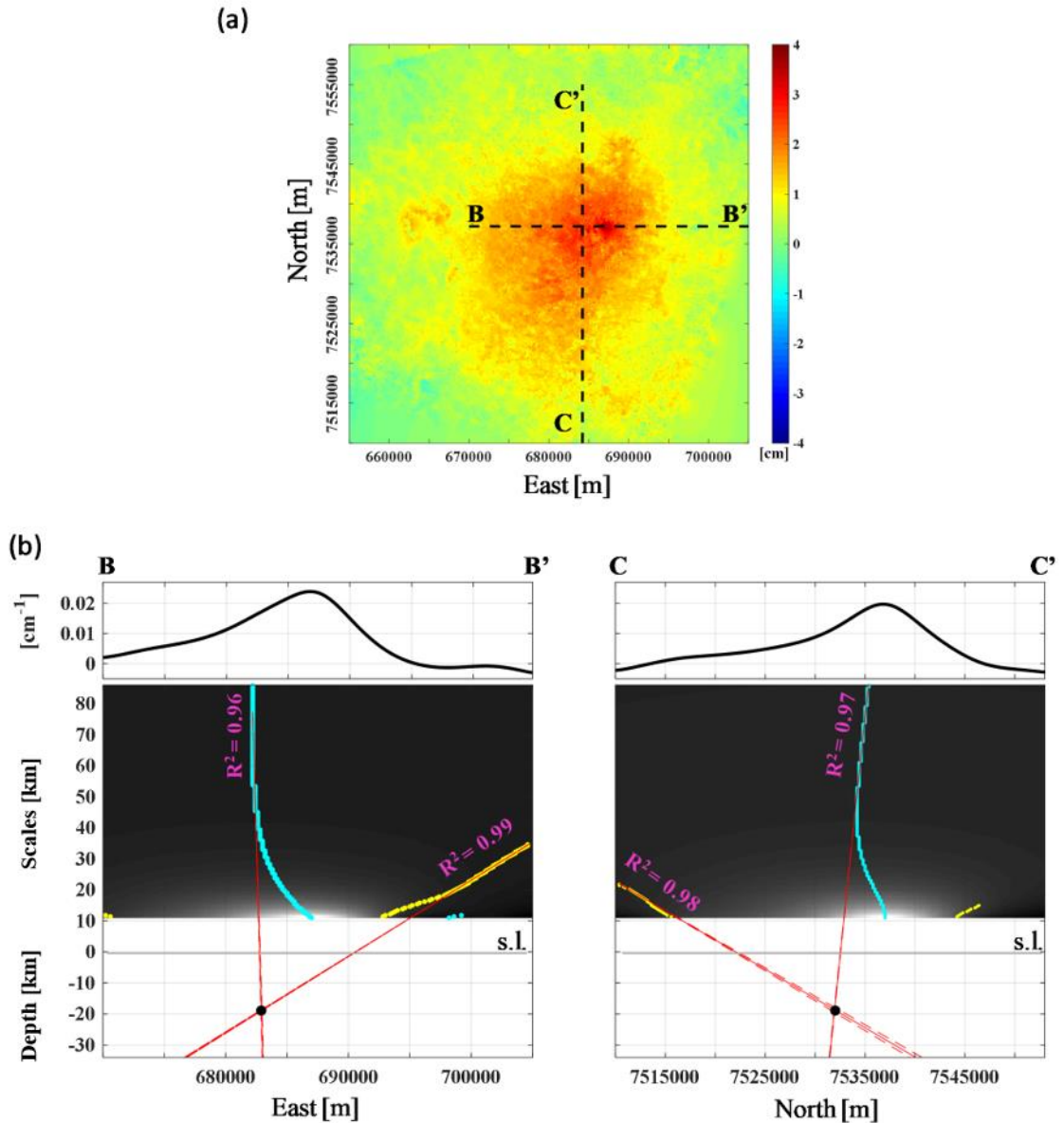


Figure 4.6. Multiridge analysis of 2005-2008 time interval. (a) Gridded vertical deformation (cm); the black dashed lines represent the BB' and CC' traces; (b) Detection of deformation sources by using Multiridge method applied to the BB' (left) and CC' (right) profiles of the VD_F of the vertical deformation map (in (a)); the red solid and dashed lines represent the best-fit regression lines and the linear regression boundary solutions within a 95% confidence interval, respectively; the black solid circles indicate the ridges intersections; for each regression line, we indicate the R^2 coefficient.

The August 2006 and February 2007 cumulative vertical deformation (**Figure 4.7a**) appears as a shorter-wavelength signal, well centred at Uturuncu volcano, and it should be not affected by long-wavelength-signal interference effects. Unlike to previous case, we apply the Multiridge method directly on the cumulative vertical deformation avoiding the increase of the high-wavenumber contributions and considering the multiridge subsets at the low scales.

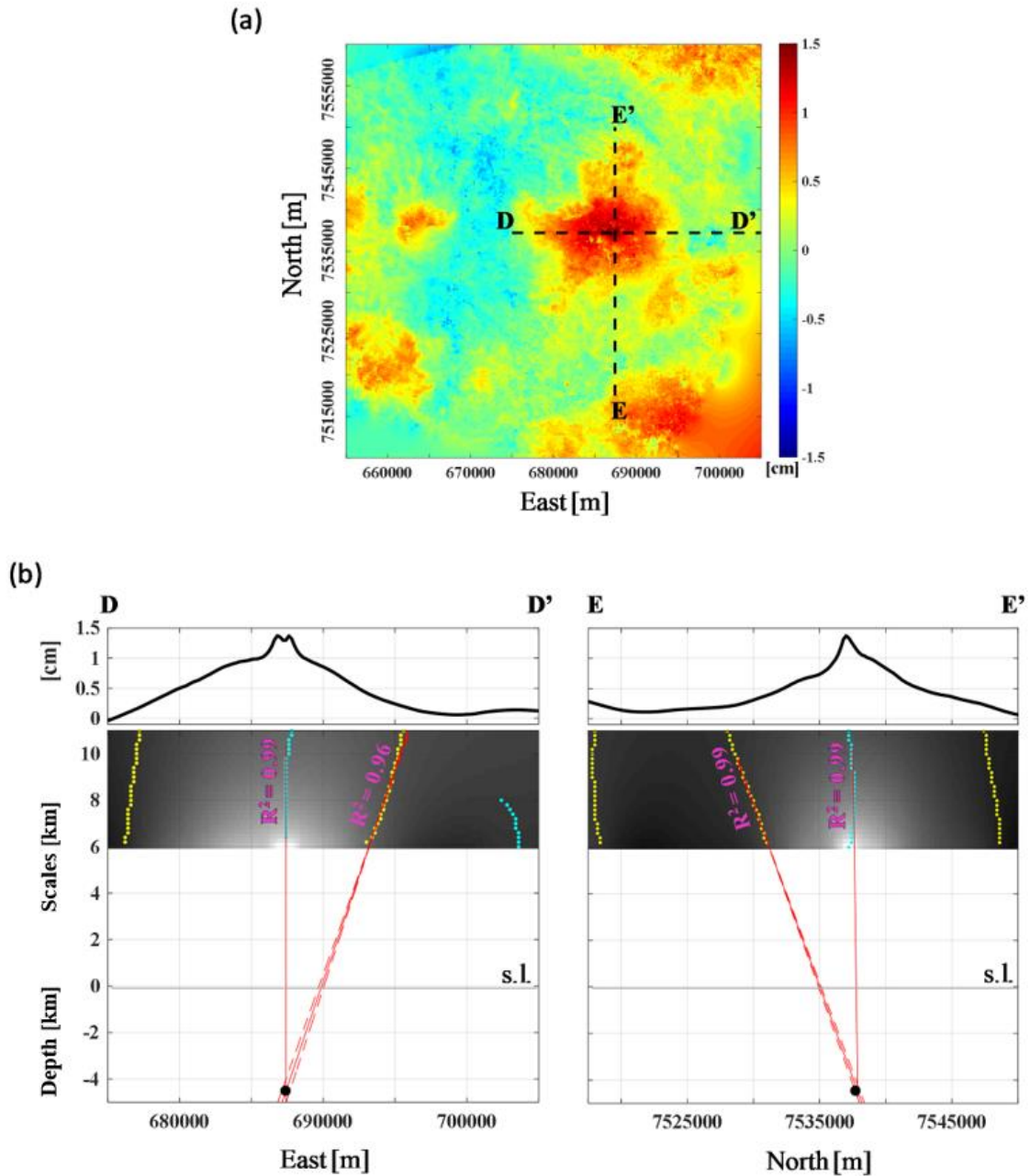


Figure 4.7. Multiridge analysis of August 2006 – February 2007 time interval. (a) Gridded vertical deformation (cm); the black dashed lines represent the DD' and EE' traces; (b) Detection of deformation sources by using Multiridge method applied to the DD' (left) and EE' (right) profiles of the vertical deformation map (in (a)); the red solid and dashed lines represent the best-fit regression lines and the linear regression boundary solutions within a 95% confidence interval, respectively; the black solid circles indicate the ridges intersections; for each regression line, we indicate the R^2 coefficient.

In **Figure 4.7b**, we show the retrieved results by considering an E-W and N-S profiles (black dashed lines), passing through the volcano edifice centre. In particular, for both cases, the depth and the horizontal position of the active source are detected at two-ridges intersection (**Figure 4.7b**): from the DD' profile analysis (along the E-W direction), we

infer a depth value equal to -4.5 ± 0.5 km at the point with East UTM coordinate equal to 687400 ± 500 m (left in the **Figure 4.7b**), while, by analysing the EE' profile (along the N-S direction), we deduce a -4.5 ± 0.3 km depth at the point with North UTM coordinate equal to 7537800 ± 200 m (right in the **Figure 4.7b**)."

From **Barone, A., Fedi, M., Tizzani, P., Castaldo, R. (2019): Multiridge Analysis of DInSAR Measurements for Multi-Source Investigation at Uturuncu Volcano (Bolivia).** Remote Sensing, 11, 703, doi:10.3390/rs11060703.

In this thesis, we integrate these results by considering the ScalFun method for the active source during the August 2006 – February 2007 time interval. We use the central cyan ridges reported in **Figure 4.7b** for both the profiles at larger scales; we characterize this source with $n \sim -2$ values (**Figure 4.8a-b**) and, since $p = 1$, with $N \sim 3$ ones.

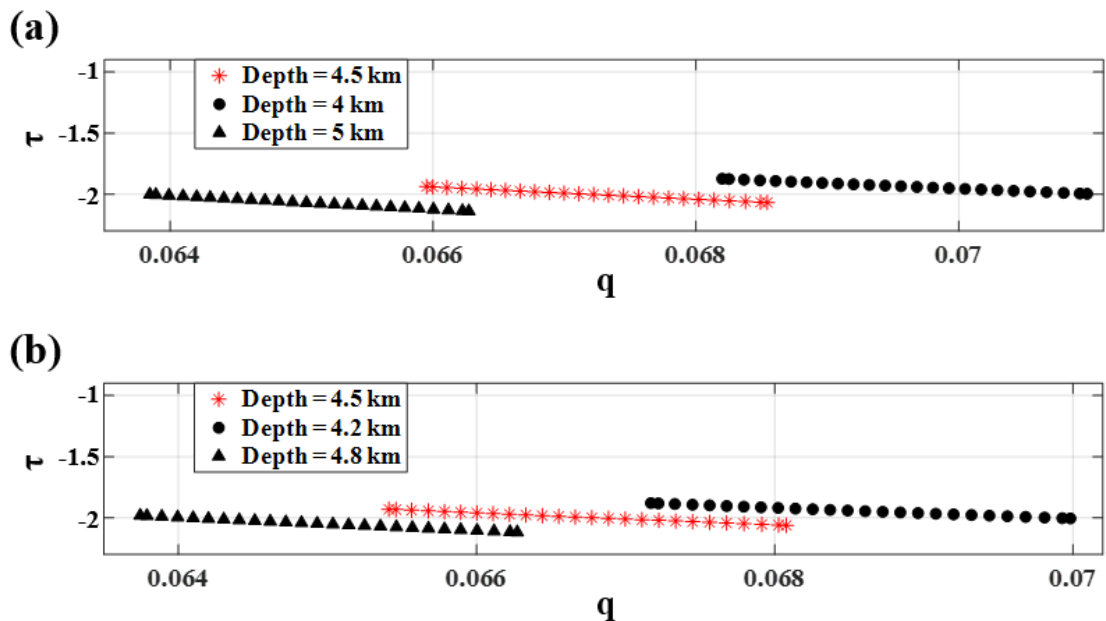


Figure 4.8. ScalFun analysis of August 2006 – February 2007 time interval. Results of the ScalFun method applied on the central cyan ridges related to the analysis of the (a) DD' and (b) EE' profiles; the red stars represent the solution by considering the intersection of the best fit linear regressions, while the black circles and triangles regard to the retrieved boundary ones; $q = \frac{1}{z}$ while $\tau = \frac{\partial \log(w(z))}{\partial \log z}$, where w and z represent the vertical deformation and the vertical scale, respectively.

4.3 THD technique: the 2012 – 2013 uplift event at Campi Flegrei caldera (Italy).

“Volcanoes are an ideal environment to test the ability of both proximal and remote-sensing techniques to characterize the internal features of the volcanic feeding system, and to model their temporal evolution [Tizzani et al., 2010; Masterlark et al. 2012; Del Negro et al. 2013; Mattia et al., 2015; Masterlark et al. 2016; Castaldo et al., 2018].

DInSAR results (i.e., mean deformation velocities maps and the corresponding time-series) are used to infer the source and dynamics of deformation phenomena in volcanic areas. In particular, these models work well for bell-shaped deformation anomalies, typical for caldera floors like Long Valley and Yellowstone [Tizzani et al. 2007; 2009; 2015]. In contrast, the relatively simple models employed to infer the location and size of deformation sources suffer from major biases if pre-existing tectonic structures [Orsi et al., 1999], shallow horizontal interfaces [Vanorio et al., 2015] and/or cold magmatic intrusions [Chiodini et al., 2015] exist. These structural constraints modulate the ground deformation pattern [Trasatti et al., 2008; Amoroso et al. 2008; Manconi et al., 2010; D’Auria et al., 2015]: without any constraint on the volcanic structures at depth, the geometry and the characteristics of the deformation sources may become uncertain, leading to incorrect interpretations of volcanic unrest from deformation data at the earlier stages of a volcanic crisis, when the signal-to-noise ratio is still low.

Seismic tomography maps the Earth subsurface using seismic waves produced by active and passive sources and recorded at a seismic network. The derived seismic models of velocity or attenuation provide an image of structural, thermal, or compositional variations inside the Earth; in volcanoes, these tomographic models can constrain geodynamical and volcanological simulations [Masterlark et al. 2012; Reuber et al., 2018]. At Campi Flegrei caldera (CFc), seismic tomography gives the structural constraints necessary to map fractures, interfaces, and older plumbing systems [Zollo et al., 2003; Vanorio et al. 2005; Battaglia et al. 2008; De Siena et al. 2010; 2017a; 2017b; Calò and Tramelli 2018]. The seismic tomography images of the onshore CFc mentioned above are built on seismic earthquake data recorded between 1982-84: they were thus an image of this period of unrest [Aster & Meyer, 1988]. The maps show that, in 1982-84, a reservoir containing high-pressure fluids was repeatedly fractured by magmatic intrusions [Amoroso et al., 2008] and/or fluid injections [Vanorio et al., 2015] under the town of Pozzuoli [De Siena et al., 2017b]. Since 1985, seismicity has mostly been limited

to the shallow hydrothermal systems, progressively shifting towards the eastern side of the caldera [Di Luccio et al., 2015]. The only seismic imaging available since 1985 was thus obtained in 2001 by using the active data of the SERAPIS seismic experiment, shot in the submerged centre of the caldera [Zollo et al. 2008; Serlenga et al. 2016], at least until De Siena et al. [2018] published an Ambient Noise Tomography (ANT) of the caldera.

With this technique, De Siena et al. [2018] have imaged the Rayleigh-wave velocity of the fluid feeder-pathway responsible for the 2011-2013 deformation unrest at CFc. The model shows-surface wave group velocities that are mostly consistent with the P- and S-wave velocity maps imaged during 1982-84, including the low-velocity fluid storage zone under Pozzuoli [Vanorio et al. 2005] and high velocity anomalies underlining the caldera rim [Battaglia et al. 2008]. The main difference between 2011-13 and 1982-84 is the presence of a high-velocity anomaly under Solfatara, at ~1.7 km which shifts towards Pisciarelli at ~1km and disappears at shallower depths. This is the first tomographic image of the onshore caldera since 1984, therefore the first that can be used in conjunction with DInSAR data.

The nucleation of microearthquakes and the spatial cutoff at depth are strongly linked to the rheological stratification of the crust beneath the CFc [Castaldo et al., 2018]. We stress that the seismicity currently recorded at CFc is too low in magnitude and sparse to apply local earthquake tomography [D'Auria et al., 2011]. On September 7th, 2012 a deep seismic swarm, possibly of magmatic origin, occurred during the rapid uplift event (2012-2013). This seismic activity diverged from the last 28 years almost exclusively driven by shallow hydrothermal processes [D'Auria et al., 2015]. Ground deformation observed in 2012-13 derived through satellite interferometry and GPS measurements has previously been interpreted as resulting from a magmatic sill intrusion of $0.0042 \pm 0.0002 \text{ km}^3$ at shallow depth ($3090 \pm 138 \text{ m}$) [D'Auria et al., 2015], whose location agrees with the low-velocity zone imaged by ANT at a depth of ~2 km [De Siena et al., 2018].

In the present study, SAR and ANT maps obtained between 2011 and 2013 provide dynamic and structural information that can be jointly used to interpret the deformation processes. While the former allows identifying the deformation source boundaries laterally and/or the involved volcanic structures that modulate the observed deformation pattern, the latter yields a velocity model characterizing the structure of the volcano in

3D. The comparison of these results with the 2005-2016 earthquake locations highlights the volume where the stresses were concentrated, confirming that the caldera structures play an active role in modulating the deformation signals.

We apply the Small BAseline Subset (SBAS) approach [Berardino et al., 2002; Pepe et al., 2005] to detect and follow the temporal evolution of the surface deformation affecting CFC during the time interval of interest. To this aim, we process the SAR data acquired from the Italian COSMO-SkyMed constellation along ascending and descending orbits. Specifically, we processed 215 ascending and 46 descending SAR data relevant to the February 2011 - January 2014 time-interval, and computed about 750 interferograms from the ascending orbits and 102 from the descending ones (selected by imposing maximum perpendicular and temporal baseline values of 800 m and 400 days, respectively). The interferograms were inverted by applying the above mentioned SBAS-DInSAR technique to generate mean deformation velocity maps (Figure 4.9a-b) and the corresponding time-series. The achieved results were computed on an output grid with $30\text{ m} \times 30\text{ m}$ spatial resolution and are referred to a reference pixel in the centre of the city of Naples.

The availability of DInSAR measurements for both the ascending and descending radar LOS (Figure 4.9a-b) allows discriminating the Vertical (V) and East–West (E-W) mean velocity components (Figure 4.9c-d) [Wright et al., 2004; Manzo et al., 2006]. Moreover, due to the non-uniform temporal sampling, the ascending and descending data were resampled to 11 days by using a linear interpolation [Del Negro et al., 2013]. This allowed the computation of time-series pairs representing the temporal evolution of the E-W and Vertical deformation components (Figure 4.9e-g).

In addition, we show that both the ascending and descending LOS mean-deformation velocity maps record a maximum of about 6 cm/year at the Pozzuoli harbor, with the velocity pattern accommodated within the caldera boundaries. Figure 4.9c-d depicts the vertical and E-W components of the mean velocity field, respectively. The first reveals an extended deformation pattern that involves the whole caldera, the latter the presence of a region of very-low velocity that separates the eastern and western sides of the caldera. Three pixels were selected to represent the Vertical and E-W components (Figure 4.9e-g) and they are located within the caldera (P1 in Figure 4.9c, P2 and P3 in Figure 4.9d).

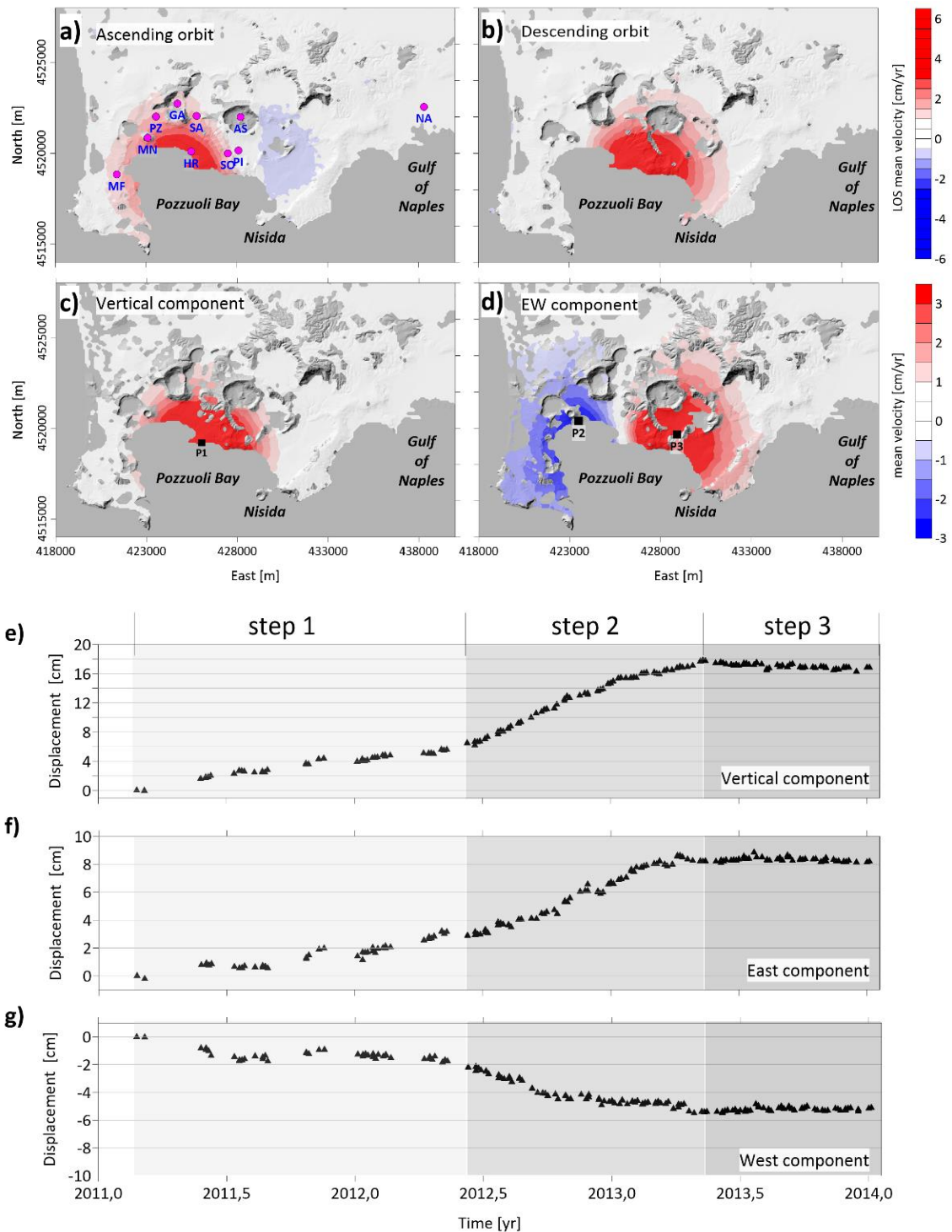


Figure 4.9: SAR Interferometry. (a-b) Contour maps of the LOS mean deformation velocity, computed by applying the SBAS algorithm to the exploited COSMO-SkyMed ascending and descending SAR data processing the 2011-2013, respectively. (c-d) Contour maps of the Vertical and E-W mean deformation velocity components; P1, P2 and P3 identify three pixels located in the areas of maximum vertical (P1), western (P2) and eastern (P3) mean velocity. The magenta filled circles represent the location of Pozzuoli site (PZ), Napoli city (NA) Monte Nuovo (NU), Pozzuoli Harbor (HR), Astroni crater (AS), Solfatarata crater (SO), Pisciarelli fumarole spring (PI), Mount Gauro (GA) and San Vito (SA), Mofete (MF). All results are superimposed on the SRTM DEM of the area. (e-g) Vertical (P1) and East-West (P2 and P3) displacement time-series. The analysed time period is divided in three steps (gray color regions) for different linear deformation trends analysis.

Note that the vertical component of the ground deformation reaches a maximum value of about 18 cm (plot of **Figure 4.9e**), while the horizontal displacements towards East and West reach maximum values of 8 cm (plot of **Figure 4.9f**) and about 6 cm (plot of **Figure 4.9g**), respectively.

The advanced DInSAR measurements, specifically, the vertical and E-W displacements of the whole caldera relevant to the three identified temporal steps (see **Figure 4.9**), are shown in **Figure 4.10**.

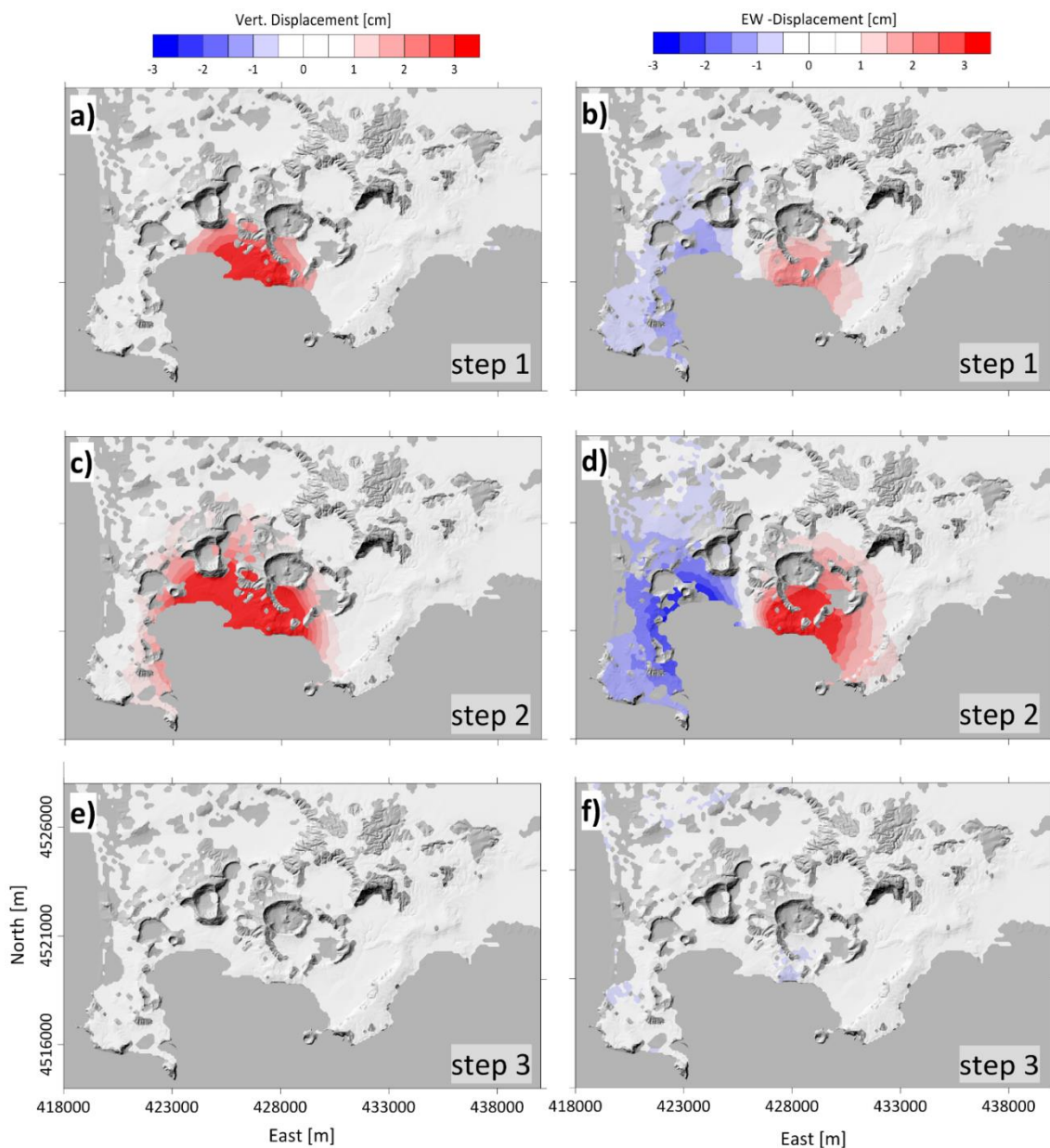


Figure 4.10: DInSAR analysis relevant to the investigated steps. (a-b) Contour maps of the vertical and E-W displacements, respectively, measured during the step 1: Feb. 2011 – May 2012, (c-d) the step 2: May 2012 – April 2013, and (e-f) the step 3: April 2013- Jan. 2014. All results are superimposed on the SRTM DEM of the area.

We observe that the E-W and Up-Down deformations drastically increase both spatially and in magnitude from step 1 to step 2 (**Figure 4.10a-d**). The region of maximum vertical displacement corresponds to the area of lowest E-W deformation, particularly at step 2 (from May 2012 to April 2013), when the maximum deformation rate is recorded.

To investigate the volcanic source boundaries (i.e., possible magmatic reservoirs) and/or the involved structures that modulate the observed deformation pattern, we apply the THD technique to the displacement occurred during the second step. We first spatially regularize the dataset via ordinary kriging [Li and Heap, 2008], then we process the gridded vertical component by performing the constant scale reduction at 200 m a.s.l. Finally, we compute the THD_w and analyse the spatial distribution of its maxima (**Figure 4.11**), which is described by a bi-lobed shape having its axis of symmetry along the WNW-ESE direction. The alignment of the maxima is clearly defined to the east of Pozzuoli harbor, while the intensity of the maxima decreases in the western part of the caldera.

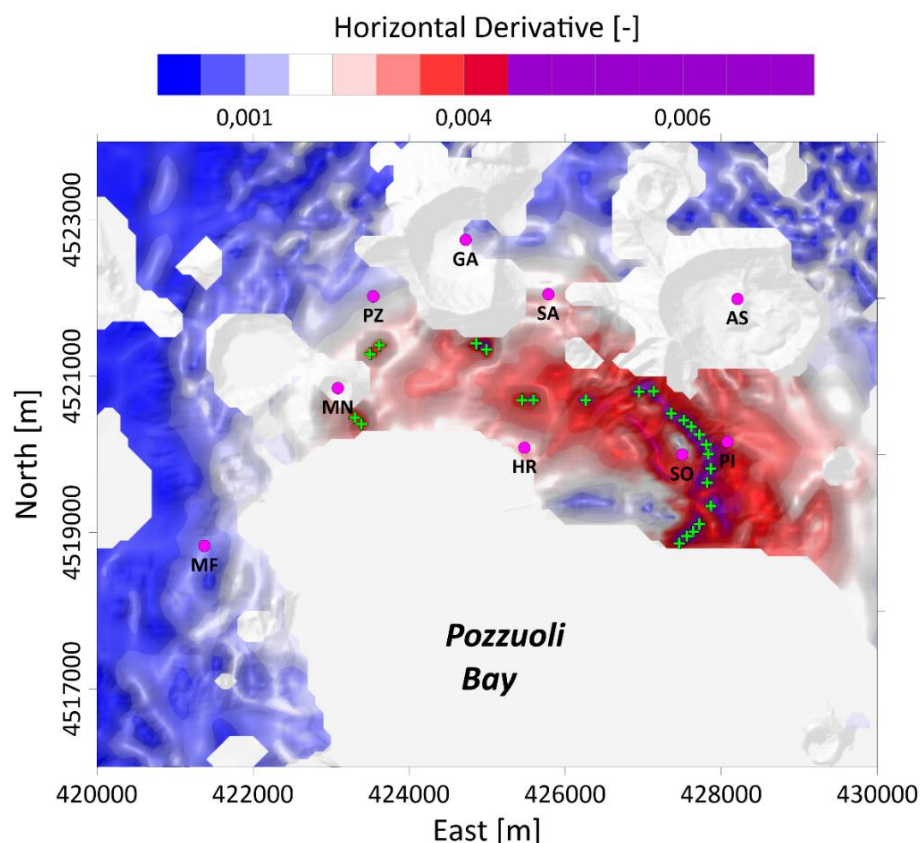


Figure 4.11: THD analysis of the temporal step 2. a) THD_w results of the deformation related to step 2 (May 2012 – April 2013). The green crosses identify the maxima of the THD. The magenta circles represent the location of Pozzuoli site (PZ), Napoli city (NA) Monte Nuovo (NU), Pozzuoli Harbor (HR), Astroni crater (AS), Solfatara crater (SO), Pisciarelli fumarole spring (PI), Mount Gauro (GA), Mofete (MF) and San Vito (SA). The results are superimposed on the SRTM DEM of the area.

Figure 4.12 shows the contour maps of the ANT group-velocity model obtained at periods 0.9 s (~0.9 km of depth), 1.2 s (~1 km of depth) and 2 s (~1.7 km of depth) by De Siena et al. [2018].

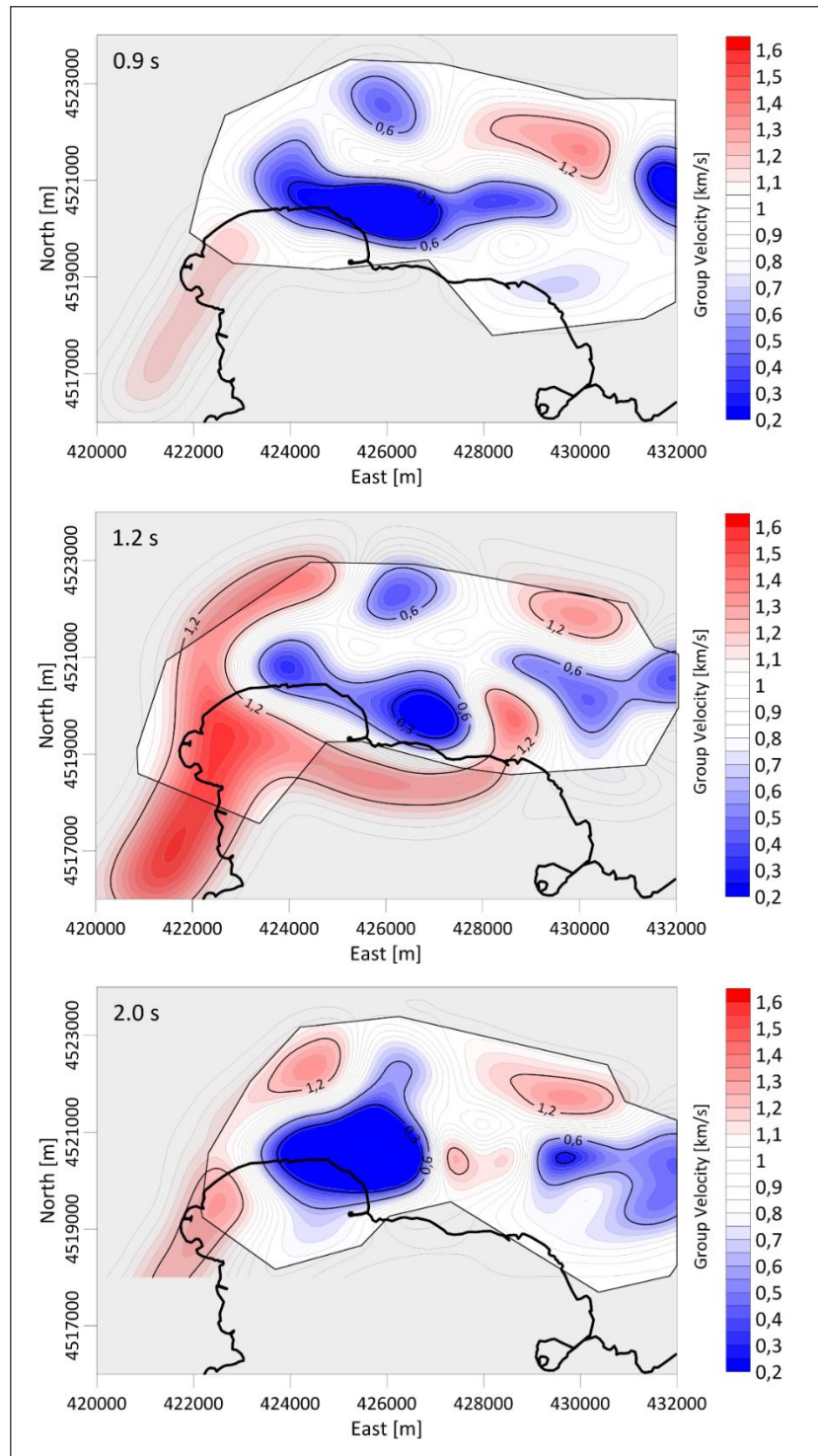


Figure 4.12: ANT group-velocity model at different periods. Surface-wave (Rayleigh) group-velocity contour maps retrieved at different periods (0.9s, 1.2s, 2s) by the ANT analysis during the 2011-2013 unrest. The shaded polygon shows low-to-no resolution area.

In **Figure 4.13a**, we show the seismicity divided in three periods, considering the same time intervals identified within the SAR interferometry analysis.

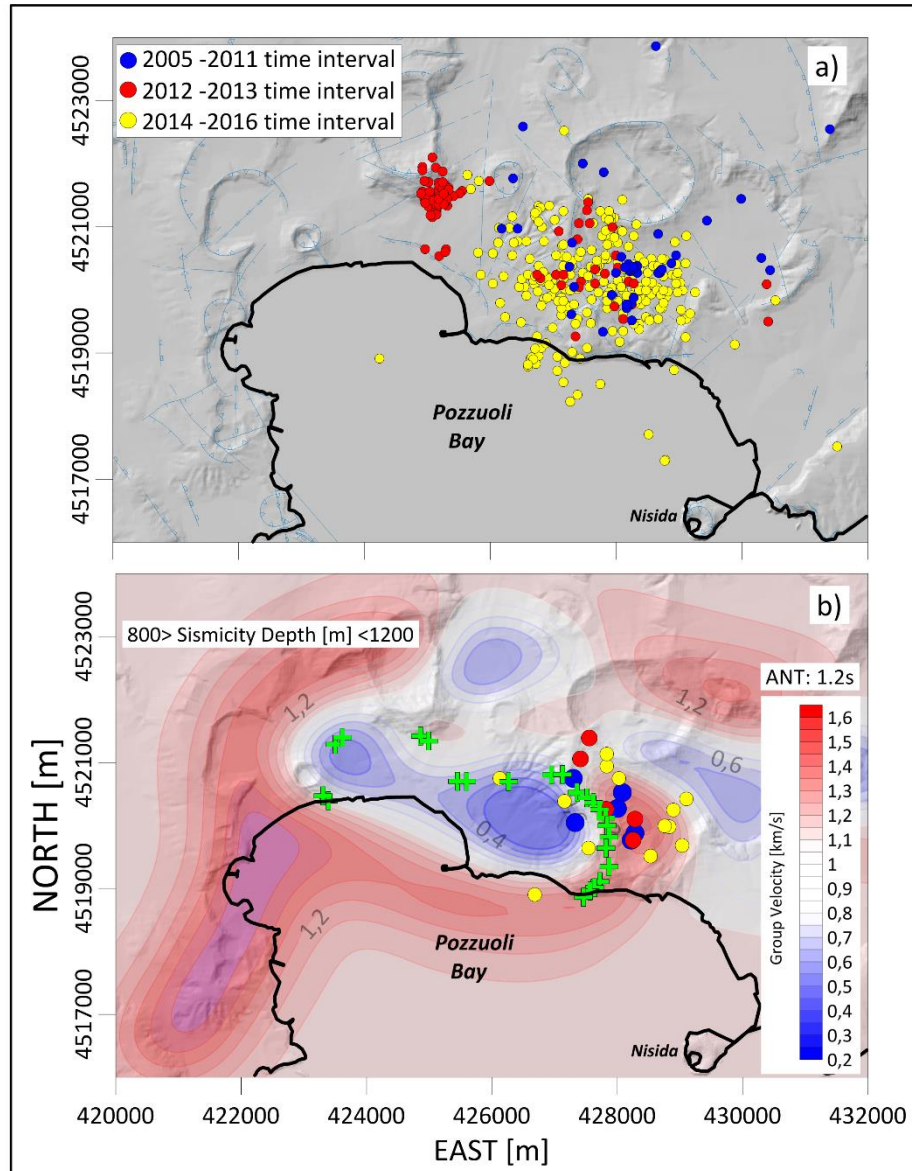


Figure 4.13: 2005-2016 seismicity and SAR vs Seismic Interferometry. (a) Epicentral distribution of local seismicity relevant to the three temporal steps reported in Figure 31. (b) Comparison between the maxima of THD_w (green crosses) and the 1.2 s period (~ 1 km depth) seismic velocity contour map with the 2005-2011 (blue circles), 2012-2013 (red circles), 2014-2016 (yellow circles) earthquake distributions between 800 m and 1200 m of depth.”

From Pepe et al. [2019].

4.4 Multiridge and ScalFun methods: the Fernandina volcano (Galapagos Archipelago, Ecuador) analysed with cumulative E-W deformation.

The Galapagos Archipelago, located on the Nazca Plate, represents the emerged portion of an oceanic hotspot. A cluster of basaltic volcanoes with large summit calderas forms the Islands and the youngest active ones lie on its western part.

Fernandina Volcano is one of the most active centres and it mainly erupts tholeiite basalt by offering examples to detect the relationship between the caldera morphology and the eruptive behaviour for basaltic shields [McBirney and Williams, 1969]. This volcano is located on the homonymous Island and it consists of a 1470 m elevated edifice with deep centred caldera and vents occurred on all parts of the volcano [Rowland, 1996]. The summit caldera shows circumferential eruptive fissures, while lower on the flanks the pattern consists of radial ones. [Simkin, 1984]. The vents alignment is the surface expression of dyke's emplacement that has propagated from both deep and shallow magma reservoirs. The interaction between stresses and the regional field characterizes this structural evidence, while the radial stress field produced by a magmatic pressure source at the centre of an axisymmetric volcanic edifice represents the explanation to the radial dykes [Odé, 1957; Pollard, 1987]; furthermore, the stress state in the volcano controls their orientations [Chadwick and Howard, 1991]. Most of the eruptions during the period 1968-2008 (13 times in this time interval) were effusive and occurred along linear fissures; instead, the 1968 eruption induced the caldera collapse [Simkin and Howard, 1970], which morphology is the result of multiple collapse features, also distributed along the NW-SE direction [Rowland and Munro, 1992]. The alternation between circumferential and radial fissure eruptions characterizes the most recent activity from the 1982 to 2009 [Rowland and Munro, 1992; Chadwick and Dieterich, 1995; Chadwick et al., 2011].

Regarding to the modeling of the volcanic deformation source, different authors have used both DInSAR and GPS measurements to retrieve for temporally different volcanic stages a source mechanism as sill- and dike-like bodies [Jonsson et al., 1999; Chadwick et al., 2011; Bagnardi and Amelung, 2012]; furthermore, Bagnardi et al. [2013] proposed a shallow dipping sill intrusion at about 1 km b.s.l. as the more appropriate deformation mechanism; this model demonstrates the change of the eruptive fissures orientations from sub horizontal to vertical and it is verified when the feeding of circumferential fissures is near to the caldera margin or when a twist occurs to feed fissure eruptions on the flanks

of the volcano [Bagnardi et al., 2013]. Recently, Pepe et al. [2017] have analysed the 2012-2013 unrest event through DInSAR measurements by proposing for the first time a pipe-like volcanic structure (with depth of about 1.5 km b.s.l.) as the more suitable geodetic solution. The authors interpret this last as the interconnection zone between shallow volcanic reservoirs and deep cumulate complex within the same extended Magmatic Feeding System (MFS) [Pepe et al., 2017].

In this scenario, we consider Multiridge and ScalFun methods to analyse the same processed dataset by Pepe et al. [2017]; in particular, we focus on the 2013 uplift event to perform the “geodetic” source shape detection under the assumptions of the validity of the Laplace’s equation and, in turn, of the homogeneity properties of the considered ground deformation field.

The used dataset consists of 26 and 34 images acquired by the CSK satellite constellation along the ascending, from 2012 March to 2013 June, and descending, from 2012 March to 2013 November, orbits, respectively, with a radar look angle at mid-scene of about 45° . The authors considered the SBAS approach [Berardino et al., 2002; Casu et al., 2014] for retrieving both the LOS mean velocity maps and time-series with a precision of 1 mm/year and 5mm/epoch, respectively [Casu et al., 2006; De Luca et al., 2015]. An exceptional resolution characterizes the data since the minimum temporal sampling interval is equal to 8 days and the spatial one is $3\text{ m} \times 3\text{ m}$. The final resolution is however reduced to $30\text{ m} \times 30\text{ m}$ after the computation of 57 ascending and 81 descending differential interferograms and the application of a multilook (averaging) factor of 10 in azimuth and range directions.

Finally, by combining the ascending and descending LOS measurements, the vertical and E-W components of the ground deformation fields are retrieved in terms of both mean velocity maps and time-series. This combination is based on a pixel-by-pixel procedure by considering only the coherent ones in both the ascending and descending mean velocity maps [Manzo et al., 2006], before having resampled the time-series to a common sampling interval of 8 days [Del Negro et al., 2013] since no intrinsically non-linear events (i.e., eruptions) occur.

We show the mean vertical (**Figure 4.14a**) and E-W (**Figure 4.14b**) velocity maps by considering as reference pixel (black triangles in **Figure 4.14a-b**) an undeformed point at the North-western sector of the Fernandina Island. In particular, during the 2012-2013

the volcano uplifts with a mean vertical velocity larger than 10 cm/yr and it horizontally deforms with a mean E-W velocity greater than 8 cm/yr.

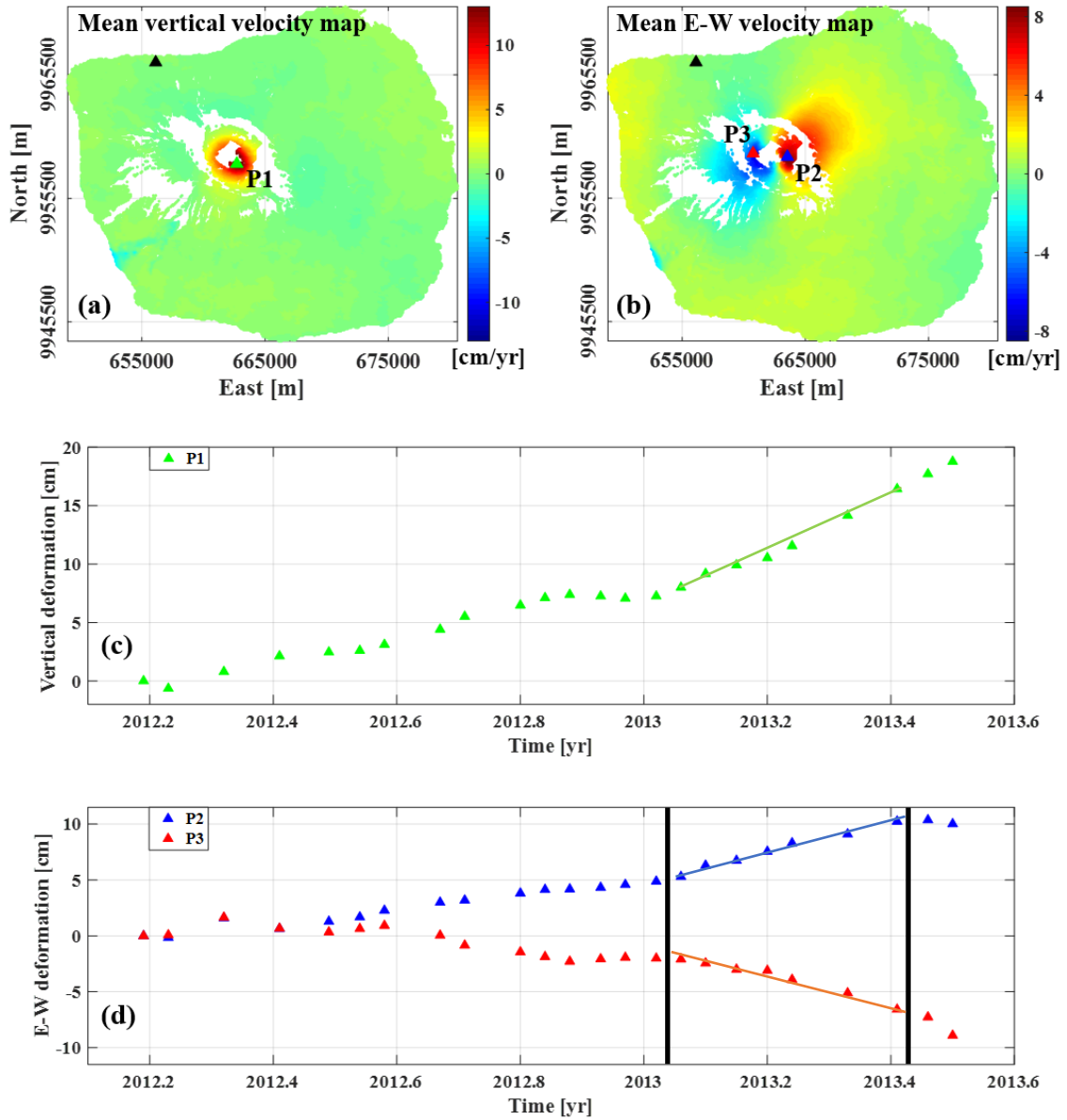


Figure 4.14. DInSAR data and mean velocity maps at Fernandina volcano. Maps of the mean (a) vertical and (b) E-W velocity [cm/yr] related to the time interval 2012-2013.5 for Fernandina Volcano; the black triangles indicate the reference pixel, while the green, blue and red triangles corresponds to location of P1, P2 and P3 pixels, respectively, along which the time-series are displayed; (c) vertical and (d) E-W components of the deformation measured during the 2012-2013.5 time interval at P1 and P2-P3 pixels, respectively; the black vertical continuous lines represent the selected temporal period for performing the proposed analysis; the green, blue and red continuous lines represent the linear regression at each pixels for the considered time interval.

We show the time-series of the vertical deformation (**Figure 4.14c**) at P1 pixel (green triangle in **Figure 4.14a**), that is at the maximum value of the mean vertical velocity map, and the E-W one (**Figure 4.14d**) by considering P2 (blue triangle in **Figure 4.14b**) and P3 (red triangle in **Figure 4.14b**) pixels, which are the points showing the maximum value of the mean velocity toward East and West, respectively.

Both the components reveal a similar deformation pattern in the considered interval: we observe a first uplift phenomenon with no very high deformation velocity until about the 2012.8 epoch; then, the volcano is almost in stasis up to the 2013 date; finally, an unrest event characterized by a greater velocity respect to the first uplift occurs.

Since the pattern of the vertical deformation component (**Figure 4.14a**) does not allow well characterizing the area of the field maxima (decorrelated signals), which is quite crucial for the ScalFun method, we analyse only the E-W deformation component. We select a time interval, within the greatest unrest episode, for which both the East and West deformations reveal the same behaviour, that is between the 2013 and the 2013.5 epochs (vertical black continuous lines in **Figure 4.14d**).

Therefore, we calculate the cumulative E-W deformation occurred during the 2013 – 2013.5 time interval and, after a gridding operation by using the natural neighbor interpolator with 0.1 km of sampling step along both the x - and y -directions, we apply the constant-level reduction procedure, with a flat scale chosen at 1.5 km a.s.l.. This procedure is necessary to relocate the analysed field on a flat measurement surface since the considered methods are based on a level-to-level algorithm.

We show the retrieved processed data in **Figure 4.15**.

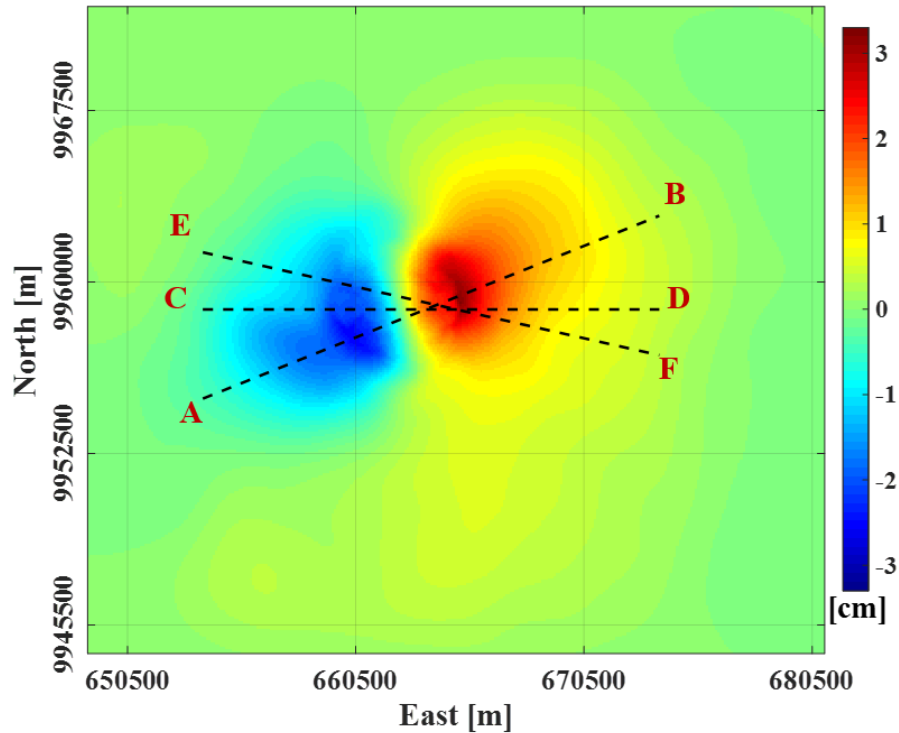


Figure 4.15. Processed 2013-2013.5 cumulative E-W deformations. Map of the processed E-W component [cm] of the ground deformation field for Fernandina Volcano in the 2013-2015 time interval; the black dashed lines represents the profiles location along which the results of Multiridge and ScalFun methods are displayed.

We select three profiles (black dashed lines in **Figure 4.15**), named as AB, CD and EF, along which we show the results of Multiridge and ScalFun methods. In particular, we analyse the first- ($p = 2$), second- ($p = 3$) and third-orders ($p = 4$) VD_F of the processed E-W component to fully characterize the deformation source in terms of depth and shape.

We specify that best-fit linear regressions within a 95% confidence interval represent the ridges, for which we calculate the determination coefficient R^2 as a statistical measure of how the multiridge subsets are close to the fitted regression line (ridges).

We also evaluate the solution uncertainties (intersection at the ridges) by considering the error on the best-fit linear regression coefficients (intercept and slope constants).

Moreover, for each analysis, we report with the green dashed lines the scale below which the multi-scale dataset is surely affected by high-wavenumber noise. We mainly associate this noise to the constant-level reduction procedure at greater slope of the

volcano topography; in particular, the noise affects the choice of the ridges and multi-scale dataset, for which we have chosen a maximum scale of 11.5 km a.s.l. with 0.1 km of continuation sampling.

We start from the AB profile (black dashed line in **Figure 4.15**), where the ridges intersect in the point with coordinates $662800 \text{ E} \pm 200 \text{ m}$, $9958500 \text{ N} \pm 200 \text{ m}$ at a depth of $1.6 \pm 0.3 \text{ km b.s.l.}$ and $662800 \text{ E} \pm 200 \text{ m}$, $9958500 \text{ N} \pm 200 \text{ m}$ at a depth of $1.6 \pm 0.4 \text{ km}$ by considering the first- (**Figure 4.16a**) and the second-order (**Figure 4.16b**) VD_F of the E-W deformation, respectively. We apply the ScalFun method to both the left and right cyan ridges of both the VD_F and we characterize these solutions with $n \sim -3$ (**Figure 4.16c-d**, respectively) and $n \sim -4$ (**Figure 4.16e-f**, respectively) values, which correspond both to $N \sim 3$ since p changes from 2 to 3 (**Table 2.1**).

Furthermore, we also analyse the third-order VD_F of the E-W deformation, which results indicate a source located in the point with coordinates $662800 \text{ E} \pm 200 \text{ m}$, $9958500 \text{ N} \pm 200 \text{ m}$ at a depth of $0.5 \pm 0.3 \text{ km b.s.l.}$ (**Figure 4.17a**). $n \sim -4$ (**Figure 4.17b**) characterizes this source, for which $N \sim 2$ since $p = 4$ (**Table 2.1**).

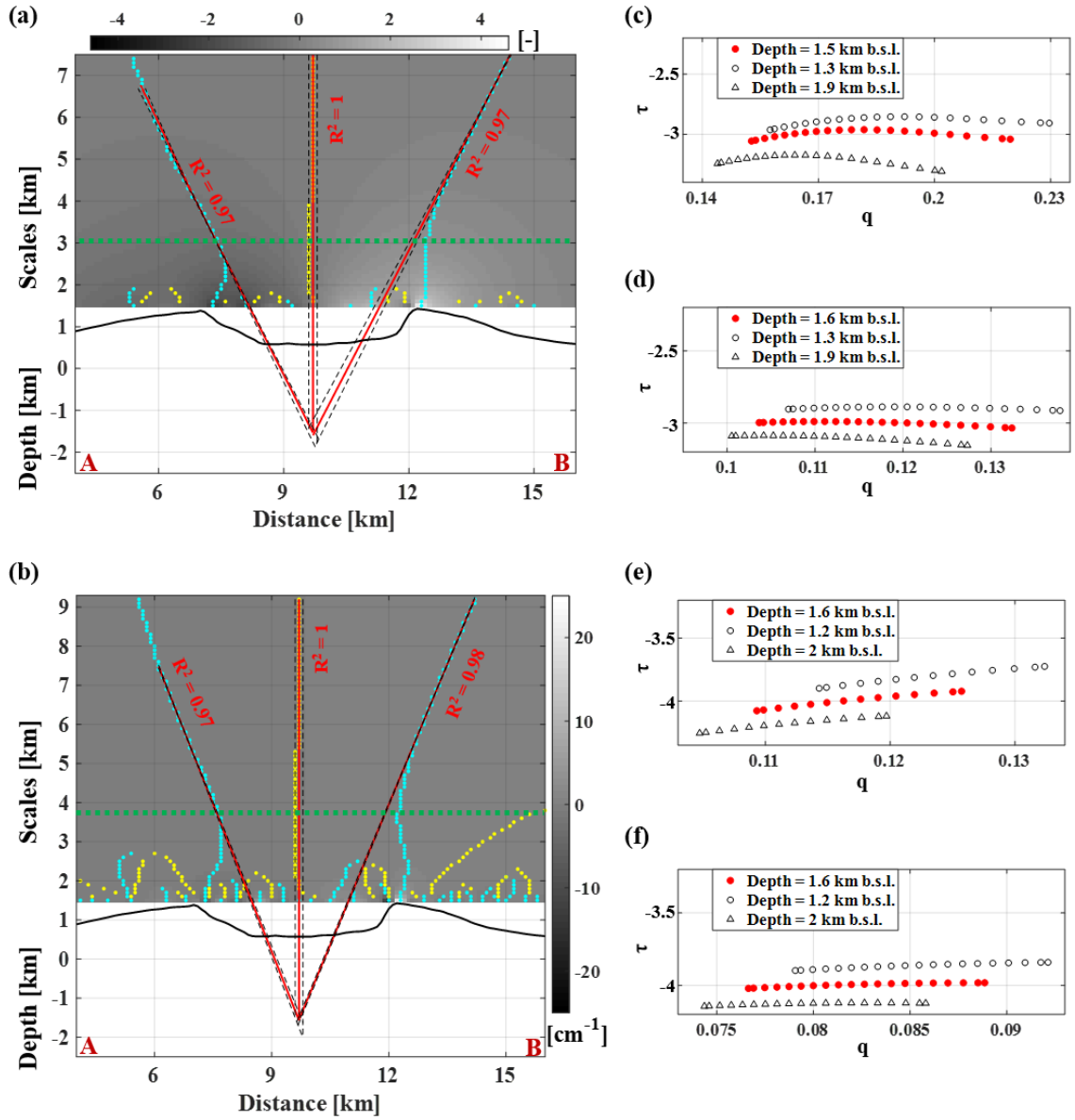


Figure 4.16. AB profile: first- and second orders VD_F . Results of the Multiridge method applied on the (a) first- and (b) second-order VD_F of the E-W deformation; the red solid and black dashed lines represent the best-fit linear regression lines and the linear regression boundary solutions within a 95% confidence interval, respectively, while the black solid lines indicate the volcano topography and the green dashed lines define the scale below which the multi-scale dataset is surely affected by high-wavenumber noise; for each regression line, we indicate the R^2 coefficient. Results of ScalFun method applied on the left and right ridges of the (c-d) first- and (e-f) second-order VD_F cases; the red dots represent the solution using the intersection of the best fit linear regressions, while the black circles and triangles regard to the retrieved boundary solutions; $q = \frac{1}{z}$ while $\tau = \frac{\partial \log(VD_F(z))}{\partial \log z}$, where z represents the vertical scale.

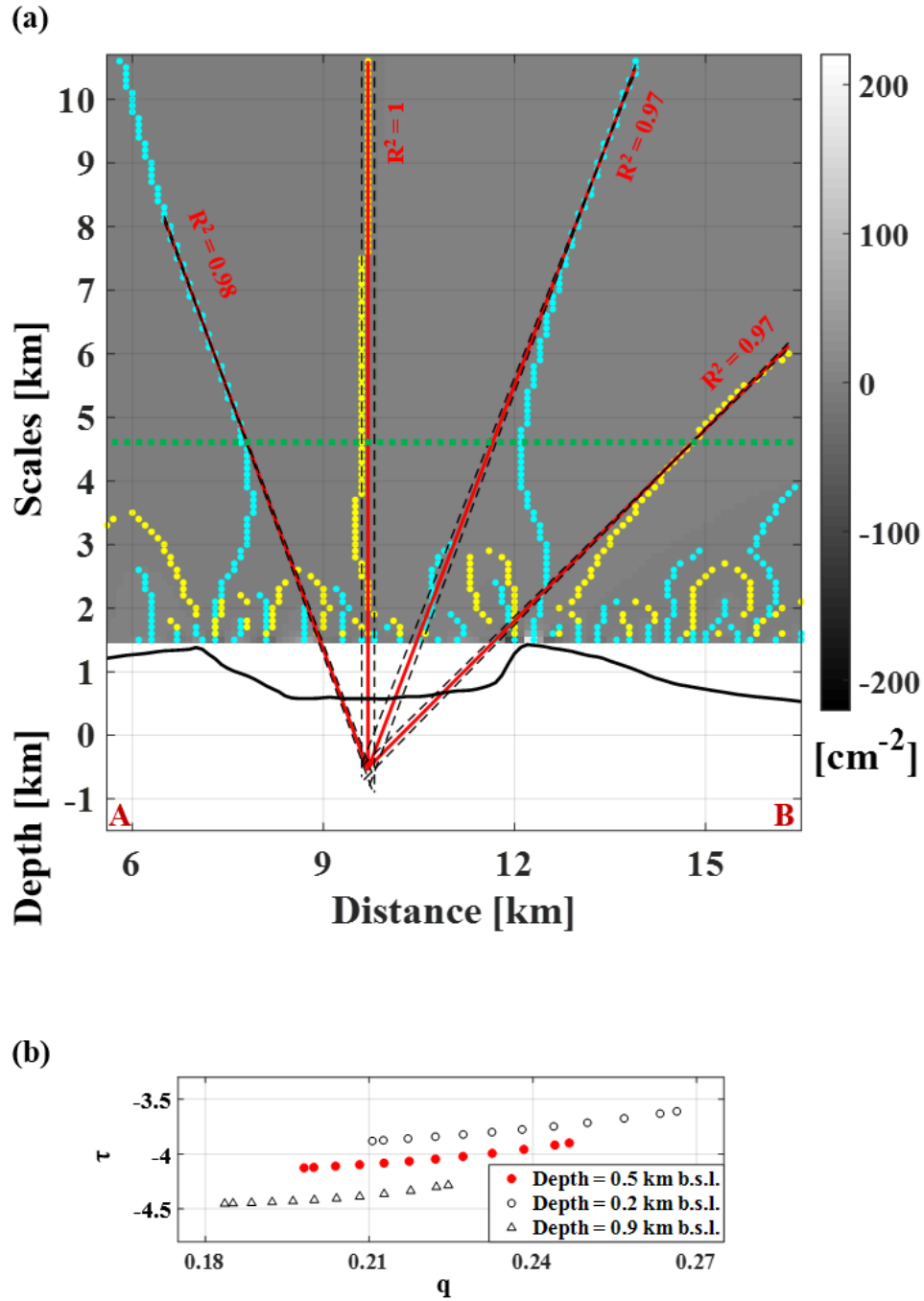


Figure 4.17. AB profile: third-order VD_F . Results of the (a) Multiridge and (b) ScalFun methods applied on the third-order VD_F of the E-W deformation; the red solid and black dashed lines represent the best-fit linear regression lines and the linear regression boundary solutions within a 95% confidence interval, respectively, while the black solid lines indicate the volcano topography and the green dashed line defines the scale below which the multi-scale dataset is surely affected by high-wavenumber noise; for each regression line, we indicate the R^2 coefficient; the red dots represent the solution using the intersection of the best fit linear regressions, while the black circles and triangles regard to the retrieved boundary solutions; $q = \frac{1}{z}$ while $\tau = \frac{\partial \log(VD_F(z))}{\partial \log z}$, where z represents the vertical scale.

Similarly to the previous case, we consider the E-W oriented CD profile (black dashed line in **Figure 4.15**), for which the Multiridge analysis provides a single intersection located in the point with coordinates $662700 \text{ E} \pm 100 \text{ m}$, 9958800 N at a depth of $1.7 \pm 0.5 \text{ km b.s.l.}$ for the first-order VD_F (**Figure 4.18a**) and $662800 \text{ E} \pm 100 \text{ m}$, 9958800 N at a depth of $1.6 \pm 0.4 \text{ km}$ for the second-order one (**Figure 4.18b**). Applying the ScalFun method to both the left and right cyan ridges of both the VD_F we characterize these solutions with $n \sim -3$ (**Figure 4.18c-d**, respectively) and $n \sim -4$ (**Figure 4.18e-f**, respectively) values, that are $N \sim 3$ since p changes from 2 to 3 (**Table 2.1**)

Moreover, the third-order VD_F analysis indicates a source located in the point with coordinates $662700 \text{ E} \pm 100 \text{ m}$, 9958800 N at a depth of $0.6 \pm 0.5 \text{ km b.s.l.}$ (**Figure 4.19a**) and characterized by values of $n \sim -4$ (**Figure 4.19b**) and $N \sim 2$, since $p = 4$ (**Table 2.1**).

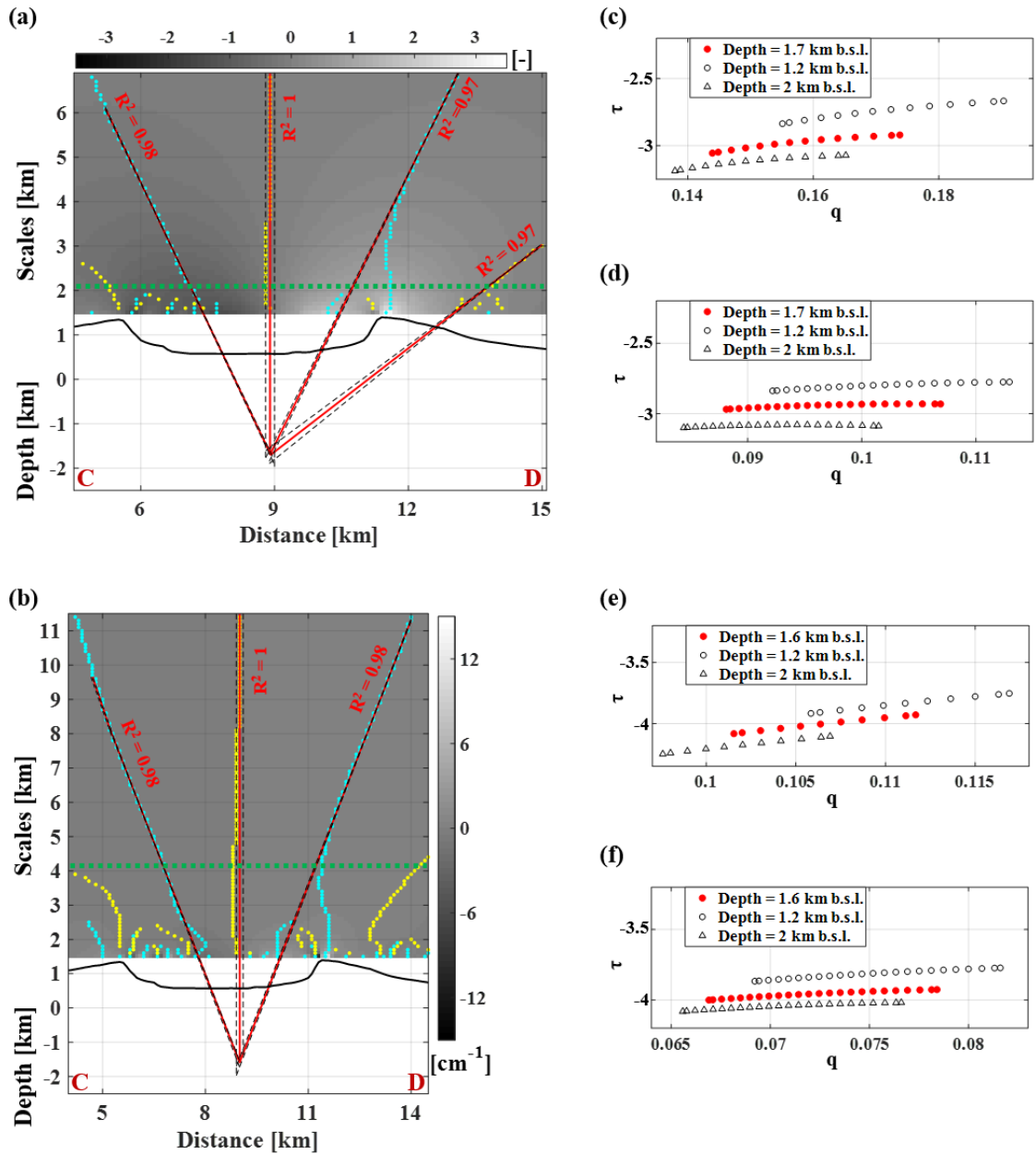


Figure 4.18. CD profile: first- and second orders VD_F . Results of the Multiridge method applied on the (a) first- and (b) second-order VD_F of the E-W deformation; the red solid and black dashed lines represent the best-fit linear regression lines and the linear regression boundary solutions within a 95% confidence interval, respectively, while the black solid lines indicate the volcano topography and the green dashed lines define the scale below which the multi-scale dataset is surely affected by high-wavenumber noise; for each regression line, we indicate the R^2 coefficient. Results of ScalFun method applied on the left and right ridges of the (c-d) first- and (e-f) second-order VD_F cases; the red dots represent the solution using the intersection of the best fit linear regressions, while the black circles and triangles regard to the retrieved boundary solutions; $q = \frac{1}{z}$ while $\tau = \frac{\partial \log(VD_F(z))}{\partial \log z}$, where z represents the vertical scale.

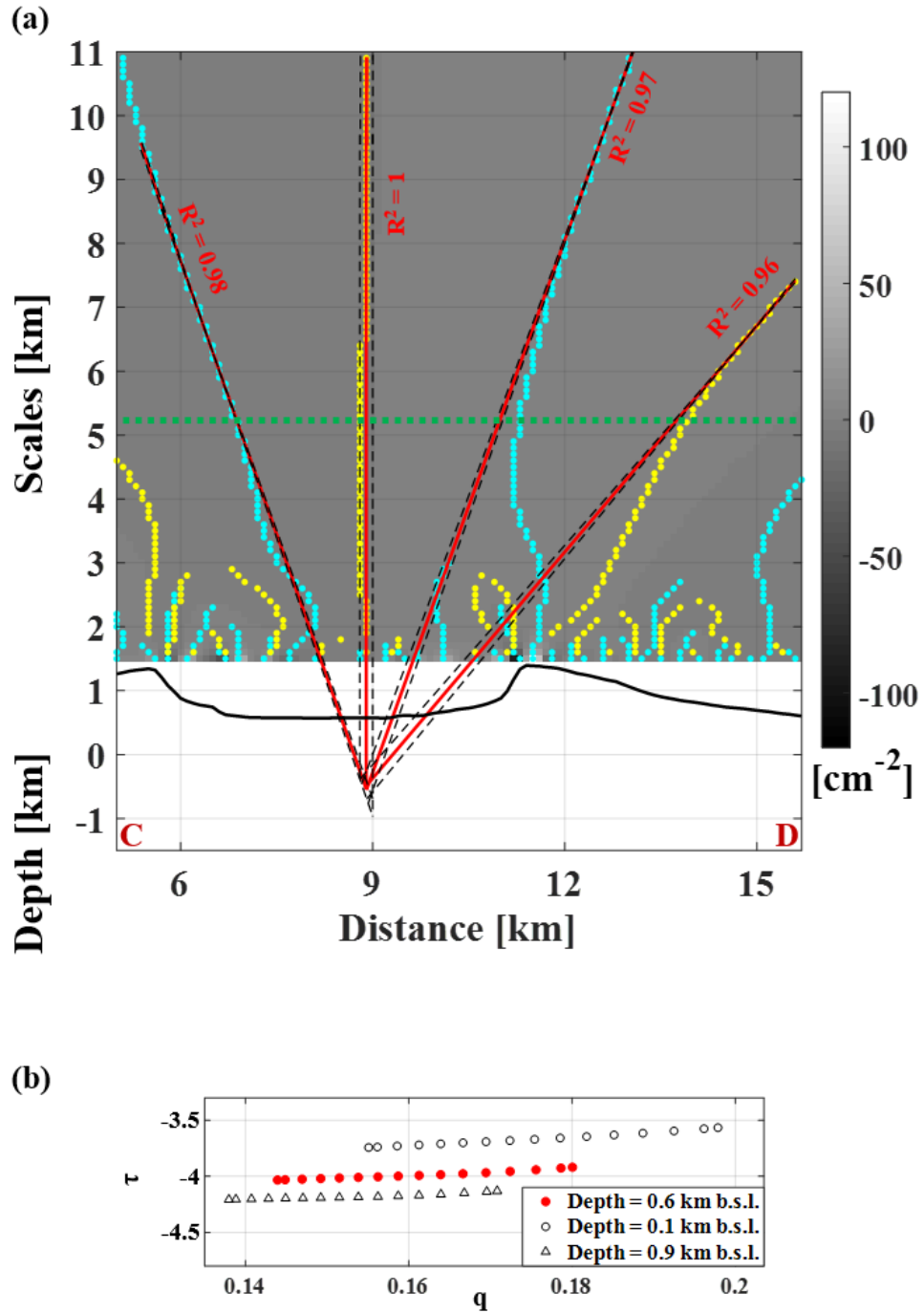


Figure 4.19. CD profile: third-order VD_F . Results of the (a) Multiridge and (b) ScalFun methods applied on the third-order VD_F of the E-W deformation; the red solid and black dashed lines represent the best-fit linear regression lines and the linear regression boundary solutions within a 95% confidence interval, respectively, while the black solid lines indicate the volcano topography and the green dashed line defines the scale below which the multi-scale dataset is surely affected by high-wavenumber noise; for each regression line, we indicate the R^2 coefficient; the red dots represent the solution using the intersection of the best fit linear regressions, while the black circles and triangles regard to the retrieved boundary solutions; $q = \frac{1}{z}$ while $\tau = \frac{\partial \log(VD_F(z))}{\partial \log z}$, where z represents the vertical scale.

The Multiridge analysis for the last analysed EF profile yields a single intersection located in the point with coordinates $662700 \text{ E} \pm 200 \text{ m}$, $9959300 \text{ N} \pm 100 \text{ m}$ at a depth of $1.7 \pm 0.5 \text{ km b.s.l.}$ and $662500 \text{ E} \pm 200 \text{ m}$, $9959300 \text{ N} \pm 100 \text{ m}$ at a depth of $1.6 \pm 0.4 \text{ km}$ by computing the first- (**Figure 4.20a**) and the second-order (**Figure 4.20b**) VD_F of the E-W deformation, respectively. The ScalFun method for both the left and right cyan ridges provides values of $n \sim -3$ (**Figure 4.20c-d**, respectively) and $n \sim -4$ (**Figure 4.20e-f**, respectively) for both the analysed VD_F . Also, $N \sim 3$ since p changes from 2 to 3 (**Table 2.1**).

Finally, the analysis of the third-order VD_F highlights a source located in the point with coordinates $662500 \text{ E} \pm 200 \text{ m}$, $9959300 \text{ N} \pm 100 \text{ m}$ at a depth of $0.6 \pm 0.5 \text{ km b.s.l.}$ (**Figure 4.21a**) and characterized by $n \sim -4$ (**Figure 4.21b**) and $N \sim 2$, since $p = 4$ (**Table 2.1**).

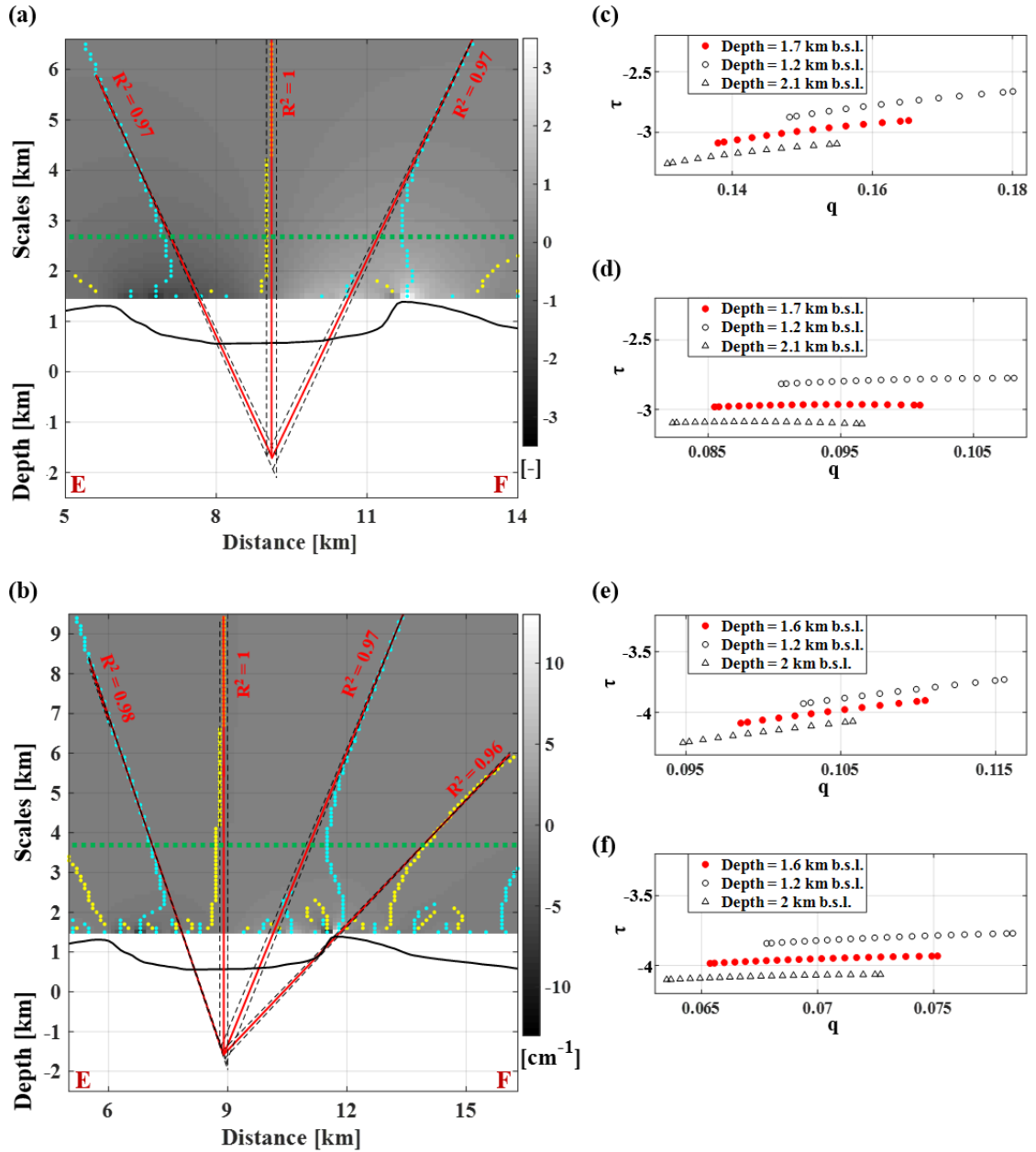


Figure 4.20. EF profile: first- and second orders VD_F . Results of the Multiridge method applied on the (a) first- and (b) second-order VD_F of the E-W deformation; the red solid and black dashed lines represent the best-fit linear regression lines and the linear regression boundary solutions within a 95% confidence interval, respectively, while the black solid lines indicate the volcano topography and the green dashed lines define the scale below which the multi-scale dataset is surely affected by high-wavenumber noise; for each regression line, we indicate the R^2 coefficient. Results of ScalFun method applied on the left and right ridges of the (c-d) first- and (e-f) second-order VD_F cases; the red dots represent the solution using the intersection of the best fit linear regressions, while the black circles and triangles regard to the retrieved boundary solutions; $q = \frac{1}{z}$ while $\tau = \frac{\partial \log(VD_F(z))}{\partial \log z}$, where z represents the vertical scale.

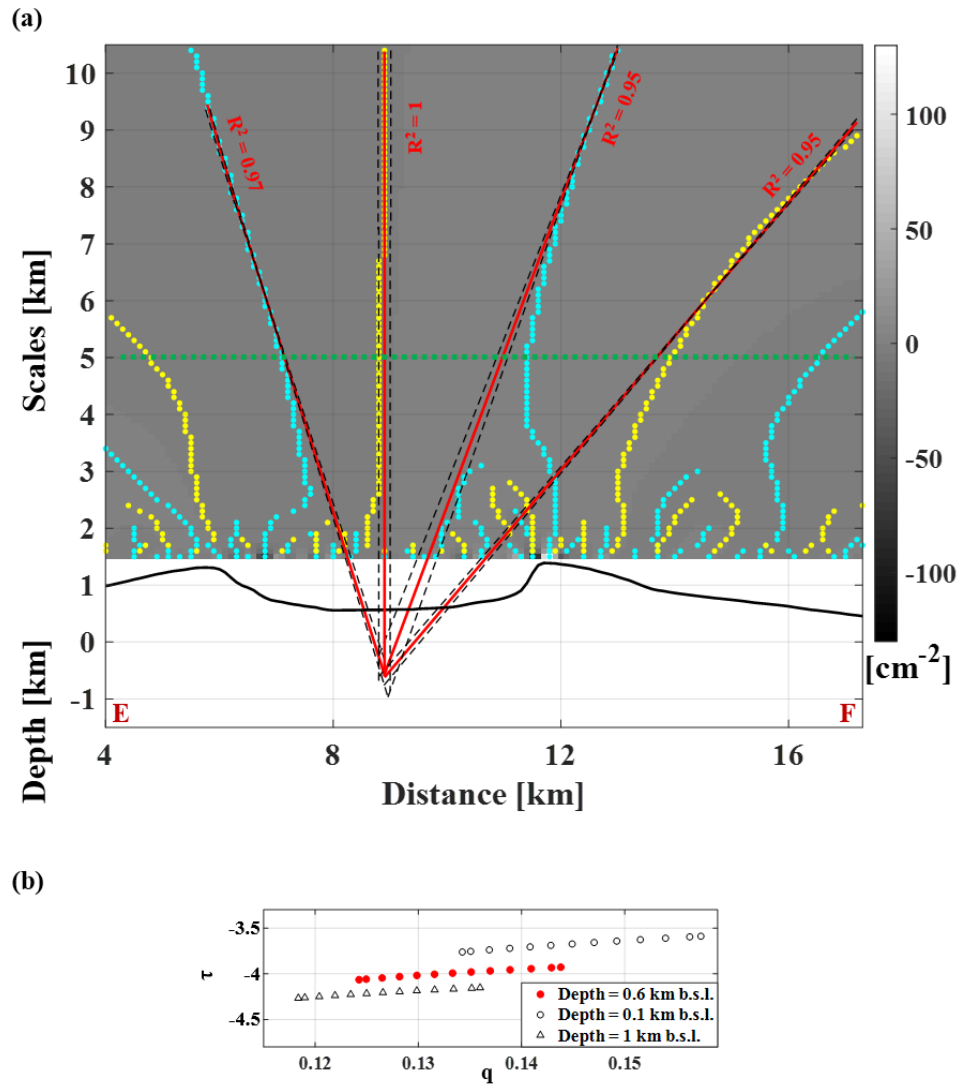


Figure 4.21. EF profile: third-order VD_F . Results of the (a) Multiridge and (b) ScalFun methods applied on the third-order VD_F of the E-W deformation; the red solid and black dashed lines represent the best-fit linear regression lines and the linear regression boundary solutions within a 95% confidence interval, respectively, while the black solid lines indicate the volcano topography and the green dashed line defines the scale below which the multi-scale dataset is surely affected by high-wavenumber noise; for each regression line, we indicate the R^2 coefficient; the red dots represent the solution using the intersection of the best fit linear regressions, while the black circles and triangles regard to the retrieved boundary solutions; $q = \frac{1}{z}$ while $\tau = \frac{\partial \log(VD_F(z))}{\partial \log z}$, where z represents the vertical scale.

In the following **Table 4.1**, we list and summarize the retrieved results for each analysed profile.

Table 4.1. “Geodetic” solutions for Fernandina volcano retrieved from the E-W deformation and its VD_f . The depth values are referred to the sea level.

PROFILE	ANALYSED TRANSFORMATION	EAST [km]	NORTH [km]	DEPTH [km]	N
AB	1^{st} -order VD_f	662.8 ± 0.2	9958.5 ± 0.2	-1.6 ± 0.3	3
	2^{nd} -order VD_f	662.8 ± 0.2	9958.5 ± 0.2	-1.6 ± 0.4	3
	3^{rd} -order VD_f	662.8 ± 0.2	9958.5 ± 0.2	-0.5 ± 0.3	2
CD	1^{st} -order VD_f	662.7 ± 0.1	9958.8	-1.7 ± 0.5	3
	2^{nd} -order VD_f	662.8 ± 0.1	9958.8	-1.6 ± 0.4	3
	3^{rd} -order VD_f	662.7 ± 0.1	9958.8	-0.6 ± 0.5	2
EF	1^{st} -order VD_f	662.7 ± 0.2	9959.3 ± 0.1	-1.7 ± 0.5	3
	2^{nd} -order VD_f	662.5 ± 0.2	9959.3 ± 0.1	-1.6 ± 0.4	3
	3^{rd} -order VD_f	662.5 ± 0.2	9959.3 ± 0.1	-0.6 ± 0.5	2

4.5 Integrated multi-scale methods: the Yellowstone caldera (Wyoming, USA) analysed with cumulative vertical deformation.

Yellowstone caldera represents a volcanic field formed by three massive caldera-forming eruptions, around 2.1, 1.3 and 0.64 Ma. After the last eruption, the Mallard Lake (ML) and Sour Creek (SC) structural resurgent domes formed in the South-western and North-eastern caldera areas. In the last 0.64 Ma, the caldera floor has been characterized by covering of rhyolitic lava flows, while outside the caldera, especially towards North and South, basaltic eruptions occurred [Christiansen, 2001]. The high convective ground water circulation affects this volcanic area and widespread hydrothermal systems with geysers, as the Norris Geysers Basin (NGB), hot springs and fumaroles testify to this feature [Fournier, 1989]. Geodetic techniques, as precise levelling, GPS and DInSAR reveals the occurrence of inflation and deflation cycles [Wicks et al., 2006; Puskas et al., 2007; Chang et al., 2007; Chang et al., 2010; Aly and Cochran 2011; Tizzani et al., 2015] and the migration of the deformation between both the resurgent domes [Wicks et al., 1998], with variable deformation rates during the years.

The volcanic mechanisms of the observed deformation at Yellowstone caldera are mainly based on hydrothermal phenomena or magmatic ones, which retrieved source depths should be shallower or deeper than the brittle-ductile transition, respectively. Concerning to the magmatic model, the authors [Wicks et al., 2006; Puskas et al., 2007; Vasco et al., 2007; Chang et al., 2007; Chang et al., 2010; Aly and Cochran 2011; Tizzani et al., 2015] have proposed geodetic solutions by using parametric inverse procedures for GPS, DInSAR and leveling measurements and providing different results for ML and SR resurgent domes. Indeed, for Chang et al. [2007; 2010] the source of deformation is a single tabular body at 6 – 16 km ranging depth beneath the caldera, while Aly and Cochran [2011] considered two point sources and one tabular body, with variable depth between 10 and 18 km below the caldera, for modeling the ML, SR and the area between them. Finally, Tizzani et al. [2015] proposed as best fitting geodetic solution a model with two prolate spheroids located beneath the brittle-ductile transition for ML and SR, respectively.

However, the 3D P-wave velocity model proposed by Farrell et al. [2014] images an unique magmatic body corresponding with a low velocity zone just below both ML and SR and at locally variable depth from 5 to 15 km b.s.l..

We specify another deformation pattern occurs at the northern caldera rim, at NGB, for which a hydrothermal model is often considered [Wicks et al., 2020].

In this framework, we apply the integrated multi-scale approach, i.e. Multiridge, ScalFun methods and THD technique, to study the geometrical features of the active deformation sources for ML and SR resurgent domes. In particular, we analyse the 2005-2007 uplift event by assuming that its cumulative vertical deformation satisfies the Laplace's equation and the local-homogeneity law.

The considered dataset (not published yet) consists of SAR images acquired by the ERS-1/2 (31) and ENVISAT (22) sensors from June 1992 to May 2007 and from May 2005 to September 2010, respectively, along both the ascending and descending orbits. The DInSAR – SBAS technique [Berardino et al., 2002; Pepe et al., 2005; Lanari et al., 2007] is used to process the dataset; the differential interferograms are computed after the estimation of the topographic phase components [Franceschetti and Lanari, 1999] by considering precise satellite orbital information and the three-arc sec Digital Elevation Model (DEM) of the study area, retrieved by the Shuttle Radar Topography Mission (SRTM) [Rosen et al., 2001]. In addition, a complex multilook operation [Rosen et al., 2000], with four and twenty looks in the range and azimuth directions, respectively, and an advanced multitemporal noise-filtering process [Yang et al., 2013], for mitigating the noise decorrelation effects [Zebker and Villasenor, 1992; Bamler and Hartl, 1998], has been applied. The original phase signals are then retrieved by using the Extended Minimum Cost Flow phase unwrapping procedure [Pepe and Lanari, 2006]. Finally, the SBAS algorithm provides the 2013-2010 mean velocity maps and the time-series in terms of LOS projection of the deformation along both the ascending and descending orbits, from which the incoherent pixels were excluded [Pepe and Lanari, 2006] and the displacement rate related to the North American Plate were removed.

We show both the ascending (**Figure 4.22a**) and descending (**Figure 4.22b**) LOS mean velocity maps as relative deformation respect to a stable reference pixel (black filled triangle in **Figure 4.22a-b**) located at the North-western part of the region. For both the orbits, we observe the NGB area moves away from the satellite, while the ML and SR resurgent domes tends to get closer to it, with a maximum deformation rate of 4 cm/yr (**Figure 4.22a-b**). This evidence reveals that the movement is predominantly vertical.

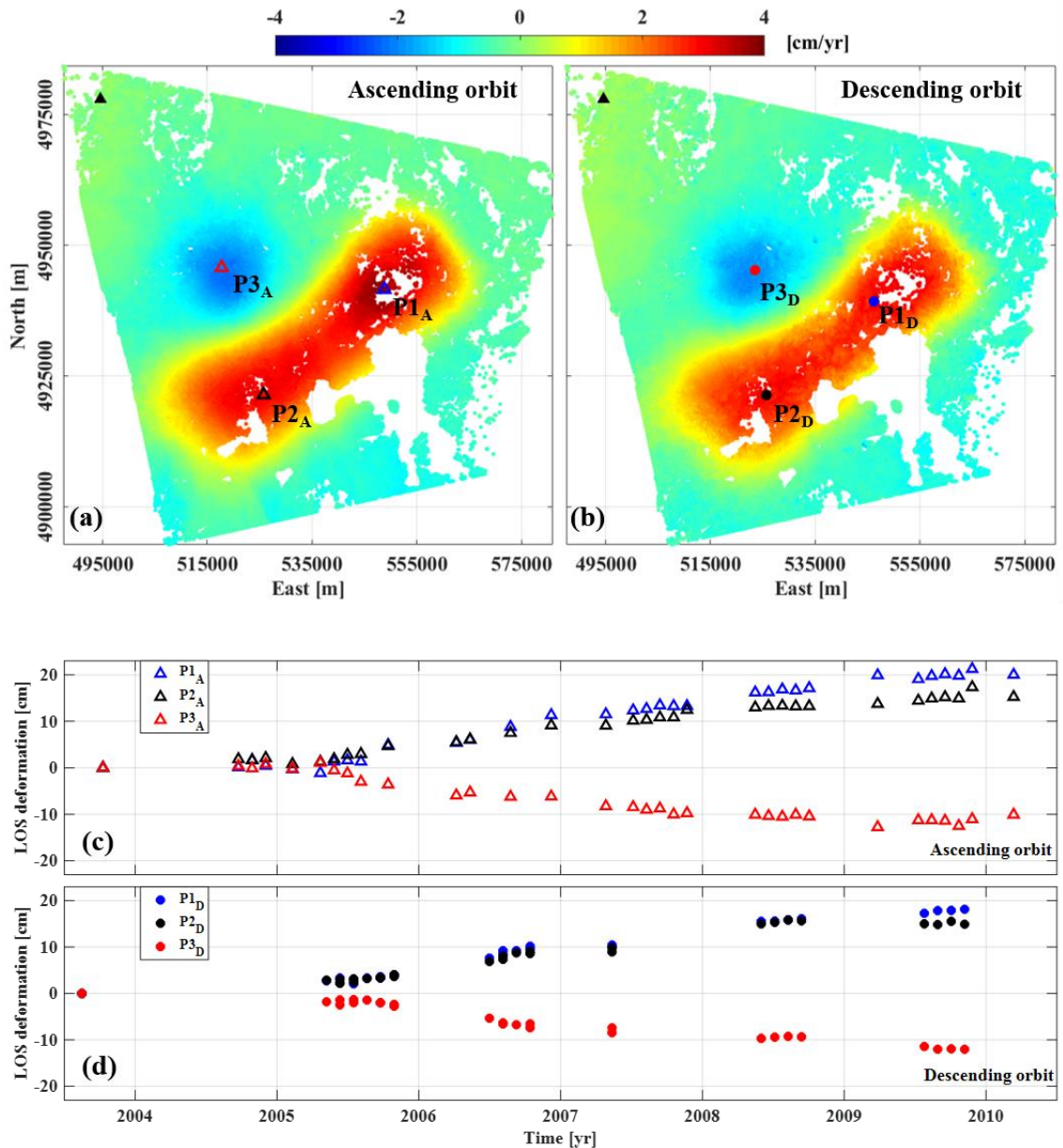


Figure 4.22. LOS data and mean velocity maps at Yellowstone caldera. Maps of the mean (a) ascending and (b) descending velocity [cm/yr] related to the 2003.5-2010 time interval for Yellowstone caldera; the black filled triangles indicate the reference pixel location, while the blue, black, red empty triangles, and the blue, black, red dots correspond to the location of P1_A, P2_A, P3_A, and P1_D, P2_D, P3_D pixels, respectively, along which the time-series are displayed; measured deformation values along the (c) ascending and (d) descending orbits during the 2003.5-2010 time interval at P1_A, P2_A, P3_A, and P1_D, P2_D, P3_D pixels, respectively.

We display the temporal behaviour of the LOS deformation pattern by selecting the pixels characterized by the maximum mean velocity around SR, P1_A (blue empty triangle in **Figure 4.22a**) and P1_D (blue dot in **Figure 4.22b**), ML, P2_A (black empty triangle in **Figure 4.22a**) and P2_D (black dot in **Figure 4.22b**), and NGB, P3_A (red empty triangle in

Figure 4.22a) and $P3_D$ (red dot in **Figure 4.22b**), for both the ascending (**Figure 4.22c**) and descending (**Figure 4.22d**) orbits. We notice the three areas reflect the same deformation trends, but with different rate during the considered time (**Figure 4.22c-d**).

To analyse the field in terms of E-W and vertical deformation, the ascending and descending LOS measurements are combined according to a pixel-by-pixel procedure based on the individuation of the coherent ones in both the mean velocity maps [Manzo et al., 2006]. Before this, the time-series have been resampled to a common temporal sampling interval [Del Negro et al., 2013], since no intrinsically non-linear events (i.e., eruptions) occur.

The mean vertical (**Figure 4.23a**) and E-W (**Figure 4.23b**) velocity maps show a comparable deformation rate respect to the previous ones in terms of intensity (i.e., 4 cm/yr). In particular, ML and SR are in uplift and they move toward East, while a subsidence phenomenon characterizes NGB, that moves toward West (**Figure 4.23a-b**). Also, we show the field patterns during the time at the pixels characterized by the maximum mean velocity around SR, $P1_V$ and $P1_H$ (black empty triangles in **Figure 4.23a-b**, respectively), ML, $P2_V$ and $P2_H$ (black dots in **Figure 4.23a-b**, respectively), and NGB, $P3_V$ and $P3_H$ (black stars in **Figure 4.23a-b**, respectively), for both the vertical (**Figure 4.23c**) and E-W (**Figure 4.23d**) components, respectively. We notice the three areas reflect the same deformation trends highlighted by the mean velocity, but with different rate during the considered time for both the components (**Figure 4.23c-d**). We observe that uplift phenomena characterize ML and SR resurgent domes, while a subsidence one affects the NGB area (**Figure 4.23c**). However, SR tends to move toward East during almost all the considered time interval, while different E-W trends seem to characterize the ML and NGB zones (**Figure 4.23d**).

For these reasons, we decide to analyse only the vertical component of the ground deformation field since it shows more definite and constant trends. Specifically, we focus on the 2005-2007 uplift event, which is characterized by the highest velocity (orange vertical continuous lines in **Figure 4.23c**).

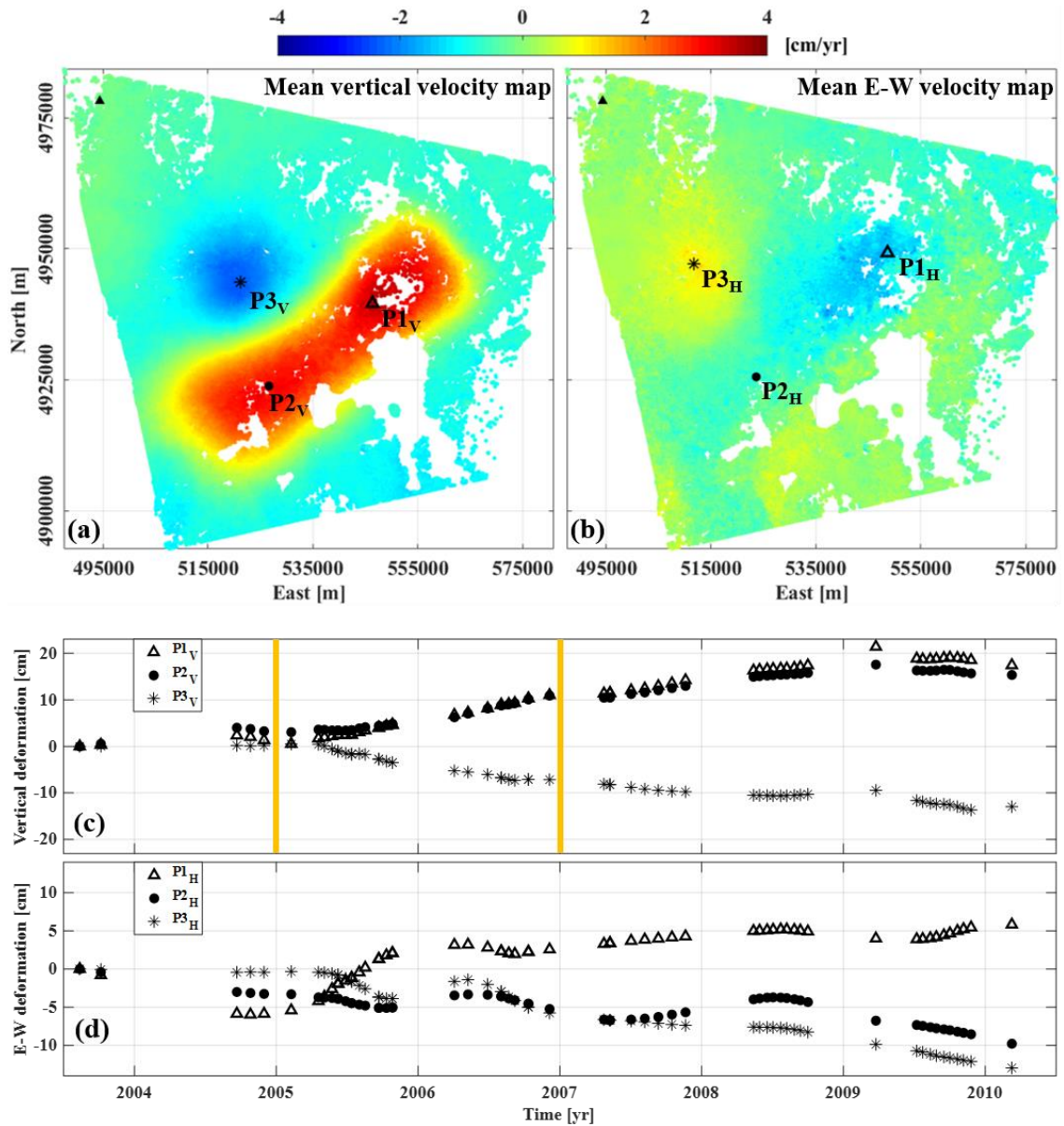


Figure 4.23. Mean velocity maps and deformation components at Yellowstone caldera. Maps of the mean (a) vertical and (b) E-W velocity [cm/yr] related to the 2003.5-2010 time interval for Yellowstone caldera; the black filled triangles indicate the reference pixel location, while the black empty triangles, the black dots, the black stars correspond to the location of P1_v and P1_h, P2_v and P2_h, P3_v and P3_h pixels, respectively, along which the time-series are displayed; measured (c) vertical and (d) E-W deformation values during the 2003.5-2010 time interval at P1_v, P2_v, P3_v, and P1_h, P2_h, P3_h pixels, respectively; the orange vertical continuous lines represent the selected temporal period for performing the proposed analysis.

Therefore, we calculate the cumulative vertical deformation occurred during the 2005 – 2007 time interval and, after a gridding operation by considering the natural neighbor interpolator with 0.1 km of sampling step along both the x - and y -directions,

we apply the constant-level reduction procedure, which flat scale is chosen to be at 4 km a.s.l.. We show the retrieved processed data in **Figure 4.24**.

To compare our results with the aforementioned ones, we study the ML and SR uplift regions by considering five profiles as spatially distributed in **Figure 4.24** (black and blue dashed lines).

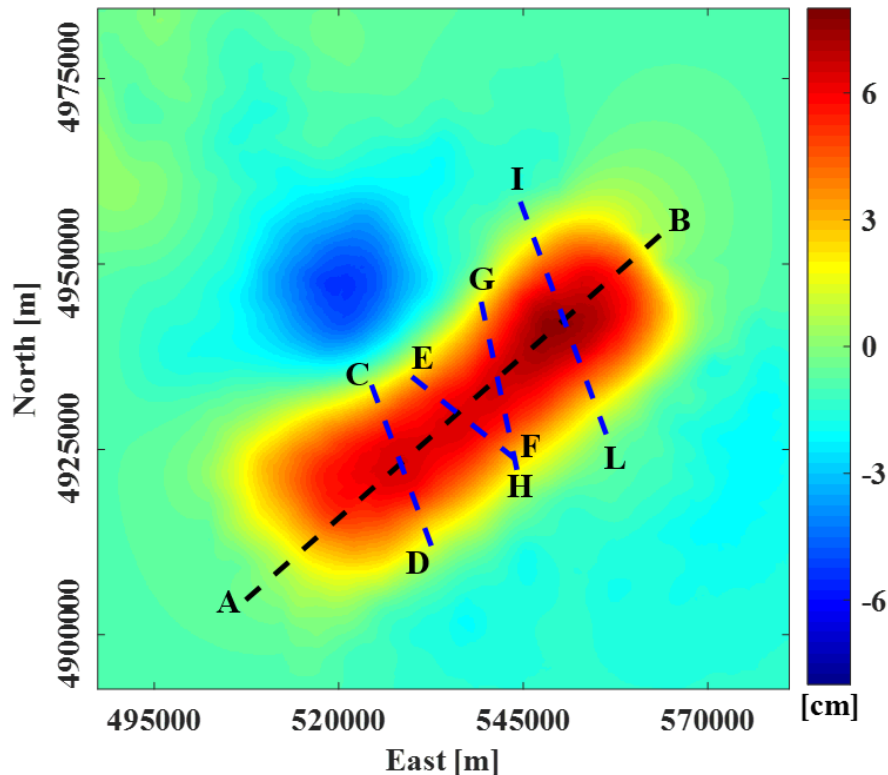


Figure 4.24. Processed 2005-2007 cumulative vertical deformation. Map of the vertical component [cm] of the ground deformation field measured at Yellowstone caldera in the 2005-2007 time interval; the original data is gridded by considering the natural neighbor interpolator with 0.1 km of sampling step along both the x - and y -directions and, then, the constant-level reduction procedure is applied to 4 km a.s.l.; the black dashed line and the blue ones represent the profiles location along which the results of Multiridge and ScalFun methods are displayed by performing the field and its second-order VD_F analyses, respectively.

We remark that the ridges are representative of the best-fit linear regressions within a 95% confidence and that we calculate the determination coefficient R^2 as a statistical measure of how the multiridge subsets are close to the fitted regression line (ridges). We also evaluate the solution uncertainties (intersection at the ridges) by considering the error on the best-fit linear regression coefficients (intercept and slope constants) and, for each

analysis, we report with the green dashed lines the scale below which the multi-scale dataset is surely affected by high-wavenumber noise.

The first considered profile is the SW – NE oriented AB profile passing through both the local deformation anomalies of ML and SC (black dashed line in **Figure 4.24**). We apply the Multiridge and ScalFun methods to the field component ($p = 1$) by considering 9 km a.s.l. as maximum scale for the multi-scale dataset, with 0.2 km of continuation sampling. The results show two possible “geodetic” sources: the first one, beneath ML, is located at 9.8 ± 1 km b.s.l. in the point with coordinate $524200 \text{ E} \pm 500 \text{ m}$, $4919400 \text{ N} \pm 500 \text{ m}$ (blue continuous lines in **Figure 4.25a**); the second one is located 9.1 ± 1.6 km b.s.l. deep beneath SR at the coordinates point $550600 \text{ E} \pm 1000 \text{ m}$, $4942500 \text{ N} \pm 1000 \text{ m}$ (red continuous lines in **Figure 4.25a**). Both the sources reflect values of $n \sim -2$ (**Figure 4.25b-c**) and, since $p = 1$, $N \sim 3$ (**Table 2.1**).

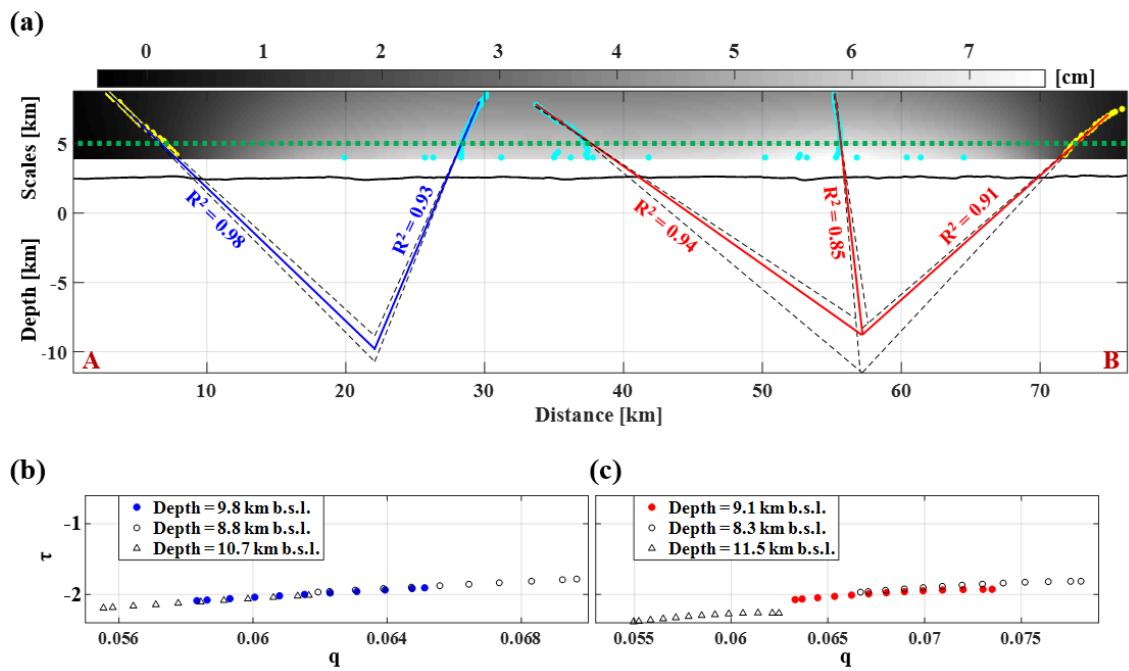


Figure 4.25. Analysis of the vertical deformation. Results of the Multiridge method applied on the (a) 2005-2007 vertical cumulative deformation; the coloured solid and black dashed lines represent the best-fit linear regression lines and the linear regression boundary solutions within a 95% confidence interval, respectively, while the black solid lines indicate the caldera topography and the green dashed lines define the scale below which the multi-scale dataset is surely affected by high-wavenumber noise; for each regression line, we indicate the R^2 coefficient; results of ScalFun method for the (b) first and (c) second retrieved intersections by Multiridge method; the coloured dots represent the solution of the best fit linear regressions, while the black circles and triangles regard to the retrieved boundary ones; $q = \frac{1}{z}$ while $\tau = \frac{\partial \log(w(z))}{\partial \log z}$, where w and z represent the vertical deformation and the vertical scale, respectively.

We consider the second-order VD_F ($p = 3$) of the same vertical deformation to analyse the other four profiles (blue dashed line in **Figure 4.24**), which transversely cross the AB one, by considering ~ 12 km as maximum scale for the multi-scale dataset, with 0.2 km of continuation sampling.

We briefly report the results (**Figure 4.26**): from the CD profile, passing through the ML resurgent dome, we individuate one ridges intersection to the depth of 6.9 ± 0.6 km b.s.l. at the coordinates point $528250 \text{ E} \pm 200 \text{ m}$, $4923500 \text{ N} \pm 200 \text{ m}$ (**Figure 4.26a**), characterized by a locally stable values of $n \sim -2.6$ (**Figure 4.26e**) and $N \sim 1.6$; from the EF profile, passing between the ML and SR resurgent domes, we individuate one ridges intersection to the depth of 7.5 ± 0.5 km b.s.l. at the coordinates point $536600 \text{ E} \pm 200 \text{ m}$, $4929500 \text{ N} \pm 200 \text{ m}$ (**Figure 4.26b**), characterized by a locally stable values of $n \sim -2.6$ (**Figure 4.26f**) and $N \sim 1.6$; from the GH profile, also passing between the ML and SR resurgent domes, we individuate one ridges intersection to the depth of 8 ± 0.4 km b.s.l. at the coordinates point $541600 \text{ E} \pm 200 \text{ m}$, $4933950 \text{ N} \pm 200 \text{ m}$ (**Figure 4.26c**), characterized by a locally stable values of $n \sim -2.55$ (**Figure 4.26g**) and $N \sim 1.55$; finally, from the IL profile, passing through the SR resurgent dome, we individuate one ridges intersection to the depth of 6 ± 0.6 km b.s.l. at the coordinates point $550600 \text{ E} \pm 200 \text{ m}$, $4942200 \text{ N} \pm 200 \text{ m}$ (**Figure 4.26d**), characterized by a locally stable values of $n \sim -2.4$ (**Figure 4.26h**) and $N \sim 1.4$.

In the **Table 4.2**, we list and summarize the retrieved results for each profile.

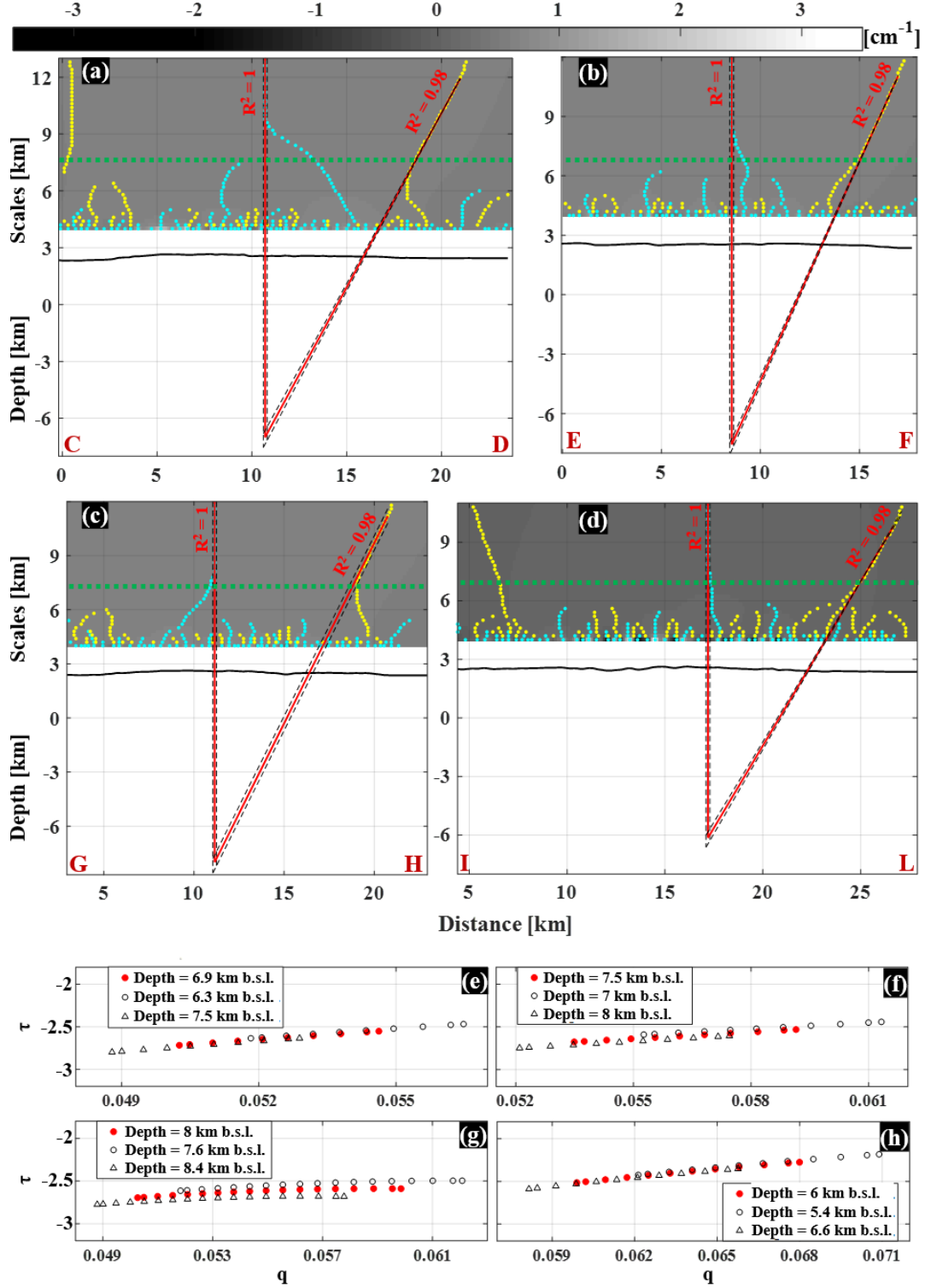


Figure 4.26. Analysis of the second-order VD_F . Results of (a-d) Multiridge and (e-h) ScalFun methods for the CD, EF, GH and IL profiles; the red solid and black dashed lines represent the best-fit linear regression lines and those of the boundary solutions within a 95% confidence interval, respectively, while the black solid lines indicate the caldera topography and the green dashed lines define the scale below which the multi-scale dataset is surely affected by high-wavenumber noise; for each regression line, we indicate the R^2 coefficient; the red dots represent the solutions of the best fit linear regressions, while the black circles and triangles regard to the retrieved boundary solutions; $q = \frac{1}{z}$ while $\tau = \frac{\partial \log(VD_F(z))}{\partial \log z}$, where z represents the vertical scale.

Finally, we consider the THD technique for the boundary analysis of the deformation sources. We apply this technique on the 2005-2007 cumulative vertical deformation, and we map the results, THD_w , in **Figure 4.27**.

THD shows clear extreme alignments, whose seems to delineate the presence of a single 50×20 km extended body (blue dashed lines in **Figure 4.27**). In particular, the maxima intensity increases at NE and NW respect to the caldera. We specify the results related to the southern part of the caldera are strictly depending on the data spatial distribution.

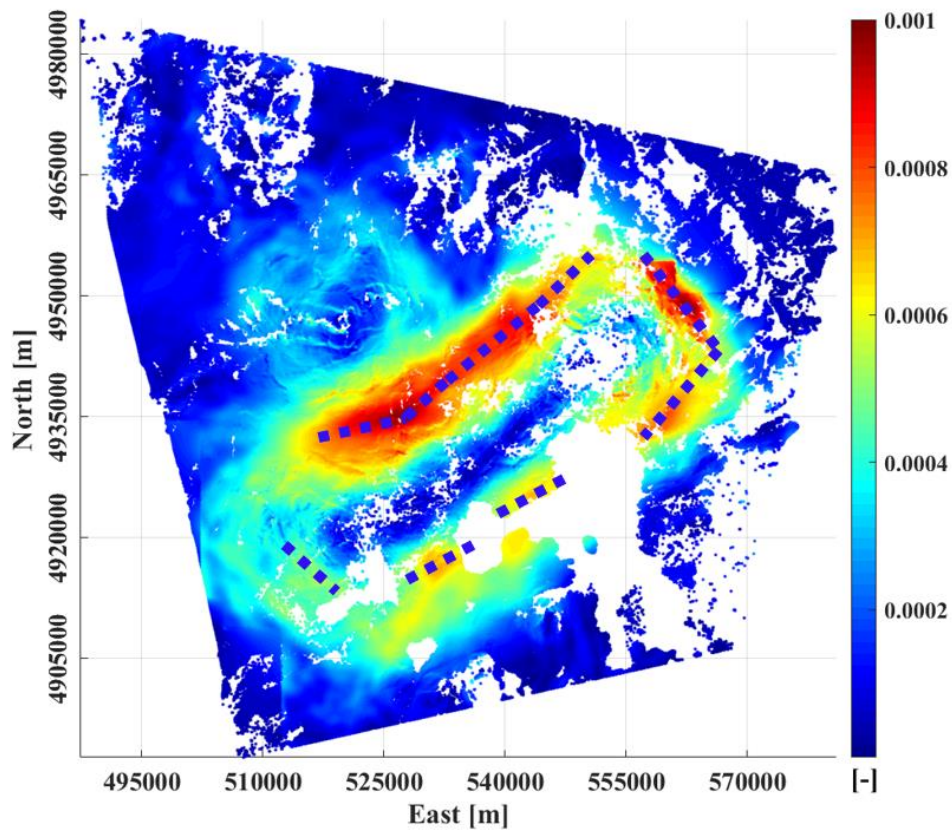


Figure 4.27. THD_w results at Yellowstone caldera. Results of THD_w [-] calculated on the 2005-2007 cumulative vertical component of the ground deformation field measured at Yellowstone caldera. The blue dashed lines follow the main maxima alignments.

Table 4.2. “Geodetic” solutions for resurgent domes at Yellowstone caldera from the analysis of the vertical deformation and its VD_F . The depth values are referred to the sea level.

PROFILE	LOCATION	EAST [km]	NORTH [km]	DEPTH [km]	N
AB	ML	524.2 ± 0.5	4919.4 ± 0.5	-9.8 ± 1	3
AB	SR	550.6 ± 1	4942.5 ± 1	-9.1 ± 1.6	3
CD	ML	528.25 ± 0.2	4923.5 ± 0.2	-6.9 ± 0.6	1.6
EF	Between domes	536.6 ± 0.2	4929.5 ± 0.2	-7.5 ± 0.5	1.6
GH	Between domes	541.6 ± 0.2	4933.95 ± 0.2	-8 ± 0.4	1.55
IL	SR	550.6 ± 0.2	4942.2 ± 0.2	-6 ± 0.6	1.4

CHAPTER 5

DISCUSSION

We propose and validate an integrated multi-scale approach for modeling volcanic deformation sources by DInSAR measurements; in particular, we consider the Multiridge, ScalFun and THD methods to retrieve information on geometrical parameters of the causative bodies.

Modeling volcanic deformation sources is commonly accomplished with inverse methods and the use of the AM. This approach is mostly based on the general solution of the elastic problem, which describes the deformation field as a biharmonic but non-harmonic function. Many problems affect these procedures, including the inherent ambiguity, the theoretical ambiguity, the choice of a priori information and the availability of constraints. Moreover, the inverse methods and the AM may not well approximate the real physical scenario. This approach however represents the fastest way allowing an acceptable modeling of the volcanic deformation sources.

We studied the integrated multi-scale approach; we prove its validity in the case of a volcanic region approximated by hydrostatic pressure variation within the source embedded in a homogeneous elastic half-space. In this physical scenario, we can indeed use Multiridge, ScalFun and THD methods to retrieve unambiguous solutions in terms of depth, horizontal position, shape, and horizontal extent of the deformation sources. This information represents a reliable source model, which can be also used as constraint for a subsequent inverse modeling, characterizing the volcanic system from both geometrical and physical point of views.

We demonstrate that the proposed methods do not require defining complex forward and inverse problems, do not depend on the distribution of the medium elastic parameters within the elastic regime (i.e., small variations of the elastic parameters), and are stable vs. noise; they are also crucial in case of a single component availability and for multi-source scenarios, while their solutions only depend on the harmonic properties of the analysed field, which has to satisfy the Laplace's equation. We remark that Laplace Equation is surely satisfied in the case of hydrostatic pressure variation of a source embedded in a homogeneous elastic half-space, which often also characterize the AM expressions.

However, some general limitations affect the proposed approach, as the sampling ambiguity, experimental/instrumental errors, the scale, and the high gradients of the measurement surface.

In addition, we also consider the homogeneity and local-homogeneity properties of harmonic deformation field. Specifically, the first one allows the analysis of sources whose field properties do not particularly vary with the scale, while the second one allows studying volcanic bodies with a geometrically irregular shape. Moreover, we introduce the VD_F to emphasize the high-wavenumber contributions to the signal.

In the following paragraphs, we report some comments about the use of the proposed approaches on the already described simulated and real ground deformation field, highlighting their advantages and limitations.

5.1 Comments on the applications to the synthetic cases.

3D finite bodies often represent the volcanic reservoirs, and, in many cases, regular geometries can approximate them. The simplest model of magma chamber is the spherical source, for which the Mogi's model [Mogi, 1958] is widely used; volcanic mechanisms as ascent pipes or sills/dikes emplacement are instead modeled with the Yang's [Yang and Davis, 1988] or Okada's [Okada, 1985] AM, respectively. Therefore, we performed many tests to study these sources with the Multiridge and ScalFun methods and by resorting to the FEM environment, to accurately reproduce fields which satisfy the Laplace's equation.

We first consider the vertical deformation analysis and the Sphere Case (**Figure 3.2**), for which the ridges have constant slopes vs. scale: ridges exactly converge to the centre of the body (green dashed lines in **Figure 3.2e**). Indeed, the spherical source is the common example of source distribution having its support in its centre at any considered scale, that is typical of the ideal source with $N \sim 3$ (**Table 2.1**) according to the homogeneity law. The ScalFun analysis confirms this result by providing values of $n \sim -2$ (green stars in **Figure 3.2f**) and, in turn, $N \sim 3$ (**Table 2.1**). Indeed, the spherical source, as expressed by the Mogi's model, is the most evident example of inherent ambiguity of the deformation field, for which an unambiguous model about its radius, its pressure variation and the half-space physical parameters cannot be achieved.

In the Ellipsoid 2 Case (**Figure 3.2**), that is representative of the ascent pipe mechanisms and of the Yang's AM, we can define two sets of ridges because these last change their slope with the scale; in particular, at low scales they tend to intersect nearby the top of the source (red dashed lines in **Figure 3.2e**), that is at its shallowest singular point, while, at larger scales, the ridges tend to converge to the source centre (red continuous lines in **Figure 3.2e**) and their features are similar to those of the Sphere Case (green dashed lines in **Figure 3.2e**). This is consistent with the asymptotic expression of the multipolar expansion of potential fields, for which, at large scales, the field behaviour is like that of a point ideal source. The ScalFun methods indeed provides values of $n \sim -2$ (red stars in **Figure 3.2f**) and, in turn, $N \sim 3$ (**Table 2.1**). Moreover, we can make similar comments for the Ellipsoid 1 Case (**Figure 3.2**).

The change of the ridge slopes with the scale also occurs in the Prism 2 Case (**Figure 3.3**), which we consider for representing mechanisms of sill emplacement and the

Okada's AM. In particular, at low scales the ridges are strongly affected by the body edges, that are the singular points of the sources, while, at larger ones they exactly intersect to the source centre (red continuous lines in **Figure 3.3e**) since the multipolar terms of the field expression vanish with the scale increase; we indeed characterize this last depth estimate by ScalFun method with values of $n \sim -2$ (red stars in **Figure 3.3f**) and, in turn, $N \sim 3$ (**Table 2.1**). The results of the Prism 1 and Cube Case (**Figure 3.3e-f**) are also consistent with the asymptotic expression of the multipolar expansion of potential fields: they indeed show how the deformation field tend to that of a point ideal source with the decrease of the bodies extent, which acts as the scale increase.

Similar comments arise from the analysis of the E-W components, for which we only show the results of the Ellipsoid 2 and Prism 2 cases (**Figure 3.4**).

At this stage, we use the VD_F of the field since it allows enhancing the high-wavenumber contributions of the signal and, in turn, the multipolar terms of the field expressions. For this reason, we only consider the Ellipsoid 2 and Prism 2 cases, which are a good approximation of linear and planar ideal sources, respectively.

For the Ellipsoid 2 Case, we apply the Multiridge and ScalFun analysis on the first-order VD_F (**Figure 3.5**), observing that the central ridges just intersect at the source top (blue continuous lines in **Figure 3.5e**). The ScalFun analysis provides value as $n \sim -2$ (blue stars in **Figure 3.5f**), which corresponds to $N \sim 2$ since $p = 2$. This is in accordance with the homogeneity law (**Table 2.1**), for which this value characterizes the linear source and the depth estimate by Multiridge refers to its top. Therefore, although this body is only an approximation of ideal sources, as can also be seen from the intersection nearby the centre of the ridges far from the source (blue dashed lines in **Figure 3.5e**), the use of the VD_F allows deriving crucial morphological information of the causative body by highlighting the multipolar terms of the field expression that, in this case, are related to the source top. Indeed, we can correctly interpret the field as generated by a vertical elongated source at the expected depth.

We can make similar comments for the Prism 2 Case (**Figure 3.5**), where we consider the second-order VD_F by observing the intersections of the ridges nearby the body edges (red continuous lines in **Figure 3.5e**). We characterize these solutions by ScalFun method with values of $n \sim -2$ and $N \sim 1$ (**Table 2.1**) since $p = 3$ (red stars in **Figure 3.5f**). This result agrees with the homogeneity law, for which $N \sim 1$ arises by considering the edges

depth of planar sources. Therefore, also in this case we can correctly interpret the field as generated by a planar source, although the modeled field is just an approximation of the homogeneous ones.

Such observations are also valid for the E-W deformation, as shown in **Figure 3.6**.

These tests show that Multiridge and ScalFun methods are valid tools to study deformation sources since they provide the horizontal position of the bodies and their depth to the centre, whose estimate is affected by 6.7 % error in the worst case. However, we note that this value has characterized the Ellipsoid 2 Case analysis, where the difference between the estimated and expected values is equal to 0.2 km, that is less than the sampling step of the modeled dataset. Moreover, the use of the VD_F also provides information about the shape of the considered source, and the position of its top/edges, with a difference between the observed and expected parameters of only 0.1 km, in the worst considered case, and less than the sampling step of the dataset. Regarding the ScalFun method, the maximum retrieved discrepancies between the observed and expected n value correspond to an approximation of 0.07 respect to integer expected number. However, this last also occurs because the modeled bodies approximate the ideal sources.

We conclude the tests of the regular sources with the application of the THD method for both the low- and large-scale cases for the detection of the source horizontal sizes (**Figure 3.7**). The results confirm a well-known limitation of this technique since it provides an overestimation of the horizontal extent of field sources that increases vs. the scale. We again point out that the accuracy of the THD outcomes also depend on the data sampling.

In the case of volcanic reservoirs of geometrically irregular sources, we need to use the generalized homogeneity theory, allowing the study of complex bodies through fractional N values and the definition of the local-homogeneity properties of the inhomogeneous fields [Fedi et al., 2015]. To briefly introduce this approach, we build other tests by considering two cases of source with irregular shape (**Figure 3.8**). The results (**Figure 3.9-3.17**) show that the integrated multi-scale approach provides valid information also for these cases; specifically, we show that the Multiridge solutions related to the centre of the analysed sources, or near this last, are characterized by N values ranging from 3 to 2, while the depth estimates related to the top and the boundaries

of the bodies are described by values of N ranging from 2 to 1. Moreover, in the multi-source case characterized by only one anomalous pattern, we can distinguish the source regions from the surroundings by the retrieved unstable and not acceptable N values. Finally, the THD technique is still a supporting tool, which provides information about the source horizontal extent and the number of the active sources.

Furthermore, we discuss a last set of simulations, whose physical scenario does not satisfy the Laplace's equation. We remember that the deformation field does not enjoy the harmonic properties mainly in two cases: non-constant distribution in the space of the elastic parameters within the half-space; non-hydrostatic variation of the source pressure.

In the first case, we analyse the simple scenario of a multi-layered half-space by considering the increasing of the E parameter with the depth, acceptable within the elastic regime. We show that the proposed approach provides valid results characterized by only 5 % on the source depth estimate (**Figure 3.18**). When the variation of the medium elastic parameters is larger, the modeled system moves away from the homogeneous half-space condition, and the proposed approach can also provide source depth value with 20 % of error respect to the expected one (**Figure 3.19**).

For the second case, we consider a source with over-pressure applied only along the z -direction; this condition causes an underestimation of the source depth with the Multiridge and ScalFun methods that, in this particular simulation, is affected by 35 % error (**Figure 3.20c**). Also, the ScalFun method provides unstable results especially for the larger scales, where the error related to the upward continuation transform is as much larger (**Figure 3.20d**).

Regarding the THD technique, we consider the tensile component of rectangular source calculated by the Okada's AM. This test confirms that the THD_w (**Figure 3.21**) depends on the scale since we are able to define the horizontal extent of the body even if the generated field does not satisfy the Laplace's equation.

5.2 Comments on the applications to the real cases.

In this paragraph, we report some comments about the application of the proposed methods to the ground deformation patterns.

5.2.1 The case study of Okmok volcano.

“We use the interferogram related to the period 15 July 2003 – 29 June 2004, with images acquired by the ENVISAT satellite along the descending orbit (**Figure 4.1**). The Okmok volcano deformation field has been studied by many authors [[Lu et al., 2005](#); [Masterlark et al., 2010](#); [Biggs et al., 2010](#); [Masterlark et al., 2012](#)], which all interpreted that deformation was due to the inflation or deflation of a spherical magma chamber. In most of these studies, the source model type was a priori assumed, and the elastic parameters were fixed before inverting the data. Only in one case [[Masterlark et al., 2012](#)] did the authors use seismic tomography as a priori information to set the heterogeneous distribution of the elastic parameters. For these authors, the source depth ranged from 3.1 to 3.5 km, while the source position ranged from 690.3 km to 690.72 km for the East UTM coordinate and 5923.6 km to 5923.98 km for the North UTM coordinate (**Table 5.1**). Our results (**Figure 4.2**) are in good agreement with those of the aforementioned works, indicating a depth source equal to 3.4 ± 0.06 km and a horizontal position at 690.9 ± 0.08 km E and 5924 ± 0.07 km N (**Table 5.1**). Moreover, we estimated a Structural Index of $N \sim 3$ and, therefore, we can state that the geodetic source geometry is well represented by the point-spherical model.

Table 5.1. Source locations for the Okmok magma chamber retrieved from the DInSAR measurements.

STUDY	PERIOD	EAST [km]	NORTH [km]	DEPTH* [km]
<i>Zhong Lu et al., 2005</i>	1992-2003	690.55	5923.85	-3.2
<i>Masterlark et al., 2010</i>	1995-1997	690.72	5923.98	-3.11
<i>Biggs et al., 2010</i>	1992-2008	690.30	5923.60	-3.4
<i>Masterlark et al., 2012</i>	1995-1997	690.70	5923.91	-3.52
<i>This study</i>	2003-2004	690.90	5924.00	-3.4

*Depths are below sea level.”

From Castaldo et al. [[2018b](#)].

5.2.2 The multi-source case study of Uturuncu volcano.

“The results retrieved by the application of multi-scale approaches for the analysis of DInSAR measurements support the hypothesis of a multi-source scenario for APVC and Uturuncu volcano region. A first evidence is provided by the mean vertical velocity field (Figure 4.4a,b), which highlighted a higher deformation rate at Uturuncu respect to the pattern measured at the APVC; indeed, different deformation trends are shown at P1 and P2 selected pixels (Figure 4.4c), located at centre of APVC and at Uturuncu volcano, respectively. Specifically, the APVC area is characterized by a quasi-linear vertical deformation rate, while the P2 time-series points out a higher vertical velocity pattern between August 2006 and February 2007.

The Cross-correlation maps (Figure 4.5) remark the existence of two areas with different vertical deformation behavior both in space and in time, providing a further evidence of multi-source scenario.

Subsequently, we have used the Multiridge method to investigate the sources responsible of the observed DInSAR measurements, detecting their depths and horizontal positions. The findings about the sources location provided a better characterization of the volcanic scenario; in particular, we retrieve a depth of 18.7 ± 0.8 km (Figure 4.6), and we identify a shallow source, beneath the Uturuncu volcano, at a depth of 4.5 ± 0.5 km (Figure 4.7). To interpret our geodetic results, we take into account other information assessing the volcanic system configuration.

Regarding to the deep source, we interpret the retrieved result as referred to the APMB deformation source. To support our interpretation, we compared our results with those achieved by other works based on DInSAR measurements (Table 5.2 and Figure 5.1). In particular, the retrieved depth values and horizontal position about the APMB source are in good agreement with the findings of several geodetic modeling [Pritchard and Simons, 2004; Fialko and Pearse, 2012; Henderson and Pritchard, 2013; Hickey et al., 2013; Walter and Motagh, 2014; Gottsmann et al., 2017; Henderson and Pritchard, 2017;], as well as with petrological observations [Sparks, 2008] and geophysical studies [Pritchard et al., 2018; Chmielowski et al., 1999; Zandt et al., 2003; Kukarina et al., 2017; Ward et al., 2014; McFarlin et al., 2017; Del Potro et al., 2013; Comeau et al., 2015; Comeau et al., 2016].

Table 5.2. Summary of deformation sources. Volcanic source modeling for APMB and Uturuncu volcano retrieved from satellite geodetic measurements. Where not specified, depths are referred to sea level.

<i>Study</i>	<i>Period</i>	<i>Depth [km]</i>	<i>Source type</i>
<i>Pritchard et al.</i>	1992-2000	17.3	<i>Sphere</i>
		18.8	<i>Horizontal Ellipsoid</i>
		18.2	<i>Vertical Ellipsoid</i>
		25	<i>Point Crack</i>
		12	<i>Finite Crack</i>
<i>Fialko et al.</i>	1992-2010	> 15	<i>Prolate spheroid and tabular body</i>
<i>Henderson et al.</i>	1992-2011	19-20	<i>Point-spherical</i>
<i>Hickey et al.</i>	1996-2010	20.6 (18-25) b.g.l.	<i>Prolate spheroid</i>
		32.8 (30-35) b.g.l.	<i>Oblate spheroid</i>
		30.4 (28-33) b.g.l.	<i>Sphere</i>
<i>Walter et al.</i>	2003-2009	17-18 ± 9	<i>Inflating flat-topped body</i>
<i>Gottsmann et al.</i>	1992-2011	6-14 (top and bottom)	<i>Magmatic column</i>
		13-25 (top and bottom)	<i>APMB</i>
<i>Henderson et al.</i>	1992-2011	15.4-30.4	<i>Point source (top of a dipole source)</i>
<i>This study</i>	2005-2008	18.7 ± 0.8	<i>Deep inflation body</i>
	2006-2007	4.5 ± 0.5	<i>Shallow inflation body</i>

Several studies based on the classical procedure of geodetic modeling examine only the existence of a deep source (Table 5.2 and Figure 5.1), although [Gottsmann et al., 2017; Lau et al., 2018] suppose the existence of a shallow hydrothermal active system beneath Uturuncu volcano. In this context, our approach reveals a transient inflating shallower source, characterizing the August 2006 - February 2007 unrest event. The retrieved source location (depth 4.5 ± 0.5 km) matches with the interpretation of a hybrid system beneath Uturuncu volcano, formed by an igneous mush and fractured plutonic complex through which exsolved fluids migrate toward the surface. These fluids, being temporarily trapped, could cause an overpressured reservoir and an uplift phenomenon [Pritchard et al., 2018; Gottsmann et al., 2017]. In addition, the proposed interpretation is in accordance with the existence of low resistivity zone at this depth, explained by saline fluids of magmatic and/or meteoric origin [Comeau et al., 2015; Comeau et al., 2016]

and with the shallow anomaly achieved by geophysical and petrological data analysis [Pritchard et al., 2018 and the references within]. Moreover, the shallow overpressured source is located just beneath the cluster of the seismicity between 4 and 6 km of depth b.g.l. occurred during 2009-2010 time interval [Jay et al., 2012; Pritchard et al., 2018].

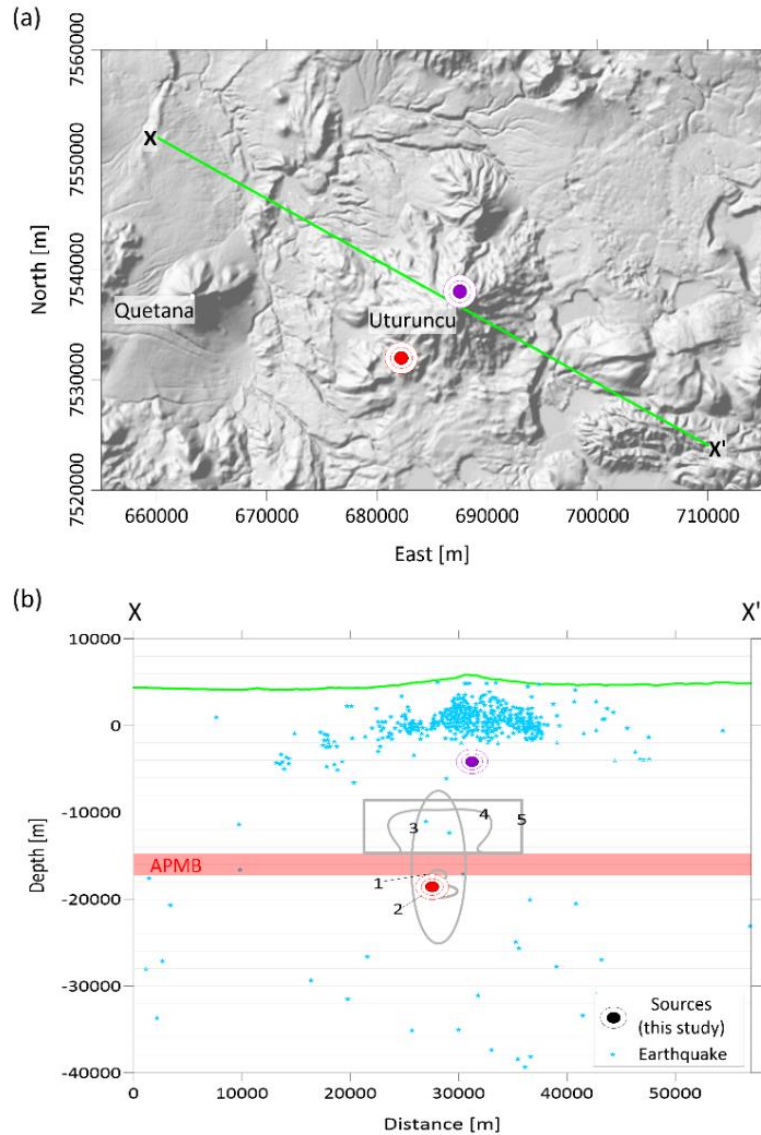


Figure 5.1. Location and depth of deformation sources. (a) SRTM DEM of the study area with the green continuous line representing the XX' trace and the red and the violet solid circles indicating the position of the deep and the shallow deformation sources, respectively; (b) XX' section redrawn from [21,23-24], in which the location and depth of retrieved deformation sources are reported; the solid blue stars represent the earthquakes location; the red solid rectangle indicates the depths to the APMB [15], while the green continuous line represents the topography; the grey continuous lines, numbered from 1 to 5, indicate the solutions proposed by 1-Pritchard and Simons [26], 2-Pritchard and Simons [26], 3-Hickey et al. [29], 4-Fialko and Pearce [27], 5-Walter and Motagh [30], respectively.”

From Barone et al. [2019].

5.2.3 The THD technique as supporting tool for Campi Flegrei caldera.

“The joint analysis of DInSAR and seismic interferometry results provides further insight into how geological structures modulate the deformation processes of the CFC caldera. The comparison of the THD_w maxima computed from the ground deformation measurements with the contrasts in the ANT group-velocity model (between 0.8 and 1.1 km/s) of different periods (0.9 s, 1.2 s and 2 s) indicates that the best spatial correlation is obtained at 1.2 s (i.e., depths of about 1km). Both the THD and ANT analyses resolve the same bi-lobed feature with an axis of symmetry along the WNW-ESE direction (**Figure 4.13b**). The distribution of the THD_w maxima intensifies toward the East of Pozzuoli and is paired by an increased group-velocity contrast of the eastern lobe (**Figure 4.13b**). A good spatial correlation between the THD_w maxima and the ANT velocity contrasts is also found in the region at West of the Pozzuoli, but this contrast is aseismic (**Figure 4.13a**) except for the 2012 deeper swarm [D’Auria et al. 2015].

The eastern THD_w maxima and the achieved ANT velocity contrasts intersect a significant hydrothermal vent near Pisciarelli, which activated in 2013 [Chiodini et al., 2015]. Sparse background seismicity between 2005 and 2016 is spread throughout the eastern CFC; however, earthquakes located at a depth of 1 ± 0.2 km (i.e., ANT 1.2 s period) are predominantly concentrated under Pisciarelli, just east of the boundary retrieved by THD and ANT technique (**Figure 4.13b**). The most relevant aspect of our study is thus that the eastern structure lineaments detected by the ANT at 1km of depth are the only dynamically-active structures in the considered period, as they show (1) high rates of the ground deformation (see THD_w maxima) and (2) earthquakes concentrated on the eastern side of the THD_w maxima (**Figure 4.13b**).

The high velocity contrasts and high values of THD_w (corresponding to the boundaries of the source of deformation) mark the secondary deformation source (depth of ~1 km) modeled by Amoruso et al. [2014] at Solfatara/Pisciarelli (**Figure 4.11**). This region of secondary deformation and seismicity corresponds to volcanic vents last active in 1982-84 [Vilardo et al., 2010; Vitale et al., 2014; De Siena et al., 2017b]. We infer that during the 2011-2013 unrest the shallower secondary source of deformation and seismicity recorded at Solfatara is the result of a structural effect, triggered by pressure/thermal gradient [Chiodini et al., 2015] and induced stress produced by the primary deformation source [Amoruso et al. 2014]. The structures modulating stress, secondary deformation, and seismicity, are likely those in the shallower part of the high-

V_p (>4.4 km/s), low V_p/V_s (<1.45) and low-scattering body recently imaged by Calò and Tramelli [2018] under the eastern sector of the caldera.

Several authors have shown the significant role played by pre-existing tectonic structures [Orsi et al., 1999, De Natale et al., 2006; Trasatti et al., 2008; Manconi et al., 2010], horizontal interfaces [Amoruso et al. 2014; D'Auria et al., 2015; Vanorio et al., 2015] and/or cold magmatic intrusions (Chiodini et al., 2015) on the modulation of the ground deformation pattern at CFC. This role is confirmed by our maps and becomes crucial to understand the stress variations due to magmatic intrusion within sills [Amoruso et al. 2014], contributing to the dynamic assessment of vent opening probability at CFC [Giudicepietro et al, 2016]. The spatial distribution of the anomalies (Figure 4.13b) indicates that these shallower structures are able to channel fluids in the Solfatara/Pisciarelli area, where they produce stress and propagate to surface along almost-vertical structures. This inference is supported by the high-resistivity vertical plume recently imaged by audiomagnetotellurics studies under Solfatara [Siniscalchi et al. 2019]; this plume coincides with the boundaries retrieved by THD and ANT techniques, with the 1km seismicity concentrated east of it. In this scenario, the source boundaries at depth overlap to the pre-existing tectonic structures due to the magma and/or hydrothermal fluids predisposition to fill the voids during the unrest events. The fluids travel from the central feeder-pathway through the fractures to the eastern part of the caldera; here, they are ultimately channeled by the high-velocity structures to (1) activate vents at the end of the unrest (Pisciarelli, Figure 4.12); (2) produce the vertical high-resistive plume [Siniscalchi et al. 2019]; (3) enhance the secondary deformation source depicted by the THD analysis [Amoruso et al., 2014]. In summary, our results and published literature depict Solfatara as an almost-vertical very-low rigidity, low-velocity, highly-fractured zone [D'Auria et al. 2015; Di Luccio et al 2015; Isaia et al. 2016; Siniscalchi et al. 2019], dynamically stressed from the west or SW at least since the 1982–1984 crisis [De Siena et al. 2017].

The shape of the low-velocity anomaly at ~1km is comparable with that retrieved by gravity and magnetic fields data analysis in the past [Florio et al., 1999]; especially in its northern boundary it spatially corresponds to an alignment of maxima obtained by using these techniques in the offshore caldera. This correlation suggests that a similar boundary may be present offshore, on the SW side of the anomaly. Nevertheless, the

resolution of the seismic tomography images is much lower offshore [De Siena et al. 2018], while the SAR measurements are of course missing.

The main evidence against the existence of a setting similar to that at Solfatara across the western onshore boundaries retrieved by THD and ANT techniques (e.g. Monte Nuovo, the location of the last eruption at CFc, De Vito et al. [2016]) is the absence of recorded seismicity between 0 and 2 km. This absence can be affected by the sparser distribution of station in the western caldera but agrees with the weaker volcanic activity, e.g., at Mofete, with respect to Solfatara. The only seismic activity of the last 15 years detected in the western caldera is the September 7th, 2012, magmatic swarm. The swarm was located at a depth of ~3 km (red circles in **Figure 4.13a**) and at the boundary between the high-velocity anomaly at Monte Gauro and the low-velocity primary anomaly [De Siena et al. 2018]. Its occurrence corresponded to a local increase in the shear stress, modeled by the inflation of a sill-shaped reservoir located a depth of 2.5-3.1 km [D'Auria et al., 2015]. Considering this swarm, both the lower contrast in ANT velocities and the decrease in density of THD_w maxima across the western caldera can be interpreted as a marker of deeper magmatic dynamics. The rim of the caldera [Battaglia et al. 2008] and especially the residual of eruptive conduits created during the last eruption [Chiodini et al. 2015; De Vito et al. 2016; De Siena et al. 2018] are structures that may hinder shallower magmatic propagation in the western caldera or dampen its deformation signals.

In conclusion, we present the first comparison of SAR and ANT interferometric images at CFc, in order to achieve relevant information about the subsurface structures and caldera dynamics. A significant spatial correlation was identified between the ANT velocity contrasts and the THD_w maxima distribution under Solfatara/Pisciarelli between May 2012 and March 2013, which DInSAR data define as the main phase of deformation unrest. The comparison with both the spatial seismicity distribution between 2005 and 2013 and the patterns of extinct volcanic vents in the eastern caldera part (specifically at Solfatara/Pisciarelli and Astroni crater) demonstrate that these boundaries are dynamically active, with seismicity concentrated at ~1km to the east of the boundary. We infer that the imaged ANT velocity contrasts constrain the dynamics of the deformation source and the propagation of the magmatic intrusion within a sill-like structure also channeling the eastward propagation of magmatic fluids. Both the absence of seismicity

and fading of the THD_w maxima in the first 2 km of the crust suggest that deeper (or no) magma dynamics are likely affecting the western side of CFC.

This work shows the importance of imaging shallow lateral heterogeneities when modeling the ground deformation patterns. Indeed, secondary structural effects may amplify local deformation in the early stage of an unrest: these signals can be mistakenly defined as early signs of impending eruptions [Del Gaudio et al. 2009]. Accordingly, the importance of these structural effects should not be underestimated when interpreting geodetic data, modeling deformation sources or in the design of future monitoring networks. The joint exploitation of the DInSAR measurements and seismic data revealed to be an excellent option to better understand the nature and the spatio-temporal pattern of the ground deformation source(s) at CFC. A combined application of DInSAR and seismic tomography techniques like the one proposed here can provide a new perspective to understand the origin of deformation signal at other volcanoes, especially in calderas where magma propagation is expected to occur preferentially within sills.”

From Pepe et al. [2019].

5.2.4 Source shape detection at Fernandina volcano via homogeneity properties of the ground deformation field.

We perform the geometrical modeling of the volcanic deformation source responsible of the 15 cm uplift occurred in 2013 at Fernandina volcano, for which several authors use different sources as sill, dike, and pipe mechanisms at about 1 km b.s.l. to simulate the measured deformation dataset [Jonsson et al., 1999; Chadwick et al., 2011; Bagnardi and Amelung, 2012; Bagnardi et al., 2013; Pepe et al., 2017].

In this framework, we discuss on one of the methods limitations regarding the entirety of the observed deformation anomaly. Indeed, the vertical component at summit caldera (**Figure 4.14a**) is not well defined and, therefore, the results of ScalFun method may be unreliable since the data gridding operation may provide an equally unreliable outcomes; this last procedure is certainly more reliable in the specific case of the E-W component (**Figure 4.14b**), although less data accuracy characterizes this retrieved component. Therefore, we apply the Multiridge and ScalFun methods on the 2013-2013.5 cumulative E-W deformation, and its VD_F , by showing the results along three profiles.

Here, we consider the homogeneity theory assumptions for the harmonic ground deformation field since we expect the presence of a single geometrically regular source. The retrieved outcomes are robust in terms of East and depth coordinates source position; we indeed define two clusters of solutions: ranging coordinates 662500-663000 E, 1.5-1.7 km b.s.l. depth and $N \sim 3$ for the deeper one, while 0.5-0.7 km b.s.l. of depth, and $N \sim 2$ for the shallower one (**Figure 5.2a-b**). We instead estimate the North coordinate source position with a wider range of solutions (9958500 – 9959500 N); although its high variability, the result represents a good constraint for the North coordinate parameter of the deformation source.

We associate both the retrieved clusters to the same volcanic body; in particular, we interpret the analysed ground deformation pattern as produced by a vertically elongated source characterized by the depth of the centre at 1.5-1.7 km and the top depth at 0.5-0.6 km b.s.l.. This interpretation is supported by the retrieved values of the Structural Index parameter, which are typical of the centre ($N \sim 3$) and of the top ($N \sim 2$) of an ideal linear vertical source.

The interpretation of our results is in agreement with those proposed by Pepe et al. [2017], where a closed pipe-like source could represent one of possible paths of the MFS

through which the magma migrate from a higher to a lower energy level (from the deep to the surface) during the 2012-2013 time interval.

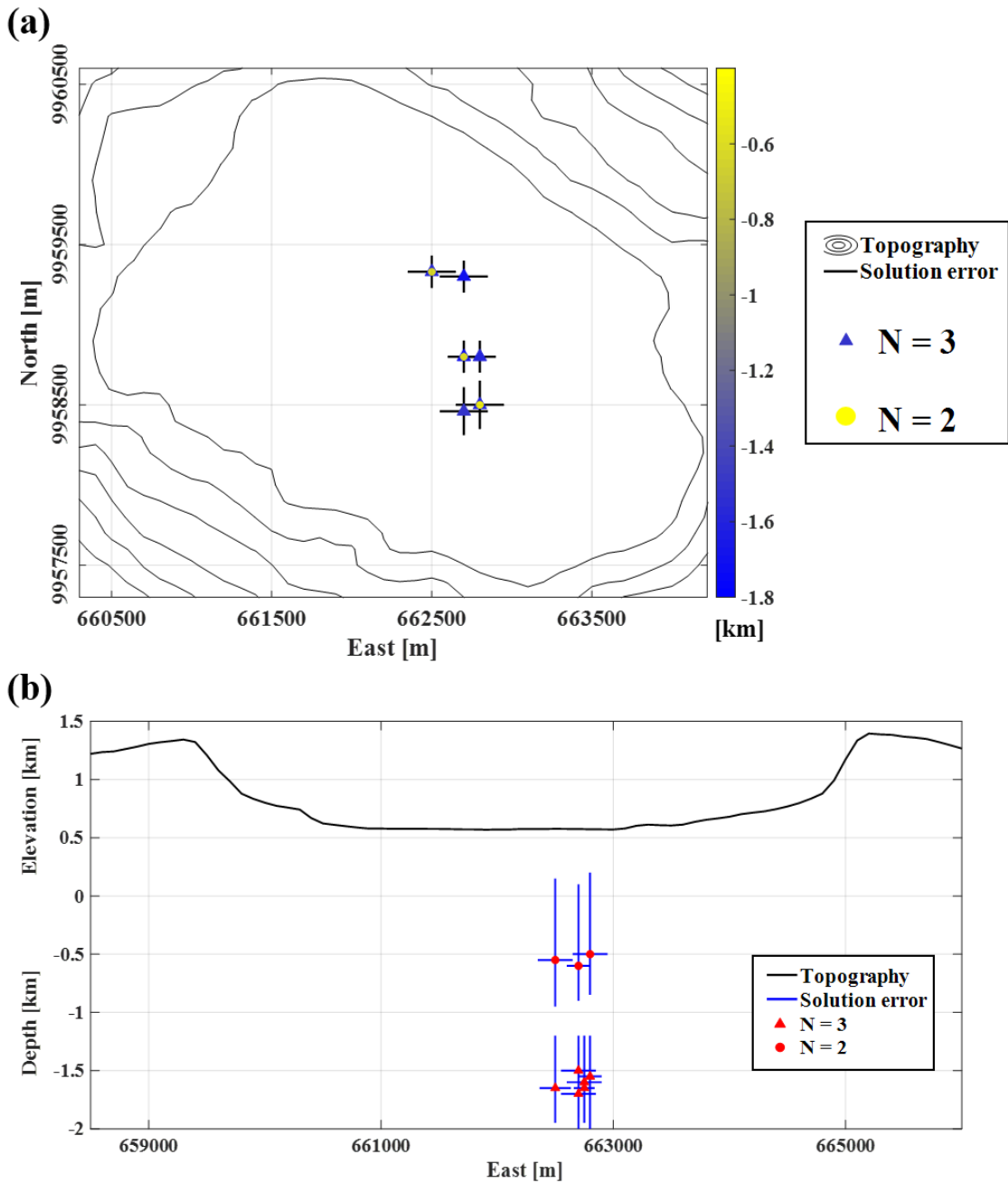


Figure 5.2. Location and depth of deformation sources at Fernandina volcano. (a) contour map of SRTM DEM of the study area with the blue triangles and the yellow dots indicating the position of the two retrieved clusters of solution characterized by $N \sim 3$ and $N \sim 2$, respectively; the black continuous lines represent the solution ranges. (b) CD section (black dashed lines in **Figure 4.15**) in which the location and depth of retrieved solutions are reported; the red triangles and dots indicate the solutions with $N \sim 3$ and $N \sim 2$, respectively; the blue continuous lines represent the solution range, while the black continuous line describes the volcano topography.

5.2.5 *Source analysis at Yellowstone caldera via local-homogeneity properties of the ground deformation field.*

We apply Multiridge, ScalFun methods, and THD technique to detect the deformation source(s) at Yellowstone caldera. We focus on the caldera region related to the ML and SC resurgent domes for which different results have been published [Wicks et al., 2006; Puskas et al., 2007; Vasco et al., 2007; Chang et al., 2007; Chang et al., 2010; Aly and Cochran 2011; Tizzani et al., 2015] and we analyse the vertical cumulative deformation, and its VD_F , related to the 2005-2007 time interval and by considering the local-homogeneity properties of the field. In particular, we retrieve two solutions of depth 9.8 and 9.1 km b.s.l. beneath ML and SC, respectively, with $N \sim 3$; furthermore, we investigate the region between the two resurgent domes with four different depth solutions, ranging between 6 – 8 km b.s.l. and with not integer values of N ranging from 1 to 2 (**Figure 5.3a-b**). We interpret these solutions as characterizing the same unique geometrically irregular deformation source beneath ML and SC; therefore, we associate the $N \sim 3$ depth values to the local centres of the extended volcanic body, while we consider the $1 < N < 2$ ones as coordinates of its top surface.

The THD_w (**Figure 5.3a-b**) supports the proposed interpretation since there is no maxima distribution between the resurgent domes, but only maxima alignments, which seem to outline a single about 50×20 km large planar body or surrounding fault systems. Hence, the THD maxima may represent an overestimation of the horizontal extension of the magmatic bodies since they coincide at NE with quaternary faults, which behaves as secondary sources modulating the measured ground deformation pattern. Finally, we specify the NGB deformation source could contribute to increase the maxima intensity in correspondence of the North-western boundary of the analysed body.

Our interpretation agrees with the results proposed by Chang et al., [2007; 2010] based on geodetic measurements and proposing as source mechanism a single tabular body beneath ML and SC resurgent domes. Moreover, these results are in agreement with the three-dimensional P-wave velocity model proposed by Farrell et al. [2014], in which a unique geometrically irregular magmatic structure is imaged below this area.

Finally, we highlight the deepest retrieved deep solution are characterized by different values of Structural Index respect to $N \sim 3$ and, therefore, we do not consider as acceptable in the scenario of the proposed interpretation.

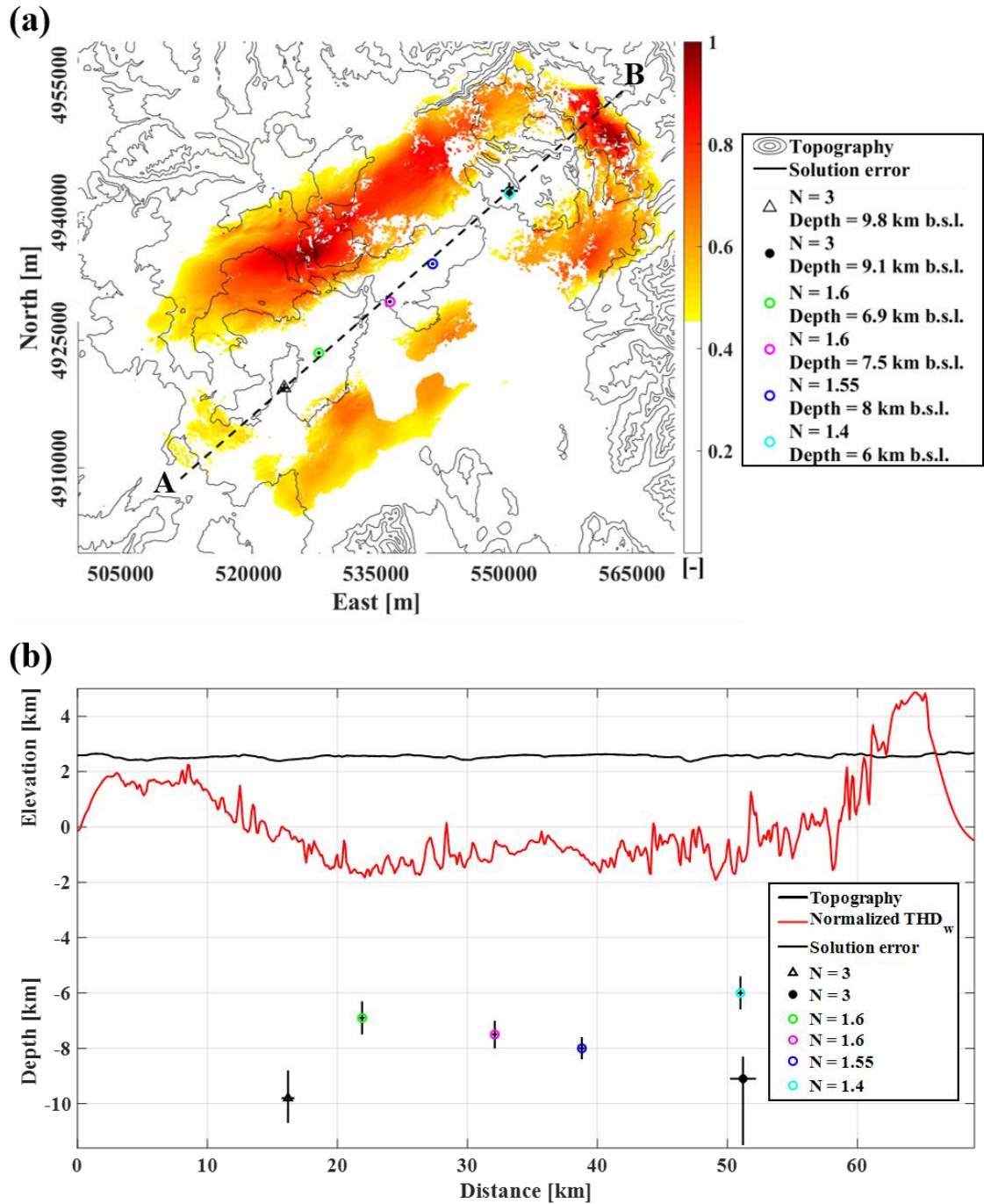


Figure 5.3. Location and depth of deformation sources at Yellowstone caldera. (a) Map of the normalized THD_w superimposed on the SRTM DEM of the study area with the colored circles and the black dashed line representing the location of the retrieved solutions and the AB trace; (b) AB section in which the location and depth of retrieved solutions are reported with the colored symbols, while the red continuous line represents the normalized THD_w; the black continuous lines indicate the uncertainties of the retrieved solutions, while the black dashed line describes the volcano topography.

CONCLUSIONS

We proposed and validated a new approach for the modeling of deformation sources in the volcanic environment by using the DInSAR measurements and their large sampling density; we revealed its features that also make it a valid tool for the volcanoes monitoring purposes.

Differently from the commonly used procedures, we proposed a solution of the elastic problem which satisfies the Laplace's equation, and we considered the properties of the harmonic functions for using integrated multi-scale methods, such as Multiridge, ScalFun and THD methods; this approach provides source information about its geometrical parameters, as the location, the depth, the shape and the horizontal extent (or its overestimation).

In particular, we showed that the Laplace's equation is satisfied for the deformation field in the case of hydrostatic pressure variation within a source embedded in a homogeneous elastic half-space. Accordingly, we can use the Multiridge method for univocally estimating the location and the depth parameters of the analysed field sources.

Then, we considered a particular class of harmonic functions which also satisfy the homogeneity theory and we used the ScalFun method for retrieving information about the morphological attributes through the Structural Index parameter. This analysis allows the investigation of geometrically regular sources. Therefore, we extended the proposed approach by considering the generalized form of the homogeneity laws and we also introduced the case of complex and irregular bodies. Finally, we integrated the approach with one more common technique, here named as THD, as supporting tool since it provides information about the horizontal extent of the field sources.

We demonstrated with several synthetic tests that the proposed approach represents the fastest way to provide results, especially because they do not require a priori assuming a specific, and often complex, formulation of the forward problem and of the distribution of the elastic parameters within the elastic regime (i.e., small variations of the elastic parameters). Moreover, they do not depend on the signal-to-noise ratio and are also reliable in the case of one component analysis and multi-source scenario, while their solutions only depend on the harmonic properties of the analysed field, which has to satisfy the Laplace's equation; this condition is surely satisfied in the case of hydrostatic

pressure variation of a source embedded in a homogeneous elastic half-space, which often also characterize the forward problem formulations of AM.

We validated the proposed approach by applying Multiridge, ScalFun and THD methods to simulated deformation patterns in the FEM environment, whose modeled field enjoy the properties of the harmonic functions. In particular, we firstly considered geometrically regular volcanic source for modeling pipe- and sill-like reservoirs, and we showed the possibility to correctly detect the depth, the horizontal position, the morphological attributes and the horizontal extent of these simple sources, by analysing only one component between the vertical and the E-W ones.

Then, we treated the geometrically irregular bodies, and we briefly show how to retrieve valid information about the source geometrical parameters by considering the local-homogeneity properties of the inhomogeneous field.

We also highlighted the advantages and the limitations of the proposed approach through its application to study simulated fields which do not satisfy the Laplace's equation. Specifically, we retrieved acceptable results in the case of acceptable variation of the medium elastic parameters within the elastic regime; while, in the other cases, they may be characterized by also a 30 % of discrepancies respect to the real scenario.

Finally, we applied the proposed approach for investigating different five case studies by using the ground deformation patterns measured via DInSAR technique. The first analysed case is the Okmok volcano (Alaska, USA), where we applied the Multiridge and ScalFun methods, for the first time, on a single interferogram related to measurements acquired along descending orbit. We characterized the depth and the horizontal position of the spherical source approximating its volcanic reservoir.

We performed the second analysis to study the multi-source scenario of Uturuncu Volcano (Bolivia). We mainly applied the Multiridge method on the vertical deformation to detect the existence of two different active sources: the first one is related to the deep APMB volcanic body and the second one is characterizing shallow hydrothermal phenomenon beneath Uturuncu volcano.

In the third case, we considered the THD technique for the analysis of Campi Flegrei caldera and to jointly compare DInSAR and ANT data. In particular, THD_w is crucial to

interpret ANT results and to understand the depth and the mechanism of the volcanic source.

The fourth analysed case regarded the application of Multiridge and ScalFun methods on the E-W deformation of the 2013 unrest at Fernandina volcano. The retrieved solution agrees with the pipe-like source proposed by Pepe et al. [2017], as guiding structure for magma migration from deeper to shallower portions of the same volcanic system.

Finally, we analysed the case of the Yellowstone caldera by considering Multiridge, ScalFun methods and THD technique. We modeled the 2005-2007 cumulative vertical deformation as caused by a unique horizontally planar single source beneath ML and SC resurgent domes and characterized by an irregular geometry. We remark that the retrieved results agree with other geodetic [Chang et al., 2007; Chang et al., 2010] and seismic [Farrell et al., 2014] studies.

The proposed solution of the elastic problem allows solving ambiguous cases for modeling volcanic deformation sources. However, we point out some limitations affecting this approach, which are mainly associated to the sampling ambiguity, the experimental/instrumental errors, and the high gradient of the measurement surface. Furthermore, it provides a certain error when the harmonic properties of the field are not satisfied; these discrepancies are still comparable to those of the widely used inverse modeling. We remark that the proposed approach does not provide information about the whole set of physical parameters of the volcanic system, but its solutions represent a good constraint for possible subsequent accurate modeling.

We conclude this thesis by introducing some possible future developments:

- automation of the proposed procedure for the geometrical modeling of volcanic deformation sources, in order to fully take advantages of the properties of the fields satisfying the Laplace's equation;
- use of the DInSAR time series to allows retrieving real time information about the evolution of magmatic sources in space and in time, which is the crucial feature to consider the proposed approach as a superb tool for monitoring purposes;
- deeply study and use of the local-homogeneity theory for the ground deformation field to provide exhaustive information on the analysed volcanic deformation source in the case of complex magmatic bodies, generating inhomogeneous deformation fields.

APPENDIX A

Table A.1. Results of the Upward Continuation test by considering fields satisfying the Laplace's equation. The outcomes are expressed as maximum percentage error.

	<i>Sphere</i>	<i>Cube</i>	<i>Horizontal prism</i>	<i>Vertical prism</i>	<i>Vertical cylinder</i>	<i>Vertical prolate ellipsoid</i>
<i>Vertical component</i>	0.36	0.36	0.44	0.37	0.47	0.42
<i>E-W component</i>	0.65	0.77	0.65	0.64	0.65	0.64

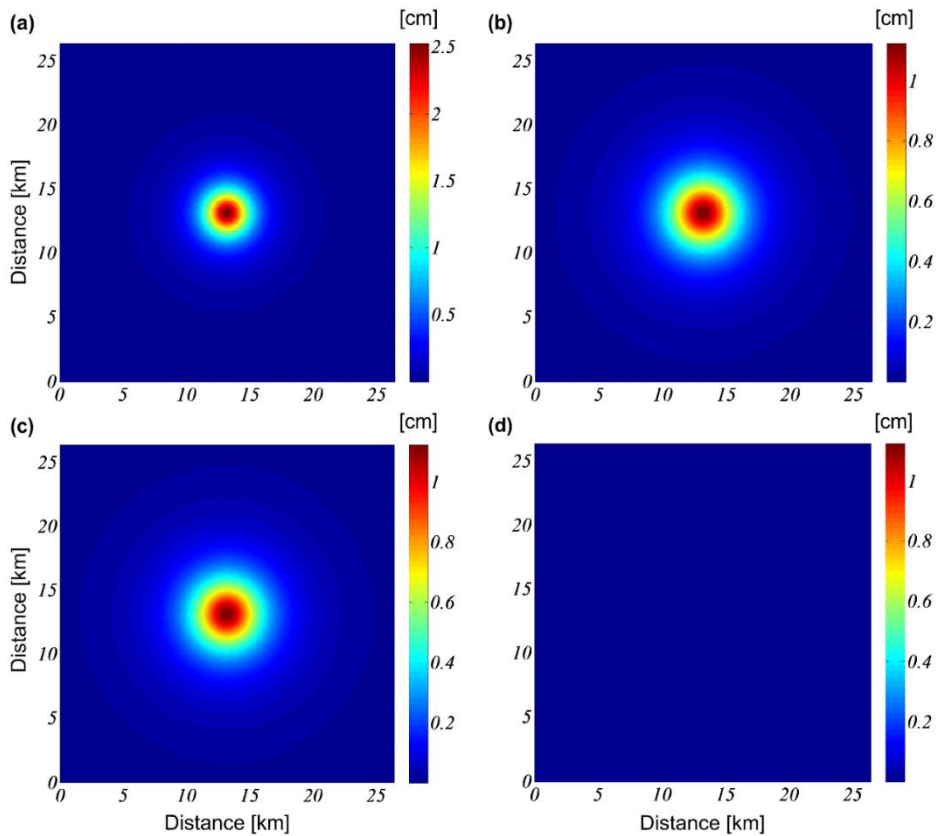


Figure A.1. Mogi model vertical component: Upward continuation results. (a) Map of the modeled vertical component of deformation field generated by a Mogi source located at 2 km of depth and calculated on a flat surface level of $z = 0$; (b) Upward-continued field at 1 km. (c) Map of the modeled vertical component of deformation field generated by a Mogi source, located at 3 km of depth and calculated on a flat surface level of $z = 0$. (d) Differences between (b) and (c) maps. The model parameters are: radius = 0.3 [km], $\Delta P = 5$ [MPa], $G = 1$ [GPa], $\nu = 0.25$ [-].

From Castaldo et al. [2018b].

APPENDIX B

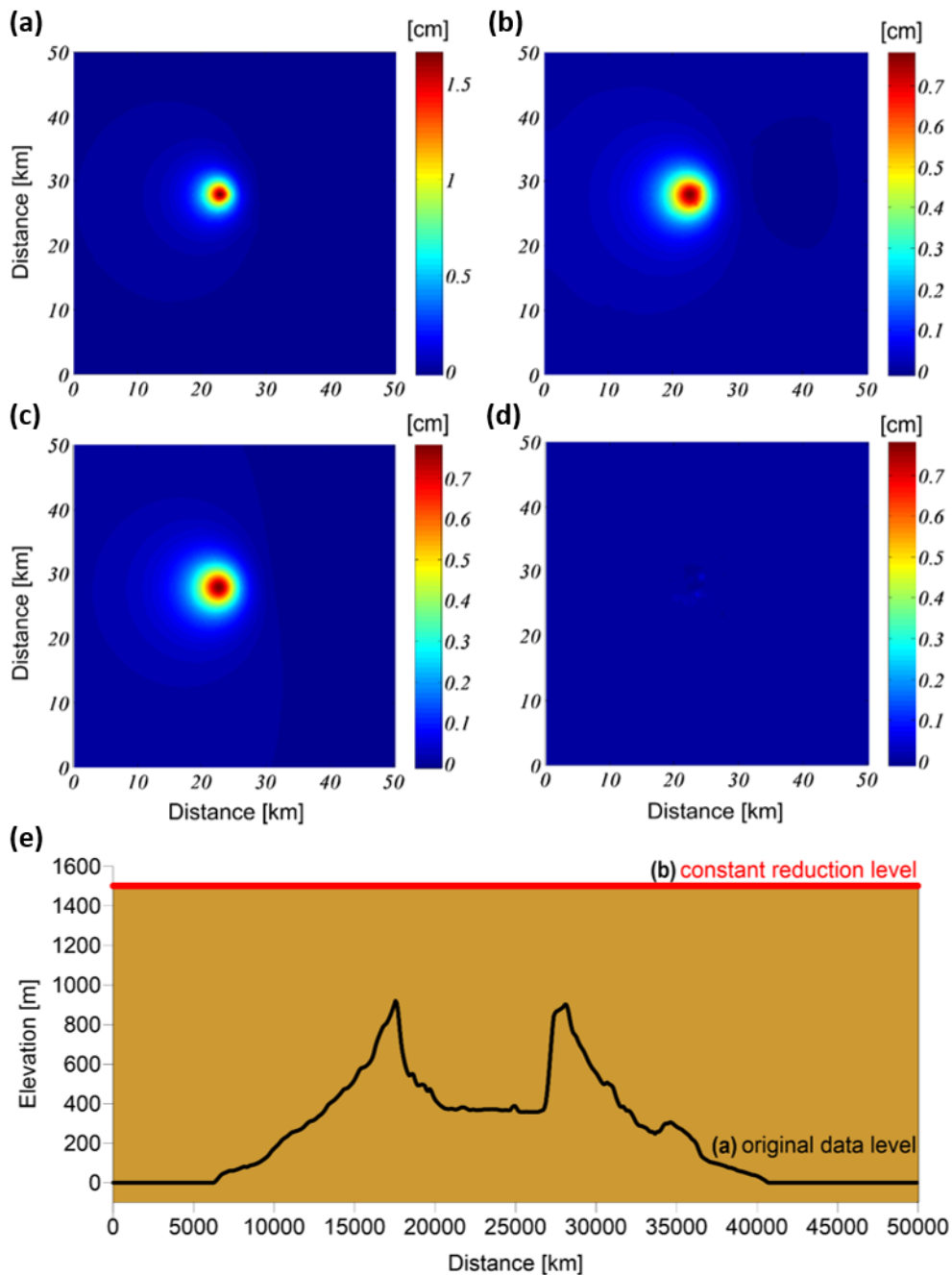


Figure B.1. LOS-projected Mogi model deformation field: constant-level reduction procedure. (a) Map of the modeled Ascending LOS deformation calculated on Okmok volcano topography and generated by a Mogi source at 2 km depth. (b) Ascending LOS deformation map reduced to the constant-level starting from (a); the flat surface is at 1.5 km a.s.l.. (c) Ascending LOS modeled deformation field generated by a Mogi source located at 3.5 km depth and measured on a flat surface $z = 0$. (d) Differences between (b) and (c). (e) Sketch showing the different data level between the case (a) and (b). The model parameters are: radius = 0.3 [km], $\Delta P = 5$ [MPa], $G = 1$ [GPa], $\nu = 0.25$ [-]. The used mean LOS vector $([0.346, -0.081, 0.935])$ is related to a 23° satellite look angle.

From Castaldo et al. [2018b].

“We consider an oblate spheroidal over-pressurized model ($\Delta P = 0.2$ MPa), located at 15 km of depth, and with semimajor and semiminor axes extended for 5 and 1 km, respectively. The elastic half-space is characterized by a shear modulus and Poisson’s coefficient equal to 1 GPa and 0.25 (-), respectively. In particular, to validate this procedure, we firstly calculate the modeled vertical deformation measured on the detailed measurement surface of the Uturuncu volcano topography (**Figure B.2a**); we process the latter by applying the constant-level reduction procedure, which level is chosen to be at 6 km a.s.l. (**Figure B.2b**). Then, we compute the modeled vertical deformation measured directly on a flat measurement surface at 6 km a.s.l. (**Figure B.2c**) and, finally, we compare both the processed (blue continuous line in the **Figure B.2d**) and the computed (red continuous line in the **Figure B.2d**) vertical components referring to the same scale. This test shows how the used procedure provides results in agreement with the expected ones.

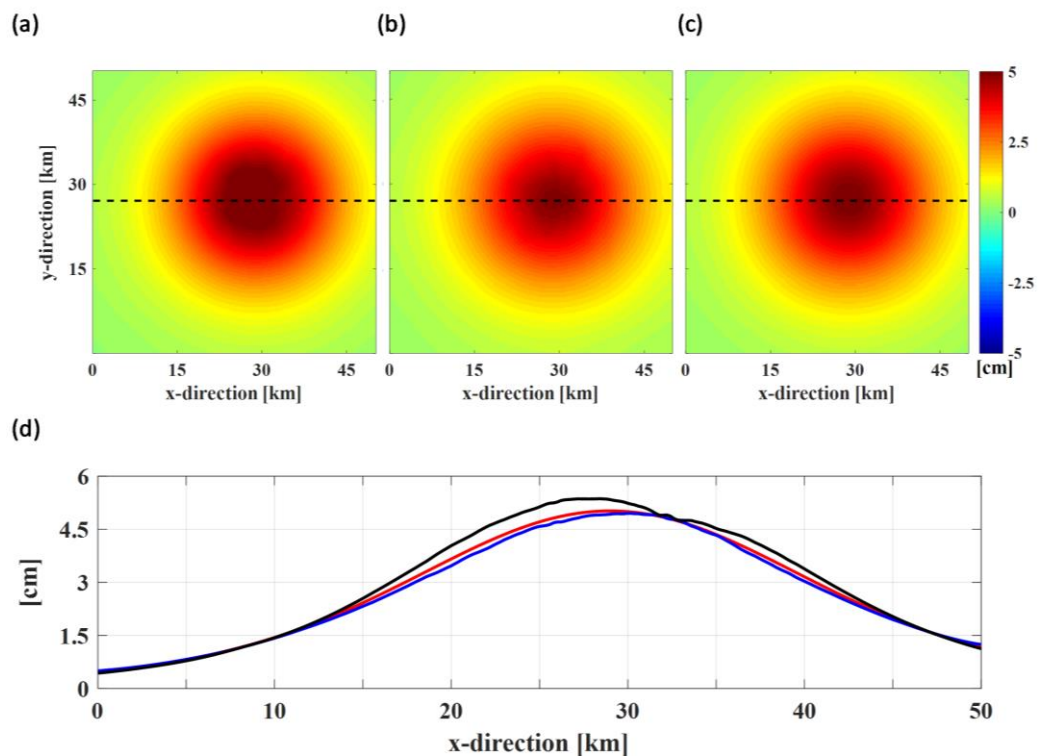


Figure B.2. Constant-level reduction procedure test. (a) Modeled vertical deformation measured on the ground surface of Uturuncu volcano; (b) Results of the constant-level reduction procedure (cm) applied on (a); the constant-level reduction is chosen to be at 6 km a.s.l.; (c) Modeled vertical deformation (cm) measured on a flat level at 6 km a.s.l.; the black dashed lines represent the traces passing from the maxima; (d) Black, blue and red profiles extrapolated from (a), (b) and (c), respectively, along the above mentioned traces.”

From Barone et al. [2019].

APPENDIX C

We show the correctness of VD_F , equation (2.35), by a comparison with VD_S , expressed by relation (2.34), through synthetic modeled deformations. The computation of VD_S is not a simple task because of the difficulties in simulating in FEM environment the fields of the same source at infinitesimally different depths. Therefore, we will show how the VD_S tends to VD_F when the depth difference (Δz) decreases.

We consider the same model setting of the paragraph 3.1, where the vertical deformation is generated by a spherical source at a depth $z_0 = 1$ km and the minimum mesh dimension of the model is set to 0.2 km. We calculate the VD_F on this field and the VD_S by fixing $\Delta z = 0.2$ km, which corresponds to the minimum mesh dimension of the model. We compute the error as the difference between the VD_S and the VD_F , normalized by the VD_S maximum value (**Figure C.1a**). We repeat the same procedure by considering a smaller Δz , and, in turn, changing the minimum mesh dimension of the model, sized 0.05 km (**Figure C.1b**) by 0.02 km (**Figure C.1c**). The results confirm that the matching between VD_F and VD_S improves reducing Δz ; in particular, the maximum modulus of the error decreases from $\sim 27\%$ (**Figure C.1a**) to $\sim 8\%$ (**Figure C.1b**), even reaching 3% (**Figure C.1c**) for a 0.02 km Δz .

Specifically, for lower discrepancies between we need to consider a very small Δz , and, to exactly appreciate changes between fields of sources spaced by a so small Δz , we should set the minimum mesh dimension of the model along the z -direction at least less than the considered Δz value. The synthetic models with these conditions are computationally hard to be calculated.

We propose an alternative approach to overcome this issue: we calculate the VD_C as the equation (2.34) but substituting the term $f(x, y, z_0 + \Delta z)$ with the upward continued field to the Δz scale. The upward continuation procedure allows considering very small Δz , without incurring computational issues as in the case of FEM model. With this aim, we first compare VD_S and VD_C ; then, we use this last to validate the VD_F .

We consider the case of $\Delta z = 0.05$ km and we compare VD_C and VD_S ; we do not consider the 0.02 km case since mesh irregularity are noticeable (**Figure C.1c**). The error map (**Figure C.1d**) shows both the procedures provide results with only $\sim 0.1\%$ discrepancy, suggesting we can use VD_C instead of the VD_S for the VD_F validation.

Finally, we calculate the VD_C for $\Delta z = 0.001$ and 0.0001 km and we compare them with VD_F . The results indicate the VD_F tends even more to VD_C as well as Δz decreases; indeed, VD_F reproduces the expected VD_S with negligible errors equal to $\sim 0.15\%$ (**Figure C.1e**) and $\sim 0.015\%$ (**Figure C.1f**) for $\Delta z = 0.001$ and 0.0001 km, respectively.

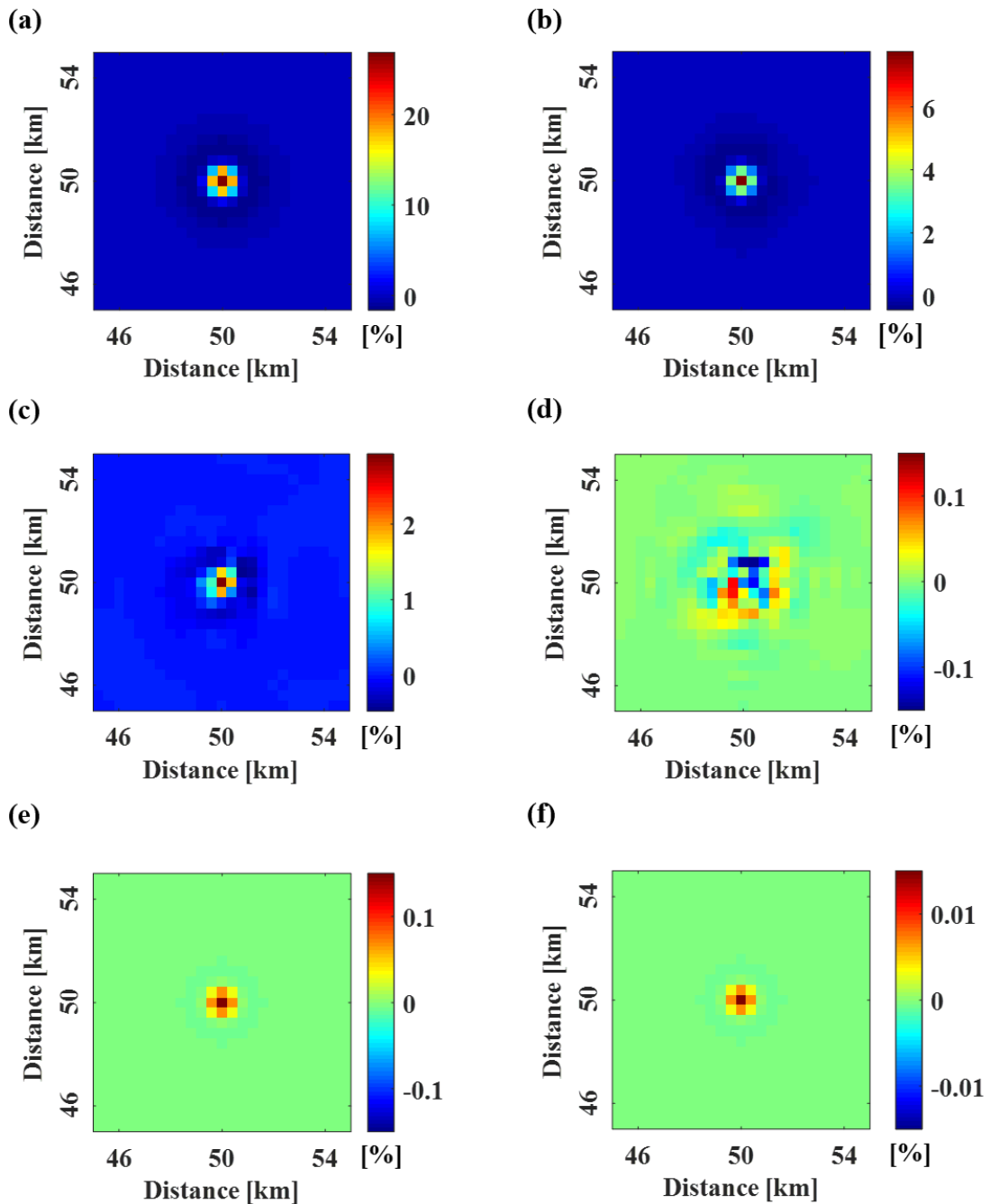


Figure C.1. Validation of VD_F . Error maps [%] related to the comparison between: VD_S and VD_F by considering $\Delta z = 0.2$ km (a), 0.05 km (b) and 0.02 km (c); VD_S and VD_C by setting $\Delta z = 0.05$ km (d); VD_C and VD_F in the case of $\Delta z = 0.001$ (e) and 0.0001 km (f); the model parameters are specified in the main text.

We show the validity of the VD_F for vertical and E-W deformations of source geometries different from the spherical one. In particular, we calculate the error of VD_F to VD_C by considering the Ellipsoid 2 and Prism 2 cases (please refer to the paragraph 3.2 for model descriptions). The results (**Figure C.2**) confirm VD_F reproduce VD_S for $\Delta z = 0.0001$ km and for both the components with maximum errors of ~ 0.012 % (**Figure C.2a** and **C.2b**) and ~ 0.003 % (**Figure C.2c** and **C.2d**) in the case of the Ellipsoid 2 (**Figure C.2a** and **C.2b**) and Prism 2 (**Figure C.2c** and **C.2d**), respectively.

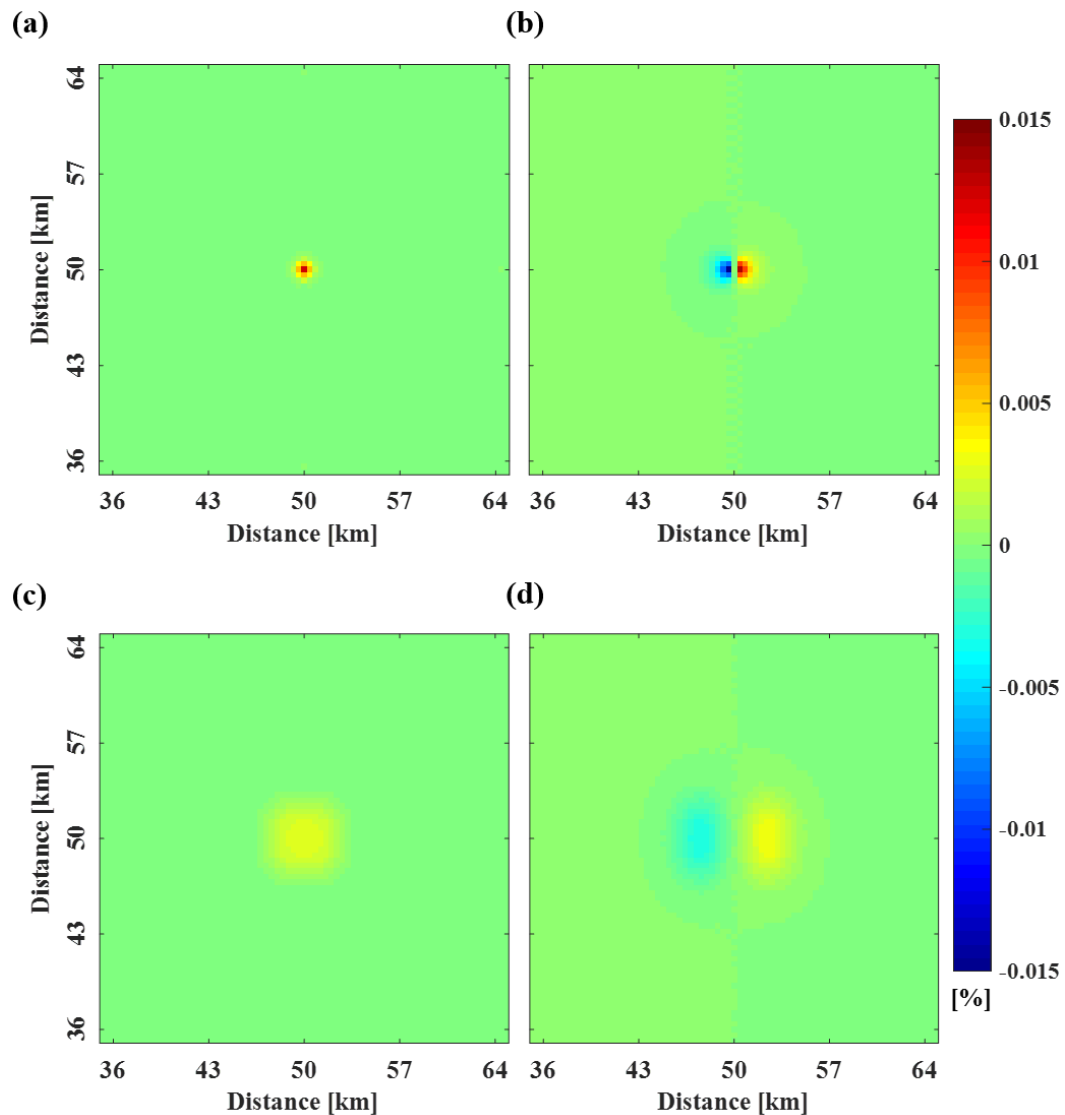


Figure C.2. VD_F test for different source geometries. Error maps [%] of VD_F to VD_S considering the (a) vertical and (b) E-W components for Ellipsoid 2 and (c-d) Prism 2 cases. The VD_C are calculated by fixing $\Delta z = 0.0001$ km.

“We consider an oblate spheroidal over-pressurized model ($\Delta z = 0.2$ MPa) located at 15 km of depth, and with semimajor and semiminor axes extended for 5 and 1 km, respectively. The elastic half-space is characterized by a shear modulus and Poisson’s coefficient equal to 1 GPa and 0.25 (-), respectively.

We calculate VD_S by setting $\Delta z = 0.05$ km with respect to the referred depth, 15 km (Figure C.3a). Then, we compute VD_F according to equation (2.35) (Figure C.3b). In Figure C.3c, we show the results along a profile passing from the maxima of VD_S and VD_F (black dashed lines in Figure C.3a-b): VD_F (Figure C.3b and blue continuous line in the Figure C.3c) provides well approximated results, within the 5 % root mean square error, respect VD_S (Figure C.3a and red continuous line in the Figure C.3c).

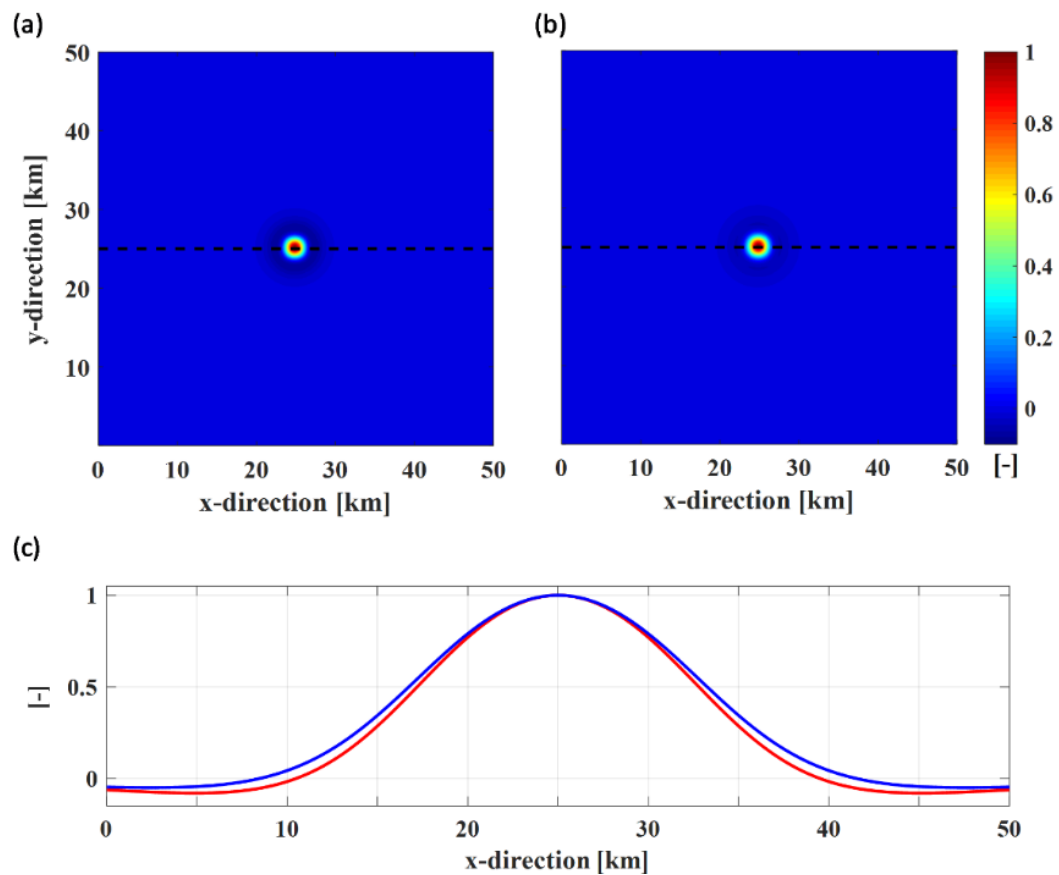


Figure C.3. VD_F test. (a) Results of VD_S of the modeled vertical deformation (cm) and (b) VD_F ; the black dashed lines represent the traces passing from the maxima; (c) Red and blue continuous lines represent the VD_S and VD_F values, respectively.”

From Barone et al. [2019].

APPENDIX D

“We perform several synthetic tests based on the analysis of the deformation field of a spherical source. We chose Cartesian reference system, with the origin of the system located at the point $\mathbf{O}(0,0)$; the x - and y -axes are oriented in the E-W and N-S directions, respectively, and the z -axis is negative downward. For all of the following tests, the deformation field is simulated with a grid of 120 km x 120 km sampled at 0.1 km intervals.

*We generate the vertical component of the ground deformation field on a flat surface ($z = 0$) by using the Mogi model, as produced by the overpressured ($\Delta P = 10$ MPa) spherical magma chamber (**Figure D.1a**). The active source depth is -2 km and it is located 60 km along both the x - and y -directions; its radius is 0.3 km, while the medium shear modulus and Poisson's coefficient are 1 GPa and 0.25 [-], respectively.*

*We apply the Multiridge method to the vertical component and we analyse the AA' E-W profile passing for the maximum value of the field (**Figure D.1b**). The results allow us to easily identify a source at an approximate -2.05 ± 0.01 km depth and located at 60 ± 0.02 km along the x -direction (**Figure D.1c**). The estimation reliability is supported by the high values of R^2 .*

*Then, we apply the ScalFun method to the central ridge (cyan) and we achieve a homogeneity degree of $n \sim -2$ (**Figure D.1d**). This value corresponds to the Structural Index $N \sim 3$, suggesting that the representative geometry of the source is spherical, which agrees with the features of the true source.*

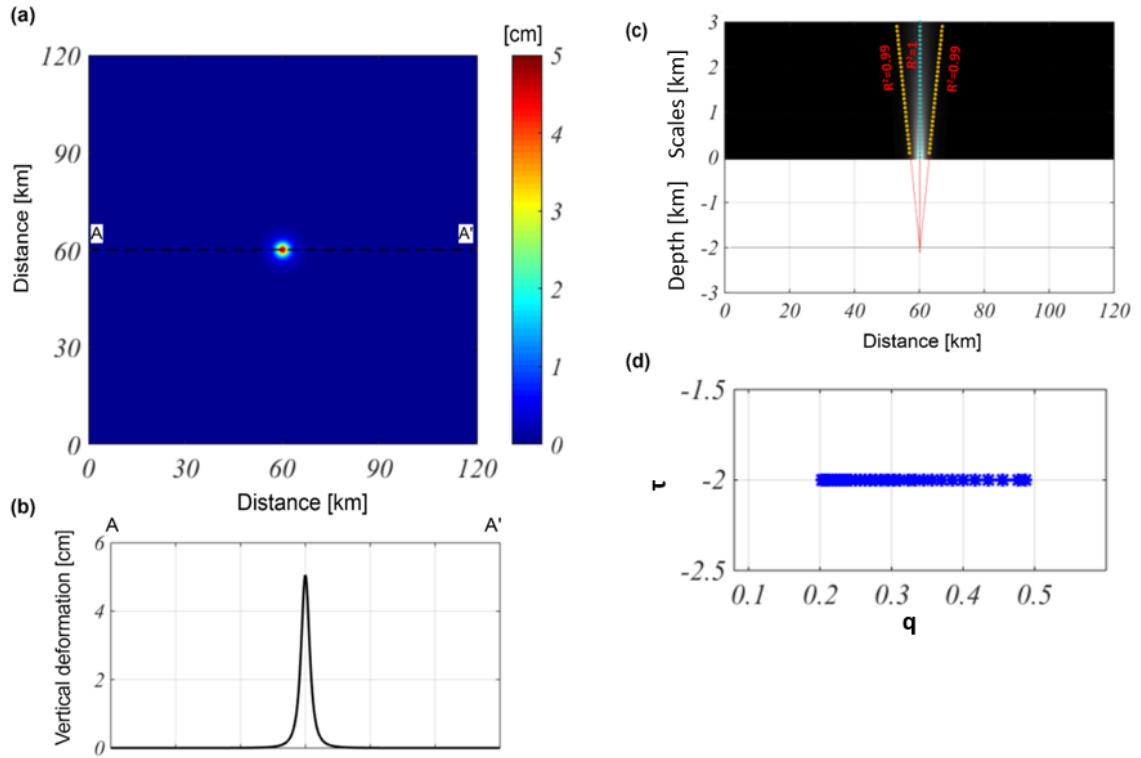


Figure D.1. Multiridge and ScalFun methods: the Mogi model vertical component. (a) Map of the modeled vertical component of the deformation field calculated on a flat surface level of $z = 0$. The black dashed line indicates the AA' trace. (b) AA' profile of the vertical component of the deformation field; (c) The results of the Multiridge method applied to the AA' profile; the red solid lines, which represent the regression lines, estimate the source position at their intersection, and the black solid line indicates the real source depth. For each regression line we indicate the coefficient of determination (R^2); (d) the results of the ScalFun method applied to the central cyan multiridge subset reported in (c); $q = \frac{1}{z}$ while $\tau = \frac{\partial \log(w(z))}{\partial \log z}$, where w and z represent the vertical deformation and the vertical scale, respectively.

Subsequently, we consider the previous test adding to the modeled vertical component a 10% of high-wavenumber noise (with respect to the maximum value of the anomaly) (**Figure D.2a-b**). The results show that the estimates are not conditioned by the lower signal-to-noise ratio since and (also in this case) we identify a source depth of approximately -2.04 ± 0.02 km, and a location of 60 ± 0.03 km along the x -direction (**Figure D.2c**). Then, we apply the ScalFun method to the central ridge (cyan) in order to evaluate the homogeneity degree of the field, $n \sim -2$ ($N \sim 3$) which, in turn, gives us an evaluation of the geometric shape of the source (**Figure D.2d**).

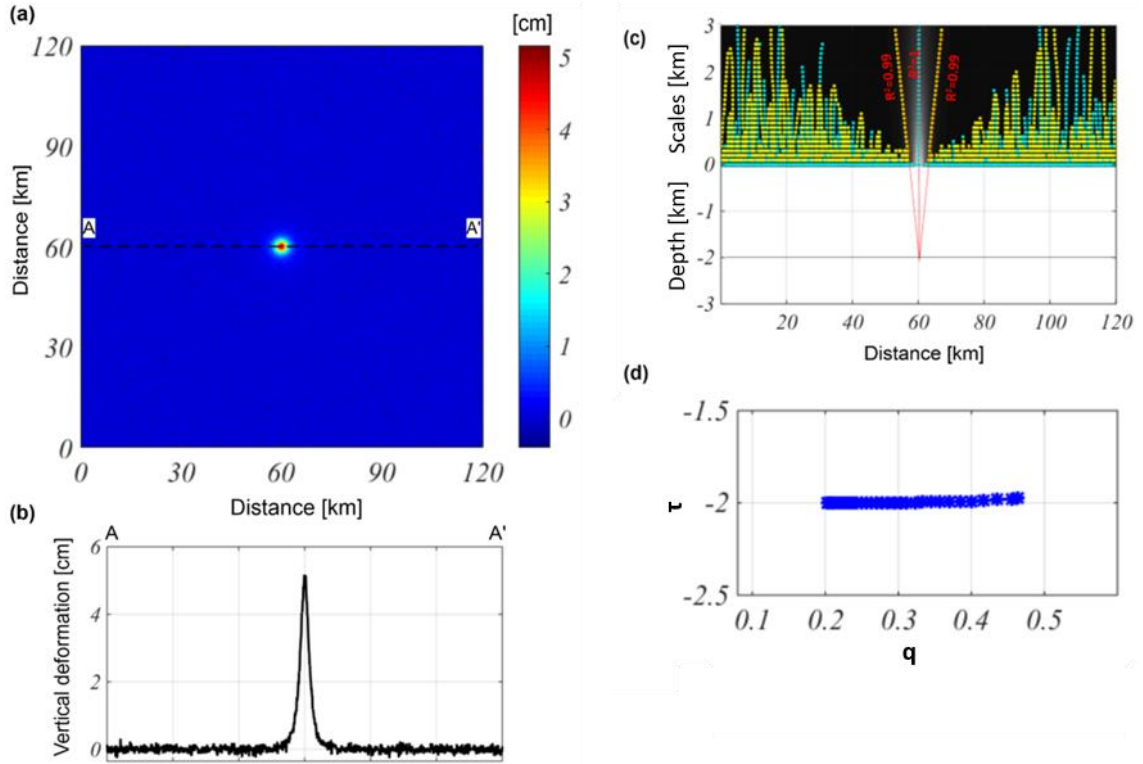


Figure D.2. Multiridge and ScalFun methods: the Mogi model vertical component with noise. (a) Map of the modeled vertical component of the deformation field calculated on a flat surface level of $z = 0$ and perturbed by 10% (with respect to the maximum value) of high-wavenumber noise. The black dashed line indicates the AA' trace. (b) AA' profile of the vertical component of the noisy deformation field. (c) The results of the Multiridge method applied to the AA' noisy profile; the red solid lines, which represent the regression lines, estimate the source position at their intersection, and the black solid line indicates the real source depth. For each regression line we indicate the coefficient of determination (R^2); (d) the results of the ScalFun method applied to the central cyan multiridge subset reported in (c); $q = \frac{1}{z}$ while $\tau = \frac{\partial \log(w(z))}{\partial \log z}$, where w and z represent the vertical deformation and the vertical scale, respectively.

We consider the same source model parameters as those of the first test, changing only the horizontal position beneath the caldera floor: 58 km in the x -direction and 53 km in the y -direction. By combining the simulated components of the ground deformation field with the LOS unit vectors $[-0.346, -0.081, 0.935]$: mean values for ascending orbit; $[0.346, -0.081, 0.935]$: mean values for descending orbit), we obtain the projected field along the ascending (**Figure D.3a-c**) and descending (**Figure D.3b-d**) orbits. In both cases, the retrieved source depth is approximately -2.05 ± 0.02 km, and the location equal to 58.02 ± 0.02 km along the x -direction (**Figure D.3e-f**). The application of the ScalFun method to both the ascending and descending cases confirms the expected value of the Structural Index ($N \sim 3$) (**Figure D.3g-h**).

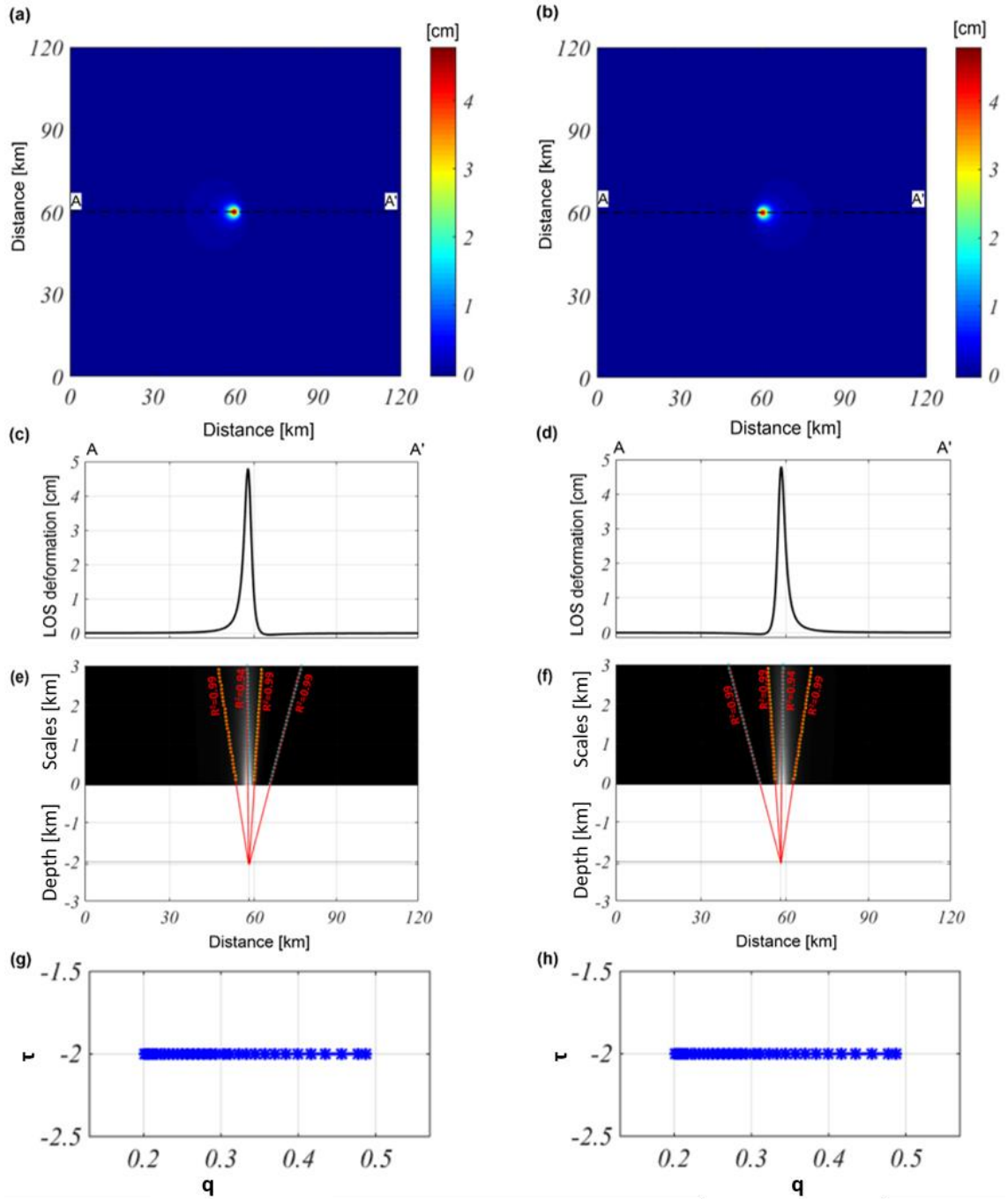


Figure D.3. Multiridge and ScalFun methods: LOS-projected Mogi model. (a-b) LOS deformation maps projected along ascending and descending orbits, respectively; the fields are calculated on a flat measurement level of $z = 0$. The black dashed lines indicate the positions of the AA' traces. (c-d) LOS deformation profiles evaluated along the AA' traces for both the ascending and descending orbits. (e-f) The results of the Multiridge method applied to the AA' profiles; (c) the red solid lines, which represent the regression lines, estimate the source position at their intersection, and the black solid line indicates the real source depth. For each regression line we indicate the coefficient of determination (R^2); (g-h) the results of the ScalFun method applied to the central cyan multiridge subsets reported in (e-f) for ascending and descending orbits, respectively; $q = \frac{1}{z}$ while $\tau = \frac{\partial \log(\chi(z))}{\partial \log z}$, where χ and z represent the LOS deformations and the vertical scale, respectively.

Then, we consider the previous test configuration projected along the descending LOS by changing only the surface measurements from $z = 0$ to z equal to the Okmok volcano topography. We process the simulated dataset to relocate the analysed field at the new constant reduction level, which is chosen to be 1.5-km a.s.l. After this transformation, the expected depth is equal to -3.5 km. We apply the Multiridge and ScalFun methods to the processed field shown in **Figure D.4a** by considering the AA' profile (**Figure D.4b**): the first method allows us to identify the source at an approximate -3.53 ± 0.02 km depth (**Figure D.4c**), and the horizontal position at 58.01 ± 0.02 km along the x -direction; the second method reveals the homogeneity degree of the field, $n \sim -2$ (**Figure D.4d**). This value corresponds to a source with a Structural Index of $N \sim 3$, suggesting that the source geometry is well represented by a spherical geometry.

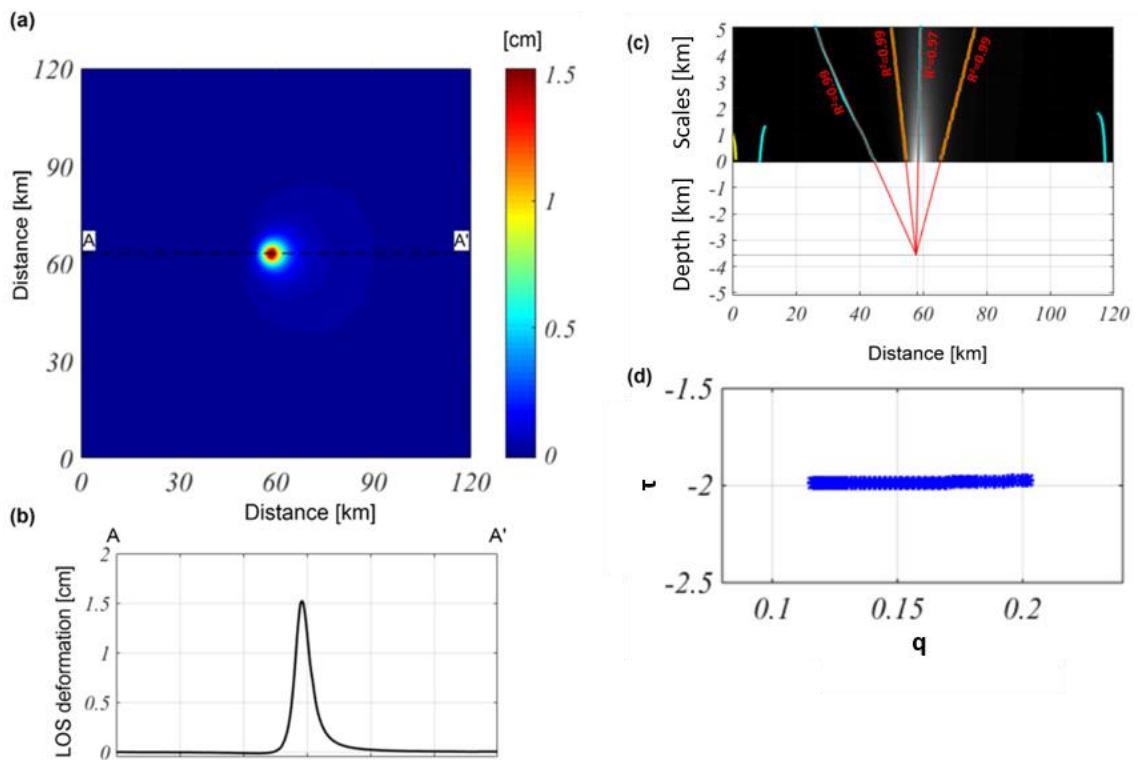


Figure D.4. Multiridge and ScalFun methods: LOS-projected Mogi model evaluated at a constant reduction level. (a) Descending LOS modeled deformation map retrieved on a 1.5 km flat surface a.s.l.; the original data level is represented by the Okmok volcano topography. The black dashed line indicates the position of the AA' trace. (b) The LOS deformation profile evaluated along the AA' trace. (c) The results of the Multiridge method applied to the AA' profile; the red solid lines, which represent the regression lines, estimate the source position at their intersection, and the black solid line indicates the real source depth. For each regression line we indicate the coefficient of determination (R^2); (d) the results of the ScalFun method applied to the central cyan multiridge subset reported in (c); $q = \frac{1}{z}$ while $\tau = \frac{\partial \log(\chi(z))}{\partial \log z}$, where χ and z represent the LOS deformation and the vertical scale, respectively.

Finally, we consider the aforementioned test configuration, with 10% high-wavenumber noise (with respect to the maximum value), on the descending LOS deformation field (Figure D.5a-b). The achieved results confirm that the estimated geometric parameters of the source (-3.55 ± 0.04 km for depth and 58.01 ± 0.02 km for horizontal position) are not influenced by the presence of high-wavenumber noise in the dataset (Figure D.5c-d).

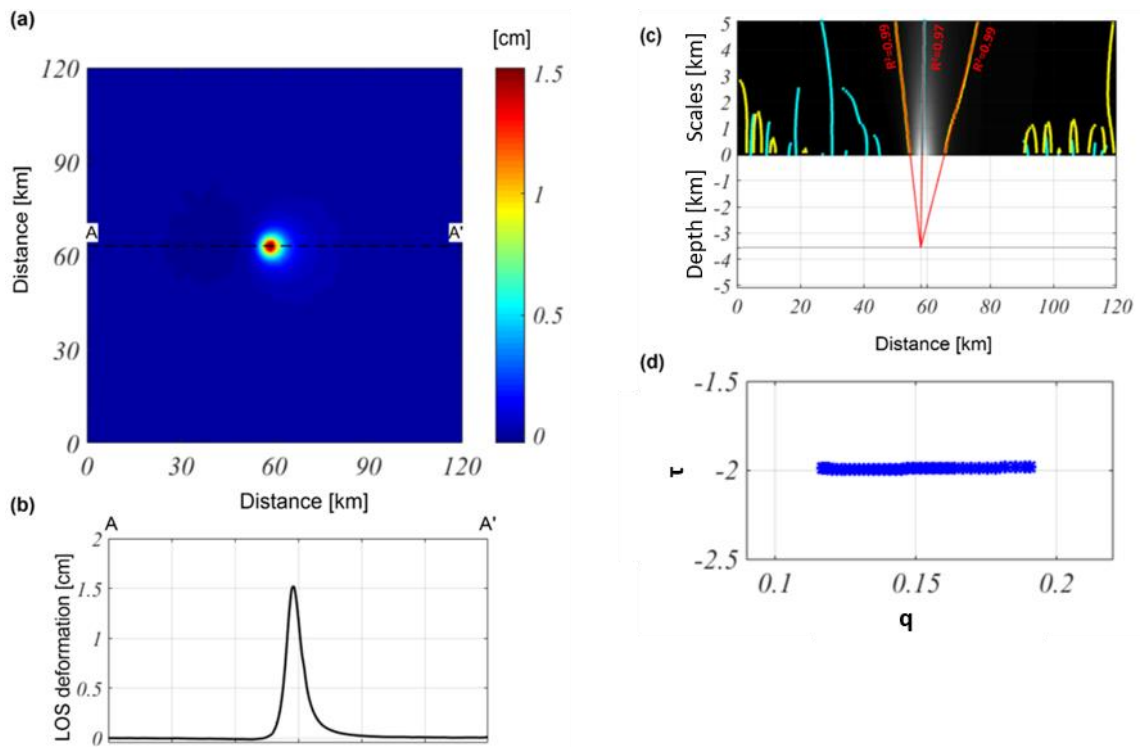


Figure D.5. Multiridge and ScalFun methods: the LOS-projected Mogi model evaluated at a constant reduction level with noise. (a) Descending LOS modeled deformation map perturbed by 10% (with respect to the maximum value) of the high-wavenumber noise and retrieved on a 1.5-km flat surface a.s.l.; the original data level is represented by the Okmok volcano topography. The black dashed line indicates the position of the AA' trace. (b) LOS deformation profile evaluated along the AA' trace. (c) The results of the Multiridge method applied to the AA' noise profile; the red solid lines, which represent the regression lines, estimate the source position at their intersection, and the black solid line indicates the real source depth. For each regression line we indicate the coefficient of determination (R^2); (d) the results of the ScalFun method applied to the central cyan multiridge subset reported in (c); $q = \frac{1}{z}$ while $\tau = \frac{\partial \log(\chi(z))}{\partial \log z}$, where χ and z represent the LOS deformation and the vertical scale, respectively.”

From Castaldo et al. [2018b].

REFERENCES

- Allmendinger, R. W., Jordan, T. E., Kay, S. M. and Isacks, B. L. (1997): *The evolution of the Altiplano-Puna plateau of the central Andes*. *Annu. Rev. Earth Planet. Sci.*, 25, 139-174.
- Almansi, E. (1899): *Sull'integrazione dell'equazione differenziale $\nabla^{2n}F = 0$* . *Ann. Di Mat. Ser.* 3, 2, 1.
- Aloisi, M., Mattia, M., Ferlito, C., Palano, M., Bruno, V. and Cannavò, F. (2011): *Imaging the multi-level magma reservoir at Mt. Etna volcano (Italy)*. *Geophysical Research Letters*, 38, L16306, doi:10.1029/2011GL048488.
- Aloisi, M., Bonaccorso, A., Cannavò, F., Currenti, G. and Gambino, S. (2020): *The 24 December 2018 Eruptive Intrusion at Etna Volcano as Revealed by Multidisciplinary Continuous Deformation Networks (CGPS, Borehole Strainmeters and Tiltmeters)*. *Journal of Geophysical Research: Solid Earth*, 125, e2019JB019117, doi:10.1029/2019JB019117.
- Alvizuri, C. and Tape, C. (2016): *Full moment tensors for small events at Uturuncu volcano, Bolivia*. *Geophysical Journal International*, 206, 1761-1783, doi:10.1093/gji/ggw247.
- Aly, M. H. and Cochran, E. S. (2011): *Spatio-temporal evolution of Yellowstone deformation between 1992 and 2009 from InSAR and GPS observations*. *Bulletin of Volcanology*, 73, 9, 1407-1419, doi:10.1007/s00445-011-0483-y.
- Amoruso, A., Crescentini, L. and Berrino, G. (2008): *Simultaneous inversion of deformation and gravity changes in a horizontally layered half-space: evidences for magma intrusion during the 1982-1984 unrest at Campi Flegrei caldera (Italy)*. *Earth and Planetary Science Letters*, 272, 181-188.
- Amoruso, A., Crescentini, L., Sabetta, I., De Martino, P., Obrizzo, F. and Tammaro, U. (2014): *Clues to the cause of the 2011-2013 Campi Flegrei caldera unrest, Italy, from continuous GPS data*. *Geophysical Research Letters*, 41, 3081-3088, doi:10.1002/2014GL059539.
- Aster, R. C. and Meyer, R. P. (1988): *Three-dimensional velocity structure and hypocenter distribution in the Campi Flegrei caldera, Italy*. *Tectonophysics*, 149, 3-4, 195-218.
- Avallone, A., Zollo, A., Briole, P., Delacourt, C. and Beauducel, F. (1999): *Subsidence of Campi Flegrei (Italy) detected by SAR interferometry*. *Geophysical Research Letters*, 26, 15, 2303-2306.
- Bagnardi, M., Amelung, F. and Poland, M. P. (2013): *A new model for the growth of basaltic shields based on deformation of Fernandina volcano, Galapagos Islands*. *Earth and Planetary Science Letters*, 337-378, 358-366, doi:10.1016/j.epsl.2013.07.016.
- Bagnardi, M. and Amelung, F. (2012): *Space-geodetic evidence for multiple magma reservoirs and subvolcanic lateral intrusions at Fernandina Volcano, Galapagos Islands*. *J. geophys. Res.*, 117, B10406, doi:10.1029/2012JB009465.
- Bamler, R. and Hartl, P. (1998): *Synthetic aperture radar interferometry*. *Inverse Probl.*, 14, R1-R54.
- Baranov, W. (1975): *Potential fields and their transformations in applied geophysics*. Geopublication Associates.

- Barone, A., Fedi, M., Tizzani, P. and Castaldo, R. (2019): *Multiscale Analysis of DInSAR Measurements for Multi-Source Investigation at Uturuncu Volcano (Bolivia)*. Remote sensing, 11, 703, doi:10.3390/rs11060703.
- Battaglia, M., Gottsmann, J., Carbone, D. and Fernandez, J. (2008): *4D volcano gravimetry*. Geophysics, 73, 6.
- Battaglia, M., Cervelli, P. F. and Murray, J. R. (2013): *dMODELS: A MATLAB software package for modeling crustal deformation near active faults and volcanic centers*. Journal of Volcanology and Geothermal Research, 254, 1-4, doi:10.1016/j.jvolgeores.2012.12.018.
- Berardino, P., Fornaro, G., Lanari, R. and Sansosti, E. (2002): *A new algorithm for surface deformation monitoring based on small baseline differential SAR interferograms*. IEEE Transactions on Geoscience and Remote Sensing, 40, 11, 2375-2383.
- Berardino, P., Casu, F., Fornaro, G., Lanari, R., Manunta, M., Manzo M. and Sansosti E. (2004): *A Quantitative Analysis of the SBAS Algorithm Performance*. IEEE Transactions on Geoscience and Remote Sensing, 40, 11.
- Biggs, J., Lu, Z., Fournier, T. and Freymueller, J. T. (2010): *Magma flux at Okmok Volcano, Alaska, from a joint inversion of continuous GPS, campaign GPS, and interferometric synthetic aperture radar*. Journal of Geophysical Research, 115, B12401, doi:10.1029/2010JB007577.
- Biggs, J. and Pritchard, M. (2017): *Global volcano monitoring: What does it mean when volcanoes deform?* Elements, 13, 17-22, doi:10.2113/gselements.13.1.17.
- Blakely, J. R. (1996): *Potential theory in gravity and magnetic applications*. Cambridge University Press.
- Bonaccorso, A. and Davis, P. M. (1999): *Models of ground deformation from vertical volcanic conduits with application to eruptions of Mount St. Helens and Mount Etna*. Journal of Geophysical Research, 104, B5, 10531-10542.
- Butler, D. K. (1984): *Microgravimetric and gravity gradient techniques for detection of subsurface cavities*. Geophysics, 49, 7, 1084-1096, doi:10.1190/1.1441723.
- Byers, F. M. (1959): *Geology of Umnak and Bogoslof Islands Aleutian Islands Alaska*. Geological Survey Bulletin, 1028-L.
- Calò, M. and Tramelli, A. (2018): *Anatomy of the Campi Flegrei caldera using Enhanced Seismic Tomography Models*. Scientific reports, 8, 1: 16254.
- Camacho, A. G., Nunes, J. C., Ortiz, E., Franca, Z. and Vieira, R. (2007): *Gravimetric determination of an intrusive complex under the Island of Faial (Azores): some methodological improvements*. Geophysical Journal International, 171, 478-494, doi:10.1111/j.1365-246X.2007.03539.x.
- Camacho, A. G., Gonzalez, P. J., Fernandez, J. and Berrino, G. (2011): *Simultaneous inversion of surface deformation and gravity changes by means of extended bodies with a free geometry: Application to deforming calderas*. Journal of Geophysical Research, 116, B10401, doi:10.1029/2010JB008165.

- Camacho, A. G. and Fernandez, J. (2019): *Modeling 3D Free-geometry Volumetric Sources Associated to Geological and Anthropogenic Hazards from Space and Terrestrial Geodetic data*. Remote Sensing, 11, 2042, doi:10.3390/rs11172042.
- Camacho, A., Fernandez, J., Samsonov, S. V., Tiampo, K. F. and Palano M. (2020): *3D multi-source model of elastic volcanic ground deformation*. Earth and Planetary Science Letters, 547, 116445, doi:10.1016/j.epsl.2020.116445.
- Castaldo, R., Gola, G., Santilano, A., De Novellis, V., Pepe, S., Manzo, M., Manzella, A. and Tizzani, P. (2017): *The role of thermo-rheological properties of the crust beneath Ischia Island (Southern Italy) in the modulation of the ground deformation pattern*. Journal of Volcanology and Geothermal Research, 344, 154-173, doi:10.1016/j.jvolgeores.2017.03.003.
- Castaldo, R., D'Auria, L., Pepe, S., Solaro, G., De Novellis, V. and Tizzani, P. (2018): *The impact of crustal rheology on natural seismicity: Campi Flegrei caldera case study*. Geoscience Frontiers, 10, 453-466, doi:10.1016/j.gsf.2018.02.003.
- Castaldo, R., Barone, A., Fedi, M. and Tizzani, P. (2018b): *Multiridge Method for Studying Ground-Deformation Sources: Application to Volcanic Environments*. Scientific Reports, 8:13420, doi:10.1038/s41598-018-31841-4.
- Casu, F., Manzo, M. and Lanari, R. (2006). *A quantitative assessment of the SBAS algorithm performance for surface deformation retrieval from DInSAR data*. Remote Sens. Environ., 102, 195–210.
- Casu, F., Elefante, S., Imperatore, P., Zinno, I., Manunta, M., De Luca, C. and Lanari, R. (2014): *SBAS-DInSAR Parallel Processing for Deformation Time-Series Computation*. IEEE Journal of Selected Topics in Applied Earth Observations and Remote Sensing, 7, 8, 3285-3296, doi:10.1109/JSTARS.2014.2322671.
- Cella, F. and Fedi, M. (2015): *High-resolution Geophysical 3D Imaging for Archaeology by Magnetic and EM data: The Case of the Iron Age Settlement of Torre Galli, Southern Italy*. Survey in Geophysics, 36:831-850, doi:10.1007/s10712-015-9341-3.
- Cervelli, P., Murray, M. H., Segall, P., Aoki, Y. And Kato, T. (2001): *Estimating source parameters from deformation data, with an application to the March 1997 earthquake swarm off the Izu Peninsula, Japan*. Journal of Geophysical Research, 106, B6, 11217-11237.
- Chang, W. L., Smith, R. B., Wicks, C., Farrell, J. M. and Puskas, C. M. (2007): *Accelerated uplift and magmatic intrusion of the Yellowstone Caldera, 2004–2006*. Science, 318, 952–956, doi:10.1126/science.1146842.
- Chang, W. L., Smith, R. B., Farrell, J. and Puskas, C. M. (2010): *An extraordinary episode of Yellowstone caldera uplift, 2004-2010, from GPS and InSAR observations*. Geophysical Research Letters, 37, L23302, doi:10.1029/2010GL045451.
- Chadwick, W. W. and Howard, K. A. (1991): *The pattern of circumferential and radial eruptive fissures on the volcanoes of Fernandina and Isabela Islands, Galapagos*. Bull. Volcanol., 53, 259–275.
- Chadwick, W. W. and Dieterich, J. H. (1995): *Mechanical modeling of circumferential and radial dike intrusion on Galapagos volcanoes*. J. Volc. Geotherm. Res., 66, 37–52.

Chadwick, W. W., Jonsson, S., Geist, D., Poland, M., Johnson, D., Batt, S., Harpp, K. and Ruiz, A. (2011): *The May 2005 eruption of Fernandina volcano, Galapagos: the first circumferential dike intrusion observed by GPS and InSAR*. Bull. Volcanol., 73, 6, 679–697.

Chauhan, M. S., Fedi, M. and Sen, M. K. (2018): *Gravity inversion by Multi-Homogeneity Depth Estimation method for investigating salt domes and complex sources*. Geophysical Prospecting, 66, 175-191, doi:10.1111/1365-2478.12603.

Chauhan, M. S., Cannavò, F., Carbone, D. and Greco F. (2020): *Insights Into Mount Etna December 2018 Eruption From Joint Inversion of Deformation and Gravity Data*. Geophysical Research Letters, 47, e2020GL087786, doi:10.1029/2020GL087786.

Chiodini, G., Vandemeulebrouck, J., Caliro, S., D'Auria, L., De Martino, P., Mangiacapra, A. and Petrillo, Z. (2015): *Evidence of thermal-driven processes triggering the 2005–2014 unrest at Campi Flegrei caldera*. Earth and Planetary Science Letters, 414, 58-67.

Chmielowski, J., Zandt, G. and Haberland, C. (1999): *The Central Andean Altiplano-Puna Magma Body*. Geophysical Research Letters, 26, 6, 783-786.

Christiansen, R. L. (2001): *The Quaternary and Pliocene Yellowstone Plateau Volcanic Field of Wyoming, Idaho, and Montana*. U.S. Geol. Surv. Prof. Pap., 729-G, 145.

Comeau, M. J., Unsworth, M. J., Ticona, F. and Sunagua, M. (2015): *Magnetotelluric images of magma distribution beneath Volcan Uturuncu, Bolivia: Implications for magma dynamics*. Geology, 43, 3, 243-246, doi:10.1130/G36258.1.

Comeau, M. J., Unsworth, M. J. and Cordell, D. (2016): *New constraints on the magma distribution and composition beneath Volcan Uturuncu and the southern Bolivian Altiplano from magnetotelluric data*. Geosphere, 12, 5, 1391-1421, doi:10.1130/GES01277.1.

Cooper, G. R. J. (2004): *A semi-automatic Procedure for the Interpretation of Geophysical Data*. Exploration Geophysics, 35, 182-187.

D'Auria, L., Giudicepietro, F., Aquino, I., Borriello, G., Del Gaudio, C., Lo Bascio, D., and Ricco, C. (2011): *Repeated fluid-transfer episodes as a mechanism for the recent dynamics of Campi Flegrei caldera (1989–2010)*. Journal of Geophysical Research: Solid Earth, 116, B4.

D'Auria, L., Pepe, S., Castaldo, R., Giudicepietro, F., Macedonio, G., Ricciolino, P., Tizzani, P., Casu, F., Lanari, R., Manzo, M., Martini, M., Sansosti, E. and Zinno, I. (2015): *Magma injection beneath the urban area of Naples: a new mechanism for the 2012-2013 volcanic unrest at Campi Flegrei caldera*. Scientific Reports, 5:13100, doi:10.1038/srep13100.

De Luca, C., Cuccu, R., Elefante, S., Zinno, I., Manunta, M., Casola, V., Rivolta, G., Lanari, R. and Casu, F. (2015): *An On-Demand Web Tool for the Unsupervised Retrieval of Earth's Surface Deformation from SAR data: The P-SBAS Service within the ESA G-POD Environment*. Remote sensing, 7, 15630-15650, doi:10.3390/rs71115630.

De Luca, C., Zinno, I., Manunta, M., Lanari, R. and Casu, F. (2017): *Large areas surface deformation analysis through a cloud computing P-SBAS approach for massive processing of DInSAR time series*. Remote Sensing of Environment, 202, 3-17, doi:10.1016/j.rse.2017.05.022.

- De Natale, G., Troise, C., Pingue, F., Mastrolorenzo, G., Pappalardo, L., Battaglia, M. and Boschi, E. (2006): *The Campi Flegrei caldera: unrest mechanisms and hazards*. Mechanisms of Activity and Unrest at Large Calderas, Geological Society, London, Special Publications, 269, 25-45.
- De Siena, L., Del Pezzo, E. and Bianco, F. (2010): *Seismic attenuation imaging of Campi Flegrei: Evidence of gas reservoirs, hydrothermal basins, and feeding systems*. Journal of Geophysical Research: Solid Earth, 115, B09312, doi:10.1029/2009JB006938.
- De Siena, L., Amoruso, A., Del Pezzo, E., Wakeford, Z., Castellano, M. and Crescentini, L. (2017a): *Space-weighted seismic attenuation mapping of the aseismic source of Campi Flegrei 1983–84 unrest*. Geophysical Research Letters, 44, 4, 1740-1748.
- De Siena, L., Chiodini, G., Vilardo, G., Del Pezzo, E., Castellano, M., Colombelli, S., Tisato, N. and Ventura, G. (2017b): *Source and dynamics of a volcanic caldera unrest: Campi Flegrei, 1983–84*. Scientific Reports, 7:8099.
- De Siena, L., Sammarco, C., Cornwell, D. G., La Rocca, M., Bianco, F., Zaccarelli, L. and Nakahara, H. (2018): *Ambient seismic noise image of the structurally-controlled heat and fluid feeder pathway at Campi Flegrei caldera*. Geophysical Research Letters 45, 13, 6428- 6436.
- de Silva, S. L. (1989): *Altiplano-Puna volcanic complex of the central Andes*. Geology, 17, 12, 1102-1106.
- de Silva, S. L. and Gosnold, W. D. (2007): *Episodic construction of batholiths: Insights from the spatiotemporal development of an ignimbrite flare-up*. Journal of Volcanology and Geothermal Research, 167, 320-335, doi:10.1016/j.jvolgeores.2007.07.015.
- Del Gaudio, C., Aquino, I., Ricco, C. and Serio, C. (2009): *Monitoraggio geodetico dell'area vulcanica napoletana: risultati della livellazione geometrica di precisione eseguita ai Campi Flegrei a settembre 2008*. Quaderni di Geofisica.
- Del Negro, C., Currenti, G. and Scandura, D. (2009): *Temperature-dependent viscoelastic modeling of ground deformation: Application to Etna volcano during the 1993-1997 inflation period*. Physics of the Earth and Planetary Interiors, 172, 299-309, doi:10.1016/j.pepi.2008.10.019.
- Del Negro, C., Currenti, G., Solaro, G., Greco, F., Pepe, A., Napoli, R., Pepe, S., Casu, F. and Sansosti, E. (2013): *Capturing the fingerprint of Etna volcano activity in gravity and satellite radar data*. Scientific Reports, 3:3089.
- del Potro, R., Diez, M., Blundy, J., Camacho, A. G. and Gottsmann, J. (2013): *Diapiric ascent of silicic magma beneath the Bolivian Altiplano*. Geophysical Research Letters, 40, 2044-2048, doi:10.1002/grl.50493.
- Di Luccio, F., Pino, N. A., Piscini, A. and Ventura, G. (2015): *Significance of the 1982–2014 Campi Flegrei seismicity: Preexisting structures, hydrothermal processes, and hazard assessment*. Geophysical Research Letters, 42, 18, 7498-7506.

- Di Vito, M. A., Acocella, V., Aiello, G., Barra, D., Battaglia, M., Carandente, A., Del Gaudio, C., de Vita, S., Ricciardi, G. P., Ricco, C., Scandone, R. and Terrasi, F. (2016): *Magma transfer at Campi Flegrei caldera (Italy) before the 1538 AD eruption*. Scientific Reports, 6, 32245.
- Dzurisin, D. (2007): *Volcano Deformation, Geodetic Monitoring Techniques*. Praxis Publishing, Springer.
- Farrell, J., Smith, R. B., Husen, S. and Diehl, T. (2014): *Tomography from 26 years of seismicity revealing that the spatial extent of the Yellowstone crustal magma reservoir extends well beyond the Yellowstone Caldera*. Geophys. Res. Lett., 41, 3068–3073, doi:10.1002/2014GL059588.
- Fedi, M. and Florio, G. (2001): *Detection of potential fields source boundaries by enhanced horizontal derivative method*. Geophysical Prospecting, 49, 40-58.
- Fedi, M., Hansen, P. C. and Paoletti, V. (2005): *Analysis of depth resolution in potential-field inversion*. Geophysics, 70, 6 A1-A11, doi:10.1190/1.2122408.
- Fedi, M. (2007): *DEXP: A fast method to determine the depth and the structural index of potential fields sources*. Geophysics, 72, 1, I1-I11, doi:10.1190/1.2399452.
- Fedi, M., Florio, G. and Quarta, T. A. M. (2009): *Multiridge analysis of potential fields: Geometric method and reduced Euler deconvolution*. Geophysics, 74, 4, L53-L65, doi:10.1190/1.3142722.
- Fedi, M., Florio, G. and Cascone, L. (2012): *Multiscale analysis of potential fields by a ridge consistency criterion: the reconstruction of the Bishop basement*. Geophysical Journal International, 188, 103-114, doi:10.1111/j.1365-246X.2011.05259.x.
- Fedi, M., Florio, G. and Paoletti, V. (2015): *MHODE: a local-homogeneity theory for improved source-parameter estimation of potential fields*. Geophysical Journal International, 202, 887-900, doi:10.1093/gji/ggv185.
- Fedi, M. (2016): *Scaling laws in geophysics: Application to potential fields of methods based on the laws of self-similarity and homogeneity*. Fractal solutions for understanding complex systems in Earth sciences, Springer Earth System Sciences.
- Fernandez, J., Yu, T. T., Rogriduez-Velasco, G., Gonzalez-Matesanz, J., Romero, R., Rodriguez, G., Quiros, R., Dalda, A., Aparicio, A. and Blanco, M.J. (2003): *New geodetic monitoring system in the volcanic island of Tenerife, Canaries, Spain. Combination of InSAR and GPS techniques*. Journal of Volcanology and Geothermal Research, 124, 241-253, doi:10.1016/S0377-0273(03)00073-8.
- Fialko, Y., Khazan, Y. and Simons, M. (2001): *Deformation due to a pressurized horizontal circular crack in an elastic half-space, with applications to volcano geodesy*. Geophysical Journal International, 146, 181-190.
- Fialko, Y. and Pearse, J. (2012): *Sombrero Uplift Above the Altiplano-Puna Magma Body: Evidence of a Ballooning Mid-Crustal Diapir*. Science, 338, 6104, 250-252.
- Finney, B., Turner, S., Hawkesworth, C., Larsen, J., Nye, C., George, R., Bindeman, I. and Eichelberger, J. (2008): *Magmatic Differentiation at an Island-arc Caldera: Okmok Volcano, Aleutian Islands, Alaska*. Journal of Petrology, 49, 5, 857-884, doi:10.1093/petrology/egn008.

- Florio, G., Fedi, M., Cella, F. and Rapolla, A. (1999): *The Campanian Plain and Phlegrean Fields: structural setting from potential field data*. Journal of Volcanology and Geothermal Research, 91, 361-379.
- Franceschetti, G., and Lanari, R. (1999): *Synthetic Aperture Radar Processing*. CRC Press.
- Fournier, R. O. (1989): *Geochemistry and dynamics of the Yellowstone National Park hydrothermal system*. Annu. Rev. Earth Planet. Sci., 17, 13.
- Galerkin, B. G. (1930): *Studying stresses and strains in an elastic isotropic body*. DAN SSSR, A.
- Geerstma, J. and Van Opstal, K. (1973): *A numerical technique for predicting subsidence above compacting reservoirs, based on the nucleus of strain concept*. Verhandelingen Kon. Ned. Geol. Mijnbouw. Gen., 28, 63-78.
- Giudicepietro, F., Macedonio, G., D'Auria, L. and Martini, M. (2016): *Insight into vent opening probability in volcanic calderas in the light of a sill intrusion model*. Pure and Applied Geophysics, 173, 5, 1703-1720.
- Gottsmann, J., Blundy, J., Henderson, S., Pritchard, M. E. and Sparks R. S. J. (2017): *Thermomechanical modeling of the Altiplano-Puna deformation anomaly: Multiparameter insights into magma mush reorganization*. Geosphere, 13, 4, doi:10.1130/GES01420.1.
- Gudmundsson, A. (2012): *Magma chambers: Formation, local stresses, excess pressures, and compartments*. Journal of Volcanology and Geothermal Research, 237-238, 19-41, doi:10.1016/j.jvolgeores.2012.05.015.
- Gupta, V. K. and Ramani, N. (1982): *Optimum second vertical derivatives in geologic mapping and mineral exploration*. Geophysics, 47, 12, 1706-1715, doi:10.1190/1.1441320.
- Henderson, S. T. and Pritchard, M. E. (2013): *Decadal volcanic deformation in the Central Andes Volcanic Zone revealed by InSAR time series*. Geochemistry Geophysics Geosystems, 14, 5, 1358-1374, doi:10.1002/ggge.20074.
- Henderson, S. T. and Pritchard, M. E. (2017): *Time-dependent deformation of Uturuncu volcano, Bolivia, constrained by GPS and InSAR measurements and implications for source models*. Geosphere, 13, 6, 1834-1854, doi:10.1130/GES01203.1.
- Hickey, J., Gottsmann, J. and del Potro, R. (2013): *The large-scale surface uplift in the Altiplano-Puna region of Bolivia: A parametric study of source characteristics and crustal rheology using finite element analysis*. Geochemistry Geophysics Geosystems, 14, 3, 540-555, doi:10.1002/ggge.20057.
- Isaia, R., Vitale, S., Di Giuseppe, M. G., Iannuzzi, E., Tramparulo, F. D. A. and Troiano, A. (2015): *Stratigraphy, structure, and volcano-tectonic evolution of Solfatara maar-diatreme (Campi Flegrei, Italy)*. GSA Bulletin, 127, 9-10, 1485-1504.
- Jay, J. A., Pritchard, M. E., West, M. E., Christensen, D., Haney, M., Minaya, E., Sunagua, M., McNutt, S. R. and Zabala, M. (2012): *Shallow seismicity, triggered seismicity, and ambient noise tomography at the long-dormant Uturuncu Volcano, Bolivia*. Bulletin of Volcanology, 74, 817-837, doi:10.1007/s00445-011-0568-7.

- Jonsson, S., Zebker, H., Cervelli, P., Segall, P., Garbeil, H., Mougini-Mark, P. and Rowland, S. (1999): *A Shallow-Dipping Dike fed the 1995 Flank Eruption at Fernandina Volcano, Galapagos, Observed by satellite Radar Interferometry*. *Geophysical Research Letters*, 26, 8, 1077-1080.
- Kukarina, E., West, M., Keyson, L. H., Koulakov, I., Tsibizov, L. and Smirnov, S. (2017): *Focused magmatism beneath Uturuncu volcano, Bolivia: Insights from seismic tomography and deformation modeling*. *Geosphere* 2017, 13, 6, 1855-1866, doi:10.1130/GES01403.1.
- Lanari, R., Lundgren, P., Sansosti, E. (1998): *Dynamic deformation of Etna volcano observed by satellite radar interferometry*. *Geophysical Research Letters*, 25, 10, 1541-1544.
- Lanari, R., Casu, F., Manzo, M., Zeni, G., Berardino, P., Manunta, M. and Pepe, A. (2007): *An overview of the small baseline subset algorithm: A DInSAR technique for surface deformation analysis*. *Pure Appl. Geophys.*, 164, 637–661, doi:10.1007/s00024-007-0192-9.
- Larsen, J., Neal, C., Webley, P., Freymueller, J., Haney, M., McNutt, S., Schneider, D., Prejean, S., Schaefer, J. and Wessels, R. (2009): *Eruption of Alaska Volcano Breaks Historic Pattern*. *EOS*, 90, 20, 173-180.
- Lau, N., Tymofyeyeva, E. and Fialko, Y. (2018): *Variations in the long-term uplift rate due to the Altiplano-Puna magma body observed with Sentinel-1 interferometry*. *Earth and Planetary Science Letters*, 491, 43-47, doi:10.1016/j.epsl.2018.03.026.
- Li, J., and Heap, A. D. (2008): *A Review of Spatial Interpolation Methods for Environmental Scientists*. Geoscience Australia, Canberra, Australia.
- Love, A. E. H. (1906): *A treatise on the mathematical theory of elasticity*. Cambridge University Press, second edition.
- Lowrie, W. (2007): *Fundamentals of Geophysics*. Cambridge University Press, second edition.
- Lu, Z., Mann, D. and Freymueller, J. (1998): *Satellite Radar Interferometry Measures Deformation at Okmok Volcano*. *EOS*, 79, 39, 461-476.
- Lu, Z., Mann, D., Freymueller, J. T. and Meyer, D. J. (2000): *Synthetic aperture radar interferometry of Okmok volcano, Alaska: Radar observations*. *Journal of Geophysical Research*, 105, B5, 10791-10806.
- Lu, Z., Masterlark, T. and Dzurisin, D. (2005): *Interferometric synthetic aperture radar study of Okmok volcano, Alaska, 1992-2003: Magma supply dynamics and postemplacement lava flow deformation*. *Journal of Geophysical Research*, 110, B02403, doi:10.1029/2004JB003148.
- Luiso, P., Paoletti, V., Nappi, R., La Manna, M., Cella, F., Gaudiosi, G., Fedi, M. and Iorio, M. (2018): *A multidisciplinary approach to characterize the geometry of active faults: the example of Mt. Massico, Southern Italy*. *Geophysical Journal International*, 213, 1673-1681, doi:10.1093/gji/ggy080.
- Manconi, A., Walter, T. R., Manzo, M., Zeni, G., Tizzani, P., Sansosti, E. and Lanari, R. (2010): *On the effects of 3-D mechanical heterogeneities at Campi Flegrei caldera, southern Italy*. *Journal of Geophysical Research*, 115, B08405, doi:10.1029/2009JB007099.

- Manzo, M., Ricciardi, G. P., Casu, F., Ventura, G., Zeni, G., Borgstrom, S., Berardino, P., Del Gaudio, C. and Lanari, R. (2006): *Surface deformation analysis in the Ischia Island (Italy) based on spaceborne radar interferometry*. Journal of Volcanology and Geothermal Research, 151, 4, 399-416, doi:10.1016/j.jvolgeores.2005.09.010.
- Masterlark, T., Haney, M., Dickinson, H., Fournier, T. and Searcy, C. (2010): *Rheologic and structural controls on the deformation of Okmok volcano, Alaska: FEMs, InSAR, and ambient noise tomography*. Journal of Geophysical Research, 115, B02406, doi:10.1029/2009JB006324.
- Masterlark, T., Feigl, K. L., Haney, M., Stone, J., Thurber, C. and Ronchin, E. (2012): *Nonlinear estimation of geometric parameters in FEMs of volcano deformation: Integrating tomography models and geodetic data for Okmok volcano, Alaska*. Journal of Geophysical Research, 117, B02407, doi:10.1029/2011JB008811.
- Masterlark, T., Donovan, T., Feigl, K. L., Haney, M., Thurber, C. H. and Tung, S. (2016): *Volcano deformation source parameters estimated from InSAR: Sensitivities to uncertainties in seismic tomography*. Journal of Geophysical Research: Solid Earth, 121, 3002-3016.
- Mattia, M., Bruno, V., Caltabiano, T., Cannata, A., Cannavò, F., D'Alessandro, W., Di Grazia, G., Federico, C., Gianmarco, S., La Spina, A., Liuzzo, M., Longo, M., Monaco, C., Patanè, D. and Salerno, G. (2015): *A comprehensive interpretative model of slow slip events on Mt. Etna's eastern flank*. Geochem. Geophys. Geosys., 16, 3, 635-658.
- McBirney, A. R. and Williams, H. (1969): *Geology and petrology of the Galapagos Islands*. Geol. Soc. Am. Mem., 118, 1-197.
- McFarlin, H., Christensen, D., McNutt, S. R., Ward, K. M., Ryan, J., Zandt, G. and Thompson, G. (2017): *Receiver function analyses of Uturuncu volcano, Bolivia and vicinity*. Geosphere, 14, 1, 50-64, doi:10.1130/GES01560.1.
- McTigue, D. F. (1987): *Elastic stress and deformation near a finite spherical magma body: resolution of the point source paradox*. Journal of Geophysical Research, 92, B12, 12931-12940.
- Michelfelder, G. S., Feeley, T. C. and Wilder, A. D. (2014): *The Volcanic Evolution of Cerro Uturuncu: A High-K, Composite Volcano in the Back-Arc of the Central Andes of SW Bolivia*. International Journal of Geosciences, 5, 1263-1281, doi:10.4236/ijg.2014.511105.
- Milano, M., Fedi, M. and Fairhead, J. D. (2016): *The deep crust beneath the Trans-European Suture Zone from a multiscale magnetic model*. Journal of Geophysical Research: Solid Earth, 121, doi:10.1002/2016JB012955.
- Miller, T. P., McGimsey, R. G., Richter, D. H., Riehle, J. R., Nye, C. J., Yount, M. E. and Dumoulin, J. A. (1998): *Catalog of the historically active volcanoes of Alaska*. USGS.
- Mogi, K. (1958). *Relation between eruptions of various volcanoes and the deformations of ground surfaces around them*. Bulletin of the Earthquake Research Institute, University of Tokyo, 36, 99-134.
- Muir, D. D., Blundy, J. D., Rust, A. C. and Hickey, J. (2014): *Experimental Constraints on Dacite Pre-eruptive Magma Storage Conditions beneath Uturuncu Volcano*. Journal of Petrology, 55, 4, 749-767, doi:10.1093/petrology/egu005.

- Newman, A. V., Dixon, T. H. and Gourmelen, N. (2006): *A four-dimensional viscoelastic deformation model for Long Valley Caldera, California, between 1995 and 2000*. Journal of Volcanology and Geothermal Research, 150, 244-269, doi:10.1016/j.jvolgeores.2005.07.017.
- Odé, H. (1957): *Mechanical analysis of the dike pattern of the Spanish Peaks area, Colorado*. Bull. geol. Soc. Am., 68, 567–576.
- Okada, Y. (1985): *Surface deformation due to shear and tensile faults in a half-space*. Bulletin of Seismological Society of America, 75, 4, 1135-1154.
- Okada, Y. (1992): *Internal deformation due to shear and tensile faults in a half-space*. Bulletin of Seismological Society of America, 82, 2, 1018-1040.
- Olmsted, J. M. A. (1961): *Advanced calculus*. Prentice-Hall.
- Orsi, G., Civetta, L., Del Gaudio, C., De Vita, S., Di Vito, M. A., Isaia, R., Petrazzuoli, S. M., Ricciardi, G. P. and Ricco, C. (1999): *Short-term ground deformations and seismicity in the resurgent Campi Flegrei caldera (Italy): an example of active block-resurgence in a densely populated area*. Journal of Volcanology and Geothermal Research, 91, 2-4, 415-451.
- Paoletti, V., Fedi, M. and Florio, G. (2017): *The structure of the Ischia Volcanic Island from magnetic and gravity data*. Annals of Geophysics, 60, doi:10.4401/ag-7550.
- Papkovich, P. F. (1932): *The representation of the general integral of the fundamental equations of elasticity theory in terms of harmonic functions*. Izv. Akad. Nauk SSSR, Phys-Math, 10, 1425.
- Pepe, A., Sansosti, E., Berardino, P. and Lanari, R. (2005): *On the generation of ERS/ENVISAT DInSAR time-series via the SBAS technique*. IEEE Geosci. Remote Sens. Lett., 2, 3, 265–269.
- Pepe, A. and Lanari, R. (2006): *On the extension of the minimum cost flow algorithm for phase unwrapping of multitemporal differential SAR interferograms*. IEEE Trans. Geosci. Remote Sens., 44, 9, 2374–2383.
- Pepe, S., Castaldo, R., De Novellis, V., D’Auria, L., De Luca, C., Casu, F., Sansosti, E. and Tizzani, P. (2017): *New insights on the 2012-2013 uplift episode at Fernandina Volcano (Galapagos)*. Geophysical Journal International, 211, 673-685, doi:10.1093/gji/ggx330.
- Pepe, S., De Siena, L., Barone, A., Castaldo, R., D’Auria, L., Manzo, M., Casu, F., Fedi, M., Lanari, R., Bianco, F. and Tizzani, P. (2019): *Volcanic structures investigation through SAR and seismic interferometric methods: The 2011-2013 Campi Flegrei unrest episode*. Remote Sensing of Environment, 234, 111440, doi:10.1016/j.rse.2019.111440.
- Perkins, J. P., Ward, K. M., de Silva, S. L., Zandt, G., Beck, S. L. and Finnegan, N. J. (2016): *Surface uplift in the Central Andes driven by growth of the Altiplano Puna Magma Body*. Nature Communications, 7, 13185, 1-10, doi:10.1038/ncomms13185.
- PLUTONS project. Probing Lazufre and Uturuncu TOgether: Nsf (USA), Nerc (UK), Nserc (Canada), Sergeotecmin (Bolivia), Sernageomin (Chile), observatorio San calixto (Bolivia), universidad nacional de Salta (Argentina), universidad major San andres (Bolivia), universidad de poto Si (Bolivia), Sernap (Bolivia), chilean Seismological service, universidad de San Juan (Argentina)*. The PLUTONS Project is funded by the National Science Foundation Continental Dynamics Program and the Natural Environment Research Council. The PLUTONS Group.

Oregon State University, Dept. of Geosciences, 104 Wilkinson Hall, Corvallis, OR 97331-5506 541-737-1201.

Pritchard, M. E. and Simons, M. (2002): *A satellite geodetic survey of large-scale deformation of volcanic centres in the central Andes*. *Nature*, 418, 167-171.

Pritchard, M. E. and Simons, M. (2004): *Surveying Volcanic Arcs with Satellite Radar Interferometry: The Central Andes, Kamchatka, and Beyond*. *GSA Today*, 14, 8.

Pritchard, M. E., de Silva, S. L., Michelfelder, G., Zandt, G., McNutt, S. R., Gottsmann, J., West, M. E., Blundy, J., Christensen, D. H., Finnegan, N. J., Minaya, E., Sparks, R. S. J., Sunagua, M., Unsworth, M. J., Alvizuri, C., Comeau, M. J., del Potro, R., Diaz, D., Diez, M., Farrell, A., Henderson, S. T., Jay, J. A., Lopez, T., Legrand, D., Naranjo, J. A., McFarlin, H., Muir, D., Perkins, J. P., Spica, Z., Wilder, A. and Ward, K. M. (2018): *Synthesis: PLUTONS: Investigating the relationship between pluton growth and volcanism in the Central Andes*. *Geosphere*, 14 (3), 954-982, doi:10.1130/GES01578.1.

Puskas, C. M., Smith, R. B., Meertens, C. M. and Chang W. L. (2007): *Crustal deformation of the Yellowstone–Snake River Plainvolcano-tectonic system: Campaign and continuous GPS observations, 1987–2004*. *J. Geophys. Res.*, 112, B03401, doi:10.1029/2006JB004325.

Rao, D. A., Ram Babu, H. V. and Sanker Narayan, P. V. (1981): *Interpretation of magnetic anomalies due to dikes: The complex gradient method*. *Geophysics*, 46, 11, 1572-1578, doi:10.1190/1.1441164.

Reid, A. B., Allsop, J. M., Granser, H., Millett, A. J. and Somerton, I. W. (1990): *Magnetic interpretation in three dimensions using Euler deconvolution*. *Geophysics*, 55, 1, 80-91, doi:10.1190/1.1442774.

Reuber, G. S., Kaus, B. J. P., Popov, A. A. and Baumann, T. S. (2018): *Unraveling the Physics of the Yellowstone Magmatic System Using Geodynamic Simulations*. *Front. Earth Sci.*, 6, 117.

Ridsdill-Smith, T. A. and Dentith, M. C. (1999): *The wavelet transform in aeromagnetic processing*. *Geophysics*, 64, 4, 1003-1013, doi:10.1190/1.1444609.

Rodriguez-Molina, S., Gonzalez, P. J., Charco, M., Negredo, A. M. and Schmidt, D.A. (2021): *Time-Scales of Inter-eruptive Volcano Uplift Signals: Three Sisters Volcanic center, Oregon (USA)*. *Frontiers in Earth Science*, 8, 645: 1-30, doi:10.3389/feart.2020.577588.

Rosen, P. A., Hensley, S., Joughin, I. R., Li, F. K., Madsen, S. N., Rodríguez, E. and Goldstein, R. M. (2000): *Synthetic aperture radar interferometry*. *IEEE Trans. Geosci. Remote Sens.*, 48, 333–382.

Rosen, P. A., Hensley, S., Gurrola, E., Rogez, F., Chan, S. and Martin, J. (2001): *SRTM C-band topographic data quality assessment and calibration activities*. in *Proc. IGARSS*, 739–741, Sydney, Australia.

Rowland, S. K. and Munro, D. C. (1992): *The caldera of Volcan Fernandina: a remote sensing study of its structure and recent activity*. *Bull. Volcanol.*, 55, 97–109.

- Rowland, S. K. (1996): *Slopes, lava flow volumes, and vent distributions on Volcano Fernandina, Galapagos Islands*. Journal of Geophysical Research, 101, 27657–27673.
- Sadd, M. H. (2005): *Elasticity. Theory, Applications, and Numerics*. Elsevier.
- Schilling, F. R., Partzsch, G. M., Brasse, H. and Schwarz, G. (1997): *Partial melting below the magmatic arc in the central Andes deduced from geoelectromagnetic field experiments and laboratory data*. Physics of the Earth and Planetary Interiors, 103, 17-31.
- Schmitz, M., Heinsohn, W. D. and Schilling, F. R. (1997): *Seismic, gravity and petrological evidence for partial melt beneath the thickened Central Andean crust*. Tectonophysics, 270, 313-326.
- Sen, M. K. and Stoffa, P. L. (2013): *Global Optimization Methods in Geophysical Inversion*. Cambridge University Press, second edition.
- Serlenga, V., de Lorenzo, S., Russo, G., Amoroso, O., Garambois, S., Virieux, J. and Zollo, A. (2016): *A three-dimensional QP imaging of the shallowest subsurface of Campi Flegrei offshore caldera, southern Italy*. Geophysical Research Letters, 43, 21, 11-209.
- Sigurdsson, H. (1999): *The Encyclopedia of Volcanoes*. Academic Press, Elsevier.
- Simkin, T. and Howard, K. A. (1970): *Caldera collapse in the Galapagos islands*. Science, 169, 429–437.
- Simkin, T. (1984): *Geology of Galapagos Islands, in Galapagos*, ed. Perry, R., 15–41, Pergamon, Oxford, UK.
- Siniscalchi, A., Tripaldi, S., Romano, G., Chiodini, G., Improta, L., Petrillo, Z., D’Auria, L., Caliro, S. and Avino, R. (2019): *Reservoir Structure and Hydraulic Properties of the Campi Flegrei Geothermal System Inferred by Audiomagnetotelluric, Geochemical and Seismicity Study*. Journal of Geophysical Research: Solid Earth, 124, 5336-5356.
- Sparks, R. S. J., Folkes, C. B., Humphreys, M. C. S., Barfod, D. N., Clavero, J., Sunagua, M. C., McNutt, S. R. and Pritchard, M. E. (2008): *Uturuncu volcano, Bolivia: volcanic unrest due to mid-crustal magma intrusion*. American Journal of Science, 308, 727-769, doi:10.2475/06.2008.01.
- Stanton, J. M. (2001): *Galton, Pearson and the Peas: a brief history of linear regression for statistics instructors*. Journal of Statistics Education, 9, 3.
- Stavrev, P., Reid, A. (2007): *Degrees of homogeneity of potential fields and structural indices of Euler deconvolution*. Geophysics, 72, 1, L1-L12, doi:10.1190/1.2400010.
- Sun, R. J. (1969): *Theoretical Size of Hydraulically Induced Horizontal Fractures and Corresponding Surface Uplift in an Idealized Medium*. Journal of Geophysical Research, 74, 25.
- Thompson, D. T. (1982): *EULDPH: A new technique for making computer-assisted depth estimates from magnetic data*. Geophysics, 47, 1, 31-37, doi:10.1190/1.1441278.
- Tizzani, P., Berardino, P., Casu, F., Euillades, P., Manzo, M., Ricciardi, G. P., Zeni, G. and Lanari, R. (2007): *Surface deformation of Long Valley caldera and Mono Basin, California*,

investigated with the SBAS-InSAR approach. Remote Sensing of Environments, 108, 3, 277-289, doi:10.1016/j.rse.2006.11.015.

Tizzani, P., Battaglia, M., Zeni, G., Atzori, S., Berardino, P. and Lanari, R. (2009): *Uplift and magma intrusion at Long Valley caldera from InSAR and gravity measurements*. Geology, 37, 1, 63-66.

Tizzani, P., Manconi, A., Zeni, G., Pepe, A., Manzo, M., Camacho, A. and Fernandez, J. (2010): *Long-term versus short-term deformation processes at Tenerife (Canary Islands)*. Journal of Geophysical Research, 115, B12412.

Tizzani, P., Battaglia, M., Castaldo, R., Pepe, A., Zeni, G. and Lanari, R. (2015): *Magma and fluid migration at Yellowstone Caldera in the last three decades inferred from InSAR, levelling, and gravity measurements*. Journal of Geophysical Research: Solid Earth, 120, 2627-2647, doi:10.1002/2014JB011502.

Trasatti, E., Casu, F., Giunchi, C., Pepe, S., Solaro, G., Tagliaventi, S., Berardino, P., Manzo, M., Pepe, A., Ricciardi, G. P., Sansosti, E., Tizzani, P., Zeni, G. and Lanari, R. (2008): *The 2004-2006 uplift episode at Campi Flegrei caldera (Italy): Constraints from SBAS-DInSAR ENVISAT data and Bayesian source inference*. Geophysical Research Letters, 35, 7.

Vanorio, T., Virieux, J., Capuano, P. and Russo, G. (2005): *Three-dimensional seismic tomography from P wave and S wave microearthquake travel times and rock physics characterization of the Campi Flegrei Caldera*. Journal of Geophysical Research: Solid Earth, 110, B3.

Vanorio, T. and Kanitpanyacharoen, W. (2015): *Rock physics of fibrous rocks akin to Roman concrete explains uplifts at Campi Flegrei Caldera*. Science, 349, 6248, 617-621.

Vasco, D. W., Puskas, C. M., Smith, R. B. and Meertens, C. M. (2007): *Crustal deformation and source models of the Yellowstone volcanic field from geodetic data*. J. Geophys. Res., 112, B07402, doi:10.1029/2006JB004641.

Vilardo, G., Isaia, R., Ventura, G., De Martino, P. and Terranova, C. (2010): *InSAR Permanent Scatterer analysis reveals fault re-activation during inflation and deflation episodes at Campi Flegrei caldera*. Remote Sensing of Environment, 114, 10, 2373-2383.

Vitale, S. and Isaia, R. (2014): *Fractures and faults in volcanic rocks (Campi Flegrei, southern Italy): insight into volcano-tectonic processes*. International Journal of Earth Sciences, 103, 3, 801-819.

Vitale, A. and Fedi, M. (2020): *Self-constrained inversion of potential fields through a 3D depth weighting*. Geophysics, 85, 6, G143-G156, doi:10.1190/GEO2019-0812.1.

Walter, T. R. and Motagh, M. (2014): *Deflation and inflation of a large magma body beneath Uturuncu volcano, Bolivia? Insights from InSAR data, surface lineaments and stress modelling*. Geophysical Journal International, 198, 462-473, doi:10.1093/gji/ggu080.

Ward, K. M., Zandt, G., Beck, S. L., Christensen, D. H. and McFarlin, H. (2014): *Seismic imaging of the magmatic underpinnings beneath the Altiplano-Puna volcanic complex from the joint*

inversion of surface wave dispersion and receiver functions. Earth and Planetary Science Letters, 404, 43-53, doi:10.1016/j.epsl.2014.07.022.

Ward, K. M., Delph, J. R., Zandt, G., Beck, S. L. and Ducea, M. N. (2017): *Magmatic evolution of a Cordilleran flare-up and its role in the creation of silicic crust*. Scientific Reports, 7, 9047, 1-8, doi:10.1038/s41598-017-09015-5.

Wicks, C., Thatcher, W. and Dzurisin, D. (1998): *Migration of fluids beneath Yellowstone Caldera inferred from satellite radar interferometry*. Science, 282, 458–462.

Wicks, C., Thatcher, W., Dzurisin, D. and Svarc, J. (2006): *Uplift, thermal unrest and magma intrusion at Yellowstone Caldera*. Nature, 440, 72–75.

Wicks, C. W., Dzurisin, D., Lowenstern, J. B. and Svarc, J. (2020): *Magma Intrusion and Volatile Ascent Beneath Norris Geyser Basin, Yellowstone National Park*. Journal of Geophysical Research: Solid Earth, 125, e2019JB018208, doi:10.1029/2019JB018208.

Wright, T. J., Lu, Z. and Wicks, C. (2003): *Source model for the Mw 6.7, 23 October 2002, Nenana Mountain Earthquake (Alaska) from InSAR*. Geophysical Research Letters, 30, 18, 1974, doi:10.1029/2003GL018014.

Xue, X., Freymueller, J. And Lu, Z. (2020): *Modeling the Postruptive Deformation at Okmok Based on the GPS and InSAR Time Series: Changes in the Shallow Magma Storage System*. Journal of Geophysical Research: Solid Earth, 125, e2019JB017801, doi:10.1029/2019JB017801.

Yang, X. M. and Davis, P. M. (1988): *Deformation from inflation of a dipping finite prolate spheroid in an elastic half-space as a model for volcanic stressing*. Journal of Geophysical Research, 93, B5, 4249-4257.

Yang, Y., Pepe, A., Manzo, M., Bonano, M., Liang, D. N. and Lanari, R. (2013): *A simple solution to mitigate noise effects in time-redundant sequences of small baseline multi-look DInSAR interferograms*. Remote Sens. Lett., 4, 609–618, doi:10.1080/2150704X.2013.771826.

Zandt, G., Leidig, M., Chmielowski, J., Baumont, D. and Yuan, X. (2003): *Seismic Detection and Characterization of the Altiplano-Puna Magma Body, Central Andes*. Pure and Applied Geophysics, 160, 789-807.

Zebker, H. A. and Villasenor, J. (1992): *Decorrelation in interferometric radar echoes*. IEEE Trans. Geosci. Remote Sens., 30, 950–959.

Zollo, A., Judenherc, S., Auger, E., D'Auria, L., Virieux, J., Capuano, P. and Musacchio, G. (2003): *Evidence for the buried rim of Campi Flegrei caldera from 3-d active seismic imaging*. Geophysical Research Letters, 30, 19.

ACKNOWLEDGEMENTS

This PhD project has been supported by the Institute for Electromagnetic Sensing of the Environment of the National Research Council of Italy (IREA – CNR) and the Department of Earth, Environmental and Resources Science (DiSTAR) of the University of Naples Federico II.

A part of the PhD activities has been funded by IREA – CNR through the geophysical projects DIT.AD012.028 “Accordo operativo MISE – DGRME e CNR-IREA”, DTA.AD004.047 “Accordo Dipartimento Protezione Civile e CNR – IREA”, DTA.AD003.433 – PRIN 2017 – FLUIDs, DTA.AD004.286 “Accordo 2019 – 2021 Dipartimento Protezione Civile e CNR – IREA”, and by DiSTAR, which has partially funded the abroad research period of the PhD program.

I would like to acknowledge my Supervisor, Prof. Maurizio Fedi, who has supervised my PhD activities providing me with all his expert knowledge; I thank him since he has always appreciated my work and he has guided me throughout my educational career, from bachelor’s degree to doctorate, improving my skills with his experienced advice and scientific argumentations.

I would like to acknowledge my Co-Supervisor, Dr. Raffaele Castaldo, who has been the first to conceive this ambitious research project and to deeply believe in its accomplishment; I thank him for having shared his ideas and knowledge with me, guiding and assisting me every day in solving any problem.

I would like to acknowledge my Co-Supervisor, Dr. Pietro Tizzani, who has supported and advised me throughout the PhD program; I thank him for having deeply contributed to my education, allowing me to gain experience in academic, research and professional frameworks.

I thank again both my Co-Supervisors, Dr. Pietro Tizzani and Dr. Raffaele Castaldo, for having always appreciated my work, giving me the great opportunity of funding my PhD scholarship, as well as almost all the activities for my education.

I would like to acknowledge and thank Prof. Valeria Paoletti, who has supervised my PhD activities and who has always been available for help.

I would like to acknowledge Dr. Antonio Pepe, Dr. Susi Pepe and Dr. Giuseppe Solaro since they have doubtless been available to process and provide me the data to accomplish my PhD thesis. Also, I thank them for their availability to help me in any issue.

I would like to acknowledge and thank Prof. José Fernandez Torres, who has welcomed me at Instituto de Geociencias (IGEO) and supervised my abroad research activities in Madrid. Also, I thank Dr. Antonio Camacho for having shared with me his expertise during this period.

I would like to thank the PhD board of DiSTAR for having appreciated my work, allowing me in the final defence of my PhD thesis.

I would like to acknowledge the reviewers of my PhD thesis, Dr. Mahak Singh Chauhan and Dr. Maria Charco Romero, for having approved and enjoyed my work; I thank them for their advice, which have surely contributed to the improvement of the thesis.